Experimental Analysis and Reconstruction of the Morphology of Particulate and Monolithic Chromatographic Beds

Dissertation

zur
Erlangung des Doktorgrades
der Naturwissenschaften
(Dr. rer. nat.)

dem

Fachbereich Chemie
der Philipps-Universität Marburg

vorgelegt von

Dipl.-Chem. Stefan Bruns

aus Hannover/Niedersachsen

Marburg an der Lahn 2013

Vom Fachbereich Chemie der Philipps-Universität Marburg (Hochschulkennziffer: 1180)
als Dissertation angenommen am: 21.10.2013

Erstgutachter: Prof. Dr. Ulrich Tallarek
Zweitgutachter: Prof. Dr. Andreas Seubert

Tag der mündlichen Prüfung: 24.10.2013

Die vorliegende Arbeit wurde in der Zeit von Juni 2009 bis August 2013 am Fachbereich Chemie der Philipps-Universität Marburg unter der Leitung von Herrn Prof. Dr. Ulrich Tallarek angefertigt.

In den folgenden Artikeln wurden Teile dieser Dissertation bereits veröffentlicht:

Bruns, S.; Müllner, T.; Kollmann, M.; Schachtner, J.; Tallarek, U. *Anal. Chem.* **2010**, *82*, 6569–6575. *"Confocal Laser Scanning Microscopy Method for Quantitative Characterization of Silica Monolith Morphology"*.

Bruns, S.; Tallarek, U. *J. Chromatogr., A* **2011**, *1218*, 1849–1860. *"Physical Reconstruction of Packed Beds and their Morphological Analysis: Core-shell Packings as an Example"*.

Bruns, S.; Hara, T.; Smarsly, B. M.; Tallarek, U. *J. Chromatogr., A* **2011**, *1218*, 5187–5194. *"Morphological Analysis of Physically Reconstructed Capillary Hybrid Silica Monoliths and Correlation with Separation Efficiency"*.

Bruns, S.; Grinias J. P.; Blue, L. E.; Jorgenson, J. W.; Tallarek, U. *Anal. Chem.* **2012**, *84*, 4496–4503. *"Morphology and Separation Efficiency of Low-aspect-ratio Capillary Ultrahigh Pressure Liquid Chromatography Columns"*.

Bruns, S.; Stoeckel, D.; Smarsly, B. M.; Tallarek, U. *J. Chromatogr., A* **2012**, *1268*, 53–63. *"Influence of Particle Properties on the Wall Region in Packed Capillaries"*.

Bruns, S.; Höltzel, A.; Tallarek, U. *LC-GC North Am.* **2013**, *31*, 486–493. *"Morphological Comparison of Silica Based Monolithic and Particulate Beds by Confocal Laser Scanning Microscopy"*.

Bruns, S.; Franklin, E. G.; Grinias, J. P.; Godinho, J. M.; Jorgenson, J. W.; Tallarek, U. *J. Chromatogr., A* **2013**, submitted. *"Slurry concentration effects on bed morphology and separation efficiency of capillaries packed with sub-2 micron particles"*.

Danksagung

Ohne die Unterstützung anderer Leute wäre diese Arbeit nicht möglich gewesen. Mein Dank gilt deshalb allen, welche in den letzten vier Jahren mit mir gearbeitet und mich unterstützt haben. Ganz besonders gilt dieses natürlich für Prof. Dr. Ulrich Tallarek, welcher mir auf seinem Forschungsgebiet ein spannendes und abwechslungsreiches Thema in einem interdisziplinären Feld zur Verfügung gestellt hat. Ich danke ihm für die gewährten Freiräume und die Möglichkeit große Teile meiner Forschungsarbeit nach Frankfurt hin zu meiner Lebensgefährtin Wiebke Reiche auszulagern. Ich freue mich die Zeit dort mit ihr verbracht haben zu können.

Es freut mich besonders, dass mit Prof. Dr. Andreas Seubert das Zweitgutachten von einem Professor übernommen wird, welcher mich bereits in meinen ersten Studienjahren als Mentor betreut hat.

Meinen Kollegen gilt Dank für eine Arbeitsatmosphäre, welche motiviert morgens ins Labor zu fahren. Die weltweiten Dienstreisen, die wir zusammen unternommen haben, sind Erfahrungen gewesen, welche ich nicht missen möchte.

Der Arbeit meiner Kooperationspartner ist es zu großen Teilen zu verdanken, dass komparative Studien entstehen konnten, welche internationale Anerkennung gefunden haben. Für zahllose Silikamonolithen danke ich Dr. Takeshi Hara. Daniela Stoeckel und James P. Grinias danke ich für die Zeit, welche sie in das Packen und die chromatographische Charakterisierung von gepackten Kapillaren gesteckt haben. Ihren Doktorvätern Prof. Dr. Bernd Smarsly und Prof. Dr. James. W. Jorgenson danke ich, dass sie dieses ermöglicht haben.

Dankeschön und "thank you very much"!

Table of Contents

I. Zusammenfassung

Die vorliegende Arbeit basiert auf den Grundlagen, welche durch die vorangegangene Diplomarbeit *"Dreidimensionale Rekonstruktion monolithischer Festphasen mittels konfokaler Lasermikroskopie"* geschaffen wurden [1]. Sie beschäftigt sich mit der Erfassung dreidimensionaler Bilddaten von Chromatographiesäulen im Kapillarformat sowie deren Rekonstruktion und Auswertung im Hinblick auf die dispersiven Eigenschaften der Trennsäulen. Ein besonderer Schwerpunkt liegt hierbei auf der Charakterisierung von radialen Heterogenitäten. Diese tragen in der UHPLC zu einem Großteil der dispersiven Signalverbreiterung bei und sind deshalb von besonderer Bedeutung bei der Entwicklung von Chromatographiesäulen verbesserter Trenneffizienz [2]. Die dreidimensionale Rekonstruktion ist zudem ein wichtiges Hilfsmittel um den Einfluss von Prozessparametern im Packprozess bei der Darstellung von partikulären Säulen aufzuklären und kann als Modellstruktur für die numerische Simulation der Hydrodynamik in diesen Strukturen dienen. Die in den einzelnen Kapiteln behandelten Thematiken seien hier nachfolgend zusammengefasst:

Kapitel 1 setzt sich mit der Entwicklung eines Probenaufbaus auseinander, welcher die reproduzierbare und präzise dreidimensionale Erfassung von silicabasierten Monolithen im Kapillarformat mittels konfokaler Lasermikroskopie ermöglicht. Es wird eine zweistufige Oberflächenmodifikation zur Fluoreszenzaktivierung eines unmodifizierten Silicamonolithen (Chromolith CapRod) vorgestellt. Hierzu wird die Oberfläche des Monolithen aminiert. Anschließend werden die so eingebrachten Aminofunktionen mit einem Succinimidylester des Fluoreszenzfarbstoffs V450 gekoppelt. Das Kapitel beschreibt einen Probenaufbau für die Mikroskopie, welcher es ermöglicht Aberrationen zu minimieren. Dieses wurde umgesetzt indem der Brechungsindex von Einbettungs- und Immersionsmedium an den Brechungsindex von Quarzglas angepasst wurde. Unter Annahme der Additivität von optischen Aberrationen konnte so durch den Einsatz eines verdünnten Deckglases die Auflösung im Experiment nahe an das Beugungslimit gebracht werden. Die Bilddaten wurden durch eine Entfaltung restauriert und zwecks quantitativer Bildanalyse mittels Hochpassfilter in einen binären Datensatz überführt. Ausgewertet wurde die Porengrößenverteilung anhand von Sehnenlängenverteilungen, welches einen Vergleich mit Daten von Courtois et al. [3] ermöglichte. Diese hatten zuvor bereits Aufnahmen von ver-

gleichbarem Material mittels Transmissionselektronenmikroskopie gemacht und mit Sehnenlängenverteilungen ausgewertet.

Kapitel 2 stellt eine Erweiterung der Messmethode auf partikuläre Festbetten dar. Dieses geschieht anhand einer beispielhaften Rekonstruktion einer 100 µm i.d. Kapillarsäule, welche mit Kinetex Core–Shell Partikeln gepackt wurde. Eine wichtige Verbesserung im Probenaufbau im Vergleich zu Kapitel 1 ist hierbei der Einsatz einer ternären Mischung aus Glycerol, Dimethylsulfoxid und Wasser zur Anpassung des Brechungsindexes von Quarzglas, welche die wellenlängenabhängige chromatische Dispersion mitberücksichtigt. Da die Signalintensität im Verlauf einer mikroskopischen Messung häufig deutlich nachlässt, wurde die Bildverarbeitung um eine tiefenabhängige Korrektur der Signalintensität erweitert. Im Gegensatz zu monolithischen Medien, kann die Rekonstruktion im Fall von gepackten Festbetten unter der Annahme der Sphärizität der Partikel erfolgen. Das Kapitel beschreibt, wie die einzelnen Partikel mittels Bandbreitenfilter lokalisiert und deren Durchmesser abgeschätzt werden können. Es werden eine Visualisierung von Packungsdefekten sowie radiale Porositätsprofile eingeführt. Letztere ermöglichten es zwei Wandeffekte in der Packung zu visualisieren. Zum Einen ist dieses der notwendige geometrische Wandeffekt, welcher seine Ursache darin findet, dass feste sphärische Partikel nicht mit beliebiger Dichte gegen eine feste Wand gepackt werden können [4]. Die Realisierung einer zufällig dichten Packung ist in den ersten, an der Säulenwand angelagerten Partikellagen also nicht möglich. Der zweite beobachtete Wandeffekt ist nicht in jeder Partikelschüttung zu finden. Für die Core–Shell Partikel wurde eine Heterogenität in der Porosität beobachtet, welche sich von der Kapillarwand aus nach einem Porositätsminimum 4–5 Partikeldurchmesser (d_p) von der Kapillarwand aus bis zu ~10.5 d_p tief in die Säule erstreckte. Die Auswertung des Partikelzwischenraums erfolgte erneut anhand von Sehnenlängenverteilungen. Hierbei wurde festgestellt, dass die Verteilungsfunktion durch eine *k*-Gamma-Funktion beschrieben werden kann, welche bereits bei der Beschreibung von Voronoi Volumen-Verteilungen verwendet wurde [5–7]. Die zwei Parameter der *k*-Gamma-Funktion beschreiben die mittlere Sehnenlänge und deren Dispersion. Da Letztere vorwiegend durch längere Sehnen bestimmt wird, welche sich über mehrere Durchflusskanäle erstrecken, folgt, dass die Parameter als Deskriptoren für die Transchannel-Dispersion und Short-range Interchannel-Dispersion nach Giddings [8] herangezogen werden können.

Eine Anwendung der *k*-Gamma-Funktion wird in Kapitel 3 gezeigt. Elf Silicamonolithen in 100 µm i.d. Kapillaren, davon einer C18-modifiziert wurden hinsichtlich ihrer Trenneffizienz und der dazugehörigen Dispersionsbeiträge ausgewertet. Transchannel und Short-range Interchannel-Beiträge werden durch die *k*-Gamma-Funktion der Sehnenlängenverteilung beschrieben. Der Transcolumn-Beitrag wird durch radiale Porositätsprofile und die lokale Porengröße abgedeckt. Es zeigte sich, dass die Trenneffizienz primär mit der Porengröße skaliert. Monolithen welche diesem Verhalten nicht folgten zeigten Unregelmäßigkeiten in ihrer radialen Struktur. Diese äußerten sich in einer erhöhten Porosität oder Porengröße in der direkten Umgebung der Säulenwand. Da der Monolith in der Kapillare hergestellt wird und bei der dabei erfolgenden Kondensationsreaktion die Struktur zwangsweise schrumpft, fand sich der Grund für diese Heterogenitäten in einzelnen von der Säulenwand abgelösten Monolithsträngen. Diese Stränge haben der strukturellen Spannung nicht standgehalten, welches ein grundlegendes Problem bei der Herstellung von Kapillarmonolithen aufzeigt.

Eine erste Studie zum Einfluss von Packparametern auf die Trenneffizienz und Bettstruktur von gepackten Säulen wurde mit Kapitel 4 durchgeführt. Ausgewertet wurden sechs Kapillarsäulen mit variierendem Innendurchmesser von 10–75 µm. Weitere Packparameter wurden hierbei möglichst konstant gehalten. Gepackt waren die Kapillaren mit C18-modifizierten 1.7 µm Acquity BEH Partikeln. Es zeigte sich, dass mit steigendem Innendurchmesser der Kapillaren die Trenneffizienz deutlich abnahm. Dieses kann nicht alleine durch die Geometrie der Säule, d.h. die größere transversale Diffusionslänge über den Säulenradius, erklärt werden, weshalb eine Veränderung in der Morphologie des Bettes vorliegen musste. Das Kapitel zeigt ausführlich, wie die C18-modifizierten Partikel mit dem Fluoreszenzfarbstoff Bodipy 493/503 durch Adsorption angefärbt und in den Bilddaten lokalisiert und rekonstruiert werden können. Zudem wurde die Bildverarbeitung um eine Korrektur des Photonenrauschens und potentieller Drift der Säule während der Messung erweitert. Es zeigte sich, dass mit steigendem Innendurchmesser der Säulen die Packungsdichte in der Wandregion deutlich abnahm. Die verringerte chromatographische Effizienz lässt sich folglich erneut durch einen vergrößerten Transcolumn-Beitrag zur Eddy Dispersion erklären. Zusätzlich wurde beobachtet, dass die Partikelgrößenverteilung über den Säulenquerschnitt keineswegs als konstant angesehen werden kann. Eine im Vergleich zu anderen Säulen verringerte Trenneffizienz ging gleichermaßen auch immer mit

einer Größensegregation der Partikel einher, wobei die Wahrscheinlichkeit kleinere Partikel in der Nähe der Säulenwand zu finden erhöht war.

Kapitel 5 beschreibt eine Studie mit vergleichbarem Ansatz. Sechs verschiedene Partikelsorten wurden hierbei unter gleichbleibenden Bedingungen in Säulen von 100 µm i.d. gepackt. Betrachtet wurden vollporöse 3 µm Atlantis, 3 µm Luna und 3.5 µm Zorbax Partikel sowie 2.7 µm Halo, 2.6 µm Kinetex und 2.5 µm Poroshell Partikel repräsentativ für Core–Shell Materialien. Letztere zeigen aufgrund ihrer abweichenden Produktion eine weitaus engere Partikelgrößenverteilung als vollporöse Partikel, welches häufig als Ursache für eine homogenere Packungsstruktur und daraus resultierenden hervorragenden Trenneffizienz dieser Materialen ($h_{min} < 1.6$) vermarktet wird. Es werden Besonderheiten, wie Agglomerate und Defektpartikel, welche sich in den Packungen der verschiedenen Partikeltypen finden, diskutiert. Leitende Fragestellung für die Studie war jedoch ob Core–Shell Partikel tatsächlich eine homogenere und dadurch effizientere Packungsstruktur ausbilden als vollporöse Materialien. Zuvor hatten Simulationen unserer Arbeitsgruppe bereits gezeigt, dass bei Annahme einer Chromatographiesäule unendlichen Durchmessers die chromatographischen Effizienzgewinne, welche durch eine enge Partikelgrößenverteilung von RSI = 3.4% gegenüber einer Packung aus Partikeln mit einer Partikelgrößenverteilung von RSI = 25.3% erreicht werden, in der chromatographischen Praxis vernachlässigbar sind [9]. Die Rekonstruktionen bestätigen dieses Ergebnis. In der Hauptmasse der Säule waren Core–Shell Materialien mit Hilfe der Auswertung der Sehnenlängenverteilungen nicht von vollporösen Materialien zu unterscheiden. Das Kapitel zeigt jedoch auch, dass die Packungsstruktur dieser beiden Partikeltypen in der Wandregion einer Säule grundlegend verschieden ist. Während Atlantis, Luna und Zorbax Partikel eine gegenüber der Hauptmasse der Säule erhöhte Porosität in der Wandregion der Säule zeigen (0–5 d_p von der Säulenwand entfernt), ist die Porosität von Halo, Kinetex und Poroshell Partikeln hier verringert. Bei den Core–Shell Materialien findet sich benachbart zur direkten Wandregion (0–5 d_p) eine Übergangsregion (5–10 d_p) in der sich die lokale Porosität der Porosität der Hauptmasse annähert. Die Packungen der vollporösen Partikel zeigen hier bereits eine zufällig dichte Packung. Gezeigt wurde dieses über die von der Porosität der Hauptmasse abweichenden Integralflächen im radialen Porositätsprofil, welches Integral Porosity Deviation (IPD) genannt wurde. Das Kapitel zeigt, dass die Wandeffekte in Packungen von vollporösen Materialien einen größeren maximalen Unterschied in der lokalen Fließge-

schwindigkeit des Eluenten verursachen als Packungen von Core–Shell Partikeln. Jedoch erstrecken sich die Wandeffekte im letzteren Fall über einen größeren Bereich des Säulenvolumens, weshalb herausragende Effizienzen mit Core–Shell Partikelsäulen derzeit fast ausschließlich in Säulen mit einem Innendurchmesser > 1 mm zu finden sind.

Eine Aussage, welche sich häufig in den früheren Kapiteln der Arbeit findet, ist, dass der bildgebende Ansatz der Rekonstruktion von Chromatographiesäulen einen Vergleich von partikelbasierten Chromatographiesäulen und monolithischen Säulen ermöglicht. Dieses wird in Kapitel 6 durch einen Vergleich eines Silicamonolithen und einer sub-2 µm Partikelpackung in 20 µm i.d. Kapillaren gezeigt. Die Studie wertet die Mikrostruktur der Säulen im Hinblick auf Transchannel-, Short-range Interchannel- und Transcolumn-Dispersion mit Hilfe der zuvor eingeführten Deskriptoren aus. Es zeigt sich, dass Monolithen das Potenzial haben weitaus homogenere Strukturen auszubilden als Partikelschüttungen. Jedoch ist der Transchannel-Beitrag in den derzeit verfügbaren monolithischen Medien noch weitaus höher als in partikulären Betten. Dieses ist in der Größe der Durchflussporen begründet. Das Ziel der Monolithpreparation muss es folglich sein die Strukturelemente des Materials weiter zu verkleinern ohne dabei die Homogenität des Materials zu verringern, während Partikelpackungen das Ziel haben müssen Wandeffekte abzuschwächen.

Kapitel 7 nimmt die Ergebnisse aus Kapitel 4 noch einmal auf und zeigt, wie die Konzentration der beim Packprozess eingesetzten Partikelsuspension die Mikrostruktur einer Chromatographiesäule beeinträchtigen kann. Hierzu wurden Kapillaren mit Suspensionen unterschiedlicher Partikel (0.9, 1.5 und 1.7 µm Acquity BEH sowie 1.7 µm Kinetex Partikel) und Konzentration (c_s) gepackt und hinsichtlich ihrer Mikrostruktur und chromatographischen Effizienz ausgewertet. Es zeigte sich, dass die Größensegregation der Partikel, welche bei Suspensionen mit $c_s < 1\%$ auftritt, bei $c_s = 2\%–10\%$ unterdrückt werden kann. Die Effizienz der Säulen verbesserte sich dadurch von $h_{min} \approx 2.0$ auf $h_{min} \approx 1.5$. In den Säulen, welche mit Kinetex Partikeln gepackt wurden, ist eine Größensegregation der Partikel aufgrund der engen Partikelgrößenverteilung nicht möglich. Dennoch wurden hier mit höheren c_s Verbesserungen der Effizienz beobachtet. Um die Messunsicherheit, welche mit der Bestimmung der Partikelgröße einhergeht zu eliminieren erfolgte eine Auswertung der lokalen Partikelabstände. Hierbei war zu erkennen, dass die beobachtete Effizienzsteige-

rung einer Verdichtung der Packungsstruktur an der Säulenwand zuzuordnen ist. Der Nachteil höherer Suspensionskonzentrationen zeigte sich in einer erhöhten Anzahl an Packungslücken, sowohl bei vollporösen, als auch bei Core–Shell Materialien. Das Kapitel unterstreicht noch einmal das Potential der kombinierten Anwendung von mikroskopischer Rekonstruktion und makroskopischer chromatographischen Effizienzmessungen. Es zeigt, dass das Packen von Kapillaren steigenden Innendurchmesser eine Erhöhung der Suspensionskonzentration bedarf. Diese sollte so hoch gewählt sein, dass eine Größensegregation der Partikel unterdrückt wird, die Zahl der Packungslücken jedoch minimal bleibt.

Quellenangaben

[1] Bruns, S. *Dreidimensionale Rekonstruktion monolithischer Festphasen mittels konfokaler Lasermikroskopie.* Diplomarbeit, Fachbereich Chemie, Philipps-Universität, Marburg, Germany, **2009**.

[2] Gritti, F.; Guiochon, G. Anal. Chem. 2013, 85, 3017–3035.

[3] Courtois, J.; Szumski, M.; Georgsson, F.; Irgum, K. *Anal. Chem.* **2007**, *79*, 335–344.

[4] de Klerk, A. *AIChE J.* **2003**, *49*, 2022−2029.

[5] Aste, T.; Di Matteo, T. *Phys. Rev. E* **2008**, *77*, 021309.

[6] Schenker, I.; Filser, F. T.; Gauckler, L. J.; Aste, T.; Herrmann, H. *J. Phys. Rev. E* **2009**, *80*, 021302.

[7] Khirevich, S.; Daneyko, A.; Höltzel, A.; Seidel-Morgenstern, A.; Tallarek, U. *J. Chromatogr., A* **2010**, *1217*, 4713–4722.

[8] Giddings, J. C. *Dynamics of Chromatography, Part 1: Principles and Theory*; Marcel Dekker, New York, **1965**.

[9] Daneyko, A.; Höltzel, A.; Khirevich, S.; Tallarek, U. *Anal. Chem.* **2011**, *83*, 3903–3910.

II. Abstract

This work is based upon the fundamentals that were introduced by the preceding diploma thesis *"Dreidimensionale Rekonstruktion monolithischer Festphasen mittels konfokaler Lasermikroskopie"* [1]. It is concerned with the acquisition of three-dimensional image data of chromatography columns in the capillary format as well as their reconstruction and analysis in view of the dispersive properties of the separation column. Key aspect in the characterization are radial heterogeneities because in UHPLC these heterogeneities contribute in large part to dispersive band broadening [2]. Therefore, radial heterogeneities carry a particular significance in the development of chromatography columns of improved separation efficiency. Additionally, the three-dimensional reconstruction of stationary phase support material can aid to shed light on the influence of process parameters in the slurry packing process or be used as a model structure for benchmark simulations in computational studies of hydrodynamic dispersion. Consecutively, the subjects that are covered in the individual chapters of this work are being summarized:

Chapter 1 deals with the development of a sample setup for the reproducible and accurate three-dimensional recording of silica-based capillary monoliths via confocal laser scanning microscopy. It presents a two-step surface modification of unmodified silica monoliths (Chromolith CapRod) that allows for fluorescence activation. This is achieved by aminating the surface of the monolith and coupling a succinimidyl ester of the dye V450 to the introduced amino functions. The chapter describes a sample setup for microscopy that enables the minimization of aberrations by matching the refractive index of embedding and immersion medium to the refractive index of fused silica. Assuming additivity of optical aberrations, the introduction of a thinner than standard cover slip allows for experimental resolutions that are close to the diffraction limit. The image data that were recorded from the monolith were restored by deconvolution and segmented into a binary dataset for quantitative image analysis. The pore size distribution of the monolith's macropores was evaluated using chord length distributions. This enabled a comparison with data recorded by Courtois et al. [3] who already made recordings of a comparable material via transmission electron microscopy.

Chapter 2 extends the imaging method to particulate beds. This is represented by a reconstruction of a 100 µm i.d. capillary column packed with Kinetex core–shell particles. The sample setup in Chapter 1 is improved by using a ternary mixture composed of glycerol, dimethyl sulfoxide, and water for refractive index matching of fused silica. This allowed compensating for wavelength dependent chromatic dispersion. Additionally, a depth dependent correction for signal intensity was introduced. Opposed to monolithic media particle packed beds allow the reconstruction to be guided by the building unit of the structure, i.e., the particle. The chapter describes how individual core–shell particles can be located using a bandpass filtering technique. Their size is estimated assuming perfect sphericity of each particle. The reconstruction is analyzed by visualizing packing defects and introduces a radial transcolumn porosity profile that enabled identifying two distinct wall effects in the bed. One is the geometrical wall effect that is caused by the inability of rigid particles to pack densely to a solid wall [4]. Thus, a random close packing in particle layers next to a confinement is not possible. The second wall effect observed cannot be found in every particle packed bed. The core–shell bed displayed minimal porosity 4–5 particle diameters (d_p) in the column before slowly increasing to bulk porosity at ~10.5 d_p distance from the capillary wall. Again, the interstitial void space was characterized by a chord length distribution. It was realized that its distribution function can be described by a *k*-gamma function that already had been used for the analysis of Voronoi volume distributions [5–7]. The two parameters of the function provide a measure for pore size and pore size dispersion. Since the latter is predominantly determined by chords that reach through 1–2 flow through pores it followed that these parameters could be used a descriptors for transchannel and short-range interchannel dispersion as described by Giddings [8].

An application of the *k*-gamma function is provided in Chapter 3. Eleven silica monoliths prepared in 100 µm i.d. capillaries, one of them C18-modified, were evaluated for their chromatographic separation efficiency and microstructural dispersive contributions. Transchannel and short-range interchannel contribution were described by *k*-gamma fits to the chord length distributions. The transcolumn contribution was covered by radial porosity and pore size distributions. The chapter illustrates that the separation efficiency of silica monoliths primarily scales with the macropore size. Whenever a monolith performed poorer than its pore size suggested, reasoning could be found in irregularities of the radial struc-

ture. The monolith would show an increased porosity or pore size in the vicinity of the capillary wall. Since the monolith is prepared directly within the capillary it is exposed to stress from structural shrinkage during condensation. Stress is elevated by single monolithic rods that snap off from the capillary wall. Thus, Chapter 3 outlines a fundamental problem that accompanies the preparation of capillary monoliths.

A first study on the influence of packing parameters on separation efficiency and bed morphology of packed beds was performed in Chapter 4. Six capillary columns of varying inner diameter from 10 µm to 75 µm were evaluated while other packing parameters were kept constant. The capillaries were packed with C18-modified 1.7 µm Acquity BEH particles. It was observed that separation efficiency would drop with increasing capillary i.d.. This cannot be explained by the geometry of the column alone, i.e., an increasing transverse diffusion length over the column radius. Hence, a change in the bed microstructure has to be observable. The chapter discusses in detail how the C18-modified particles can be stained by adsorption of the fluorescent dye Bodipy 493/503 and how they are localized and reconstructed from the image data. Surplus, the image processing procedure was extended by a correction for photon noise and capillary drift during measurements. It was shown that with increasing capillary i.d. the packing density in the wall region of the capillaries would drop considerably. Thus, again the loss in separation efficiency could be explained by an increased transcolumn contribution to eddy dispersion. It was observed that the particle size distribution could not be seen as a constant along the column diameter. Whenever a column performed poorly a size segregation of particles was observable, i.e., the likelihood of finding small particles in the vicinity of the capillary wall was increased.

Chapter 5 illustrates a study with a comparable approach. Six different particle types where packed with identical conditions in capillaries of 100 µm i.d.. The particles were fully porous 3 µm Atlantis, 3 µm Luna, and 3.5 µm Zorbax particles as well as 2.7 µm Halo, 2.6 µm Kinetex, and 2.5 µm Poroshell particles representing core–shell materials. The latter do have a particle size distribution (PSD) that is much narrower than the PSD of fully porous particles. This is owed to the differing preparation process and frequently marketed as an intrinsic advantage that would yield more homogeneous beds to explain the excellent separation efficiencies of $h_{min} < 1.6$ that can be observed in analytical columns packed with core–shell particles. The chapter discusses anomalies, like agglomerated parti-

cles and defective particles that can be observed in the beds of these different particle types. Guiding topic for the study was if core–shell particles do in fact form beds of higher homogeneity than beds packed with fully porous particles. Previously, simulations in our working group had shown that, under the assumption of an infinite diameter column, the gain in column performance that can be expected due to a narrow PSD of RSI 3.4% can be neglected in chromatographic praxis when compared with the efficiency of a bed packed with particles of a wide PSD (RSI = 25.3%) [9]. The reconstructions confirm these findings since core–shell materials were not distinguishable from fully porous materials using the chord length approach in the bulk of the capillaries. But, the chapter also illustrates that the packing microstructure of these two particle types is fundamentally different in the wall region. While Atlantis, Luna, and Zorbax particles show an increased porosity in the wall region (at 0–5 d_p distance from the capillary wall) when compared with the bulk of the column, the porosity is decreased for Halo, Kinetex, and Poroshell packed beds. Additionally, core–shell materials displayed a transition region (5–10 d_p) in which the local porosity approaches the bulk porosity. At this distance in the column fully porous materials already exhibited bulk properties. This was shown using the integral areas of deviations from the bulk porosity in the porosity profiles, termed integral porosity deviation (IPD). The chapter shows that the maximal velocity inequalities of eluent flow that can be expected in beds of fully porous materials are larger than for core–shell materials. Yet, the volume that is covered by wall effects is larger for core–shell packed beds. Thus, the excellent separation efficiencies observed with core–shell particles are currently limited almost exclusively to columns of > 1 mm i.d..

A statement that can be found in earlier chapters of this work is that the imaging approach of chromatography columns enables an unbiased comparison of monolithic and particulate stationary phase supports. Chapter 6 is dedicated to this by comparing a silica monolith and a sub-2 µm packing in 20 µm i.d. capillaries. The study discusses the microstructure of these columns with regard to transchannel, short-range interchannel, and transcolumn dispersion using the already established descriptors. The chapter illustrates that silica monoliths do have a more homogeneous structure than packed beds. Still, the transchannel contribution in the currently available monolithic media is much higher than for state of the art particulate columns. Thus, silica monolith preparation has to target a

reduction in pore size while conserving the structural homogeneity of the present materials, whereas particulate packings have to focus on an attenuation of the wall effects.

Chapter 7 picks up the results of Chapter 4 and shows how the bed microstructure is affected by the slurry concentration (c_s) used in the slurry packing process. For this purpose capillaries were packed with slurries of varying particles (0.9, 1.5, and 1.7 µm Acquity BEH and 1.7 µm Kinetex particles) and concentration. The beds were characterized for their separation efficiency and microstructural properties. The study showed that size segregation of particles that occurs at $c_s < 1\%$ can be suppressed at $c_s = 2\%–10\%$. The efficiency of these columns was improved by this from $h_{min} \approx 2.0$ to $h_{min} \approx 1.5$. For the capillaries packed with Kinetex material particle size segregation was not possible because of the narrow particle size distribution of these particles. Still, improvements in efficiency were observable when c_s was increased. To eliminate the uncertainty that comes with estimating the particle size the local distance of particles was discussed. This enabled to visualize that higher separation efficiencies can be explained by a densification of the bed in the crucial wall region. The trade-off that higher slurry concentrations showed was an increased number of packing gaps, both in fully porous and core–shell packed beds. Once again, the chapter highlights the potential of using microscopic reconstruction and an analysis of macroscopic separation efficiency comprehensively. It illustrates that the packing of beds of increasing inner diameter requires higher slurry concentrations. The concentrations should be chosen to suppress particle size segregation while keeping the amount of packing gaps as small as possible.

References

[1] Bruns, S. *Dreidimensionale Rekonstruktion monolithischer Festphasen mittels konfokaler Lasermikroskopie.* Diplomarbeit, Fachbereich Chemie, Philipps-Universität, Marburg, Germany, **2009**.

[2] Gritti, F.; Guiochon, G. Anal. Chem. 2013, 85, 3017–3035.

[3] Courtois, J.; Szumski, M.; Georgsson, F.; Irgum, K. *Anal. Chem.* **2007**, *79*, 335–344.

[4] de Klerk, A. *AIChE J.* **2003**, *49*, 2022−2029.

[5] Aste, T.; Di Matteo, T. *Phys. Rev. E* **2008**, *77*, 021309.

[6] Schenker, I.; Filser, F. T.; Gauckler, L. J.; Aste, T.; Herrmann, H. *J. Phys. Rev. E* **2009**, *80*, 021302.

[7] Khirevich, S.; Daneyko, A.; Höltzel, A.; Seidel-Morgenstern, A.; Tallarek, U. *J. Chromatogr., A* **2010**, *1217*, 4713–4722.

[8] Giddings, J. C. *Dynamics of Chromatography, Part 1: Principles and Theory*; Marcel Dekker, New York, **1965**.

[9] Daneyko, A.; Höltzel, A.; Khirevich, S.; Tallarek, U. *Anal. Chem.* **2011**, *83*, 3903–3910.

III. Introduction

The chromatographic characterization of an HPLC column is essentially limited to bulk parameters such as porosity, permeability, peak shape, or most prominently separation efficiency. Frequently, shortcomings in separation efficiency are associated with heterogeneities in the bed structure but this is neither easily proofed nor improved if the origins of these heterogeneities remain unknown. Therefore, it is an essential requirement for column technology and the fundamental understanding of dispersion in chromatography to be able to visualize and quantify microstructural features in a separation column.

During the course of this work the chromatographic community experienced a landslide development in particle technology. Commonly, a reduced plate height value in the minimum of the plate height curve of $h_{min} \approx 2$ has been seen to provide a bed packed homogenously with fully porous particles. Now a new generation of core–shell particles was released that allows for remarkably efficient beds with $h_{min} < 1.6$ (in the analytical column format) [1–4]. Higher pressure instrumentation gave rise to UHPLC and enabled using columns packed with sub-2 µm fully porous particles. At present columns packed with 1.3 µm Kinetex core–shell particles constitute the smallest particles ever commercially available in a chromatography column [5].

Although their development stalled for several years silica monolith based chromatography columns have established themselves as an alternative to particle packed beds in small molecule separations providing high permeability and thus the capability of high speed separations. Finally, in 2012 the Merck KGaA (Darmstadt, Germany) announced the release of the 2nd generation of Chromolith columns named Chromolith High-Resolution. With these columns a $H_{min} \approx 7$ µm is now achievable [6,7]. The reasons that allowed for these severe improvements in separation efficiency are a reduced pore size when compared with the 1st generation and an improved cladding procedure minimizing potential void region at the column–monolith interface [7,8].

All these developments in column technology moved the relevance of bed heterogeneities in a renewed perspective. Misleadingly, it was speculated that the excellent performance of core–shell particles is based on their narrow particle size distribution that allows for a higher homogeneity in the bulk of the bed [9]. Again, a higher radial homogeneity seems a far more likely explanation [10]. In a recent perspective by Gritti and Guiochon

the transcolumn dispersion, which is caused by column cross-sectional heterogeneities in a packing, dominates the efficiency of particle-packed beds with up to 70% of the total dispersion in UHPLC columns [11]. Notably, the available UHPLC instrumentation is already working at full capacity with the sub-2 µm particle packed columns due to pressure limitations. Thus, the biggest potential in further plate height reduction can be found in improving the transcolumn homogeneity in particulate and monolithic beds alike.

Studies on columns in the analytical format have been able to characterize radial heterogeneities on the column scale via locally resolved elution profiles using an on-column local electrochemical detector [12–14]. Although only a handful of data points can be generated over a column inner diameter (i.d.) of 4.6 mm by this method the measurements already impressively demonstrated how the separation efficiency of a column is deteriorated by the presence of wall effects, i.e., heterogeneities in packing density that are induced by the presence of a confining column wall. Such porosity biases directly translate into velocity biases in the mobile phase causing eddy dispersion and the awareness of the relevance of transcolumn dispersion has led to developments that aim to minimize its impact on separation efficiency, e.g., the parallel segmented flow technique [15–18].

In capillary chromatography the above methods are all not applicable. Therefore, the purpose of this thesis was to develop and apply an approach that allows detecting and quantifying heterogeneities in capillary columns; preferably on all the length scales that are relevant to eddy dispersion [19,20]. For this a straightforward and comprehensive approach is to generate an image of the bed microstructure itself and apply appropriate morphological descriptors to it. Yet, standard scanning electron microscopy, which is applied most frequently to describe the morphology of a stationary phase support, does not transport sufficient morphological information, i.e., the features in the bed microstructure cannot be localized accurately due to a lack of depth information. The minimum requirement for localization of structural features and quantitative characterization of the bed morphology via imaging are two-dimensional slices, e.g., images from transmission electron microscopy [21]. Apparently, three-dimensional reconstructions of a column segment are even preferable over two-dimensional images because the available sample volume that can be characterized is much larger and all morphological information of the bed microstructure is conserved, e.g., the pore connectivity which is lost in 2D.

Simulations have proven to be an unexcelled tool in unraveling the complex morphology–transport relationships that exist in a separation column [10,20,22–33]. They allow for

an incremental variation of morphological parameters, like porosity or disorder, with an amount of control that is unobtainable in an experiment. Yet, algorithms that simulate the packing of particles in a column cannot account for all interrelationships between experimental packing parameters and resulting bed morphology. This is especially critical when wall effects are to be considered. Even more model structures of monolithic media that have been used for simulations [34–36] lack a sound physical background which provides another reason to pursue three-dimensional reconstructions of chromatography columns. These reconstructions can form an invaluable bridging element between the simulation of hydrodynamic dispersion and experimental data. They can serve to compute benchmark simulations or provide a model structure of a monolith that can be expected to provide results that are far more reliable than simulations based on a model structure that assumes a tetrahedral geometry for the monolith.

Apart from interests that might seem to be of a primarily academic origin, three-dimensional reconstructions may also aid the manufacturer of monolithic and particle packed columns to improve their preparation conditions. The efficient preparation of silica monoliths and particle packed beds has always been a great secret among practitioners and the industry. The effects of individual packing parameters on the bed morphology are poorly understood and seldom explored systematically. Again, this requires quantitative knowledge of the bed microstructure. Only controlled preparation conditions combined with comprehensive knowledge of bed microstructure and macroscopic separation efficiency allow deducting the impact of varying preparation conditions and call for the three-dimensional reconstruction of a bed that has been prepared and characterized chromatographically.

From the pool of available methods for three-dimensional image acquisition confocal laser scanning microscopy (CLSM) was the first choice for this project. It is convenient that the instrumentation is available at many research facilities and image acquisition can be performed in a matter of minutes. But, more importantly the dimensions that can be covered by CLSM match with the dimensions of capillary HPLC columns and sectioning of a sample is performed optically, i.e., mechanically invasive preparation steps that might alter the microstructure of the bed can be avoided.

As a matter of fact this thesis is not the first to apply CLSM to chromatographic support material. Jinnai and co-workers [37–42] already approached the formation process and geometrical properties like pore shape and connectivity of custom prepared polymer and

silica-based monoliths using three-dimensional reconstructions acquired by CLSM. Yet, the investigated samples were either unconfined or confined between two coverslips and transferring their method to an actual separation column is far from being trivial. Present chromatographic support media show features on the size close to the resolution capacities of a confocal microscope requiring an optimized optical setup for accurate imaging. However, capillary columns do have a curved surface and are made of fused silica which requires compensation because the refractive index of fused silica deviates from the specifications required for a standard CLSM sample. The preceding diploma thesis [44] to this thesis already explored the potential of CLSM for an on-column characterization of capillary HPLC columns that formed the basis for this work.

It is the scope of this work to establish a reproducible and robust method for three-dimensional imaging and reconstruction of capillary columns in a silica monolithic and particulate layout. Chapter 1 and 2 are almost exclusively dedicated to this introducing the reconstruction and analysis of a tetramethoxysilane-based monolithic and a column packed with core–shell particles. Later chapters deal with the application of the method to the preparation of capillary HPLC columns and the refinement of morphological descriptors that provide a correlation to separation efficiency. These studies all have a strong focus on radial heterogeneities that may occur in a separation column. They are ordered chronologically. In Chapter 3 the morphology of tetramethoxysilane–methyltrimethoxysilane hybrid monoliths is investigated and related to their separation efficiency. The study illustrates how the efficiency of these monoliths is affected by detachments of monolithic rods from the capillary wall. The preparation conditions in the slurry packing of particulate columns are in the focus of Chapter 4, 5, and 7. Chapter 4 discusses the effects of a varying capillary inner diameter on the bed structure of capillaries packed with sub-2 µm particles. Deviations in radial porosity from the bulk porosity are quantified and related to the separation efficiency of the columns. It is the first work that visualizes particle size-segregation effects in a capillary column. Chapter 5 outlines differences in bed morphology that come with different particle types. Three types of fully porous and three types of core–shell particles are compared for their microstructural properties and radial heterogeneity. The findings in Chapter 4 and 5 suggested investigating the effects of slurry concentration on bed morphology both for fully porous and core–shell materials. This is done in Chapter 7 and outlines how the slurry concentration affects packing defects and particle size-segregation. Finally, Chapter 6 provides a comparison of a 20 µm i.d. silica monolithic capillary and a

20 µm i.d. particle packed capillary. The chapter shows the advantages and disadvantages of the two different stationary phase support concepts by analyzing their microstructural properties. Although the conclusions of this study seem little surprising it provides a comparison that would not be possible without the availability of three-dimensional reconstructions.

References

[1] Kirkland, J. J.; Langlois, T. J.; DeStefano, J. J. *Am. Lab.* **2007**, *39*, 18–21.

[2] Gritti, F.; Leonardis, I.; Shock, D.; Stevenson, P.; Shalliker, A.; Guiochon, G. *J. Chromatogr., A* **2010**, *1217*, 1589–1603.

[3] Gritti, F.; Guiochon, G. *J. Chromatogr., A* **2010**, *1217*, 8167–8180.

[4] Guiochon, G.; Gritti, F. *J. Chromatogr., A* **2011**, *1218*, 1915–1938.

[5] Farkas, T.; Chitty, M.; Layne, J.; Anspach, J.; Sanchez, C. *The New Cutting Edge in Reversed-Phase UHPLC Performance: 1.3 µm Core-Shell Particles*. Oral presentation at HPLC 2013, Amsterdam, The Netherlands, **2013**.

[6] Cabrera, K. *LC-GC North Am.* **2012**, *S*, 56–60.

[7] Hormann, K.; Müllner, T.; Bruns, S.; Höltzel, A.; Tallarek, U. *J. Chromatogr., A* **2012**, *1222*, 46–58.

[8] Hlushkou, D.; Hormann, K.; Höltzel, A.; Khirevich, S.; Seidel-Morgenstern, A.; Tallarek, U. *J. Chromatogr., A* **2013**, 1303, 28–38.

[9] Cabooter, D.; Fanigliulo, A.; Bellazzi, G.; Allieri, B.; Rottigni, A.; Desmet, G. *J. Chromatogr., A* **2010**, *1217*, 7074–7081.

[10] Daneyko, A.; Höltzel, A.; Khirevich, S.; Tallarek, U. *Anal. Chem.* **2011**, *83*, 3903–3910.

[11] Gritti, F.; Guiochon, G. *Anal. Chem.* 2013, 85, 3017–3035.

[12] Abia, J. A.; Mriziq, K. S.; Guiochon, G. A. *J. Chromatogr., A* **2009**, *1216*, 3185–3191.

[13] Abia, J. A.; Mriziq, K. S.; Guiochon, G. A. *J. Sep. Sci.* **2009**, *32*, 923–930.

[14] Gritti, F.; Leonardis, I.; Abia, J.; Guiochon, G. *J. Chromatogr., A* **2010**, *1217*, 3819–3843.

[15] Camenzuli, M.; Ritchie, H. J.; Ladine, J. R.; Shalliker, R. A. *J. Chromatogr., A* **2012**, *1232*, 47–51.

[16] Shalliker, R. A.; Camenzuli, M.; Pereira, L.; Ritchie, H. J. *J. Chromatogr., A* **2012**, *1262*, 64–69.

[17] Camenzuli, M.; Ritchie, H. J.; Ladine, J. R.; Shalliker, R. A. *J. Liq. Chromatogr. Related Technol.* **2013**, *36*, 1379–1390.

[18] Gritti, F.; Guiochon, G. *J. Chromatogr., A* **2013**, *1297*, 64–76.

[19] Giddings, J. C. *Dynamics of Chromatography, Part 1: Principles and Theory*; Marcel Dekker, New York, **1965**.

[20] Khirevich, S.; Höltzel, A.; Seidel-Morgenstern, A.; Tallarek, U. *Anal. Chem.* **2009**, *81*, 7057–7066.

[21] Courtois, J.; Szumski, M.; Georgsson, F.; Irgum, K. *Anal. Chem.* **2007**, *79*, 335–344.

[22] Maier, R. S.; Kroll, D. M.; Bernard, R. S.; Howington, S. E.; Peters, J. F.; Davis, H. T. *Phys. Fluids* **2000**, *12*, 2065–2079.

[23] Maier, R. S.; Kroll, D. M.; Bernard, R. S.; Howington, S. E. Peters, J. F.; Davis, H. T. *Philos. Trans. R. Soc. Lond., A* **2002**, *360*, 497–506.

[24] Kandhai, D.; Hlushkou, D. Hoekstra, A. G.; Sloot, P. M. A.; Van As, H.; Tallarek, U. *Phys. Rev. Lett.* **2002**, *88*, 234501.

[25] Schure, M. R.; Maier, R. S.; Kroll, D. M.; Davis, H. T. *Anal. Chem.* **2002**, *74*, 6006–6016.

[26] Maier, R. S.; Kroll, D. M.; Bernard, R. S.; Howington, S. E.; Peters, J. F.; Davis H. T., *Phys. Fluids* **2003**, *15*, 3795–3815.

[27] Schure, M. R.; Maier, R. S. *J. Chromatogr., A* **2006**, *1126*, 58–69.

[28] Maier, R. S.; Kroll, D. M.; Davis, H. T. *AIChE J.* **2007**, *53*, 527–530.

[29] Khirevich, S.; Höltzel, A.; Ehlert, S.; Seidel-Morgenstern, A.; Tallarek, U. *Anal. Chem.* **2009**, *81*, 4937–4945.

[30] Khirevich, S.; Höltzel, A.; Tallarek, U. *Philos. Trans. R. Soc. Lond., A* **2011**, *369*, 2485–2493.

[31] Khirevich, S.; Höltzel, A.; Daneyko, A.; Seidel-Morgenstern, A.; Tallarek, U. *J. Chromatogr., A* **2011**, *1218*, 6489–6497.

[32] Daneyko, A.; Khirevich, S.; Höltzel, A.; Seidel-Morgenstern, A.; Tallarek, U. *J. Chromatogr., A* **2011**, *1218*, 6746–6753.

[33] Daneyko, A.; Hlushkou, D.; Khirevich, S.; Tallarek, U. *J. Chromatogr., A* **2012**, *1257*, 98–115.

[34] Vervoort, N.; Gzil, P.; Baron, G. V.; Desmet, G. *Anal. Chem.* **2003**, *75*, 843–850.

[35] Vervoort, N.; Gzil, P.; Baron, G. V.; Desmet, G. *J. Chromatogr., A* **2004**, *1030*, 177–186.

[36] Gzil, P.; Vervoort, N.; Baron, G. V.; Desmet, G. *J. Sep. Sci.* **2004**, *27*, 887–896.

[37] Saito, H.; Kanamori, K.; Nakanishi, K.; Hirao, K.; Nishikawa, Y.; Jinnai, H. *Colloids Surf., A* **2007**, *300*, 245–252.

[38] Saito, H.; Nakanishi, K.; Hirao, K.; Jinnai, H. *J. Chromatogr., A* **2006**, *1119*, 95–104.

[39] Saito, H.; Kanamori, K.; Nakanishi, K.; Hirao, K.; Nishikawa, Y.; Jinnai, H. *Colloids Surf., A* **2004**, *241*, 215–224.

[40] Jinnai, H.; Watashiba, H.; Kajihara, T.; Takahashi, M. *J. Chem. Phys.* **2003**, *119*, 7554–7559.

[41] Kanamori, K.; Nakanishi, K.; Hirao, K.; Jinnai, H. *Langmuir* **2003**, *19*, 5581–5585.

[42] Jinnai, H.; Nakanishi, K.; Nishikawa, Y.; Yamanaka, J.; Hashimoto, T. *Langmuir* **2001**, *17*, 619–625.

[43] Jinnai, H.; Nishikawa, Y.; Morimoto, H.; Koga, T.; Hashimoto, T. *Langmuir* **2000**, *16*, 4380–4393.

[44] Bruns, S. *Dreidimensionale Rekonstruktion monolithischer Festphasen mittels konfokaler Lasermikroskopie.* Diplomarbeit, Fachbereich Chemie, Philipps-Universität, Marburg, Germany, **2009**.

Chapter 1

Confocal Laser Scanning Microscopy Method for Quantitative Characterization of Silica Monolith Morphology

Authors:

Stefan Bruns, Tibor Müllner, Martin Kollmann, Joachim Schachtner, Alexandra Höltzel, and Ulrich Tallarek

State of Publication:

Published August 1, 2010 in *Analytical Chemistry*, Vol. 82, No. 15, p. 6569–6575.

Abstract

We present a fast, nondestructive, and quantitative approach to characterize the morphology of capillary silica-based monolithic columns by reconstruction from confocal laser scanning microscopy images. The method comprises column pretreatment, image acquisition, image processing, and statistical analysis of the image data. The received morphological data are chord length distributions for the bulk macropore space and skeleton of the silica monolith. The morphological information is shown to be comparable to that derived from transmission electron microscopy, but far easier to access. The approach is generally applicable to silica-based capillary columns, monolithic or particulate. It allows the rapid acquisition of hundreds of longitudinal and cross-sectional images in a single session, resolving a multitude of morphological details in the column.

1.1 Introduction

Monolithic stationary phases prepared from organic polymers or porous silica have found widespread application in separation science as an alternative to particulate beds [1-15]. In the hierarchically structured pore space of monoliths, macropores enable convective transport and mesoporous skeletons provide a large surface area accessible by diffu-

sion [16,17]. Key feature in the hydrodynamics and mass transfer kinetics of the chromatographic process is the stationary phase morphology [18].The synthesis of silica monoliths for chromatography, introduced by Nakanishi and co-workers [19-23], allows us to modify macropore size and skeleton thickness independently from each other. Macroporosity, pore size distribution, and domain size (i.e., the sum of macropore size and skeleton thickness) are statistical measures that describe the hydraulic permeability of the silica monolith, whereas eddy dispersion additionally depends on the pore interconnectivity [24-28]. Most often indirect methods like inverse size exclusion chromatography, mercury intrusion porosimetry, and gas sorption are used to measure porosity, pore size distributions, and specific surface area of porous media. However, these methods rely on assumptions about the pore geometry (e.g., a cylindrical, open pore structure) that may have limited applicability for the investigated porous medium. Thus, the results of indirect methods depend on the accuracy of the underlying model [28-33].

Imaging techniques like scanning and transmission electron microscopy (SEM and TEM, respectively) provide a direct, model-independent insight into the pore structure at nanometer resolution. Porosity, pore size distribution, and surface area of a stationary phase can be derived from cross-sectional TEM micrographs of the column by quantitative stereology [34]. Acquisition of TEM images is a time- and skill-consuming process, as it requires the sample to be embedded, cut with a microtome, and polished in the preparation process. Additionally, the fused-silica wall of capillary columns has to be removed before cutting with hydrofluoric acid [34]. SEM images are more easily accessible: the column is cut, and the resulting surface, usually the column cross section, is covered with a thin gold layer [33,25]. The morphology of newly synthesized monoliths is usually characterized by visually estimating the average domain size from SEM images. However, SEM images offer no reliable depth information and thus lack the required morphological details. At the moment, the insufficient characterization of silica monoliths limits systematic optimization of their fabrication to yield highly efficient high-performance liquid chromatography (HPLC) columns [16,17].

The usefulness of morphological information from TEM and SEM depends on the quality and number of representative cuts from the investigated column. As an alternative to these column-cutting methods, confocal laser scanning microscopy (CLSM) has been used previously for the characterization of monolithic materials. CLSM is nondestructive, widely and commercially available, enjoys simple and fast sample preparation, and allows

the rapid acquisition of longitudinal and cross-sectional images at any position in the column. Between 2000 and 2007, Jinnai and co-workers [36-42] in particular published three-dimensional (3D) reconstructions of custom-prepared organic polymer and silica-based monoliths. They investigated monolithic samples not in a column format, but either unconfined or confined between two coverslips. The 3D reconstructions gave insight into the formation process of monoliths and their geometrical properties like pore shape and connectivity.

In particulate columns the interparticle pore size and heterogeneity are intimately coupled to the particle sizes and the packing density, which makes particle size distribution and porosity suitable descriptors of pore space morphology. However, the microstructure of more complex random porous media like monoliths, which lack an elementary building unit comparable to a spherical particle, cannot be sufficiently characterized with an object-oriented approach. As an alternative, chord length distributions (CLDs) and closely related statistical analysis measures, whose calculation does not involve assumptions about the shape of morphological elements, have been frequently used to characterize the properties of random porous media [43-47]. Size and shape of a CLD are influenced by the volume ratio, surface area, anisotropy, and heterogeneity of the underlying morphological element. Therefore, the monolithic macropore morphology should be comprehensively and accurately described by statistical analysis in terms of CLDs. Although it is possible that different macropore morphologies result in identical CLDs, a narrow CLD will point to a homogeneous monolith with high separation efficiency. Courtois et al. [34] have paved the way by introducing CLDs derived from TEM micrographs for the characterization of monolith morphology. Beside several organic polymer-based monolithic columns, they also investigated silica-based Chromolith columns.

In this work we show how CLSM – though inferior in resolution – can provide quantifiable morphological information comparable to TEM. We investigate a commercially available HPLC capillary column with a bare-silica monolithic stationary phase (Chromolith CapRod). The manufacturer has specified the average macropore size of the monolith as 2 µm by mercury intrusion porosimetry. Consequently, the resolution of the optical system is critical. We will give a detailed description of all necessary steps required to image a monolithic bare-silica capillary column close to the diffraction limit and extract the desired morphological information. These steps comprise column pretreatment, image acquisition, image processing, and statistical analysis. The received CLDs are compared with the previous TEM-based characterization and discussed in terms of silica monolith morphology.

1.2 Experimental Section

1.2.1 Chemicals and Materials. Research samples of ca. 60 cm long bare-silica monolithic columns (Chromolith CapRod) in 100 µm i.d. fused-silica capillaries were provided by Merck KGaA (Darmstadt, Germany). 3-Carboxy-6-chloro-7-hydroxycoumarin was purchased from Endotherm Life Science Molecules (Saarbrücken, Germany); 3-aminopropyltriethoxysilane, N,N′-disuccinimidyl carbonate (DSC), and 4-dimethylaminopyridine (DMAP) were supplied by Alfa Aesar GmbH (Karlsruhe, Germany). Triethylamine (Et3N), dimethyl sulfoxide (DMSO), glycerol, HPLC-grade ethanol and methanol, and dimethylformamide (DMF) were purchased from Sigma Aldrich Chemie GmbH (Taufkirchen, Germany). HPLC-grade water was obtained from a Milli-Q gradient water purification system (Millipore, Bedford,MA).

1.2.2 Column Pretreatment. Figure 1.1 gives an overview of the column pretreatment steps. A succinimidyl ester of dye V450 was synthesized with 75% yield starting from 3-carboxy-6-chloro-7-hydroxycoumarin as described by Abrams et al. [48]. The bare silica surface of the monolithic column was amine-modified for covalent binding of the V450-succinimidyl ester following a method outlined by El Kadib et al. [49]. For this purpose, a ca. 12 cm long piece of the capillary column was first cleaned with 0.5 mL of methanol at a flow rate of 2 µL/min. Next, 750 µL of a 3-aminopropyltriethoxysilane solution (0.1 M in ethanol) was pumped through the column at 1 µL/min and 70 °C overnight. The amine-modified column was then flushed subsequently with 0.5 mL of ethanol and 0.5 mL of methanol/water 50/50 (v/v) at 2 µL/min. For covalent attachment of the dye to the monolith's surface, 150 µL of a V450-succinimidyl ester solution (5 mg in 250 µL of DMF) was pumped through the amine-modified column at 0.2 µL/min. Purging with 0.5 mL of DMSO/water 81/19 (v/v) at 2 µL/min removed excess dye and prepared the column for CLSM experiments.

Repeated sample preparations have shown that the optimal dye concentration varies for each column and depends on the monolith's age, surface activity, and modifications. If the dye concentration is too high ("dye overload"), the fluorescence excitation of deeper layers in the sample will be hampered, which is visible in the images as an increased shading toward the column center (Figure 1.5A). In contrast to insufficient dye coating, however, dye

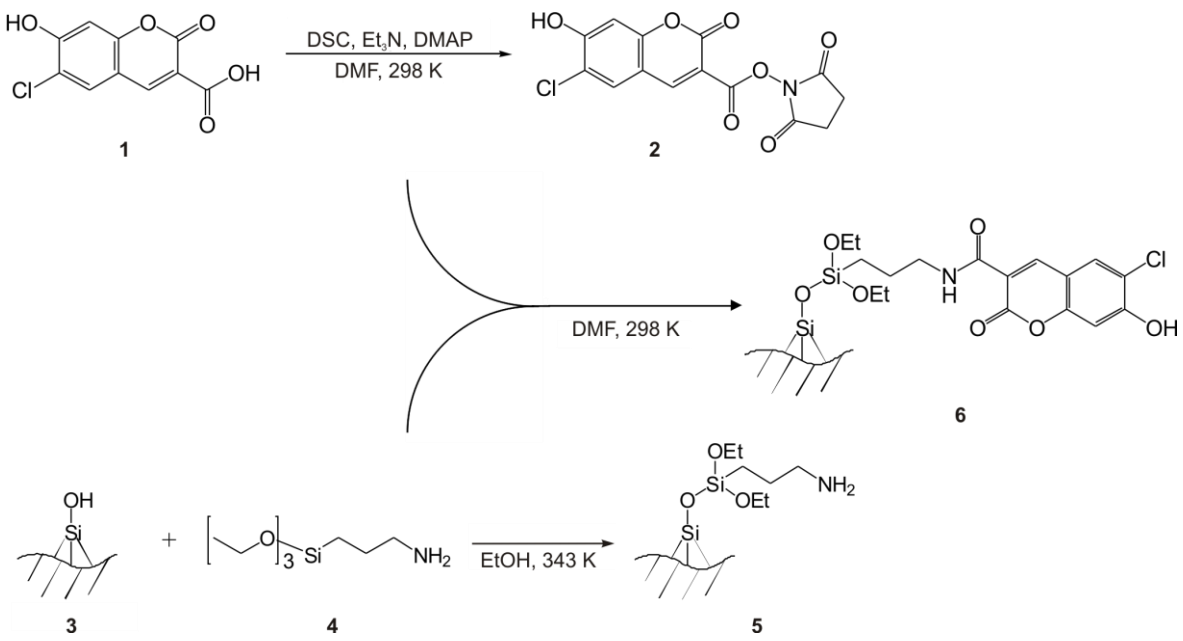

Figure 1.1: Surface modification of the bare-silica monolith for CLSM. Starting from 3-carboxy-6-chloro-7-hydroxycoumarin (**1**), the succinimidyl ester of dye V450 (**2**) was synthesized as described by Abrams et al. [48] with 75% yield. Amine modification of the bare silica surface of the monolithic column (**3**) was carried out with 3-aminopropyltriethoxysilane (**4**) according to El Kadib et al. [49]. Reaction of the amine-modified surface (**5**) with V450-succinimidyl ester (**2**) resulted in covalent attachment of the dye to the monolith's skeleton (**6**).

overload is uncritical, because excess dye in the sample can easily be removed ("bleached") by laser irradiation during or before image acquisition. The above-reported concentration of 20 mg/mL of V450-succinimidyl ester, e.g., required strong irradiation of the sample, so lower dye concentrations are possible for column pretreatment. A homogeneous luminosity distribution in the images is optimal, but as long as image foreground and background are clearly separated at the column wall and center, the subsequent image analysis is not compromised due to the employed edge-based image segmentation method (see below). In fact, a slight dye overload might be beneficial for scanning large image stacks, because the amount of dye limits the time of exposition for each volume increment until signal and background noise merge.

1.2.3 Image Acquisition. Images were acquired on a TCS SP5 confocal microscopy system equipped with a HCX PL APO 63×/1.3 GLYC CORR CS (21°) glycerol immersion objective lens from Leica Microsystems (Wetzlar, Germany). Before the column was mounted on a custom-made microscope slide, the polyimide coating was removed from an ~1 cm long segment of the capillary column with a drop of warm sulfuric acid. The column was constantly flushed with DMSO/water 81/19 (v/v) at a flow rate of 0.5 µL/min. Glycerol/water 83/17 (v/v) was used as immersion and embedding liquid. Aqueous mixtures of DMSO and glycerol were prepared in the given volumetric ratios and then calibrated to match the refractive index of the fused-silica capillary wall (n = 1.4582) with an AR200 digital refractometer (Reichert Analytical Instruments, Depew, NY). A "type 0" coverslip of 120 µm thickness separated embedding and immersion liquid.

From the excitation and emission maxima of the V450 dye at 404 and 448 nm, respectively, the Nyquist sampling criterion was calculated for the applied objective as 38 nm in lateral directions and 126 nm in axial direction. The digital zoom was chosen to match a pixel size of 30 nm. A UV diode laser was used for excitation at 405 nm. Fluorescence emission was detected in the interval between 425 and 480 nm. In total, 170 slices in the x-y plane (i.e., along the column axis) at a distance of 126 nm from each other were recorded as 16-bit grayscale images of 2048 × 2048 pixels (200 Hz, three line averages), yielding a captured volume (in x-, y-, and z-directions) of 61.5 × 61.5 × 21.4 µm³.

1.2.4 Image Processing. Huygens maximum likelihood iterative deconvolution (Scientific Volume Imaging, Hilversum, The Netherlands) was applied to the acquired image stack for a more realistic representation of the original object. The software incorporates the removal of high-frequency noise and background, which is why, as a preprocessing step to deconvolution, we only considered bleaching of the dye by fitting a second-order exponential decay to the acquired image stack's intensity distribution.

For image segmentation a copy of the acquired image stack was blurred with a Gaussian kernel and then subtracted from the deconvolved original [50]. A value of 200 σ was chosen as kernel size, a value that is large compared with image features and small compared with background variations.

1.2.5 Image Analysis. The segmented images were analyzed following the method outlined by Courtois et al. [34] using in-house software written with Visual Studio C# 2008 (Microsoft Corporation, Redmond, WA). Briefly, to analyze the macropore space points were randomly selected from the void area. From each point vectors were projected in 32 angularly equispaced directions until they either hit the skeleton or projected out of the image boundaries. The latter vectors were discarded. A chord length was then calculated as the sum of the absolute lengths of an opposed pair of vectors. Statistics for the chord lengths were collected from 4×10^5 chords randomly distributed over the image stack. Using 4×10^5 chords generated in the skeleton area a distribution of the skeleton thickness was generated in the same manner.

1.3 Results and Discussion

The specified average macropore size of the investigated Chromolith column is ~2 µm. This puts the required resolution of the optical system close to the diffraction limit. Therefore all experimental steps – from selection of the fluorescent dye to the details of image acquisition and processingswere optimized for resolution.

1.3.1 Column Pretreatment. For a fluorescent, uniform labeling of the bare-silica monolithic skeleton, the dye V450 was chosen. It can be covalently attached to the silanol groups of the silica surface (Figure 1.1). The excitation maximum of V450 (404 nm) closely matches the UV diode laser line (405 nm), and the small Stokes shift of 44 nm ensures that detection remains in the shorter wavelength part of the spectrum (448 nm), an important consideration as axial and lateral resolution both decrease with the mean of excitation and emission wavelengths [51].

1.3.2 Image Acquisition. Degeneration of resolution in optical microscopy is almost exclusively caused by spherical aberrations from a refractive index (RI) mismatch between sample and objective. This is especially critical for glycerol and water objectives, which are designed to be used with standardized coverslips. The RI mismatch introduced by deviations from the standard coverslip thickness can be partially compensated by tuning the correction collar of the objective. For an aberration-free optical system with our experimental device Nyquist-Calculator [52] simulates a point spread function with a lateral resolution (FWHM) of 0.185 µm and an axial resolution of 0.389 µm (Figure 1.2A). If spherical aberrations from, e.g., a 40 µm thick coverslip are introduced to the system, the point spread function broadens to a lateral resolution of 0.197 µm and an axial resolution of 0.894 µm (Figure 1.2B). Consequently, the quality of our measurements will be limited by the achievable resolution along the optical axis, i.e., the optical slice thickness.

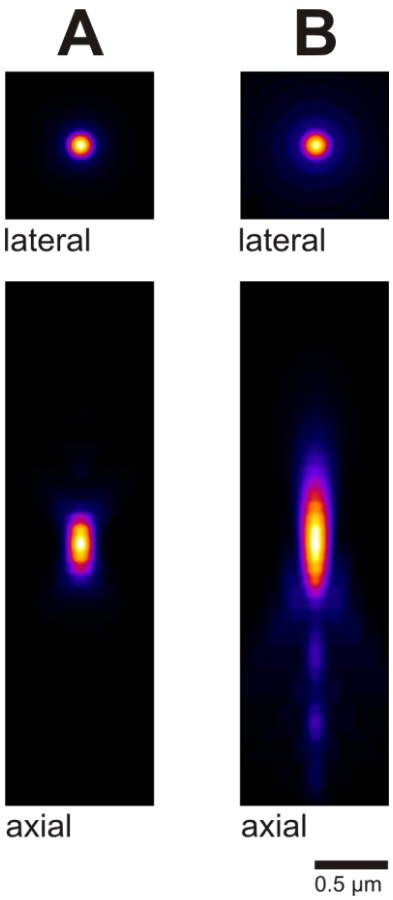

Figure 1.2: Lateral and axial point spread functions simulated with the Nyquist-Calculator [52] for (**A**) an aberration-free optical system (FWHM (lateral) ≈ 0.185 µm, FWHM (axial) ≈ 0.389 µm) and (**B**) a system with aberrations from a 40 µm thick coverslip (FWHM (lateral) ≈ 0.197 µm and FWHM (axial) ≈ 0.894 µm).

Figure 1.3 illustrates our CLSM setup. For a distortion-free image of the silica monolith, RI matching of the fused-silica capillary wall (n = 1.4582) is of predominant importance to hinder the curved wall to function as a lens. The RI of the monolithic silica skeleton is close enough to that of the fused-silica wall, and constant flushing of the column with a mixture of DMSO/water calibrated to an RI of n = 1.4582 eliminates the RI mismatch from the pore space of the monolith. Because the optimal RI for the used microscope objective is n = 1.451, spherical aberrations and a focal shift, increasing with sampling depth, will inevitably be introduced into the optical setup. Spherical aberrations could in principle be eliminated by altering the effective tube length of the objective, but this is not possible in a commercial system. However, if the immersion medium for the objective lens is also chosen to match the RI of the capillary wall, spherical aberrations in the system

become independent of sampling depth. A glycerol/water mixture also calibrated to an RI of n = 1.4582 was therefore used as immersion and embedding liquid. The spherical aberrations caused by the capillary RI matching over the free working distance of the objective were equivalent to a 40 µm thick coverslip (see example above). The coverslip thickness was then chosen such that the spherical aberrations from coverslip, immersion medium, and sample approximately added up to the spherical aberration correction of the lens system (designed for a standard coverslip of 170 µm thickness). Therefore, a coverslip thickness of 130 µm would have been optimal. However, it turned out to be more practical to use a roughly 120 µm thick "type 0" coverslip and tune the correction collar of the objective accordingly.

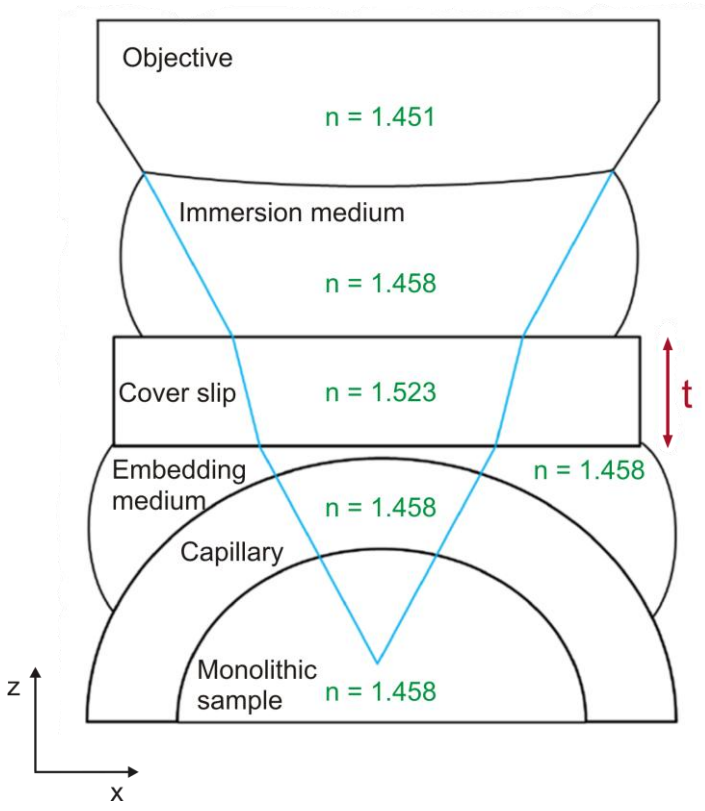

Figure 1.3: Light beam focus from microscope objective into the monolith sample displaying the respective refractive indexes of the elements in the optical pathway. A glycerol/water mixture was used as immersion and embedding liquid, and a DMSO/water mixture was used for refractive index matching of the monolith's void (pore) space. A coverslip thickness of t = 120 µm was chosen to balance the remaining spherical aberrations from coverslip, immersion medium, and sample by tuning the correction collar of the objective accordingly.

Figure 1.4 shows sections from depth profiles of the fluorescently labeled column's cross section acquired with two different coverslip types, a 160 µm thick "type 1" and a 120 µm thick "type 0" coverslip. The depth profiles are shown side by side as two quarters of the cross section for ease of comparison. The right image, acquired with the 120 µm thick coverslip, is sharper and bright regions are better resolved, because there is less stray light from adjacent optical slices as a result of balanced spherical aberrations.

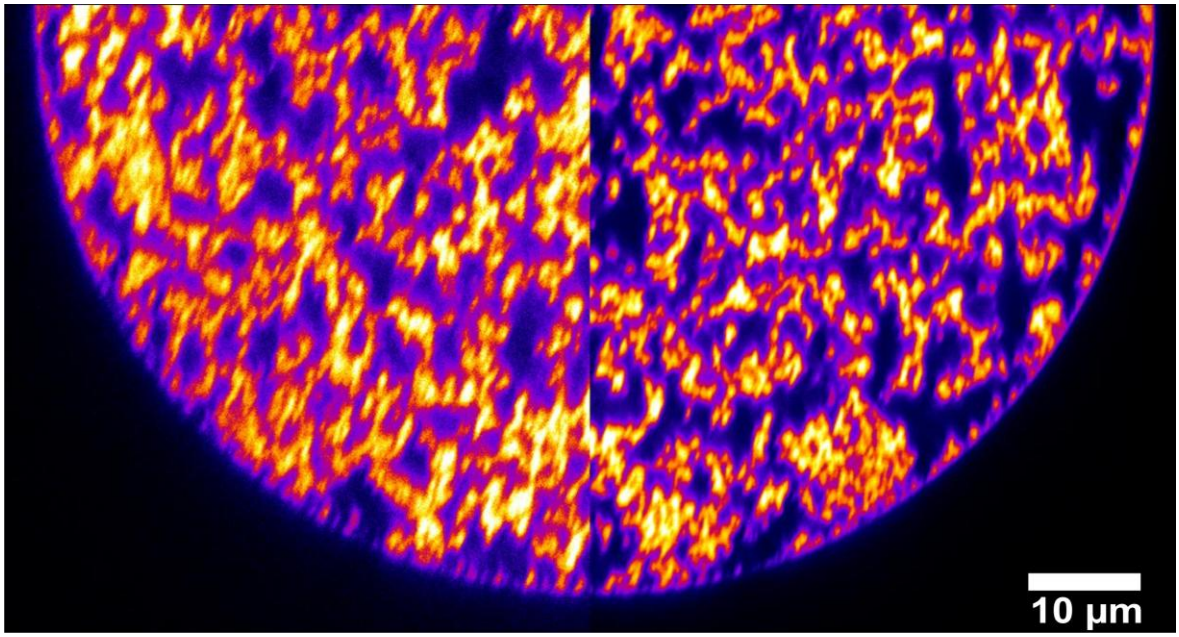

Figure 1.4: Depth profiles (x-z slices) showing the cross section of the fluorescently labeled silica monolithic capillary column. The left profile was acquired with a 160 µm "type 1" coverslip, the right profile with a 120 µm "type 0" coverslip. In each case the correction collar of the microscope objective was tuned to minimize aberrations.

Figure 1.5 shows raw CLSM images of a longitudinal section (i.e., aligned with the column axis) through the widest part of the fluorescently labeled monolithic capillary column and of its cross section. Both images reveal gaps between monolith skeleton and capillary wall, which are supposed to result from the uneven character of the mechanical stress that is experienced by the monolith–wall interface during shrinkage step of the preparation. This is a well-known problem, particularly for the rigid, but brittle, silica monoliths prepared with pure tetramethoxysilane [16]. In analytical [53] and semipreparative [54] mono-

lithic silica columns wall effects in general have been identified before to substantially affect the average cross-sectional plate height, and they are also known for capillary monoliths [55,56]. The lateral pore space heterogeneity and its large contribution to eddy dispersion is at present the main drawback of silica monoliths in chromatographic practice [16].

The presented approach of column pretreatment and CLSM image acquisition allows quick scanning along the capillary column to check for obvious defects in the monolith structure, e.g., as a process control step in silica monolith preparation. The quantitative characterization of the monolith morphology additionally requires image processing and statistical analysis of the image data.

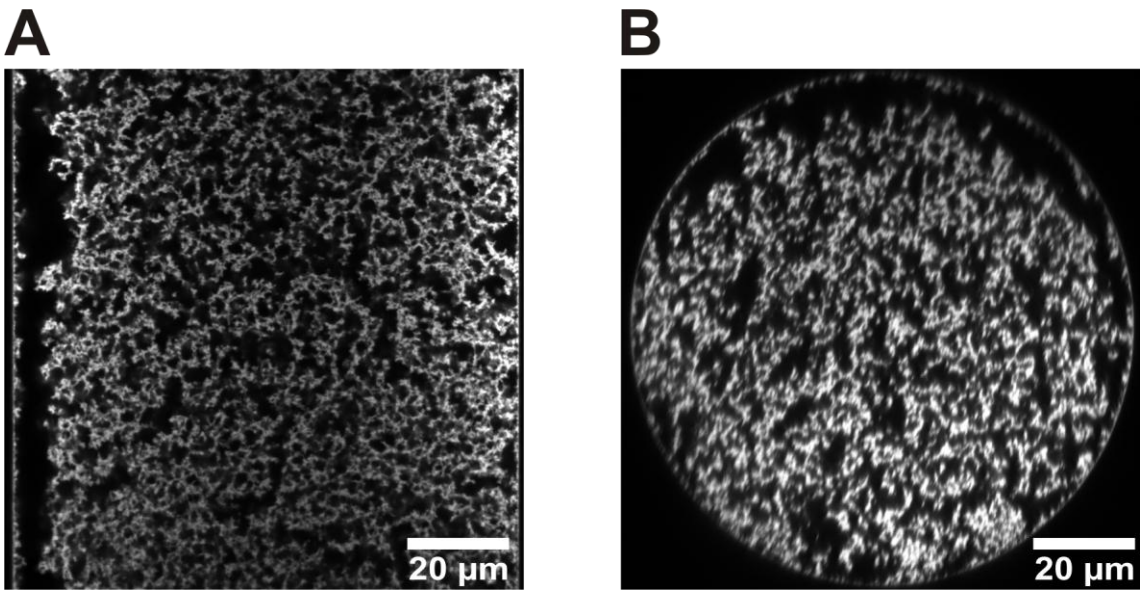

Figure 1.5: Raw CLSM images of the 100 µm i.d. fluorescently labeled silica monolithic capillary column: (**A**) longitudinal (i.e., along the column axis) central section (x-y slice, 100 µm distance from wall to wall); (**B**) cross-sectional (x-z) slice.

1.3.3 Image Processing. Image processing involved two consecutive steps: restoration and segmentation (Figure 1.6). The amount of blurring in the raw images was reduced by Huygens maximum likelihood iterative deconvolution. With the good a priori knowledge of the optical system and the point spread function, these calculations are particularly effective for CLSM and increase axial resolution by a factor of 2-4 [57]. In this way, the optical slice thickness of the CLSM images approaches the thickness of TEM micrographs.

To extract quantitative information the restored images have to be segmented into foreground and background class. High-resolution CLSM images are dim because the pinhole excludes a lot of light. As a consequence, foreground and background information in the images, i.e., silica skeleton and void space, are not completely separated by their intensity alone. Therefore, the contour of objects was considered in the segmentation process. Application of high-pass filtering to the restored images preserved any edge in the images (high-frequency information) and eliminated the remaining background noise (low-frequency information). After filtering, any positive-valued pixel was considered part of the silica skeleton (Figure 1.6). The applied segmentation method is completely automatic and not influenced by spatial variations in the detector signal, an advantage over processing steps like, e.g., intensity-based thresholding. For better visualization further image enhancing steps are possible, but these do not improve the quality of the data extracted by the subsequent image analysis.

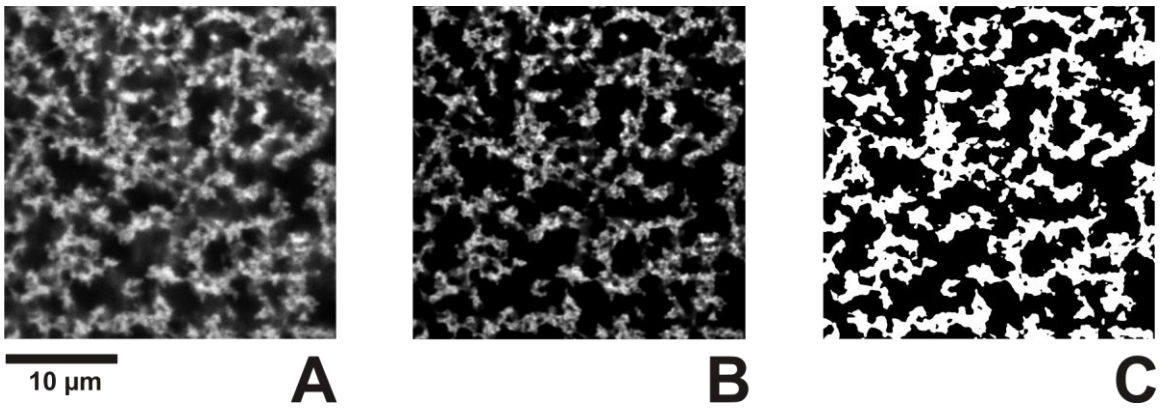

Figure 1.6: Image processing. Shown is a 25 × 25 µm2section from a longitudinal image (x-y slice) through the bulk part of the fluorescently labeled silica monolithic column: (**A**) raw image, (**B**) restored image, and (**C**) segmented image.

1.3.4 Statistical Analysis. For statistical analysis of morphological properties, an image stack of 170 longitudinal sections (x-y slices) covering a volume of 61.5 × 61.5 × 21.4 µm³ was acquired in the bulk part of the capillary. Longitudinal rather than cross-sectional slices were chosen for image analysis to take advantage of the better resolution in the focal plane. Image analysis was performed on 160 of the 170 longitudinal sections (x-y slices) in

the acquired stack. Five images from each border were excluded, because restoration is less accurate for border images. For the same reason, 1.5 µm from each side of the stack were cropped before analysis so that morphological data were finally extracted from a volume of 60 µm length and 60 × 20.2 µm² cross section. This volume is more than sufficient to represent the bulk properties of the monolith [58].

The macroporosity was determined in each slice as the ratio of void pixels to all pixels. Bulk macroporosity varied between 0.677 and 0.716 around a mean value of 0.695 (Figure 1.7), which agrees well with macroporosities of Chromolith columns determined by inverse size exclusion chromatography [32].

CLDs were calculated as outlined by Courtois et al. [34] for the macropore space (Φ_{pore}) and the silica skeleton (Φ_{skel}). The obtained Φ_{pore} is very similar to the CLD derived from TEM micrographs [34] for a Chromolith column (Figure 1.8). The median chord length of Φ_{pore} is 3.2 µm (Table 1.1), the same value as found by TEM. This demonstrates that the ability of the presented CLSM method to yield quantifiable morphological data is comparable to the TEM image analysis.

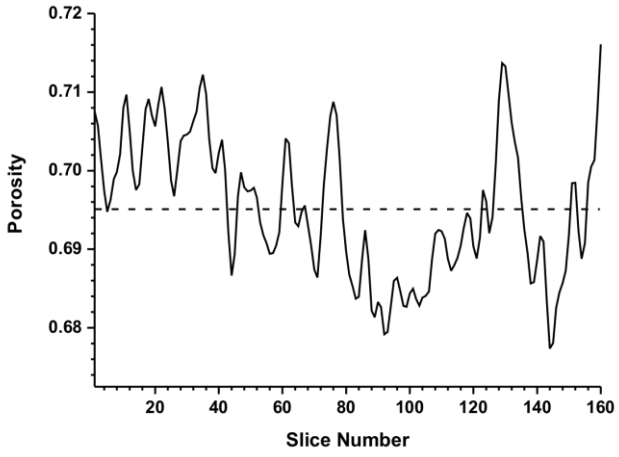

Figure 1.7: Variation of macroporosity as determined from 160 restored and segmented CLSM images of 60 × 60 µm² longitudinal sections (x-y slices) acquired in the bulk of the fluorescently labeled silica monolithic column. The dashed line indicates the mean value (0.695).

Table 1.1: Statistical properties of the chord length distributions (cf. Fig. 1.8).

	Macropore space	Monolith skeleton
Mode	2.2 µm	0.9 µm
Median	3.2 µm	1.2 µm
Arithmetic mean	3.8 µm	1.4 µm
Variance	7.6 µm	0.8 µm
Persistence length	3.1 µm	1.0 µm

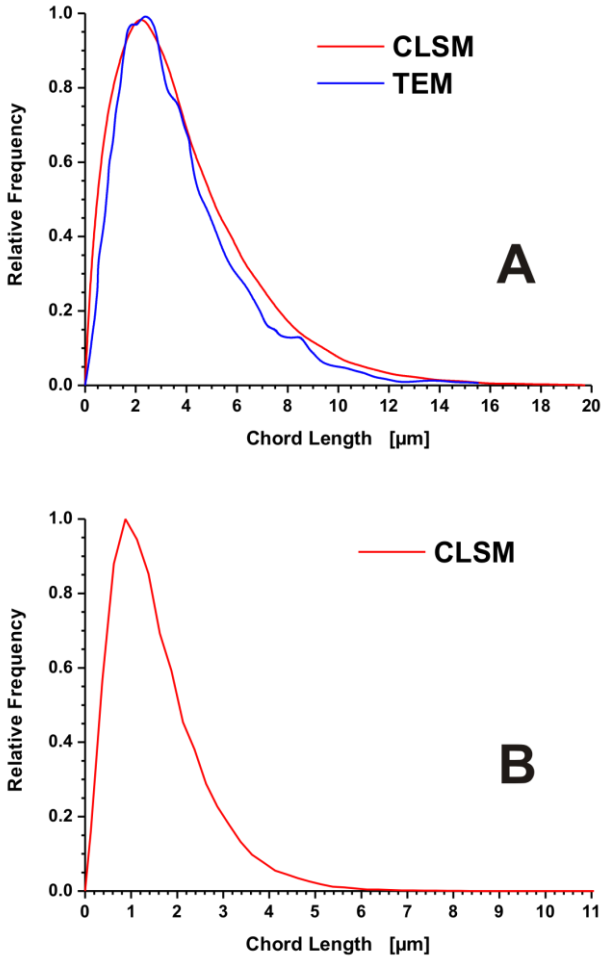

Figure 1.8: Chord length distributions for the macropore space Φ_{pore} (**A**) and the silica skeleton Φ_{skel} (**B**) of the monolith determined from CLSM images of longitudinal sections (x-y slices) through the bulk of the capillary column. The respective Φ_{pore} determined previously from TEM micrographs [34] is shown for comparison. Characteristic statistical measures of Φ_{pore} and Φ_{skel} are summarized in Table 1.1.

The arithmetic mean of the CLDs of the void space varied between 3.7 and 4.0 µm for the analyzed different spatial directions. For CLDs of the skeleton the variations were found to range from 1.4 to 1.5 µm. Because these variations are in fact smaller than those observed by Courtois et al. [34] the monolithic structure was considered to be isotropic within the scope of this work. Characteristic statistical measures of Φ_{pore} and Φ_{skel} for the bulk monolith are summarized in Table 1.1. The moments of these CLDs can be interpreted in terms of the size distribution and homogeneity of the underlying structure.

Unlike materials with Debye randomness, which show exponentially decreasing CLDs, monoliths as materials that form from spinodal decomposition exhibit correlated disorder and thus a mode in their CLDs [59], i.e., structural order exists on a length scale corresponding to the mode (correlation length). Gille et al. [60] have shown that for an infinitely long cylinder the mode of the CLD corresponds to the diameter. Therefore, it is not surprising that the mode of Φ_{pore} (2.2 µm, Table 1.1) is only slightly larger than the nominal macropore size of ~2 µm based on mercury intrusion porosimetry for Chromolith columns. The latter method assumes a cylindrical pore shape and usually underestimates the pore size due to an ink-bottle effect [61].

A chord length in the macropore space represents a straight distance between two encounters with the silica skeleton. In an open pore network like that of the monoliths, Φ_{pore} is asymmetric or skewed toward higher chord lengths. The mode then represents the *most frequent* skeleton wall-to-wall distance, whereas the arithmetic mean represents the *average* distance. CLDs with identical mode may possess very different mean values. Thus, the mean of Φ_{pore} should be a better expression for the average pore size. The mode, however, is what the estimation of the domain size from SEM images probably amounts to.

Separation efficiency of monolithic columns is not only influenced by their macropore size distribution but also by the degree of heterogeneity (or disorder) of the macropore space. In this respect, the variance of Φ_{pore} is an efficient overall measure. The disorder, however, is characterized by chords longer than the mode. The exponential decay of the determined CLDs, represented by their persistence length (Table 1.1), indicates that this disorder can be considered as random [59].

So far we focused our analysis on the characterization of Φ_{pore} because eddy dispersion, as a major limitation to improved separation efficiencies of the silica monoliths, occurs in the interskeleton macroporous (flow-through) domain where transport is convection-dominated. However, the above descriptors are also valid for Φ_{skel}, which is associated

with diffusion-limited transport and adsorption in the intraskeleton mesopores. These parameters provide a measure for the "homogeneity" (or distribution) of the intraskeleton mass transfer resistances. Therefore, a systematic optimization in the fabrication of monolithic HPLC columns could be controlled by minimization of the variances of Φ_{pore} and Φ_{skel}.

1.4 Conclusions

We presented a CLSM method composed of column pretreatment, image acquisition, and image processing, to characterize the morphology of a silica monolithic capillary column. The method is generally applicable to silica-based particulate or monolithic columns in capillary format and can be used to visualize the stationary phase structure without cutting the column first. The approach yields a multitude of longitudinal and cross-sectional images in a short time and allows fast scanning along large segments of a capillary column for heterogeneities in macropore morphology. Individual contributions to eddy dispersion, e.g., due to wall effects, can thus quickly be identified, enabling the optimization of silica monolith preparation for more efficient HPLC columns.

Statistical analysis of the CLSM images yielded quantifiable morphological information in the form of chord length distributions for the macropore space and skeleton thickness. The data are comparable to those derived by TEM image analysis, but easier to access, and describe the monolith's macropore morphology accurately and comprehensively, providing a clear advantage over estimates of the average domain size from SEM images.

Because CLSM is widely and commercially available, we anticipate its increased application for quantitative characterization of monolith morphology, following the general approach presented and validated in this work. For example, we currently investigate the effect of a feed ratio of methyltrimethoxysilane to tetramethoxysilane on the morphology of improved hybrid monolithic silica capillary columns [62]. We also plan to extend the presented method toward particulate capillary columns. The statistical analysis measures introduced in this work will be used to characterize heterogeneities and anisotropies in the column and to establish correlations with its chromatographic properties. As these descriptors do not rely on an assumption about the pore space, a link between the morphologies of particulate and monolithic beds might emerge.

In the future the CLSM approach may be combined with other techniques, e.g., pulsed field gradient nuclear magnetic resonance (PFG-NMR) [63,64] or capacitively coupled contactless conductivity detection (C^4D) [65,66]. Whereas on-column C^4D scanning cannot provide data on the lateral heterogeneity, it allows us to quickly evaluate stationary phase density variations along the column and visualize band broadening. PFG-NMR, on the other hand, records propagator distributions of the mobile phase molecules over discrete spatiotemporal domains to characterize velocity distributions and dispersion. When combined, the three techniques provide complementary information that helps to bridge the time and length scales from the pore-scale (microscopic) morphology and dynamics to the column-scale (macroscopic) transport behavior.

The presented method may be further utilized for 3D reconstruction of silica monoliths to resolve and quantify the total effect of the component plate height curves to eddy dispersion by direct pore-scale simulation within the real morphology [18] addressing time and length scales behind individual contributions, as reported for packed beds [67].

Acknowledgements

This work was supported by the Deutsche Forschungsgemeinschaft DFG (Bonn, Germany) under Grant TA 268/3-1. We thank Merck KGaA (Darmstadt, Germany) for the gift of capillary silica monoliths.

References

[1] Svec, F. *J. Chromatogr., A* **2010**, *1217*, 902–924.

[2] Bakry, R.; Huck, C. W.; Bonn, G. K. *J. Chromatogr. Sci.* **2009**, *47*, 418–431.

[3] Nordborg, A.; Hilder, E. F. *Anal. Bioanal. Chem.* **2009**, *394*, 71–84.

[4] Vlakh, E. G.; Tennikova, T. B. *J. Chromatogr., A* **2009**, 1216, 2637–2650.

[5] Urban, J.; Jandera, P. *J. Sep. Sci.* **2008**, *31*, 2521–2540.

[6] Jungbauer, A.; Hahn, R. *J. Chromatogr., A* **2008**, *1184*, 62–79.

[7] Wu, R.; Hu, L.; Wang, F.; Ye, M.; Zou, H. *J. Chromatogr., A* **2008**, *1184*, 369–392.

[8] Núñez, O.; Nakanishi, K.; Tanaka, N. *J. Chromatogr., A* **2008**, *1191*, 231–252.

[9] Potter, O. G.; Hilder, E. F. *J. Sep. Sci.* **2008**, *31*, 1881–1906.

[10] Szumski, M.; Buszewski, B. *J. Sep. Sci.* **2007**, *30*, 55–66.

[11] Eeltink, S.; Svec, F. *Electrophoresis* **2007**, *28*, 137–147.

[12] Schaller, D.; Hilder, E. F.; Haddad, P. R. *J. Chromatogr. Sci.* **2006**, *29*, 1705–1719.

[13] Maruška, A.; Kornysova, O. *J. Chromatogr., A* **2006**, *1112*, 319–330.

[14] Rieux, L.; Niederländer, H.; Verpoorte, E.; Bischoff, R. *J. Sep. Sci.* **2005**, *28*, 1628–1641.

[15] Cabrera, K. *J. Sep. Sci.* **2004**, *27*, 843–852.

[16] Guiochon, G. *J. Chromatogr., A* **2007**, *1168*, 101–168.

[17] Unger, K. K.; Skudas, R.; Schulte, M. M. *J. Chromatogr., A* **2008**, *1184*, 393–415.

[18] Hlushkou, D.; Bruns, S.; Tallarek, U. *J. Chromatogr., A* **2010**, *1217*, 3674–3682.

[19] Nakanishi, K.; Minakuchi, H.; Soga, N.; Tanaka, N. *J. Sol.-Gel Sci. Technol.* **1997**, *8*, 547–552.

[20] Minakuchi, H.; Nakanishi, K.; Soga, N.; Ishizuka, N.; Tanaka, N. *J. Chromatogr., A* **1997**, *762*, 135–146.

[21] Nakanishi, K. *J. Porous Mater.* **1997**, *4*, 67–112.

[22] Ishizuka, N.; Minakuchi, H.; Nakanishi, K.; Soga, N.; Tanaka, N. *J. Chromatogr., A* **1998**, *797*, 133–137.

[23] Nakanishi, K.; Tanaka, N. *Acc. Chem. Res.* **2007**, *40*, 863–873.

[24] Liapis, A. I.; Meyers, J. J.; Crosser, O. K. *J. Chromatogr., A* **1999**, *865*, 13–25.

[25] Leinweber, F. C.; Lubda, D.; Cabrera, K.; Tallarek, U. *Anal. Chem.* **2002**, *74*, 2470–2477.

[26] Vervoort, N.; Gzil, P.; Baron, G. V.; Desmet, G. *Anal. Chem.* **2003**, *75*, 843–850.

[27] Leinweber, F. C.; Tallarek, U. *J. Chromatogr., A* **2003**, *1006*, 207–228.

[28] Skudas, R.; Grimes, B. A.; Thommes, M.; Unger, K. K. *J. Chromatogr., A* **2009**, *1216*, 2625–2636.

[29] Grimes, B. A.; Skudas, R.; Unger, K. K.; Lubda, D. *J. Chromatogr., A* **2007**, *1144*, 14–29.

[30] Babin, J.; Iapichella, J.; Lefe`vre, B.; Biolley, C.; Bellat, J.; Fajula, F.; Galarneau, A. *New J. Chem.* **2007**, *31*, 1907–1917.

[31] Lubda, D.; Lindner, W.; Quaglia, M.; du Fresne von Hohenesche, C.; Unger, K. K. *J. Chromatogr., A* **2005**, *1083*, 14–22.

[32] Al-Bokari, M.; Cherrak, D.; Guiochon, G. *J. Chromatogr., A* **2002**, *975*, 275–284.

[33] Minakuchi, H.; Nakanishi, K.; Soga, N.; Ishizuka, N.; Tanaka, N. *J. Chromatogr., A* **1998**, *797*, 121–131.

[34] Courtois, J.; Szumski, M.; Georgsson, F.; Irgum, K. *Anal. Chem.* **2007**, *79*, 335–344.

[35] Motokawa, M.; Ohira, M.; Minakuchi, H.; Nakanishi, K.; Tanaka, N. *J. Sep. Sci.* **2006**, *29*, 2471–2477.

[36] Saito, H.; Kanamori, K.; Nakanishi, K.; Hirao, K.; Nishikawa, Y.; Jinnai, H. *Colloids Surf., A* **2007**, *300*, 245–252.

[37] Saito, H.; Nakanishi, K.; Hirao, K.; Jinnai, H. *J. Chromatogr., A* **2006**, *1119*, 95–104.

[38] Saito, H.; Kanamori, K.; Nakanishi, K.; Hirao, K.; Nishikawa, Y.; Jinnai, H. *Colloids Surf., A* **2004**, *241*, 215–224.

[39] Jinnai, H.; Watashiba, H.; Kajihara, T.; Takahashi, M. *J. Chem. Phys.* **2003**, *119*, 7554–7559.

[40] Kanamori, K.; Nakanishi, K.; Hirao, K.; Jinnai, H. *Langmuir* **2003**, *19*, 5581–5585.

[41] Jinnai, H.; Nakanishi, K.; Nishikawa, Y.; Yamanaka, J.; Hashimoto, T. *Langmuir* **2001**, *17*, 619–625.

[42] Jinnai, H.; Nishikawa, Y.; Morimoto, H.; Koga, T.; Hashimoto, T. *Langmuir* **2000**, *16*, 4380–4393.

[43] Torquato, S. *Random Heterogeneous Materials – Microstructure and Macroscopic Properties*; Springer Science & Business Media, LLC: New York, **2002**.

[44] Smarsly, B.; Antonietti, M.; Wolff, T. J. Chem. Phys. 2002, 116, 2618–2626.

[45] Gille, W.; Enke, D.; Janowski, F. *J. Porous Mater.* **2002**, *9*, 221–230.

[46] Gille, W. *Eur. Phys. J. B* **2000**, *17*, 371–383.

[47] Rulf, A.; Worlitschek, J.; Mazzotti, M. *Part. Part. Syst. Charact.* **2000**, *17*, 167–179.

[48] Abrams, B.; Diwu, Z.; Guryev, O.; Aleshkov, S.; Hingorani, R.; Edinger, M.; Lee, R.; Link, J.; Dubrovsky, T. *Anal. Biochem.* **2009**, *386*, 262–269.

[49] El Kadib, A.; Chimenton, R.; Sachse, A.; Fajula, F.; Galarneau, A.; Coq, B. *Angew. Chem., Int. Ed.* **2009**, *48*, 4969–4972.

[50] Rasband, W. S. *ImageJ*; U.S. National Institutes of Health: Bethesda, MD, **1997–2006**; http://rsb.info.nih.gov//ij/.

[51] Wilhelm, S.; Gröbler, B.; Gluch, M.; Heinz, H. *Confocal Laser Scanning Microscopy – Optical Image Formation and Electronic Signal Processing*; Monography, Carl Zeiss: Jena, Germany, **2008**.

[52] "Nyquist Rate and PSF Calculator", Scientific Volume Imaging Support Wiki Pages, http://www.svi.nl/NyquistCalculator (Accessed June 2010).

[53] Abia, J. A.; Mriziq, K. S.; Guiochon, G. A. *J. Chromatogr., A* **2009**, *1216*, 3185–3191.

[54] Abia, J. A.; Mriziq, K. S.; Guiochon, G. A. *J. Sep. Sci.* **2009**, *32*, 923–930.

[55] Tanaka, N.; Kobayashi, H.; Ishizuka, N.; Minakuchi, H.; Nakanishi, K.; Hosoya, K.; Ikegami, T. *J. Chromatogr., A* **2002**, *965*, 35–49.

[56] Kanamori, K.; Yonezawa, H.; Nakanishi, K.; Hirao, K.; Jinnai, H. *J. Sep. Sci.* **2004**, *27*, 874–886.

[57] Schrader, M.; Hell, S.; van der Voort, H. T. M. *Appl. Phys. Lett.* **1996**, *69*, 3644–3646.

[58] Bruns, S. *Dreidimensionale Rekonstruktion monolithischer Festphasen mittels konfokaler Lasermikroskopie.* Diplomarbeit, Fachbereich Chemie, Philipps-Universität, Marburg, Germany, **2009**.

[59] Levitz, P.; Tchoubar, D. *J. Phys. I* **1992**, *2*, 771–790.

[60] Gille, W.; Enke, D.; Janowski, F. *J. Porous Mater.* **2001**, *8*, 179–191.

[61] Abell, A. B.; Willis, K. L.; Lange, D. A. *J. Colloid Interface Sci.* **1999**, *211*, 39–44.

[62] Hara, T.; Makino, S.; Watanabe, Y.; Ikegami, T.; Cabrera, K.; Smarsly, B.; Tanaka, N. *J. Chromatogr., A* **2010**, *1217*, 89–98.

[63] Tallarek, U.; Rapp, E.; Scheenen, T.; Bayer, E.; Van As, H. *Anal. Chem.* **2000**, *72*, 2292–2301.

[64] Tallarek, U.; Rapp, E.; Seidel-Morgenstern, A.; Van As, H. *J. Phys. Chem. B* **2002**, *106*, 12709–12721.

[65] Gillespie, E.; Connolly, D.; Macka, M.; Nesterenko, P. N.; Paull, B. *Analyst* **2007**, *132*, 1238–1245.

[66] Connolly, D.; Barron, L. P.; Gillespie, E.; Paull, B. *Chromatographia* **2009**, *70*, 915–920.

[67] Khirevich, S.; Höltzel, A.; Seidel-Morgenstern, A.; Tallarek, U. *Anal. Chem.* **2009**, *81*, 7057–7066.

Chapter 2

Physical Reconstruction of Packed Beds and their Morphological Analysis: Core–Shell Packings as an Example

Authors:

Stefan Bruns and Ulrich Tallarek

State of Publication:

Published April 8, 2011 in *Journal of Chromatography A*, Vol. 1218, No. 14, p. 1849–1860.

Abstract

We report a fast, nondestructive, and quantitative approach to characterize the morphology of packed beds of fine particles by their three-dimensional reconstruction from confocal laser scanning microscopy images, exemplarily shown for a 100 µm i.d. fused-silica capillary packed with 2.6 µm-sized core–shell particles. The presented method is generally applicable to silica-based capillary columns, monolithic or particulate, and comprises column pretreatment, image acquisition, image processing, and statistical analysis of the image data. It defines a unique platform for fundamental comparisons of particulate and monolithic supports using the statistical measures derived from their reconstructions. Received morphological data are column cross-sectional porosity profiles and chord length distributions from the interparticle macropore space, which are a descriptor of local density and can be characterized by a simplified *k*-gamma distribution. This distribution function provides a parameter of location and a parameter of dispersion which can be correlated to individual chromatographic band broadening processes (i.e., to transchannel and short-range interchannel contributions to eddy dispersion, respectively). Together with the transcolumn porosity profile the presented approach allows analyzing and quantifying the packing microstructure from pore to column scale and therefore holds great promise in a comparative study of packing conditions and particle properties, particularly for character-

izing and minimizing the packing process-specific heterogeneities in the final bed structure.

2.1 Introduction

Flow and transport behavior in randomly packed beds of particles is a subject with major interdisciplinary significance, ranging from chemical reactors to simplified models for natural porous media and biological tissue [1–6]. In chromatography, an understanding of these phenomena promises substantial improvement in the design of better performing stationary phases and separation technology [7–9]. Transport in chromatographic columns is governed by the interaction of diffusion and advection, i.e., the phenomenon of dispersion [10,11]. The flow pattern in laminar flow through a packed bed depends on the morphology, i.e.,the topology and geometry of the available pore space, so that inherent structural heterogeneity of the packing sensitively influences time and length scales which characterize hydrodynamic dispersion [12,13]. The “scale dependence” of dispersion and its constituent contributions is central to a deeper understanding and potential reduction of dispersion under a given set of variables including the packing protocol parameters, column dimensions and particle properties, or the actual chromatographic conditions. In addition, the effect on measured or modeled transport coefficients (e.g., dispersion coefficients) of interactions between the time and length scales of observation and the natural scales of the chromatographic packings becomes a key issue in the modeling of packed-bed structure, flow and transport behavior, as well as in a comparison between theory and experiment. Detailed three-dimensional numerical simulations of flow and transport in sphere packings are particularly suited to the challenge of investigating the central structure–transport relationships in chromatographic media, because this approach allows to systematically study relevant parameters, such as the shape and average size of the particles, the particle size distribution, inter- and intraparticle porosities, as well as the column dimensions and cross-sectional geometry [14–26]. Transient dispersion can be recorded easily, thereby quantifying time and length scales required for the attainment of asymptotic dispersion behavior and providing correlations for the dependence of dispersion on the mobile phase velocity. Because all dispersion data are referenced to a particular packing microstructure and are unbiased by extra-column contributions, the numerical simulations approach establishes a systematic route towards quantitative structure–transport relationships.

Also statistical information about the structure of the simulated packings can be collected, because the position, size, and shape of the particles are precisely known. Together with a generation protocol-dependent, dedicated adjustment of the microstructural degree of heterogeneity in the sphere packings this approach promises decided progress in our understanding of the largely unknown disorder-dispersion correlations [27].

Another approach for investigating morphology and performance of chromatographic beds under working conditions, which complements the computer-generation of sphere packings, is their physical reconstruction by direct imaging. Several imaging techniques are nowadays available to investigate the three-dimensional pore structure of chromatographic media and packed beds, in general. They range from nanometer resolution with electron tomography [28–30], through micron and submicron scale with micro-X-ray computerized tomography [31–33] and confocal laser scanning microscopy (CLSM) [34–36], to several tens of micrometers with nuclear magnetic resonance (NMR) imaging [37–40]. Whereas NMR imaging consequently has been applied to visualize the interparticle pore space in confined packings of relatively large, up to millimeter-sized particles, electrontomography, on the other extreme, has been used for capturing details of the adsorbents intraparticle pore space. For the reconstruction and statistical analysis of the interparticle pore space in modern HPLC packings (of 5 µm-sized and smaller particles), the CLSM-based approach appears suitable and its adaptation for that purpose is the topic of the present work.

With the recent development and chromatographic use of sub-3 µm core–shell particles several basic research questions have attracted significant (renewed) attention [41–49]. This includes the influence of the particle size distribution and surface roughness on the packing microstructure and separation efficiency. It particularly addresses the impact of the packing process and protocol parameters on the microstructural heterogeneity of the resulting confined fixed beds. Packing microstructures are commonly classified as just “more homogeneous” or “more heterogeneous”. These intuitive, qualitative labels are usually based on the column performance. Experimentally, it would be desirable to generate packings with a known (and controllable) degree of heterogeneity. However, this requires a sound scientific quantification of the degree of heterogeneity of the underlying, individual packing microstructure. We have shown recently in an extensive numerical simulation study that the standard deviation and skewness of the Voronoi volume distributions are sensitive measures of hydrodynamic dispersion in unconfined, monodisperse, random

sphere packings, establishing a correlation between disorder and dispersion in a packing [27]. Consequently, it is desirable and will be highly diagnostic to reconstruct experimental packings obtained under easily adjustable, but carefully controlled conditions and correlate the packing microstructure with the packing protocol parameters and separation efficiency. In addition, these reconstructed packings will serve as realistic models for the three-dimensional pore scale simulation of flow and transport, allowing to quantify time and length scales of dispersion with respect to the macroscopic, chromatographic response. This complementary analysis will also allow us to resolve the initially mentioned effect on measured and modeled transport coefficients of interactions between the time and length scales of observation and the natural scales of the real packings. We therefore envisage a straightforward approach to the disorder- dispersion correlations for randomly packed beds in dependence of packing process and operational parameters as well as particle and column characteristics.

In this work we report a significant step towards this challenge. We adopt a CLSM approach, recently demonstrated for the detailed reconstruction of silica monolith morphology [50] and subsequent pore scale simulations of flow and transport [51,52], to reconstruct the interparticle pore space morphology in a 100 µm i.d. fused-silica capillary packed with 2.6 µm core–shell particles. CLSM is nondestructive, widely and commercially available, enjoys simple and fast sample preparation, and allows the rapid acquisition of longitudinal and cross-sectional images at any position in the column. The approach is generally applicable to silica-based capillary columns, monolithic or particulate. We give a detailed description of all necessary steps required to image packed capillary columns close to the diffraction limit and extract the desired morphological information. These steps comprise column pretreatment, image acquisition, image processing, and statistical analysis.

2.2 Experimental

2.2.1 Chemicals and Materials. The 2.6 µm-diameter Kinetex bare-silica particles came from Phenomenex Inc. (Torrance, CA, USA). 100 µm i.d. fused silica capillaries were obtained from Postnova Analytics GmbH (Landsberg, Germany). 3-Carboxy-6-chloro-7-hydroxycoumarin was purchased from Endotherm Life Science Molecules (Saarbrücken, Germany). 3-aminopropyltriethoxysilane, N,N´-disuccinimidyl carbonate (DSC), and 4-dimethylaminopyridine (DMAP) were supplied by Alfa Aesar GmbH (Karlsruhe, Germany). Triethylamine (Et_3N), dimethyl sulfoxide (DMSO), glycerol, HPLC-grade ethanol, dimethylformamide (DMF) and methanol came from Sigma Aldrich Chemie GmbH (Taufkirchen, Germany). HPLC-grade water was obtained from a Milli-Q gradient water purification system (Millipore, Bedford, MA, USA).

2.2.2 Column Preparation. As described previously [53,54], about 20cm of a fused-silica capillary were slurry-packed using a WellChrom K-1900 pneumatic pump (Knauer, Berlin, Germany) with a 500 µm i.d. glass-lined metal tubing as the slurry reservoir. A temporary outlet frit was provided by connecting a micro-union equipped with a 1 µm-mesh stainless-steel frit (IDEX Health & Science, Wertheim-Mondfeld, Germany) to the capillary outlet during the packing process. A 5% slurry was prepared by suspending 25 mg of dry Kinetex particles in 500 µL of methanol and applying ultrasound for 5 min.

Then, 35 µL of the slurry were injected into the slurry reservoir and transported to the methanol-rinsed capillary, first by pushing with methanol and rising the applied pressure to 500 bar over 5 min, then by applying ultrasound for 25 min. After consolidation, the capillary was removed from the packing device and methanol was replaced with an aqueous solution of sodium chloride (1 g/L) to fix the bed at 9cm bed length with sintered inlet and outlet frits using an FSM-05SV fusion splicer (Fujikura, Chessington, UK).

In order to receive a strong fluorescence signal from the surface of the Kinetex particles during CLSM a succinimidyl ester of dye V450 was covalently bound to the porous shell of the particles. It is a staining method that we previously applied for the imaging of silica monolith morphology [50] and sincere fined for pretreatment time and concentration. We therefore discuss it only briefly. Fig. 2.1 gives an overview of the column packing's chemical surface modification. A succinimidyl ester of dye V450 was synthesized with 75% yield starting from 3-carboxy-6-chloro-7-hydroxycoumarin as described by Abrams

et al. [55]. The bare-silica surface of the packed capillary was amine-modified for covalent binding of the V450-succinimidyl ester following a method outlined by El Kadib et al. [56]. For this purpose, the solvent in the capillary was changed back to methanol before 100 µL of 3-aminopropyltriethoxysilane solution (0.1 M in ethanol) were pumped through the column at 0.25 µL/min and 70 °C resulting in an amine-modification of the column. Cleaning with ethanol and subsequent treatment with 100 µL of V450-succinimidyl ester solution (0.1 mg in 1 mL of DMF at 0.1 µL/min) binds V450 to the amine sites in the column. A purging step with DMSO/water 81/19 (v/v), to eliminate excess dye and prepare the column for the CLSM measurements, completed the column preparation procedure.

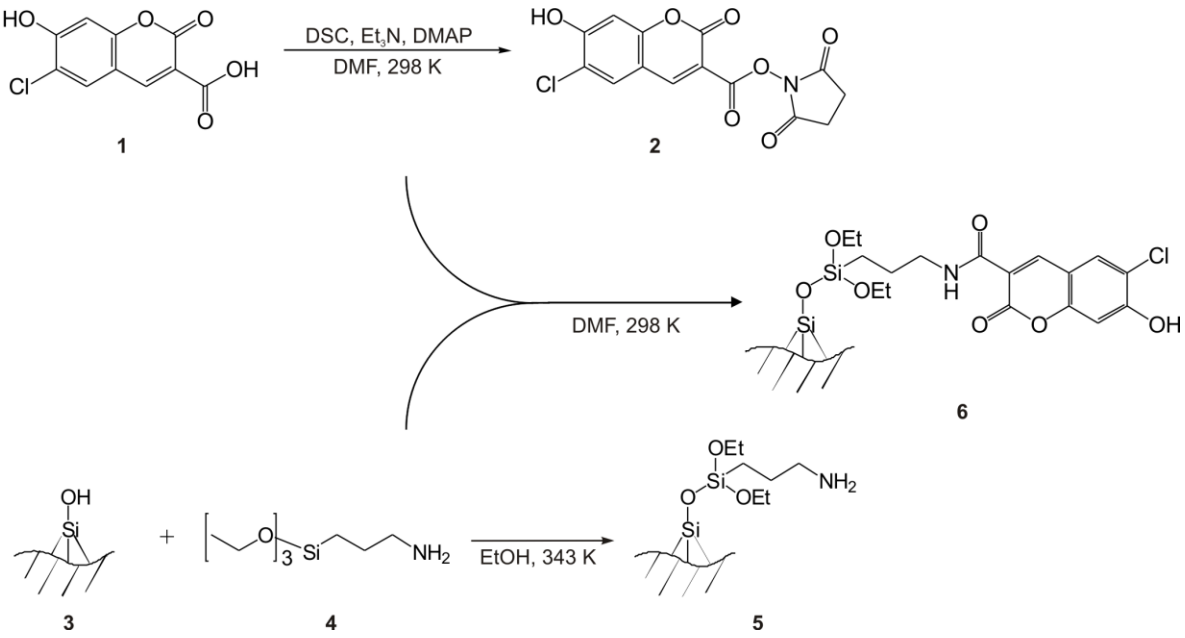

Figure 2.1: Chemical modification of the silica surfaces for CLSM. Starting from 3-carboxy-6-chloro-7-hydroxycoumarin (**1**), the succinimidyl ester of dye V450 (**2**) was synthesized as described by Abrams et al. [55] with 75% yield. Amine-modification of the particles' surface (**3**) was carried out with 3-aminopropyltriethoxysilane (**4**) according to El Kadib et al. [56]. Reaction of the amine-modified surface (**5**) with V450-succinimidyl ester (**2**) resulted in covalent attachment of the dye to the particles (**6**).

2.2.3 Image Acquisition. Images were acquired on a TCS SP5 II confocal microscopy system equipped with a HCX PL APO 63×/1.3 GLYC CORR CS (21°) glycerol immersion objective lens from Leica Microsystems (Wetzlar, Germany) by focusing into a capillary

segment where the polyimide coating was removed with a drop of warm sulfuric acid. The column itself was filled with glycerol/DMSO/water 70/19/11 (v/v) and fixed on a microscope slide within an embedding pool of the same solvent mixture before the measurements. For optimal refractive index (n) matching (cf. Fig. 2.2B) this solvent mixture was further calibrated with an AR200 digital refractometer (Reichert Analytical Instruments, Depew, NY, USA) to match the refractive index of the fused-silica capillary wall (n_D = 1.4582 [57]). The glycerol/DMSO/water mixture was also used as an immersion medium for the microscopic lens. A "type 0" coverslip (Gerhard Menzel GmbH, Braunschweig, Germany) was selected to separate embedding and immersion liquid and to minimize spherical aberrations. The resulting experimental setup is delineated in Fig. 2.2A.

Excitation of V450 was realized with a 405 nm diode laser. Fluorescence emission was detected in the interval 440–455 nm. Planar views in xy-dimensions, as defined by Fig. 2.3, were realized at a scan rate of 100Hz. The pinhole of the microscope was set to 0.5 AU, and 125 8-bit grayscale images of 4096 × 2048 pixels were recorded at 126 nm spacing in z-dimension. Using a digital zoom of 2.0 this resulted in a pixel size of 30 nm and a captured volume of 123 µm × 61 µm × 16 µm. The covered region within the packed capillary is highlighted in Fig. 2.3.

2.2.4 Image Processing. Bleaching of the fluorescent dye is an inherent feature of laser microscopy. It was corrected by fitting a first-order exponential decay to the acquired image stack's intensity distribution along the dimension of the optical axis (z-dimension). Subsequently, Huygens maximum likelihood iterative deconvolution (Scientific Volume Imaging, Hilversum, The Netherlands) was applied for image restoration.

The general idea behind segmenting the image stack into a voxelized three-phase system of solid cores, porous shells, and interparticle void space was to locate the particle centers via the Fourier transform of the 2D image stack and subsequently flood the stack from each particle center to the signal generated by its stained porous shell. The first derivative of this signal provides two maxima, which were defined as the core–shell and shell–void interfaces. An overview of the applied steps is provided by Fig. 2.4. Their implementation was as follows.

Background was subtracted from the deconvolved original image stack with a sliding paraboloid, and both a two-dimensional gradient image and a bandpass-filtered version of the stack were calculated using ImageJ for microscopy [60]. Subtracting the deconvolved

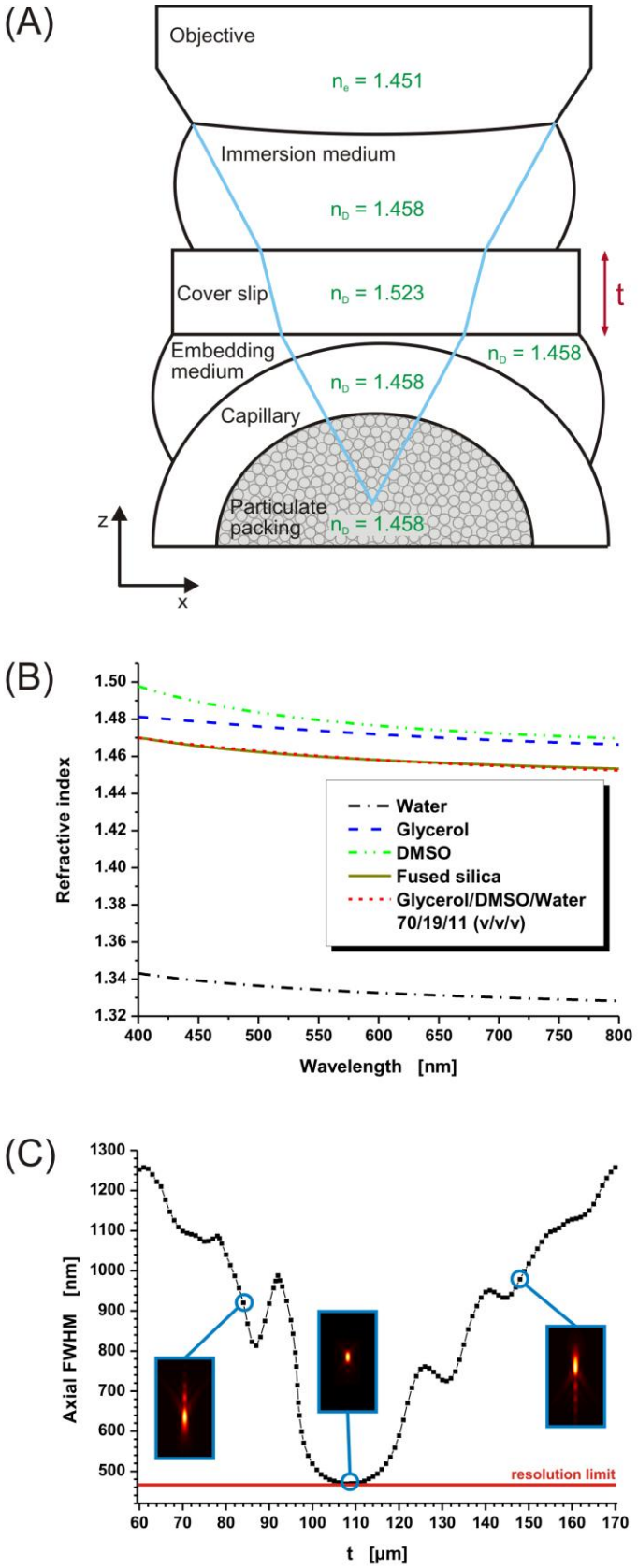

Figure 2.2:

Sample preparation. (**A**) Light beam focus from microscope objective into the packed capillary displaying the refractive indices of the individual elements in the optical pathway. A glycerol/DMSO/water mixture of 70/19/11 (v/v/v) was used as immersion liquid, as embedding liquid, and for refractive index matching of the whole void space in the packing. (**B**) Chromatic dispersion curves were calculated using the Sellmeier equation. For the refractive index matching liquid an ideal mixture of glycerol, DMSO, and water was assumed [58]. Remaining aberrations in the sample were considered to be a function of *t*, the coverslip thickness. Modeling of the system's illumination point spread functions was performed using PSF Lab [59]. The axial FWHM (along the optical axis) is very sensitive to spherical aberrations. Numerical solutions for the axial FWHM of the sample setup (**A**) are presented in (**C**). An NA of 1.3, a wavelength of 405 nm, and a focal length of 310 µm were assumed. Results suggest to use a coverslip with t = 108 µm for balancing remaining spherical aberrations from the coverslip, immersion medium, and sample. Tuning the correction collar of the objective allowed to use a "type 0" coverslip and compensate for minor deviations in *t*.

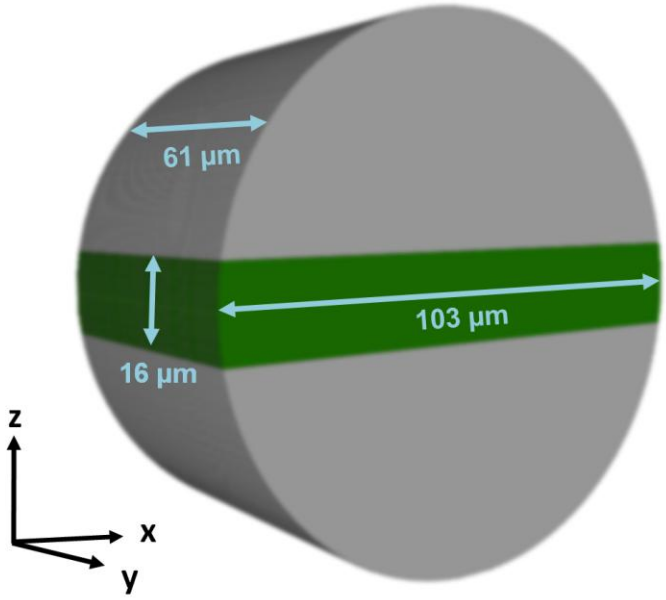

Figure 2.3: Illustration of the volume from the cylindrical column packing covered during imaging (green). The packing of the Kinetex bare-silica particles is represented by the gray cylinder.

original image-stack from the bandpass-filtered version locates intensity at the particle centers. Thus, the position of each particle can be calculated from the centroids of the resulting clusters which was done, along with the further processing steps, using in-house software written with Visual Studio C# 2008 (Microsoft Corporation, Redmond, WA, USA).

Using an overlay of the bandpass (Fig. 2.4B) and the original (Fig. 2.4A) the image stack was screened manually for obvious errors in the particle detection, which were mostly circular pores identified as particles, leaving 7307 "true" particle centers. The core–shell and shell–void interfaces in the xy-plane around the particle center were then defined as the first and second maximum of the linear intensity profiles from the respective particle center to the surface of a virtual, enclosing circle in the gradient image, resulting in a temporary core and particle diameter. Assuming good sphericity of the particles the three-dimensional interfaces of the particle's core and shell were finally detected by extrapolation of the temporary spherical diameter to neighboring slices and shifting the particle border to the brightest pixel of the gradient image in close vicinity.

Only spherical particles with captured particle center are accurately reconstructed. Thus, two nonspherical pieces of silica material contained in the image stack were segmented manually. Additionally, the image stack was cropped by 1.5 µm in the dimensions

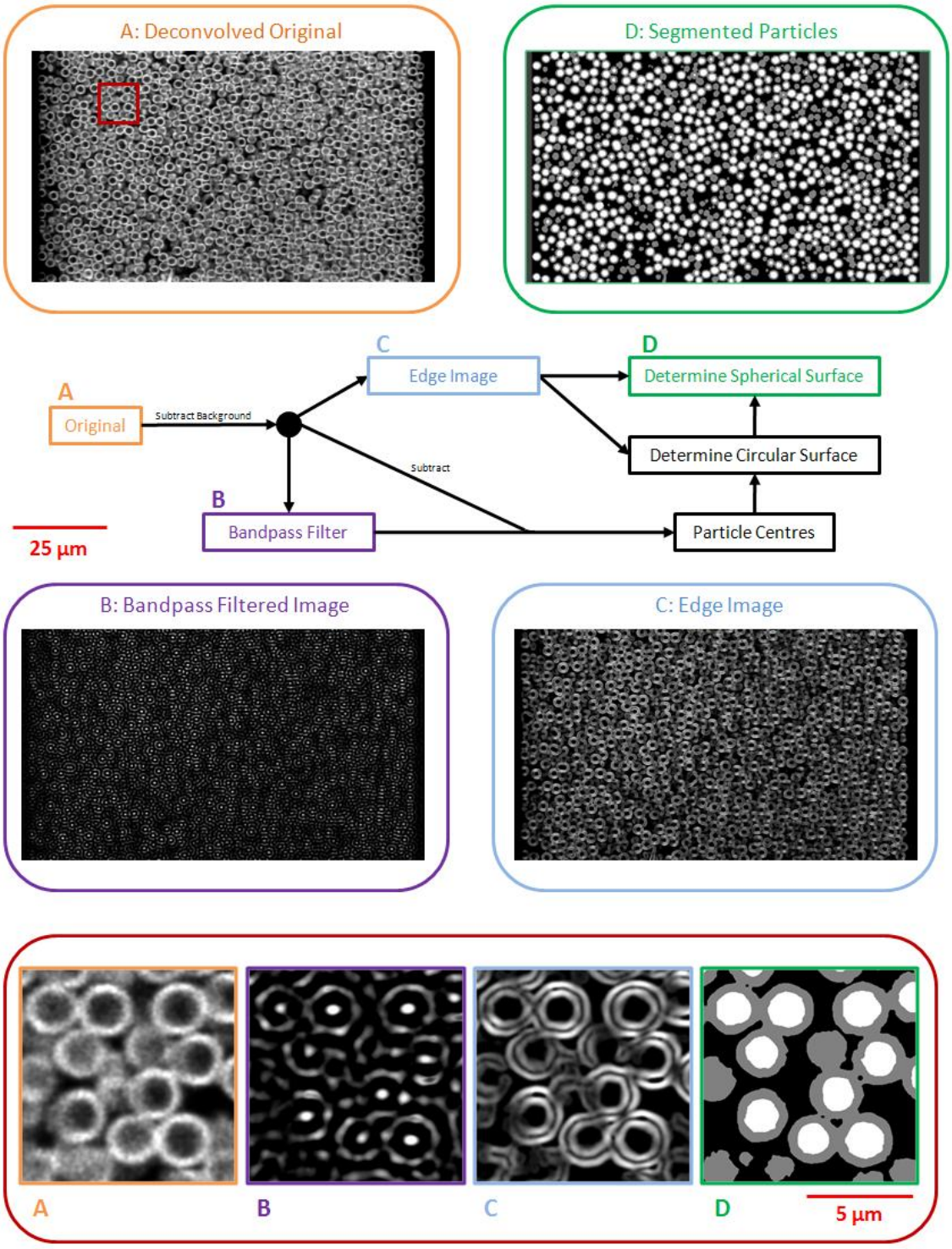

Figure 2.4: Flow chart of the reconstruction. The result of a background subtraction from the deconvolved image stack (**A**) is used to locate the centers of the recorded particles by bandpass filtering (**B**) and to calculate the first derivative, respectively, the edge image (**C**). Particle location and edge image are then combined to determine the spherical particle–void and core–shell interfaces. The final segmentation (**D**) results in four phases: solid particle core (white), porous shell (gray), interparticle void (black), and column wall (dark gray). A zoomed view on the subsequent packing reconstruction steps, as designated in (**A**), is displayed in the lower section of the figure.

where the bed continues, i.e., along y- and z-dimension (cf. Fig. 2.3). As 1.5 µm is larger than the average particle radius, no particles are ignored in the reconstruction. Thus, we obtained a reconstructed column volume of 103 µm × 58 µm × 13 µm, enclosing 5213 complete particles (Fig. 2.5).

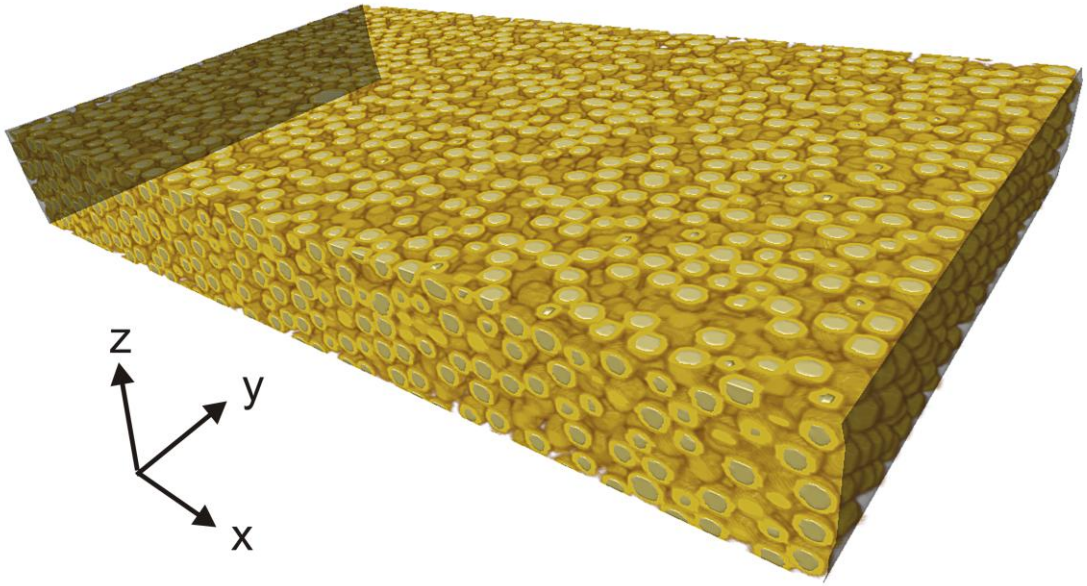

Figure 2.5: Volume rendering of the reconstructed 103 µm × 58 µm × 13 µm column volume. The reconstruction covers 5213 core–shell particles. Solid cores are displayed in gray and porous shells in yellow. Column walls are indicated by a black shadow.

2.2.5 Image Analysis. Statistical analysis of the reconstructed packing was also carried out with software written in-house. The segmentation algorithm already assigns voxels to particle centers. The calculation of the shell thickness as well as the core and particle diameters was thus performed by the calculation of sphere diameters corresponding to the voxelized volume covered by each particle and, respectively, its core or shell. As will be shown below, no particles of 2.0 µm diameter or smaller were contained in the particle size distribution. Therefore, particle centers closer than 2.0 µm could safely be merged into a multi-core particle.

The nonporous and consequently unstained and transparent column wall was defined in each slice to begin in the first and the last column in y-direction that touches a shell pixel in the upper and lower part of the image. Cavities in the packing were visualized by thresholding the Euclidean distance transform of the identified void space and drawing spheres with the radius of the Euclidean distance transform value around remaining non-zero voxels. Porosity profiles were realized by binning pixel columns according to their minimal distance from the column wall and calculating the ratio between the amount of pixels assigned to a particle and the total amount of pixels in this bin.

For the calculation of a chord length distribution points were randomly selected from the void area of the reconstruction. Due to the rotational symmetry of the column the x- and z-dimension are identical (cf. Fig. 2.3). Thus, from each point, vectors were projected in 32 angularly equispaced directions within the corresponding (higher resolving) xy-plane, until they either hit a particle shell, the column wall, or projected out of the image boundaries. The latter vectors were discarded. A chord length was then calculated as the sum of the absolute lengths of an opposed pair of vectors. Statistics for the chord lengths were collected from 4×10^5 chords randomly distributed over the image stack.

2.3. Results and Discussion

2.3.1 Accuracy of the Reconstruction. Using laser light as a high-energy light source, confocal microscopes are able to provide an almost diffraction-limited resolution, while maintaining sufficient energy density at the focal point [61]. Their resolution is typically defined as the full width at half maximum (FWHM) of the system's optical transfer function or, respectively, point spread function (PSF) in the case of a point-like object. The system PSF is a convolution of the illumination PSF, modeled in Fig. 2.2C, and the PSF resulting from the detection light path. Necessarily, the system PSF's FWHM is smaller than or equal to the FWHM of the illumination PSF. Wilhelm et al. [61] provide simple equations to estimate the FWHM of an ideal confocal microscope. It is assumed that illumination and detection PSF are identical, which is only strictly true for the diffraction-limited case of an infinitely small pinhole diameter. The FWHM in the optical plane ($FWHM_{lateral}$) and along the optical axis ($FWHM_{axial}$) are then estimated by

$$\lambda_{mean} = \sqrt{2}\frac{\lambda_{excitation}\lambda_{emission}}{\sqrt{\lambda_{excitation}^2 + \lambda_{emission}^2}} \quad \text{(Eq. 2.1)}$$

$$FWHM_{lateral} = \frac{a\lambda_{mean}}{NA} \quad \text{(Eq. 2.2)}$$

$$FWHM_{axial} = \frac{b\lambda_{mean}}{n - \sqrt{n^2 - NA^2}} \quad \text{(Eq. 2.3)}$$

with a = 0.37 and b = 0.64; λ denotes wavelength, and NA is the numerical aperture of the applied objective.

For high-resolution images it is advisable to minimize the pinhole diameter, select a dye with a small Stokes shift and an excitation wavelength as small as realizable with the available equipment. To estimate the resolution of the system under consideration the finite size of the pinhole (0.5 AU) needs to be considered by increasing the factors a and b in Eqs. (2.2) and (2.3) to 0.44 and 0.76, respectively; NA = 1.3, and $\lambda_{excitation}$ equals 405 nm, whereas $\lambda_{emission}$ is the emission maximum of the V450 dye at 448 nm. The HCX PL APO 63×/1.3 GLYC CORR CS (21°) is designed to work with glycerol/water mixtures of a re-

fractive index of 1.451 at the mercury e-line (n_e). Assuming a dispersion to 1.457 at a mean wavelength of 424 nm, the above wave-optical estimate of the FWHM yields 0.14 µm in the optical plane and 0.40 µm along the optical axis. Practically, the axial FWHM can be determined with a standard mirror test at 488 nm to characterize the quality of the applied objective [62]. For the utilized confocal system the axial FWHM was measured at 0.36 µm with this test.

The Kinetex particles examined exemplarily in this study have a nominal particle diameter of 2.6 µm. On the basis of the small ratio of particle diameter and assumed optical resolution power of the microscope system, the elimination of all residual aberrations originating from the sample setup will be of utmost importance for a reliable reconstruction of the packing, since spherical aberrations are the major source of deviation from ideal behavior and signal degeneration in optical microscopy. We therefore extend our previous discussion on sample preparation [50] by additionally considering the dispersive behavior of the matching liquids.

To design a sample setup with minimized spherical aberrations it is necessary to eliminate the capillary wall to function as a lens and avoid refractive index mismatch between sample and embedding medium. Fortunately, this is unproblematic for silica-based packings since refractive indices of capillary wall and packing medium are almost identical. They can be matched with a solvent of n_D = 1.458 that mimics the dispersive behavior of fused silica (cf. Fig. 2.2B).This will leave a slight mismatch with respect to the applied objective which works optimal for a refractive index of n_e =1.451 (cf. Fig. 2.2A). As a consequence, aberrations increase with sampling depth unless the immersion medium for the lens is also replaced by a medium with n_D = 1.458. In that case, aberrations due to the refractive index mismatch are constant and independent from sampling depth. Since glycerol objectives are designed to be used with coverslips of n_D = 1.523 an aberration correction for a 170 µm coverslip is incorporated into the lens system. Thus, it is possible to consider the resulting PSF of the system to be a function of the cov-erslip thickness t (illustrated in Fig. 2.2A) which describes a minimum when the aberrations introduced by matching liquids and coverslip are equivalent to a t = 170 µm coverslip.

Numerical solutions for the system PSF help to identify suitable values for t. We used "PSF Lab" [59] to calculate the axial FWHM in dependence from t for illumination PSFs considering a focal length of 310 µm (280 µm of free working distance + 30 µm lens guard). The refractive indices of the matching liquid and the fused-silica wall at 405 nm

were assumed to be 1.470, whereas coverslip and objective were expected to disperse to n = 1.534 and 1.458, respectively. Fig. 2.2C presents the results of these calculations and illustrates that measurements with a coverslip of about t = 108 µm instead of a 170 µm coverslip are, in principle, free of aberrations. A practical implementation of these results is to select a "type 0" coverslip and fine-tune the correction collar of the objective accordingly. This will yield optimally resolved images from any part of the capillary.

Knowing the system PSF also enables the application of deconvolution techniques to the recorded image data. Schrader et al. [63] suggested that improvements in resolution by a factor of two to four can be achieved depending on the accuracy of the determined PSF. Still, the accurate reconstruction and extraction of quantitative morphological data require the determination of the particles centers and blurred particle–void interface. The former can be achieved with high confidence by looking at the 2D-Fourier trans- form of the images. In the Fourier transform of an image all features are characterized by sets of frequencies. The highest frequencies describe the object boundaries, whereas the lowest frequencies resemble slow intensity variations in the image background. Particles for HPLC are optimized for a narrow size distribution and good sphericity. The frequencies that characterize their individual size and their intensity distribution are thus located in a narrow band, whereas information on the particles positions is contained in higher frequency domains. The application of a highpass filter with a cut-off frequency below the first harmonic of the size-characterizing frequencies or an optimized bandpass filter results in spots of maximal intensity at the particles centers in the inverse transformed image, which are dark spots in the original image. Therefore, the subtraction of the original image leaves a set of pixel-clusters whose geometrical centers define a list of all particle centers in the image. Merged particles of two or more cores are not problematic since they are typically detected by multiple particle centers close together. A manual examination of the output is still required because, e.g., circular pores of comparable size will also be detected as a particle.

The knowledge of the particle centers significantly reduces the amount of calculations required to estimate the core–shell and shell–void interfaces. Though the optical transfer function of a complex object differs from the theoretical PSF of a confocal microscope, surfaces found in the image are still readily described by a three-dimensional Airy pattern which is the typical shape of a PSF in confocal microscopy (Fig. 2.6A). The location of the exact interface of the object itself is unknown, resulting in an increased relative error in

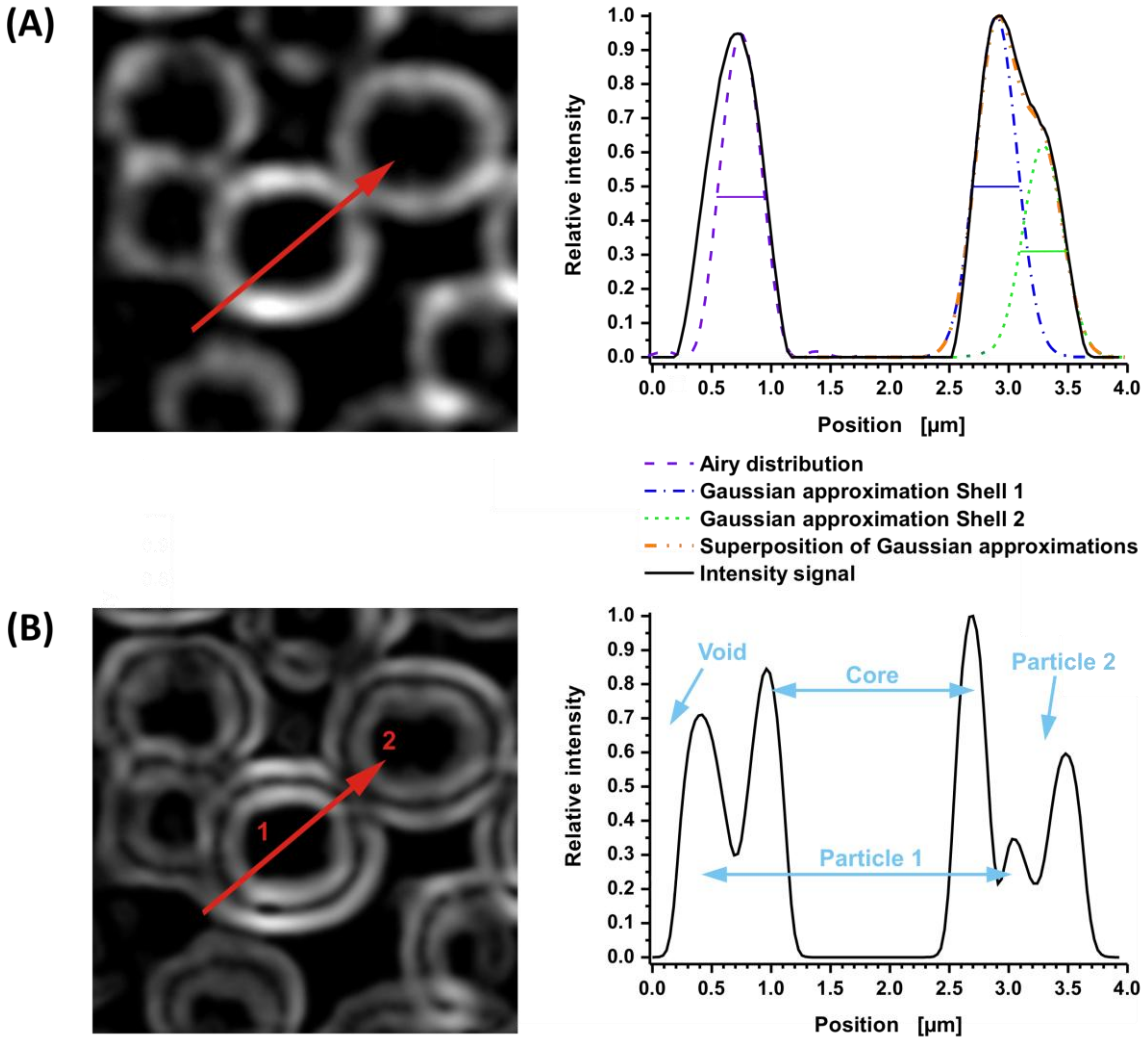

Figure 2.6: Deconvolved intensity signal along a core–shell particle (**A**) and its first derivative (**B**). The dye only reacts with the accessible silica surface, which is the porous shell, whereas the particle core remains dark resulting in a ring-like signal (**A**). However, the signal is not binary, but its intensity changes gradually. The intensity decay at the materials surface is described by an Airy function which is exemplarily displayed for a core–shell interface (purple). Since the ratio of the shell thickness to the resolution is small, the complete signal of a shell can be approximated by a Gaussian distribution (blue), or as a superposition of two Gaussian distribution functions when another particle is touched (orange). The intensity gradient becomes maximal close to the edges of the shell. Thus (**B**), which is the first derivative of (**A**), displays two maxima. Segmentation is performed at these maxima of the gradient image allocating voxels to a specific particle's core or shell (**B**).

final quantifications for objects that are merely resolved. Thus, placement of the object's interface to generate a quantifiable image with defined regions that are segmented into different features is crucial and heavily depends on the applied segmentation algorithm. However, in the case of particles additional information, like sphericity and approximate particle size, can be used to overcome the limiting depth resolution. Segmentation in the plane around the already known particle center has the highest accuracy, not only because of the better lateral microscopic resolution, but also because the particle diameter is maximal and least stray light from adjacent particles is guaranteed.

With 0.35 µm the nominal thickness of the particle shell itself is only two to three times the lateral resolution. As a consequence, the recorded intensity signal contains a single maximum and is well approximated by a Gaussian distribution (see Fig. 2.6A). The maximum of this distribution may already vary for a single particle, but segmentation based on the signal's maximum gradient can provide reproducible results. We decided to calculate the first derivative of each optical slice and draw a set of linear intensity profiles from the center of each particle to the surface of a virtually surrounding circle. In this way, each profile is recorded orthogonal to the particle surface so that any directional bias is eliminated from the calculations. Every pixel from the origin to the first maximum is identified as belonging to the core and given a label with respect to the corresponding particle center. Pixels from the first to the second maximum are assigned to the particle's shell. In the worst case, two particles of differing signal intensity touch and the interface between these particles will be shifted towards the brighter particle. Still, the difference to modeling each distribution function is only a few nanometers and does not effect the overall reconstruction or arithmetic mean of the shell thickness (Fig. 2.6). Finding the three-dimensional surface of the particle is the more error-prone task. From the segmented central particle plane we calculate a provisional core and particle diameter. We then assume the particle to be approximately spherical and extrapolate the surface to the other recorded layers. Imperfections of the particle are taken into account by shifting the assumed surface to the nearest gradient maximum which results in a three-dimensional reconstruction of the rugged particle surface (Fig. 2.5).

2.3.2 Morphological Analysis.

2.3.2.1 Size Distribution Functions. To verify the reliability of the reconstruction several morphological measures can be derived. Before, voxels were already labeled as being part of a certain particle. Calculating sphere diameters based on the volume covered by the respective voxels is thus straightforward. The scanned volume contained more than 7000 particles. 5213 of them were reconstructed as a whole and could therefore be used to determine a volume-weighted particle size distribution (PSD). Coulter counter-derived PSDs are typically based on the order of 10^4 particles, whereas the more closely related image processing of scanning electron microscopy (SEM) images is often stopped after counting particles on the order of 10^2, assuming a PSD representative for the bulk properties of the packing [64,65]. Still, SEM provides the highest precision and is considered to be the reference. With 10^3 particles counted, the CLSM reconstruction is well situated between these two methods. We found a mean particle diameter of 2.6 µm for the Kinetex particles, in agreement with the data from the manufacturer. The distribution displays a rela-tive standard deviation of 3.5%. This is narrower compared with the data we obtained from SEM (Fig. 2.7A), whereas the mean core diameter (1.8 µm) and shell thickness (0.4 µm) slightly deviate from the manufacturer data (1.9 µm core and 0.35 µm shell). Still, this deviation of about one pixel at each interface clearly excelled the agreement we expected to find.

2.3.2.2 Column Porosity. With a value of 0.362 the interparticle porosity (ε_{inter}) of the reconstructed packing was found to be around the random-close packing limit of monosized spheres: Song et al. [66] have recently shown that random hard-sphere packings in three dimensions cannot exceed a bed density of $\rho_{bed} = 0.634$ ($\varepsilon_{inter} = 1 - \rho_{bed} = 0.366$). For clarity we note that PSDs allow to realize lower values of ε_{inter} than strictly monosized spheres [67], but this interesting topic – most relevant to HPLC column technology – has not yet been intensively studied theoretically or experimentally. The interparticle (or external) porosity of the whole packed capillary is expressed by a value higher than the 0.362 since the reconstruction is a section of the capillary (cf. Fig. 2.3) that emphasizes the column center. Still, an estimate of the packing's external porosity after introduction of a weighting function that considers the cylindrical column shape increases the previous value only slightly to $\varepsilon_{inter} = 0.365$.

Schure and Maier [22] have demonstrated by numerical simulation studies of flow and transport in computer-generated sphere packings that sphere removal from the packings

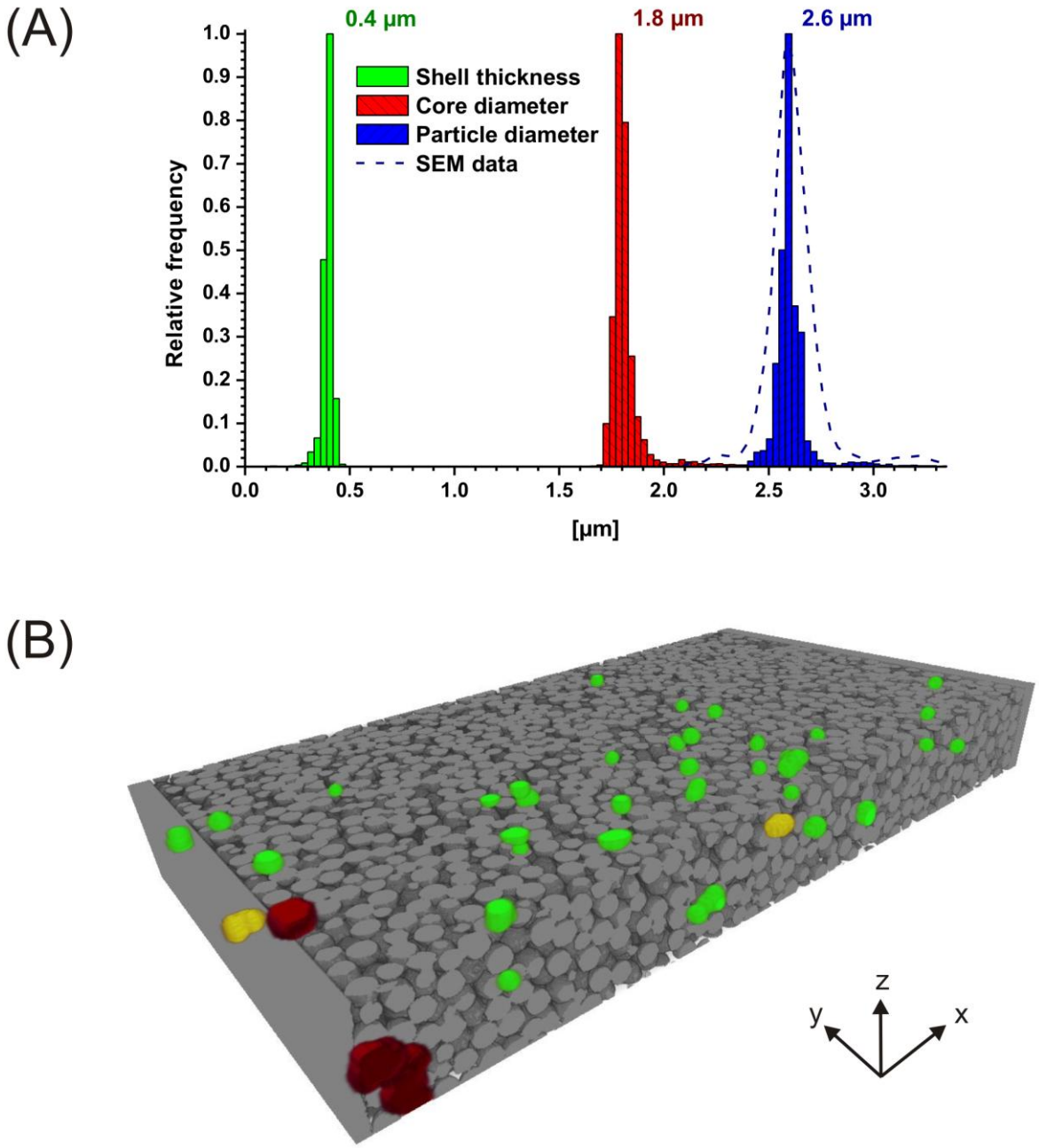

Figure 2.7: (**A**) Histograms of volume-based size distributions for the 2.6 µm Kinetex core–shell particles derived from a CLSM reconstruction of 5213 completely imaged particles, and comparison with a particle size distribution determined from scanning electron microscopy images. (**B**) Analysis of packing gaps with a minimum of 2 µm diameter in the underlying reconstruction (gray). The green volumes represent void spaces inaccessible by particles contained in the particle size distribution. Yellow volumes are defective positions accessible by 5% of the particles, whereas the red volumes can be accessed by at least 95% of the particles.

(to intentionally create defects) results in preferential flow paths and introduces new time and length scales for solute dispersion. These inhomogeneities were found to decrease strongly the chromatographic separation efficiency. In comparison to the number and quality of defects evaluated in that principal study [22], the particles analyzed in our reconstruction packed extremely dense and well, with only minor defects. In total, only four pores were found in the reconstruction that were large enough to be filled by a particle taken from the determined PSD. This is equivalent to a particle removal of less than 0.1% from a perfect packing. The smallest amount of particles removed in the study of defective packings by Schure and Maier [22] was 0.4%. However, the location of the gaps in our reconstructed packing cannot be considered as random. Three of the gaps were directly located at the column wall (Fig. 2.7B), a region of particular interest when analyzing the column cross-sectional heterogeneity of packing microstructure in confined packings and the origins of hydrodynamic dispersion, as we discuss further below.

In HPLC practice wehave accepted to “jam-pack” columns using a slurry-packing process that experience has told us to be most appropriate in terms of the traditionally measured (post-column) separation efficiency [6–8]. The packing process is complex and involves several, often strongly interrelated, parameters, among them the physicochemical properties of the stationary-phase particles (including PSD, mechanical strength, surface roughness, chemical surface modifications), interparticle forces (electrostatic, van der Waals), slurry preparation (concentration, slurry liquid, ionic strength), the application of pressure and ultrasound, as well as the coupled stress–strain-flow behavior [68]. Due to the difficulty in probing the packing microstructure systematically as a function of all relevant process parameters, column packing and consolidation are largely treated phenomenologically and considered an art rather than a science.

Confined cylindrical packings of spherical particles consist of an ordered wall region, with high porosity fluctuations over a distance of 4–5 d_p from the wall, and a random, densely packed core region [20,25,40,69,70]. These porosity oscillations result from the inability of the hard particles to form a close packing against the hard surface of the cylindrical column as particles can touch, but not penetrate the wall. The first particle layer of the bed in contact with the wall is not only highly ordered, but differs from subsequent layers, because the interstitial space between the wall and the first layer cannot be partially occupied by other particles. Subsequent particle layers towards the column center do not retain this level of order and the degree of randomness increases with the distance from the wall. This wall effect is a purely geometrical effect existing in immediate vicinity of the

column wall and is distinct from a second and more extended wall effect caused by friction between the particles of the bed and the column wall [71–73]. The latter effect is traditionally discussed in HPLC in connection with relatively large column-to-particle diameter ratios. Here, the packing density near the wall is higher than in the core region. The effect is related to the relatively high compressibility of pulverulent materials and the complex distribution of axial and radial stress during the compression of the bed. The extent of this wall effect strongly depends on packing procedure, column-to-particle diameter ratio, and operational conditions.

The geometrical wall effect was envisioned early in the chromatographic literature [74] and later carefully studied by Jorgenson and co-workers with packed capillaries [75–77]. For example, Kennedy and Jorgenson [75] and subsequently Hsieh and Jorgenson [76] have demonstrated that the performance of fused-silica capillaries packed with 5 µm particles improves significantly with decreasing capillary inner diameter between 12 and 50 µm. At these low column-to-particle diameter ratios the core region ultimately disappears and the packing structure is dominated by the wall region, i.e., the packing structure becomes effectively more ordered and homogeneous over the whole cross-section. The effects of the geometrical wall effect at increasing column-to-particle diameter ratio on hydrodynamic dispersion and chromatographic band broadening (compared with bulk packings which mimic infinitely wide, randomly packed beds “without walls”) are striking and have been quantified by extensive numerical simulation studies [20,25].

A plot of the interparticle (or external) porosity against the distance from the capillary inner surface also revealed these fluctuations characteristic of the geometrical wall effect in our reconstructed packed-bed segment (Fig. 2.8A, “external porosity”). Notably, these near-wall oscillations, over a distance of about 4 d_p from the wall, remain mostly above the mean external porosity (0.362). Within these regions, the porosity fluctuations seem to be damped by the presence of gaps in the packing (cf. Fig. 2.7B). When we add the shell volume of the particles to the interstitial void space, a porosity profile is obtained for a hypothetical packing with only the particles’ solid cores (Fig. 2.8A, “particle cores only”). This increases the mean porosity (void space between the solid cores) to a fictitious value of 0.783. Thereby, however, the relative influence of gaps in the packing is reduced and more symmetrical oscillations (around that mean porosity of 0.783), characterizing a geometrical wall effect, become visible (Fig. 2.8A).

In general, locally increased oscillations in the porosity profile suggest deviations from random packing behavior towards a more crystal-like structure as seen, for example, in the

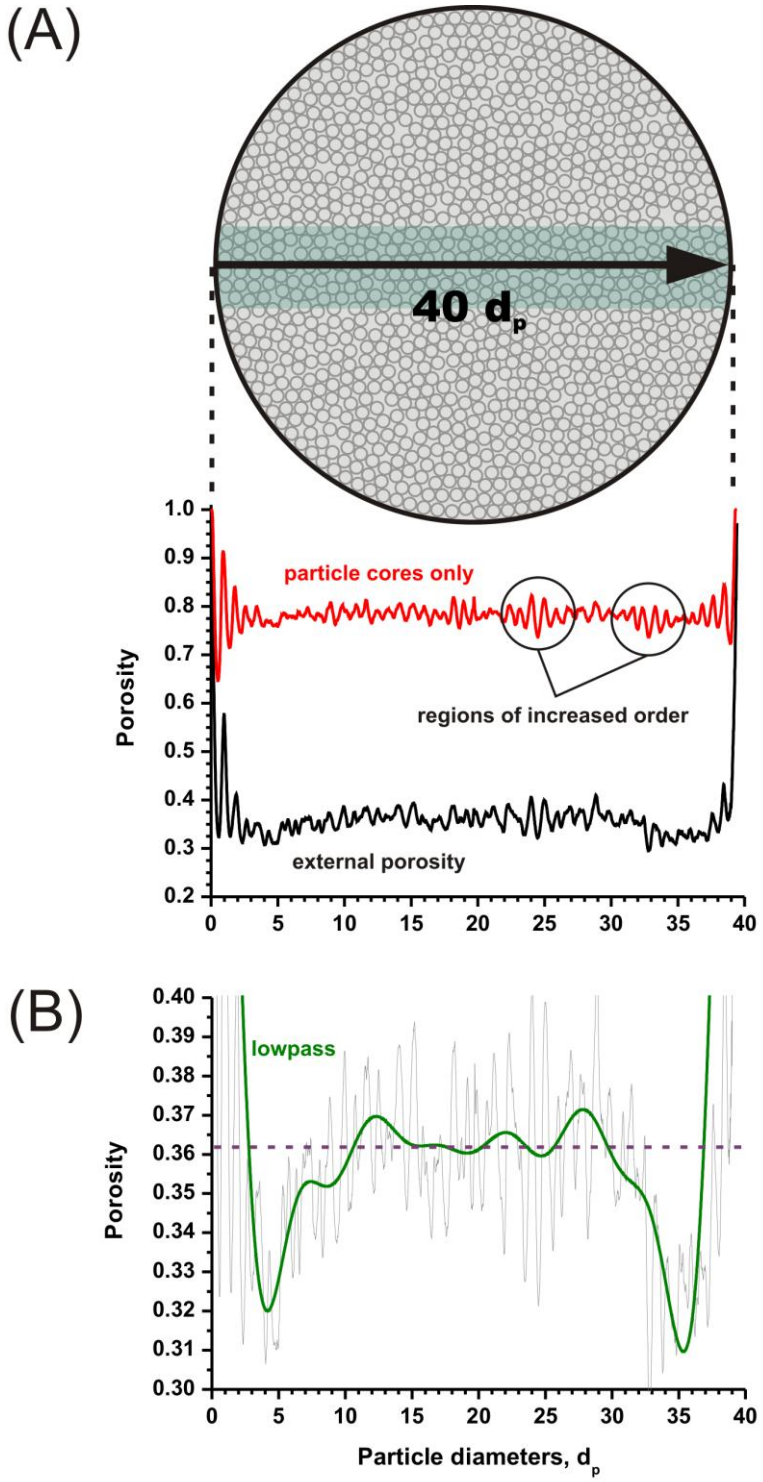

Figure 2.8: (**A**) Radial porosity profiles of the reconstructed core–shell packing plotted for the interparticle or external porosity (black line) and the hypothetical loose packing of the particles' cores only, i.e., without their shell (red line). (**B**) Lowpass of the external porosity illustrating the second wall effect, beyond the geometrical wall effect in direct vicinity of the column wall, most probably related to friction during column packing. The mean porosity is represented by the dashed line (at 0.362).

direct vicinity of the column wall. Similarly, parts of the porosity profile of our reconstruction that are shaped like beat frequencies suggest the presence of increased order (Fig. 2.8A), in this case, e.g., due to some agglomerated particles which were not dispersed during the slurry preparation and therefore could transfer this higher order into the final bed structure. Though these porosity fluctuations appear to be insignificant, their presence denotes variations in packing disorder on the scale of several particles, which inevitably increases time and length scales of dispersion in the bulk packing and generally will adversely affect separation efficiency.

In addition to the variation of packing density and disorder in the direct vicinity of the column wall and in the identified bulk regions (Fig. 2.8A), another origin of systematic radial heterogeneity in the external porosity profile of the reconstruction becomes evident by taking a look at its lowpass: Fig. 2.8B provides physical evidence for the earlier-mentioned second wall effect caused by the high radial stress applied by the bed to the wall as a consequence of friction between particles during the slurry-packing process. Because of these frictional forces, of the resulting radial stress that forces the particles against the wall and of the friction between the bed and the wall [71], a higher packing density is established in the wall region. Consequently, the bed permeability is higher in the central region than near the wall and a heterogeneous radial flow velocity distribution will develop.

For the reconstructed capillary packing (Fig. 2.8B), the external porosity profile exhibits a minimal porosity at a distance of 4–5 d_p from the wall and gradually increases, almost symmetrically, from both sides up to a distance of 10.5 d_p from the wall, until the dashed line representing the mean external porosity (0.362) is crossed for a second time and bulk packing properties seem to be approached. We are not aware of any systematic study of this wall effect in columns with a column-to-particle diameter ratio that is characteristic for capillary type stationary phases. Thus, a comparison can only be made with results published for analytical and larger bore columns where already the packing process varies markedly. Therefore, this comparison should be made with care and only aim at resolving similar physical origins of wall effects in packed beds, not their magnitudes and spatial dimensions. For example, using optical on-column visualization Shalliker et al. [72] analyzed wall effects by tracking the migration of sample bands through a 17 mm i.d. glass column packed with 21 µm particles. Their results demonstrated that two wall effects take place in chromatographic columns. The first is purely geometrical, the second is related to

friction, as explained. Our results well confirm their conclusions by a direct physical reconstruction of the chromatographic bed for a 100 µm i.d. capillary column packed with 2.6 µm particles, resulting in a column-to-particle diameter ratio of ~40: a relatively homogenous core region of roughly 19 d_p is surrounded by heterogeneous wall regions of 21 d_p including both wall effects (Fig. 2.8B).

The porosity profile in Fig. 2.8B implies that in a narrow (~2 d_p wide) region next to the column wall the mobile phase velocity is higher than its average in the whole packing, as a consequence of the geometrical wall effect, and that in a directly neighbored, but wider region (~7 d_p) towards the center of the column the mobile phase velocity is lower, most likely due to the packing process-specific second wall effect related to friction. Further analysis requires confirmation of these results, but already promises great potential in the comparative study of packing conditions, particle properties, and column-to-particle diameter ratios, particularly in view of characterizing and minimizing the packing process-specific heterogeneities in the final bed structure.

2.3.2.3 Chord Length Distributions. Giddings [1] has divided local velocity heterogeneities in a packed bed that contribute to eddy dispersion into the following categories.

(**1**) The transchannel contribution arises from the lateral distribution of velocities inside each individual channel between particles. It resembles the Hagen–Poiseuille flow profile in a cylinder, though channels in a packed bed have a more complicated geometry and flow velocity distribution [78].

(**2**) The short-range interchannel contribution is due to the existence of small groups of tightly packed particles between which more loosely packed regions are found. As demonstrated recently, and consistent with Giddings' analysis, it reflects local disorder on the scale of 1–2 d_p [25,27].

(**3**) Fluctuations of local packing density cause this pattern of tightly packed groups of particles interspersed by loosely packed regions to be erratic, which results in the long-range interchannel contribution.

(**4**) The existence of systematic variations of the mobile phase velocity between different regions of the column, i.e., in the core and the wall regions, is responsible for the transcolumn contribution.

A fifth contribution mentioned by Giddings as a source of velocity bias is the transparticle contribution in beds of porous particles. This effect should not be taken into account as an eddy dispersion term, however, as it is actually the strict equivalent of the pore diffusion mechanism [12]. The intraparticle fluid velocity is zero, as only transfer by diffusion allows the solute molecules to penetrate or leave the particles [79]. Since the intrinsic flow pattern behind eddy dispersion is a direct result of the pore space morphology, image analysis of reconstructed packings can be used to derive measures that correlate with individual dispersion contributions.

For example, the transcolumn velocity bias in a packed bed can be traced back to the porosity profile described in Fig. 48. Short-range and long-range interchannel contributions are related to much smaller length scales so that a description by a global parameter like the porosity is difficult. We therefore adopt a more fundamental view on these contributions than just fluctuations in the packing density. Image analysis provides various measures of local density whereof Voronoi volume distributions (VVDs) have been used effectively to capture the heterogeneity of granular packings [80,81] and derive disorder-dispersion correlations for the first time [27]. Aste and Di Matteo [80] used a two-parameter (*k*-gamma) function for a mathematical description of these distributions. We found that chord length distributions (CLDs) created in the interstitial void space of chromatographic beds (monoliths and sphere packings) allow to fit a similar function. These CLDs can be understood as a measure of local density of the void space where eddy dispersion takes place. The VVDs of monodisperse sphere packings also sensitively depend on their local disorder [27,81]. Therefore, both kinds of distributions (CLDs and VVDs) provide a direct connection to the heterogeneities of packed beds that are responsible for the intrinsic velocity biases and resulting eddy dispersion. Whereas the VVDs require strictly defined centers for the tessellation (e.g., sphere centers), the CLDs offer increased versatility. They can be determined for any porous medium without requiring further input parameters [50,82].

Thus, the comparison of particulate and monolithic materials becomes straightforward. To conclude our discussion and draw an analogy to our previous work on monoliths [50], a CLD for the pore space of the reconstructed packed bed of the Kinetex particles is provided in Fig. 2.9. As we adopt the *k*-gamma description to CLDs, the minimal chord length will always be zero. It follows that

$$f(l_c, k) = \frac{k^k}{\Gamma(k)} \frac{{l_c}^{k-1}}{{\mu_c}^k} \exp\left(-\frac{k \cdot l_c}{\mu_c}\right) \quad \text{(Eq. 2.4)}$$

where l_c denotes chord length, μ_c is the mean chord length as a first-moment parameter of location, and k is a second-moment parameter defining the dispersion of the distribution function. For CLDs, k is defined by the mean and the standard deviation σ as

$$k = \frac{{\mu_c}^2}{\sigma^2} \quad \text{(Eq. 2.5)}$$

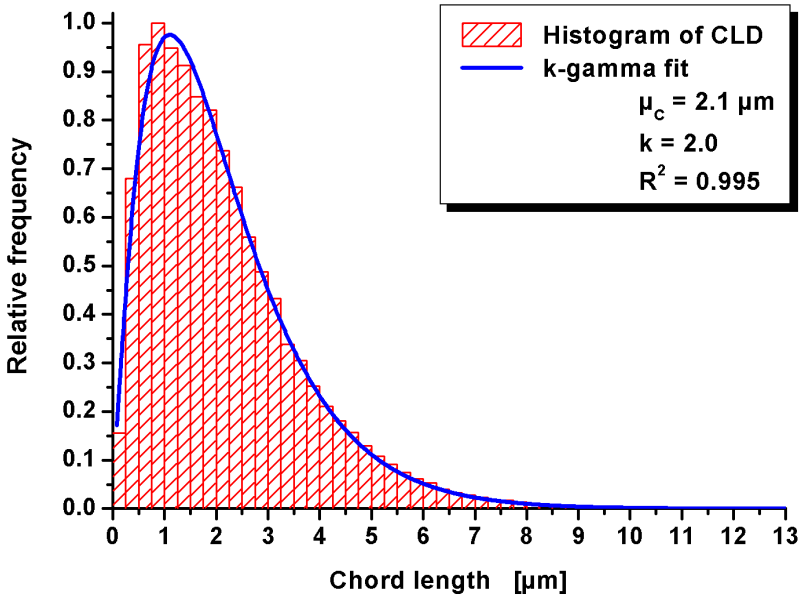

Figure 2.9: Normalized histogram representation of the 4×10^5 measured chords calculated in the void space of the reconstructed packing and fitted k-gamma distribution (solid line) (Eq. 2.4). The mean chord length (μ_c), dispersion coefficient (k), and coefficient of determination (R^2) are provided in the legend.

Schenker et al. [82] showed that the k-value of the VVDs they calculated for particle packings generated by Brownian dynamics simulations is a sensitive scalar measure for structural changes and the degree of heterogeneity; the lower k, the more heterogeneous the structure. Fig. 2.9 illustrates the good fit of the distribution function (Eq. 2.4), and provides

basic statistical parameters. These may be interpreted in terms of Gidding's eddy dispersion analysis: Chord lengths are a one-dimensional measure in space. Thus, μ_c is a measure of pore size and provides a connection to the transchannel dispersion in a packed bed, whereas the degree of heterogeneity of a packing, described by the normalized second-moment parameter *k*, effectively leads us to the short-range interchannel dispersion.

Thus, the distribution function provides a parameter of location μ_c and a parameter of dispersion *k* which were 2.1 µm and 2.0, respectively, for the reconstructed core–shell packing (Fig. 2.9). These parameters are expected to correlate with the transchannel and short-range interchannel dispersion, respectively, since in particulate materials the CLDs are nothing but an alternative statistic for the VVDs (which were already shown to correlate strongly with the resulting eddy dispersion [27]). Similarly, CLDs can be calculated and characterized by a *k*-gamma distribution for the reconstructed macropore space of silica monoliths. The mean macropore of a Chromolith capillary monolith is roughly twice the macropore size of the reconstructed Kinetex packing presented in this study, whereas *k* shows about the same value [50,83]. Thus, a hypothetical packing of 5.2 µm particles, self-similar to our reconstruction, is expected to show a comparable behavior with respect to dispersion on the transchannel and short-range interchannel scales as the silica monolith.

2.4 Conclusions

Imaging and reconstruction of modern chromatographic packings and supports in capillary format by light microscopy is possible if spherical aberrations are eliminated from the sample setup. This has been demonstrated for monoliths [50–52] as well as packings of sub-3 µm core–shell particles in the present work, and we are currently extending this approach to sub-2 µm particles. The localization of the particles can be performed at a confidence higher than the achievable resolution and should enable very systematic statistical studies on packing morphology and heterogeneity depending on packing process parameters (slurry preparation, application of pressure and ultrasound) and particle properties (size distribution, shape, and surface roughness). Statistics derived from the reconstruction confirm and visualize the effects which are known to exist in analytical columns of much higher column-to-particle diameter ratio. For example, both the geometrical and a probably friction-based second wall effect were identified in the porosity profile of the reconstruction.

Whereas the influence of transcolumn velocity gradients of various origins on the separation efficiency in HPLC is well known, the precise nature of how the microstructure of a packed bed (or monolith) and the geometry of the confinement affect the flow heterogeneity, transverse equilibration as well as the macroscopically resulting longitudinal dispersion, is still largely unresolved. The presented approach promises improvements in our understanding and optimization of chromatographic supports. It also provides a well-defined basis for comparisons between particulate and monolithic supports by means of the statistical measures derived from their reconstructions. For example, CLDs were calculated for the reconstructed packing as a descriptor of local density of the interparticle macropore space, and it was shown that they can be characterized by a simplified *k*-gamma distribution.

Finally, the reconstructed packings provide a valuable experimental benchmark for studies of structure–transport relationships in chromatographic media: they enable the evaluation of different algorithms for computer-generated packings for their ability to provide realistic model packings, but also serve as true packing microstructures for simulations of hydrodynamic flow and mass transport. These direct simulations in the physically reconstructed morphologies will quantify time and length scales of dispersion associated with a particular packing protocol and particle type, a potential that was analogously demonstrated already for silica monoliths and their fabrication process [51,52].

Acknowledgements

This work was supported by the Deutsche Forschungsgemeinschaft DFG (Bonn, Germany) under grant TA 268/5 and by Agilent Technologies with an award through Agilent's University Relations Research Grant program. We thank Martin Kollmann and Professor Joachim Schachtner (Department of Biology, Philipps-Universität Marburg) for their help with the CLSM measurements and Dr. Tivadar Farkas (Phenomenex Inc., Torrance, CA, USA) for the gift of the Kinetex particles.

References

[1] Giddings, J. C. *Dynamics of Chromatography, Part1: Principles and Theory*, Marcel Dekker, New York, **1965**.

[2] Bear J., *Dynamics of Fluids in Porous Media*, Dover Publications, New York, **1988**.

[3] Weber, S. G.; Carr, P. W. in: Brown, P. R.; Hartwick, R. A. (Eds.), *High Performance Liquid Chromatography*, Wiley, New York, **1989** (Chapter 1).

[4] Dullien, F. A. L. *Porous Media: Fluid Transport and Pore Structure*, Academic Press, San Diego, **1992**.

[5] Sahimi, M. *Flow and Transport in Porous Media and Fractured Rock*, VCH, Weinheim, **1995**.

[6] Guiochon, G.; Felinger, A.; Katti, A. M.; Shirazi, D.G. *Fundamentals of Preparative and Nonlinear Chromatography*, 2nd edition, Elsevier, Amsterdam, **2006**.

[7] Guiochon, G. *J. Chromatogr., A* **2006,** *1126*, 6–49.

[8] Unger, K. K.; Skudas, R.; Schulte, M. M. *J. Chromatogr., A* **2008**, *1184*, 393–415.

[9] Unger, K. K.; Ditz, R.; Machtejevas, E.; Skudas, R. *Angew. Chem. Int. Ed.* **2010**, *49*, 2300–2312.

[10] Delgado, J. M. P. Q. *Heat Mass Transfer* **2006**, *42*, 279–310.

[11] Hlushkou, D.; Tallarek, U. *J. Chromatogr., A* **2006**, *1126*, 70–85.

[12] Gritti, F.; Guiochon, G. *Anal. Chem.* **2006**, *78*, 5329–5347.

[13] Holland, D. J.; Scheven, U. M.; Middelberg, A. P. J.; Gladden, L. F. *Phys. Fluids* **2006**, *18*, 033102.

[14] Maier, R. S.; Kroll, D. M.; Bernard, R. S.; Howington, S. E.; Peters, J. F.; Davis, H. T. *Phys. Fluids* **2000**, *12*, 2065–2079.

[15] Mantle, M. D.; Sederman, A. J.; Gladden, L. F. *Chem. Eng. Sci*. **2001**, *56*, 523–529.

[16] Hill, R. J.; Koch, D. L.; Ladd, A. J. C. *J. Fluid Mech.* **2001**, *448*, 243–278.

[17] Maier, R. S.; Kroll, D. M.; Bernard, R. S.; Howington, S. E. Peters, J. F.; Davis, H. T. *Philos. Trans. R. Soc. Lond., A* **2002**, *360*, 497–506.

[18] Kandhai, D.; Hlushkou, D. Hoekstra, A. G.; Sloot, P. M. A.; Van As, H.; Tallarek, U. *Phys. Rev. Lett.* **2002**, *88*, 234501.

[19] Schure, M. R.; Maier, R. S.; Kroll, D. M.; Davis, H. T. *Anal. Chem.* **2002**, *74*, 6006–6016.

[20] Maier, R. S.; Kroll, D. M.; Bernard, R. S.; Howington, S. E.; Peters, J. F.; Davis H. T., *Phys. Fluids* **2003**, *15*, 3795–3815.

[21] Hlushkou, D.; Seidel-Morgenstern, A.; Tallarek, U. *Langmuir* **2005**, *21*, 6097–6112.

[22] Schure, M. R.; Maier, R. S. *J. Chromatogr., A* **2006**, *1126*, 58–69.

[23] Maier, R. S.; Kroll, D. M.; Davis, H. T. *AIChE J.* **2007**, *53*, 527–530.

[24] Khirevich, S.; Höltzel, A.; Ehlert, S.; Seidel-Morgenstern, A.; Tallarek, U. *Anal. Chem.* **2009**, *81*, 4937–4945.

[25] Khirevich, S.; Höltzel, A.; Seidel-Morgenstern, A.; Tallarek, U.; *Anal. Chem.* **2009**, *81*, 7057–7066.

[26] Maier, R. S.; Bernard, R. S. *J. Comput. Phys.* **2010**, *229*, 233–255.

[27] Khirevich, S.; Daneyko, A.; Höltzel, A.; Seidel-Morgenstern, A.; Tallarek, U. *J. Chromatogr., A* **2010**, *1217*, 4713–4722.

[28] Yao, Y.; Czymmek, K. J.; Pazhianur, R.; Lenhoff, A. M. *Langmuir* **2006**, *22*, 11148–11157.

[29] Langford, J. F.; Schure, M. R.; Yao, Y.; Maloney, S. F.; Lenhoff, A. M. *J. Chromatogr., A* **2006**, *1126*, 95–106.

[30] Midgley, P. A.; Ward, E. P. W.; Hungría, A. B.; Thomas, J. M. *Chem. Soc. Rev.* **2007**, *36*, 1477–1494.

[31] Aste, T.; Saadatfar, M.; Senden, T. J. *Phys. Rev. E* **2005**, *71*, 061302.

[32] Dong, H.; Blunt, M. J. *Phys. Rev. E* **2009**, *80*, 036307.

[33] Gommes, C. J.; Bons, A.-J.; Blacher, S.; Dunsmuir, J. H.; Tsou, A. H. *AIChE J.* **2009**, *55*, 2000–2012.

[34] Fredrich, J. T. *Phys. Chem. Earth A* **1999**, *24*, 551–561.

[35] Leinweber, F. C.; Tallarek, U. *J. Phys. Chem. B* **2005**, *109*, 21481–21485.

[36] Prasad, V.; Semwogerere, D.; Weeks, E. R. *J. Phys. Condens. Matter* **2007**, *19*, 113102.

[37] Seymour, J. D.; Callaghan, P. T. *AIChE J.* **1997**, *43*, 2096–2111.

[38] Tallarek, U.; Bayer, E.; van Dusschoten, D.; Scheenen, T.; Van As, H.; Guiochon, G.; Neue, U. D. *AIChE J.* **1998**, *44*, 1962–1975.

[39] Manz, B.; Gladden, L. F.; Warren, P.B. *AIChE J.* **1999**, *45*, 1845–1854.

[40] Sederman, A. J.; Alexander, P.; Gladden, L. F. *Powder Technol.* **2001**, *117*, 255–269.

[41] Gritti, F.; Guiochon, G. *J. Chromatogr., A* **2007**, *1157*, 289–303.

[42] DeStefano, J. J.; Langlois, T. J.; Kirkland, J. J. *J. Chromatogr. Sci.* **2008**, *46*, 254–260.

[43] Cavazzini, A.; Gritti, F.; Kaczmarski, K.; Marchetti, N.; Guiochon, G. *Anal. Chem.* **2007**, *79*, 5972–5979.

[44] Gritti, F.; Leonardis, I.; Shock, D.; Stevenson, P.; Shalliker, A.; Guiochon, G. *J. Chromatogr., A* **2010**, *1217*, 1589–1603.

[45] Olah, E.; Fekete, S.; Fekete, J.; Ganzler, K. *J. Chromatogr., A* **2010**, *1217*, 3642–3653.

[46] Baker, J. S.; Vinci, J. C.; Moore, A. D.; Colón, L. A. *J. Sep. Sci.* **2010**, *33*, 2547–2557.

[47] Kiss, I.; Bacskay, I.; Kilar, F.; Felinger, A. *Anal. Bioanal. Chem.* **2010**, *397*, 1307–1314.

[48] Gritti, F.; Leonardis, I.; Abia, J.; Guiochon, G. *J. Chromatogr., A* **2010**, *1217*, 3819–3843.

[49] Gritti, F.; Guiochon, G. *J. Chromatogr., A* **2010**, *1217*, 5137–5151.

[50] Bruns, S.; Müllner, T.; Kollmann, M.; Schachtner, J.; Höltzel, A.; Tallarek, U. *Anal. Chem.* **2010**, *82*, 6569–6575.

[51] Hlushkou, D.; Bruns, S.; Tallarek, U. *J. Chromatogr., A* **2010**, *1217*, 3674–3682.

[52] Hlushkou, D.; Bruns, S.; Höltzel, A.; Tallarek, U. *Anal. Chem.* **2010**, *82*, 7150–7159.

[53] Chen, G.; Pačes, M.; Marek, M.; Zhang, Y.; Seidel-Morgenstern, A.; Tallarek, U. *Chem. Eng. Technol.* **2004**, *27*, 417–428.

[54] Ehlert, S.; Rösler, T.; Tallarek, U. *J. Sep. Sci.* **2008**, *31*, 1719–1728.

[55] Abrams, B.; Diwu, Z.; Guryev, O.; Aleshkov, S.; Hingorani, R.; Edinger, M.; Lee, R.; Link, J.; Dubrovsky, T. *Anal. Biochem.* **2009**, *386*, 262–269.

[56] El Kadib, A.; Chimenton, R.; Sachse, A.; Fajula, F.; Galarneau, A.; Coq, B. *Angew. Chem. Int. Ed.* **2009**, *48*, 4969–4972.

[57] Malitson, I. H. *J. Opt. Soc. Am.* **1965**, *55*, 1205–1208.

[58] Reis, J. C. R.; Lampreia, I. M. S.; Santos, Â. F. S.; Moita, M. L. C. J.; Douhéret, G. *ChemPhysChem* **2010**, *11*, 3722–3733.

[59] Nasse, M. J.; Woehl, J. C. *J. Opt. Soc. Am. A* **2010**, *27*, 295–302.

[60] Rasband, W. S. *ImageJ*; U.S. National Institutes of Health: Bethesda, MD, **1997-2006**; http://rsb.info.nih.gov//ij/.

[61] Wilhelm, S.; Gröbler, B.; Gluch, M.; Heinz, H. *Confocal Laser Scanning Microscopy – Optical Image Formation and Electronic Signal Processing*; Monography, Carl Zeiss: Jena, Germany, **2008**.

[62] Zucker, R. M. *Cytometry A* **2006**, *69A*, 659–676.

[63] Schrader, M.; Hell, S.; van der Voort, H. T. M. *Appl. Phys. Lett.* **1996**, *69*, 3644–3646.

[64] Gritti, F.; Guiochon, G. *J. Chromatogr., A* **2007**, *1166*, 30–46.

[65] Cabooter, D.; Billen, J.; Terryn, H.; Lynen, F.; Sandra, P.; Desmet, G. *J. Chromatogr., A* **2008**, *1204*, 1–10.

[66] Song, C.; Wang, P.; Makse, H. A. *Nature* **2008**, *453*, 629–632.

[67] Clusel, M.; Corwin, E. I.; Siemens, A. O. N.; Brujić, J. *Nature* **2009**, *460*, 611–615.

[68] Yew, B. G.; Ureta, J.; Shalliker, R. A.; Drumm, E. C.; Guiochon, G. *AIChE J.* **2003**, *49*, 642–664.

[69] de Klerk, A. *AIChE J.* **2003**, *49*, 2022–2029.

[70] Theuerkauf, J.; Witt, P.; Schwesig, D. *Powder Technol.* **2006**, *165*, 92–99.

[71] Guiochon, G.; Drumm, E.; Cherrak, D. *J. Chromatogr., A* **1999**, *835*, 41–58.

[72] Shalliker, R. A.; Broyles, B. S.; Guiochon, G. *J. Chromatogr., A* **2000**, *888*, 1–12.

[73] Shalliker, R. A.; Wong, V.; Broyles, B. S.; Guiochon, G. *J. Chromatogr., A* **2002**, *977*, 213–223.

[74] Knox, J. H.; Parcher, J. F. *Anal. Chem.* **1969**, *41*, 1599–1606.

[75] Kennedy, R. T.; Jorgenson, J. W. *Anal. Chem.* **1989**, *61*, 1128–1135.

[76] Hsieh, S.; Jorgenson, J. W. *Anal. Chem.* **1996**, *68*, 1212–1217.

[77] Patel, K. D.; Jerkovich, A. D.; Link, J. C.; Jorgenson, J.W. *Anal. Chem.* **2004**, *76*, 5777–5786.

[78] Hlushkou, D.; Khirevich, S.; Apanasovich, V.; Seidel-Morgenstern, A.; Tallarek, U. *Anal. Chem.* **2007**, *79*, 113–121.

[79] Tallarek, U.; Vergeldt, F. J.; Van As, H. *J. Phys. Chem. B* **1999**, *103*, 7654–7664.

[80] Aste, T.; Di Matteo, T. *Phys. Rev. E* **2008**, *77*, 021309.

[81] Schenker, I.; Filser, F. T.; Gauckler, L. J.; Aste, T.; Herrmann, H. *J. Phys. Rev. E* **2009**, *80*, 021302.

[82] Courtois, J.; Szumski, M.; Georgsson, F.; Irgum, K. *Anal. Chem.* **2007**, *79*, 335–344.

[83] Bruns, S. *Dreidimensionale Rekonstruktion monolithischer Festphasen mittels konfokaler Lasermikroskopie.* Diplomarbeit, Fachbereich Chemie, Philipps-Universität, Marburg, Germany, **2009**.

Chapter 3

Morphological Analysis of Physically Reconstructed Capillary Hybrid Monoliths and Correlation with Separation Efficiency

Authors:

Stefan Bruns, Takeshi Hara, Bernd M. Smarsly, and Ulrich Tallarek

State of Publication:

Published August 5, 2011 in *Journal of Chromatography A*, Vol. 1218, No. 31, p. 5187–5194.

Abstract

We report an experimental study on the structural (especially radial) heterogeneity of eleven 100 µm i.d. capillary tetramethoxysilane–methyltrimethoxysilane hybrid silica monoliths with different pore and skeleton sizes, which were imaged by an optimized confocal laser scanning microscopy method. This method allows the optical sectioning of the monoliths, which is a prerequisite for quantitative morphological image analysis. Both radial porosity profiles and chord length distributions were calculated in the macropore domain for each column from at least 100 complete cross-sectional views along the column axis. The statistical approach visualized radial heterogeneities on different length scales in the monolithic structures. Chord length distributions followed a simplified *k*-gamma function, and a structural parameter obtained from this function is introduced to provide a scalar measure of column heterogeneity. It enables the comparison of monoliths with different pore sizes and helps to establish correlations between the microscopic properties of a column, eddy dispersion, and its separation efficiency.

3.1 Introduction

Monolithic stationary phases were developed and introduced in HPLC as an alternative to particulate fixed-beds for potentially faster and more efficient separations [1–4]. In the hierarchically structured pore space of monoliths the macropores enable convective transport, whereas the mesoporous (and often also microporous) skeletons provide a large surface area accessible by diffusion. The morphology of many organic polymer monoliths resembles that of microglobular aggregates [5–7], typically with a broad pore size distribution, whereas silica monoliths show a more fractal morphology, with discrete sets of intraskeleton mesopores and interskeleton macropores [8]. The synthesis of silica monoliths for chromatography, introduced by Nakanishi and co-workers [9–14], allows modifying macropore size and skeleton thickness independently from another. The hierarchical pore morphology of silica monoliths results from their two-step preparation, i.e., a sol–gel mechanism overlapped with a spinodal phase transition as the first step (determining the domain size and macropore diameter), followed by a solvent exchange, which leaches out the silica skeleton to create the intraskeleton mesopore space.

Although the following characteristics can be modulated by the preparation protocols, typical silica monoliths have shown to offer high sample capacity per unit adsorbent volume [15,16], a permeability comparable to that of columns packed with 11 µm particles [16,17], and an efficiency equivalent to that of 2–3 µm particulate columns [18,19]. As a consequence, silica monoliths have a much lower separation impedance than either 5 or 3.5 µm particulate packings [20]. When 5 µm particles were the standard material for analytical HPLC columns, the monolithic supports appeared as a breakthrough development. However, it was recognized early that structural features inherent to the fabrication process limit the efficiency of silica monoliths. These structural features concern [1]

(**i**) the large size distribution, random spatial distribution, and variable geometry of the interskeleton macropores;

(**ii**) the size of the throughpores (N.B. The recent trend towards finer, particularly sub-2 µm, particles [21] realizes a smaller throughpore size at an essentially unchanged morphology of the particulate bed, whereas a comparable decrease in the domain size of silica monoliths has not been achieved yet.); and

(**iii**) the macroscopic radial heterogeneity of cylindrical monolithic columns. The formation of gaps between monolith skeleton and column wall is supposed to result from the uneven character of the mechanical stress that is experienced by the monolith–wall inter-

face during the sol–gel step of the synthesis when the silica skeleton shrinks back from the confining wall. This is a well-known problem, particularly for the rigid, but brittle silica monoliths prepared from pure tetramethoxysilane (TMOS) [1].

For particle-packed columns radial heterogeneities of different origin (depending on the particle characteristics, packing process, and column-to-particle diameter ratio) are well-known to contribute strongly to eddy dispersion through local fluctuations of the external porosity, permeability, and retention factors [22–28]. In the case of analytical [29] and semi-preparative [30] silica monolithic columns wall effects were shown to substantially affect the average cross-sectional plate height, and they have also been documented for monoliths in capillary format [31]. Therefore, the key to improving the separation efficiency of silica monoliths is a (primarily radially) more homogeneous macropore morphology. To resolve this issue for monoliths from capillary to preparative column formats and in each case distinguish between the individual contributions to eddy dispersion, from the macropore level up to the column scale, experimental as well as advanced simulation approaches are required that allow us to study eddy dispersion within the real morphology and on the inherent time and length scales behind these contributions.

We recently presented a fast, non-destructive, and quantitative confocal laser scanning microscopy (CLSM) method composed of column pretreatment, image acquisition, image processing, and statistical analysis of the image data to characterize the morphology of monoliths and particle-packed beds, exemplarily shown for a Chromolith CapRod column [32] and a 100 µm i.d. capillary packed with 2.6 µm Kinetex core–shell particles [33]. The method is generally applicable to silica-based particulate or monolithic columns in capillary format and can be used to visualize stationary phase structure. The approach yields a multitude of longitudinal and cross-sectional images in a short time and allows the fast scanning along large segments of a capillary column for heterogeneities in macropore morphology. Individual contributions to eddy dispersion, e.g., due to wall effects, can thus quickly be identified, enabling the optimization of silica monolith preparation for more efficient HPLC columns. Statistical analysis of the CLSM images yielded quantifiable morphological information in the form of chord length distributions for the macropore space and the skeleton. The data are comparable to those obtained by TEM image analysis [34], but easier to access, and describe the monolith's macropore morphology accurately and comprehensively, providing a clear advantage over estimates of the average domain size from SEM images.

This approach [32] has already been used to resolve hydrodynamic flow and transport in the reconstructed bulk macroporous domain of a 100 µm i.d. capillary silica monolith by direct numerical simulations on a supercomputing platform [35,36]. Excellent agreement was observed between experimental and simulated Darcy permeabilities. The flow field was analyzed in detail, including longitudinal and transverse velocity distributions, the occurrence of negative longitudinal velocities, as well as the beginning transition to the viscous-inertial flow regime [35]. Further, the pore scale (microscopic) insight provided by the simulations into the length scales on which eddy dispersion operates in the relatively homogeneous core region of the capillary silica monolith was complemented by conventional column scale (macroscopic) chromatographic plate height analysis, providing a comparison that quantified the severe efficiency loss due to the (CLSM-visualized) wall gaps and the associated transcolumn contribution to eddy dispersion [36]. These findings demonstrated that the heterogeneity of the bulk macropore space is much smaller than currently believed, and that the excellent performance of the bulk silica monolith is obscured in chromatographic practice by a special wall effect related to irregular voids within a layer of up to ~15 µm thickness at the capillary wall. Elimination of discrete voids at the capillary wall should therefore get priority in silica monolith preparation, as this measure promises much improved separation efficiencies [37].

In the current work, we use the CLSM-based approach [32] to investigate and compare the morphology of improved capillary hybrid silica monoliths [38]. For capillary silica monoliths with 100 µm i.d. and larger prepared from TMOS, serious wall defects (as a result of shrinkage during the sol–gel step of the synthesis) have been observed in SEM images [31]. Feeding methyltrimethoxysilane (MTMS) to the sol reduces the occurrence of such critical void regions and enabled the preparation of capillary hybrid silica monoliths of larger diameters [39,40] (see also pp. 109–110 in [1]). The incorporation of methyl groups into the silicate structure hinders the condensation of hydroxyl groups and therefore reduces the shrinkage. The structure of these hybrid monoliths is less brittle and more flexible, and it thus better compensates the physical stress during shrinkage [39]. We focus on an analysis of the physically reconstructed morphology to characterize the radial heterogeneity and local density fluctuations in 100 µm i.d. capillary hybrid silica monoliths.

3.2 Experimental Section

3.2.1 Chemicals and Materials. Eleven capillary monoliths in 100 µm i.d. cylindrical fused-silica capillaries were employed for this study. They were prepared as hybrid silica columns with an additional MTMS-content of 15% following the procedures described by Hara et al. [38] (cf. Section 2.2 and Table 3.1 in [38]). In the following discussion the observed variations in chromatographic separation efficiency are explained by monolith morphology. Columns which showed chromatographic band broadening dominated by their macropore size (transchannel dispersion) according to our analysis are referred to as Hybrid Columns A1–A7, whereas columns dominated by radial heterogeneity and the associated transcolumn dispersion are referred to as Hybrid Columns B1–B4. The analyzed monoliths had an unmodified bare-silica surface, except for Hybrid Column A2, which had a C18-modified surface.

3-Carboxy-6-chloro-7-hydroxycoumarin (dye V450) was purchased from Endotherm Life Science Molecules (Saarbrücken, Germany), while 3-aminopropyltriethoxysilane came from Alfa Aesar GmbH (Karlsruhe, Germany). Glycerol, HPLC grade acetonitrile, methanol, ethanol, dimethylsulfoxide (DMSO), and dimethylformamide (DMF) were supplied by Sigma–Aldrich Chemie GmbH (Taufkirchen, Germany), and a Milli-Q gradient water purification system (Millipore, Bedford, MA, USA) was used to provide HPLC grade water.

3.2.2 Chromatographic Separation Efficiency. The HPLC configuration assembled for the chromatographic evaluation of 25–30 cm long, 100 µm i.d. capillary monoliths consisted of a K-2501 spectro-photometer (Knauer, Berlin, Germany) and an L-7100 pump (Hitachi, Tokyo, Japan) with split injection/flow mode using a Rheodyne 7125 analytical injector (Rheodyne, Cotati, CA, USA). A 30 µm i.d. fused-silica capillary was utilized as UV detection cell as well as connection from the monolith column's outlet to the detection window where the polyimide coating had been removed. This distance was fixed at 3.4 cm. The split ratio during the chromatographic measurements was controlled at ~10^{-3}, as described previously [31]. Chromatographic data were processed with Hitachi D-7000 HPLC System Manager (HSM) software. All plate heights were calculated under kinetic conditions for unretained thiourea in methanol/water 80/20 (v/v) at 30 °C and an average flow velocity of 1.0 mm/s through the monoliths. The detection wavelength was set to 210 nm.

3.2.3 Image Acquisition. Prior to imaging by CLSM the silanol groups at the surface of the mesoporous monolith skeleton were labeled with a succinimidyl ester of dye V450, as described previously [32,33]. Each monolithic column was flushed with 100 µL of 3-aminopropyltriethoxysilane solution (0.1 M in ethanol) at 0.1 µL/min and 70 °C overnight. After cleaning with 500 µL of ethanol at 0.5 µL/min, 100 µL of V450-succinimidyl ester solution at 0.25 µL/min were introduced to bind V450 covalently to the monolith's surface. For bare-silica columns a dye concentration of 0.2 mg/mL DMF was found to yield high quality images consistently, whereas the decreased amount of binding sites in the C18-column was accounted for by increasing the dye concentration to 5 mg/mL.

All images were acquired on a TCS SP5 confocal microscopy system equipped with a HCX PL APO 63×/1.3 GLYC CORR CS (21°) glycerol immersion objective lens from Leica Microsystems (Wetzlar, Germany) by focusing into a capillary segment where the polyimide coating was removed with a drop of warm sulfuric acid. The column itself was filled with glycerol/DMSO/water 70/19/11 (v/v/v) and fixed on a microscope slide in an embedding pool of the same solvent mixture. For optimal refractive index matching this mixture was further calibrated with an AR200 digital refractometer (Reichert Analytical Instruments, Depew, NY, USA) to match the refractive index of the fused-silica capillary wall (n_D = 1.4582 [41]). The glycerol/DMSO/water mixture was also used as immersion medium for the microscope lens. A "type 0" cover slip (Gerhard Menzel GmbH, Braunschweig, Germany) was selected to separate embedding and immersion liquid minimizing spherical aberrations [33].

Excitation of dye V450 was realized with a 405 nm diode laser setting the pinhole of the microscope to 0.5 AU. Fluorescence emission was detected in the interval of 440–455 nm. Stacks of 100–200 8-bit grayscale images of 4096 × 2048 pixels were recorded from the column centre along the axis of the monolithic capillaries covering their whole diameter (see Fig. 3.1A). Pixel and step size were chosen as to remain below the Nyquist sampling criterion with 30 nm and 126 nm, respectively.

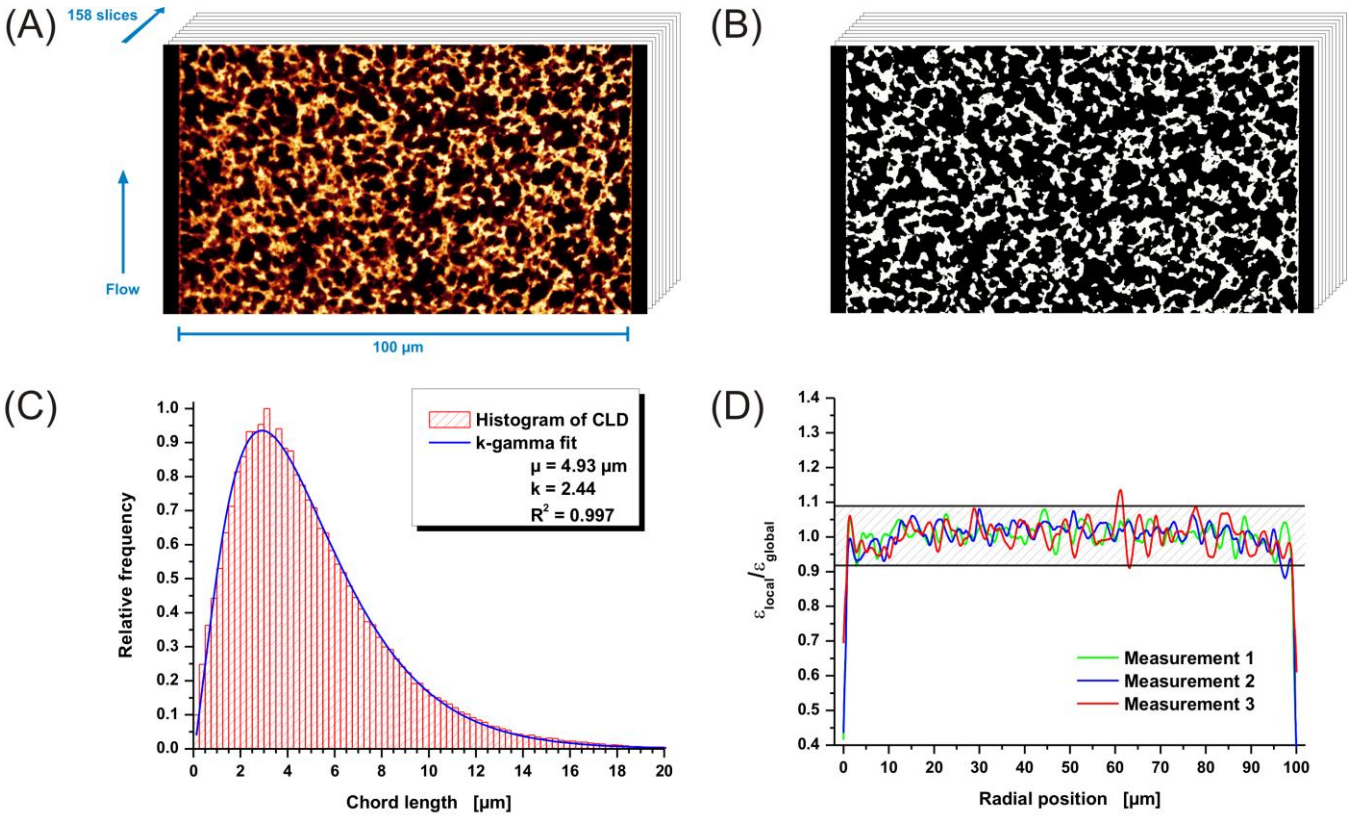

Figure 3.1: Exemplary image from the second measurement of Hybrid Column A4 (**A**) and the segmentation result (**B**). 158 slices form the image stack that was used to obtain a histogram from 1×10^6 chord lengths. The histogram was fitted with a normalized *k*-gamma distribution (**C**). Normalized radial porosity profiles calculated for a step size of 30 nm smoothed with a 1 µm moving window for three image stacks obtained at different times and positions in the detection window's volume of Hybrid Column A4 (**D**). The shading designates an area of ±1 standard deviation around the global mean porosity.

3.2.4 Image Processing and Analysis. Images were corrected for any z-drop by fitting a second-order exponential decay to the acquired image stack's intensity distribution along the dimension of the optical axis. Subsequently, Huygens maximum likelihood iterative deconvolution (Scientific Volume Imaging, Hilversum, The Netherlands) was applied for image restoration using an automated background estimate of the deconvolution software ("*in/near object*"-estimate) and a signal-to-noise ratio of 15. For image segmentation a copy of the acquired image stack was blurred with a Gaussian kernel and then subtracted from the deconvolved original [42]. Two hundred sigma were chosen as kernel size; a value that is large compared with image features and small compared with background varia-

tions [32]. This step was applied twice and any non-zero pixel was considered to be part of the monolithic skeleton (Fig. 3.1B). The image stack's faces that showed a continuing monolithic structure were cropped by 600 nm to avoid regions of poor restoration, resulting in reconstructions of the monolithic structures with macropore porosities between 0.68 and 0.72.

Image analysis was performed using custom software written with Visual Studio C# 2008 (Microsoft Corporation, Redmond, WA, USA) on at least hundred images for each column. The images were rotated to have the column walls aligned with the y-dimension of the image. Left and right column walls were defined as first and last y-column, respectively, in the image with a porosity of less than 0.98. Porosity profiles were then realized by binning pixel columns according to their minimal distance from the column wall and calculating the ratio between the amount of pixels assigned to the monolithic skeleton and the total amount of pixels in this bin.

Chord length distributions in the macropore space were calculated from random points generated in the background of the images for 32 angularly equispaced vector directions as described in [32–34]. Resulting chords describe a straight distance between two encounters with the monolith skeleton for 16 spatial directions. Chords that projected out of the image were discarded. Global statistics for the chord length distributions were collected from at least 4×10^5 chords randomly distributed over the image stack using the Levenberg–Marquardt algorithm [43] to fit a scaled *k*-gamma function, while prior binning of the seed points by their radial position in the column was used to calculate radial pore size profiles. New seeds were generated until at least 1×10^5 chords were collected for every bin.

3.3 Results and Discussion

3.3.1 Chord Length Distribution Functions. To characterize the degree of heterogeneity within granular matter Aste and Di Matteo [44] determined Voronoi volume distributions (VVDs) for a variety of experimental and simulated random sphere packings. They showed that these distributions follow a so-called *k*-gamma function. In contrast to granular media VVDs are not applicable to a monolith for the lack of a building unit that defines the Voronoi centres. But considering that Voronoi volumes measure the local density of the analyzed structure, other local density measures accessible by image analysis may achieve the desired characterization as well. In recent publications it was shown that the pore space of particulate beds and monolithic silica can also be described by chord length distributions (CLDs) [32–34]. The calculation is based on a statistically significant amount of randomly generated linear paths through the interparticle or interskeleton void space of the fixed-bed structures (image background) at varying angles, providing a distribution of linear skeleton-to-skeleton distances in the case of a monolith. Fig. 3.2 provides an illustration of this approach. A mathematical description of the collected CLDs is achieved by fitting a simplified *k*-gamma function:

$$f(l_c) = \frac{k^k}{\Gamma(k)} \frac{l_c^{k-1}}{\mu_c^k} \exp\left(-\frac{k \cdot l_c}{\mu_c}\right) \qquad \text{(Eq. 3.1)}$$

Here, l_c denotes the chord length, μ_c is the mean chord length as a first-moment parameter of location, and k is a second-moment parameter defining the dispersion of the distribution function. For CLDs, k is defined by the mean and the standard deviation σ as:

$$k = \frac{\mu_c^2}{\sigma^2} \qquad \text{(Eq. 3.2)}$$

Since image analysis by CLDs does not require any morphological prerequisites, the adoption of this approach to monoliths becomes straightforward. An example for a *k*-gamma fit using the CLD data from Hybrid Column A4 is shown in Fig. 3.1C. In the following analysis, an interpretation based on the CLDs in terms of the resulting eddy dispersion and its

individual contributions is provided using the obtained functional parameters μ_c and k (cf. Eq. 3.1 and Fig. 3.1C). As we will see this is an insightful and diagnostic connection because it explains the differences in the observed column efficiencies for a set of custom-prepared capillary hybrid silica monoliths.

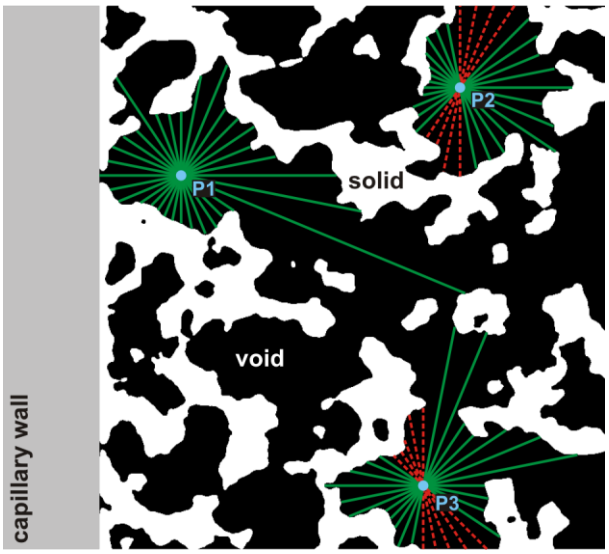

Figure 3.2: Generation of a chord length distribution. Random points P1 to P*n* are generated in the void space of a reconstructed monolith and the linear skeleton-to-skeleton distance is determined for 16 equispaced directions (green lines). If a chord reaches out of the image boundaries it is rejected (red dashed lines), whereas chords touching the capillary wall are included.

3.3.2 Reproducibility. To estimate the reproducibility of the determined morphological parameters three image stacks of the highly efficient Hybrid Column A4 (H = 4.7 µm) were recorded at different times and positions in the detection window's volume. Table 3.1 illustrates the reproducibility that can be achieved using the CLD method: these values for the mode, the mean, and k differ by no more than 2%. This implies that the analyzed microscopic region is large enough to reflect the macroscopic behavior of the column. Still, an analogous determination for a more heterogeneous monolith, like the Hybrid Column B1 (H = 8.2 µm), will increase the scatter of the data, as illustrated in Table 3.2. However, the reproducibility remains good enough to allow general conclusions with this analysis about the monolith morphology.Further, reconstructions along the whole column diameter are faced with an increased amount of signal intensity fluctuations compared to reconstructions of the bulk [32]. The main source of these fluctuations can be assigned to

an increased reabsorption of the fluorescence signal (by above dye) within regions near the column centre compared to regions close to the column wall. Therefore, for a comparative study, the image processing routine was required to be reproducible and insensitive to these fluctuations. Porosity profiles for Hybrid Columns A4 and B1 are presented in Figs. 3.1D and 3.3B, respectively. Since no systematic variations following a cylindrical shape became detectable we considered the reconstructions as suitable for morphological comparisons.

Table 3.1: Reproducibility of morphological parameters for Hybrid Column A4 (H = 4.7 µm) [a].

	Number of images	Capillary i.d. [µm]	Macropore porosity	μ_c [µm]	k	Mode [µm]
Measurement 1	155	100.8	0.697	4.96	2.39	2.89
Measurement 2	158	100.9	0.696	4.93	2.44	2.91
Measurement 3	105	100.8	0.702	4.94	2.41	2.89

[a] μ_c, k, and the mode were calculated from 1×10^6 chords fitted with a k-gamma function.

Table 3.2: Reproducibility of morphological parameters for Hybrid Column B1 (H = 8.2 µm) [a].

	Number of images	Capillary i.d. [µm]	Macropore porosity	μ_c [µm]	k	Mode [µm]
Measurement 1	113	101.3	0.693	5.00	2.29	2.80
Measurement 2	139	101.2	0.688	4.92	2.31	2.85
Measurement 3	117	100.7	0.717	5.22	2.35	2.99

[a] μ_c, k, and the mode were calculated from 1×10^6 chords fitted with a k-gamma function.

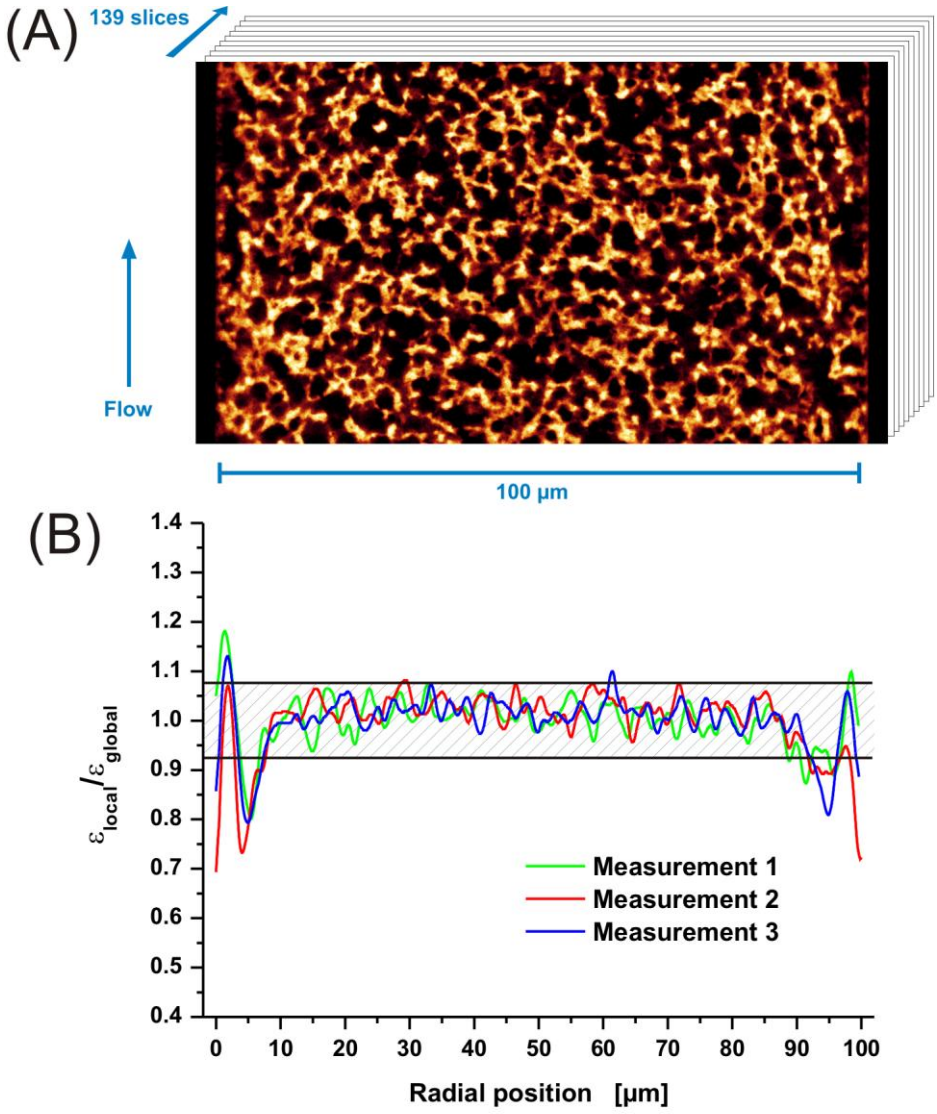

Figure 3.3: Exemplary image from the second measurement of Hybrid Column B1 (**A**) and normalized radial porosity profiles calculated for a step size of 30 nm smoothed with a 1 µm moving window for three image stacks obtained at different times and positions in the detection window's volume of Hybrid Column B1 (**B**). The shading designates an area of ±1 standard deviation around the global mean porosity.

3.3.3 Transchannel Effects. Giddings has divided velocity heterogeneities into different categories that contribute to eddy dispersion in a packed bed [45]. These time and length scale classifications can also be applied to monolithic columns [46]. Our morphological analysis focuses on the transchannel, short-range interchannel, and transcolumn contributions to eddy dispersion. The long-range interchannel contribution, introduced by Giddings to account for packing heterogeneity on a length scale of about ten particle diam-

eters in a particulate bed, will be neglected since the monoliths are not prepared through a slurry packing process [46].

The transchannel contribution to eddy dispersion arises from the lateral distribution of velocities inside each macropore (flowthrough channel). It resembles the parabolic Hagen–Poiseuille flow profile in a cylinder. Thus, if we assume self-similarity for the monoliths the linear relationship between plate height and axial dispersion coefficient results in a squared dependence of column efficiency on the macropore diameter. In a well-prepared monolithic column, without strong wall effects and a relatively homogeneously reproduced monolith domain, transchannel dispersion becomes the dominant dispersion term.

Since each derived chord is a one-dimensional measure of void distance in an analyzed image the first moment of a *k*-gamma fit (μ_c) directly provides a measure of the mean pore size and thus a correlation with the transchannel eddy dispersion. Alternatively, the mode of the fitted function, as the most frequent linear skeleton-to-skeleton distance, can be used to receive values that are more familiar with respect to other pore size estimates. It comprises the monolith's correlation length. Irrespective of the employed value (mode or mean), the column efficiency of the analyzed monoliths, in fact, mostly scaled with the macropore size. Results are summarized in Fig. 3.4A and Table 3.3. Hybrid Columns B1–B4 were found to deviate considerably from this anticipated behavior (red crosses in Fig. 3.4A). Since the mesoporosity of the monolith skeleton can be neglected for the band broadening of an unretained tracer [47], the deviations in our opinion result from a significant increase in heterogeneity on the length scale of short-range interchannel and/or transcolumn dispersion, which we consider next.

3.3.4 Short-range Interchannel Effects. The second term in eddy dispersion that we consider is the short-range interchannel contribution. Whereas transchannel dispersion on the scale of individual macropores takes place in any monolith, ordered or random, short-range heterogeneity is associated with the local disorder in real monoliths compared with perfectly ordered, crystal-like structures. For example, in random sphere packings a short-range packing heterogeneity is associated with local disorder on the scale of 1–2 particle diameters [48]. Schenker et al. [49] have shown that the parameter *k* in the *k*-gamma functions applied to the VVDs is a sensitive measure towards the degree of heterogeneity of

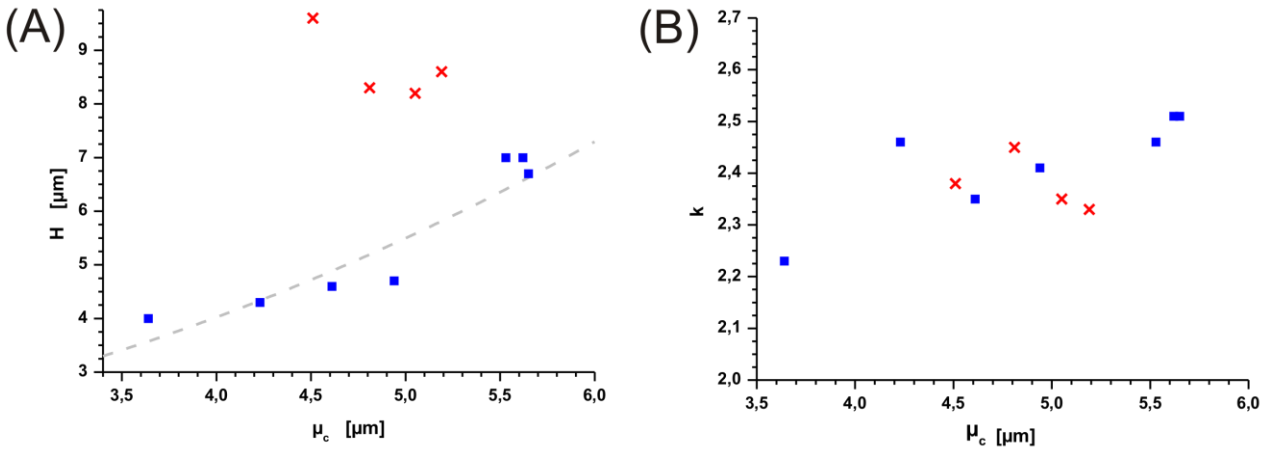

Figure 3.4: Dependence of plate height (**A**) and *k*-value (**B**) on the mean macropore size of columns dominated by transchannel dispersion (blue squares) or transcolumn dispersion (red crosses). A quadratic dependence of H on μ_c was fitted (dashed gray line) to illustrate the anticipated dependence of column efficiency on the macropore size.

Table 3.2: Morphological parameters and separation efficiency of the hybrid silica monoliths [a].

Column label	Capillary i.d. [µm]	Macropore porosity	μ_c [µm]	k	Mode [µm]	H [µm]
A1	100.5	0.678	3.64	2.23	2.01	4.0
A2–C18	100.4	0.686	4.23	2.46	2.51	4.3
A3	101.2	0.680	4.61	2.35	2.65	4.6
A4	100.9	0.698	4.94	2.41	2.90	4.7
A5	98.64	0.702	5.65	2.51	3.40	6.7
A6	98.64	0.694	5.53	2.46	3.28	7.0
A7	98.58	0.692	5.62	2.51	3.39	7.0
B1	101.1	0.699	5.05	2.35	2.90	8.2
B2	98.9	0.689	4.81	2.45	2.84	8.3
B3	99.6	0.698	5.19	2.33	2.97	8.6
B4	99.9	0.698	4.51	2.38	2.61	9.6

[a] Capillaries that revealed chromatographic band broadening dominated by their macropore size according to our analysis where labeled as A1–A7, whereas columns dominated by transcolumn dispersion were labeled as B1–B4. The label "C18" identifies a C18-modified surface.

granular packings; the lower the value of *k*, the more heterogeneous is the structure. *k* is a second-moment parameter, and thus describes the variability of the pore sizes. Concurrently, the parameter *k* in connection with the determined CLDs (Fig. 3.1C) is adaptable as an expression for the overall heterogeneity of the monolithic columns.

For particle-packed beds a reduction of particle size increases separation efficiency, although this is only strictly true, if the arrangement of the particles does not change to create a more heterogeneous microstructure, i.e., if self-similarity of the packings is given. The same reasoning applies to a reduction of macropore size in monolithic columns, which has not always yielded the expected improvements in performance [13,50]. The realized degree of structural homogeneity in a monolith is a characteristic of its chemical composition, formation mechanism, and preparation conditions (similar to the slurry-packing process for particulate beds, in which case particle properties, such as shape, density, size distribution, and surface roughness, but also column dimensions, properties of the slurry liquid, and process control parameters such as the packing pressure play a role). All three aspects are very similar for the monolithic columns analyzed in this study, and we would thus expect only minor variations in heterogeneity on the length scale characteristic of short-range interchannel dispersion. With *k* as the measure, higher *k*-values express increased homogeneity of the monolith's macropore space. The generation of CLDs and corresponding calculations for the computer-generated bulk (unconfined) packings of monosized spheres of Khirevich et al. [48] at the random-close packing limit, i.e., at an interparticle porosity of 0.366, provided us with a reference point of $k = 1.97$ for particulate beds.

The analyzed hybrid monoliths generally yielded considerably higher values of $k = 2.35 \pm 0.15$ (Table 3.3 and Fig. 3.4B). Compared to Chromolith CapRod columns in our studies, which only provide a value of $k = 1.9 \pm 0.1$ over the whole column diameter (data not shown), and the densely packed particulate column in [33] with $k = 2.0$, this is a drastic increase in the structural homogeneity and underlines the enormous potential of the silica monoliths in HPLC stationary phase design. Comparing the *k*-values for the different hybrid columns analyzed in this work no systematic variations became evident, i.e., all columns performed similar on the length scale of short-range interchannel dispersion (see Fig. 3.4B). It is tempting to assign the increased homogeneity to favorable effects of the added MTMS, which should mitigate the degree of condensation during decomposition and reduce the shrinkage of the monolith. Still, a custom-prepared bare-silica TMOS monolith presented in [51] also demonstrated a *k*-value of 2.4 after passing through our CLD

analysis, so that we have to assign the increased homogeneity to improved preparation conditions rather than to the modified material composition.

3.3.5 Transcolumn Effects. In cases where we were not able to correlate the column efficiency of the monoliths with the mean (or mode) of their CLDs and, thus, their macropore size, the radial heterogeneity and transcolumn velocity bias, as the third eddy dispersion contribution, was found responsible. In our previous study with particulate beds the radial porosity profiles already proved to be an efficient criterion to approach this measure from image analysis [33]. The transcolumn porosity profiles in Fig. 3.1D can be regarded as "reference profiles" for a hybrid column with a good radial homogeneity: beyond a lowporosity wetting layer in the vicinity of the column wall the porosity profiles rapidly become almost flat and move erratically around their mean. In contrast to these good transcolumn porosity profiles for Hybrid Column A4 in Fig. 3.1D, the profiles for Hybrid Column B1 (Fig. 3.3B) show a region of increased porosity near the column wall, before after ~5 µm towards the column centre a minimum is reached and the profiles only thereafter become flat as for Hybrid Column A4. Thus, parts of Hybrid Column B1 were snapped from the column wall and the separation efficiency of the capillary is reduced due to a nearly symmetric wall effect with respect to the column axis (Fig. 3.3B). Hybrid Columns B2 and B4 both exhibited similar profiles as Hybrid Column B1, suffering from a ~5 µm wall gap, but only at the left column wall. Hence, for Hybrid Columns B2 and B4 the wall effect became asymmetric.

While our analysis so far has provided very consistent results reflecting properly the morphology and chromatographic performance of the individual monoliths, one inconsistency remained. Hybrid Column B3 displayed an almost flat porosity profile (Fig. 3.5B) and the CLD analysis gave μ_c = 5.2 µm and k = 2.3. Consequently, we expected a better chromatographic performance than the H = 8.6 µm in Table 3.3. A closer inspection of the radial macropore size distribution provided the solution to this puzzle. Usually, the first moment of the CLDs that we calculated for these hybrid columns would vary locally in a 20%-band around its global value when plotted along radial position. This was also the case for Hybrid Columns B1 and B2, but Hybrid Column B3 demonstrated a 34% increase in the vicinity of the right column wall (Fig. 3.5C). We expect that this "second-kind" wall defect results from partial breakaways of the monolith's rods from the column wall, whereas the "first-kind" wall defect would appear when the majority of rods dismantle.

Both effects combined could only be found in Hybrid Column B4; the worst performing column in our analysis (Table 3.3).

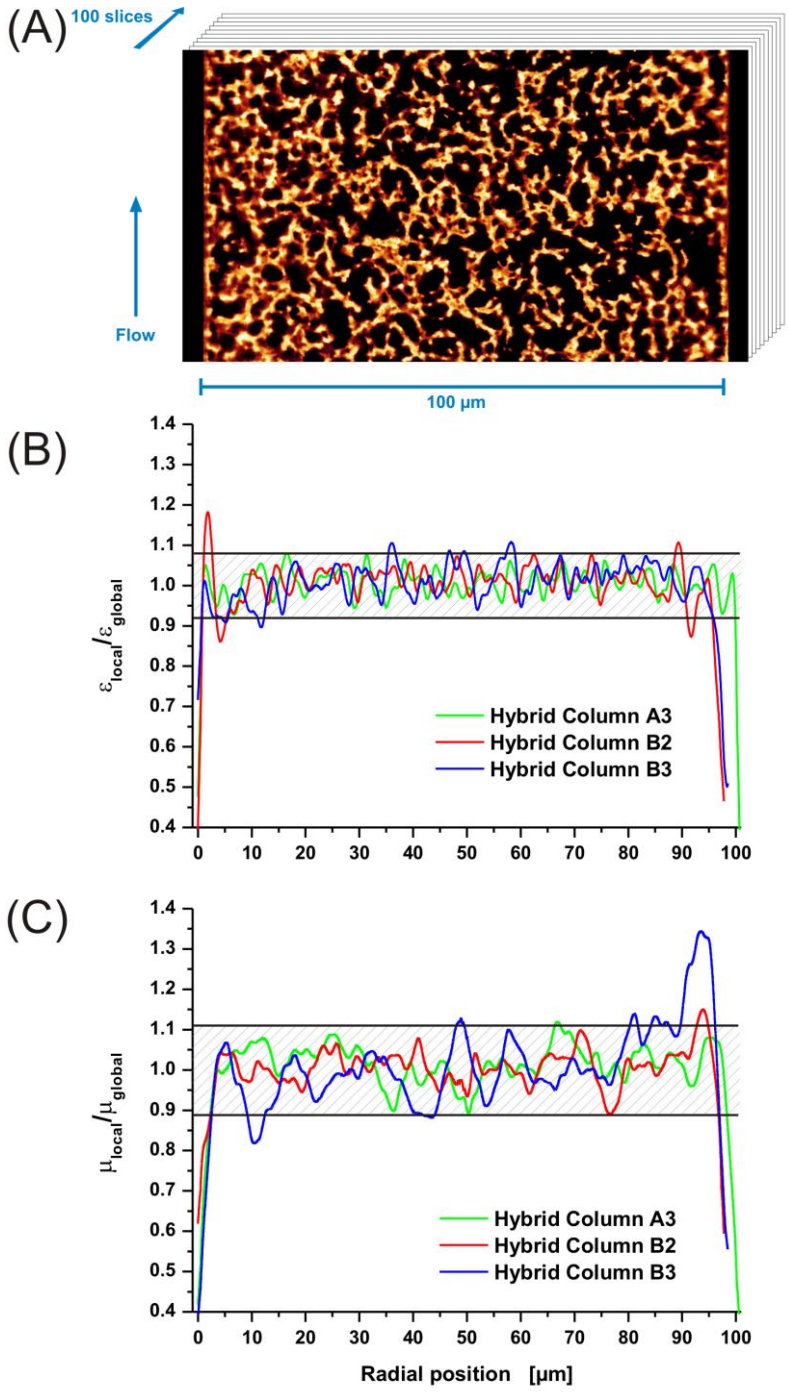

Figure 3.5: Exemplary image from the 100 images recorded for Hybrid Column B3 (**A**). The normalized macropore porosity profile (**B**) and the normalized macropore size profile (**C**) of the stack are compared with profiles of a column dominated by transchannel dispersion (Hybrid Column A3) and a column with obvious wall gap (Hybrid Column B2). The shading designates an area of ±1 standard deviation around the global mean porosity and macropore size, respectively.

3.4 Conclusions

We presented an image analysis-based characterization of capillary hybrid silica monoliths. It enabled the comparison of fixed-bed heterogeneity and transport properties of these columns. Typically porosity, as a scalar parameter for column permeability, and domain size, as an equivalent to the particle diameter of particulate beds, are provided in the characterization of a monolithic column. The presented chord length analysis carries the possibility to provide a more thorough analysis of eddy dispersion contributions in a monolithic column in terms of its characteristic length scales.

CLDs for the macropore space of particulate and monolithic silica columns follow a two-parameter distribution function. The parameter of location, the arithmetic mean, provides an alternative quantitative measure for pore size which is crucial to column efficiency. The average pore size of a column correlates with transchannel dispersion, whereas the *k*-value obtained from the CLDs provides a scalar measure for column heterogeneity on the length scale of short-range interchannel dispersion.

Capillary hybrid silica monoliths prepared by a protocol described in Hara et al. [38] resulted in higher *k*-values, i.e., less variation in macropore size, than commercial Chromolith CapRod columns. Their efficiency predominantly scaled with the macropore size (its mean or mode). A further downscaling of the macropore size and simultaneously leaving the overall structural homogeneity of the material unaffected will be a challenging task, but in the present study the single most important limitation to efficient separations was the column's radial heterogeneity, i.e., the associated transcolumn velocity bias and resulting eddy dispersion. It was analyzed using the radial profiles of macropore porosity and macropore size. Whenever the separation efficiency of a column was worse than expected from its pore size, either a wall gap, cracks, or a radially nonuniform distribution of pore size was observed along the column diameter. These defects and heterogeneities were mostly of noncylindrical nature, so that the capillary diameter (as opposed to the capillary radius) takes over as the characteristic lateral equilibration length on the column scale. This, in turn, effects a much larger chromatographic band broadening.

Because any polycondensation reaction will result in a certain degree of shrinkage, in-column prepared capillary monoliths will always exhibit a stressed structure. Thus, the above limitations cannot be resolved completely. Our analysis has shown that careful preparation conditions can increase the overall structural homogeneity of a silica monolith,

whereas the added MTMS may increase the rate of success in the preparation of a radially homogenous monolith. Resolving the presence of the CLSM-visualized and analyzed wall effects promises a substantial improvement in column performance. Still, according to our experience, even a readily prepared monolith might change its morphology later on due to ageing. For example, Hybrid Column B1 used to perform with an efficiency similar to that of Hybrid Column A4 from the same batch, but after remeasuring the efficiency of Hybrid Column B1 in a run-up to the present study its efficiency dropped due to a wall gap. A similar observation was made for a TMOS column presented in 2006 [51], and we expect that monolithic columns change their morphology gradually over time when persistently stressed by shrinkage.

Acknowledgements

This work was supported by the Deutsche Forschungsgemeinschaft DFG (Bonn, Germany) under grants TA 268/3-1 and TA 268/6-1. We thank Martin Kollmann and Professor Joachim Schachtner (Department of Biology, Philipps-Universität Marburg) for their help with the CLSM measurements.

References

[1] Guiochon, G. *J. Chromatogr., A* **2007**, *1168*, 101–168.

[2] Jungbauer, A.; Hahn, R. *J. Chromatogr., A* **2008**, *1184*, 62–79.

[3] Unger, K. K.; Skudas, R.; Schulte, M. M. *J. Chromatogr., A* **2008**, *1184*, 393–415.

[4] Aoki, H.; Tanaka, N.; Kubo, T.; Hosoya, K. *J. Sep. Sci.* **2009**, *32*, 341–358.

[5] Sinner, F.; Buchmeiser, M. R. *Macromolecules* **2000**, *33*, 5777–5786.

[6] Mayr, B.; Hölzl, G.; Eder, K.; Buchmeiser, M. R.; Huber, C. G. *Anal. Chem.* **2002**, *74*, 6080–6087.

[7] Svec, F. *J. Sep. Sci.* **2004**, *27*, 747–766.

[8] Nakanishi, K.; Tanaka, N. *Acc. Chem. Res.* **2007**, *40*, 863–873.

[9] Nakanishi, K.; Minakuchi, H.; Soga, N.; Tanaka, N. *J. Sol–Gel Sci. Technol.* **1997**, *8*, 547–552.

[10] Nakanishi, K. *J. Porous Mater.* **1997**, *4*, 67–112.

[11] Minakuchi, H.; Nakanishi, K.; Soga, N.; Ishizuka, N.; Tanaka, N. *J. Chromatogr., A* **1997**, *762*, 135–146.

[12] Nakanishi, K.; Minakuchi, H.; Soga, N.; Tanaka, N. *J. Sol–Gel Sci. Technol.* **1998**, *13*, 163–169.

[13] Minakuchi, H.; Nakanishi, K.; Soga, N.; Ishizuka, N.; Tanaka, N. *J. Chromatogr., A* **1998**, *797*, 121–131.

[14] Ishizuka, N.; Minakuchi, H.; Nakanishi, K.; Soga, N.; Tanaka, N. *J. Chromatogr., A* **1998**, *797*, 133–137.

[15] Gritti, F.; Piatkowski, W.; Guiochon, G. *J. Chromatogr., A* **2002**, *978*, 81–107.

[16] Leinweber, F. C.; Tallarek, U. *J. Chromatogr., A* **2003**, *1006*, 207–228.

[17] Kele, M.; Guiochon, G. *J. Chromatogr., A* **2002**, *960*, 19–49.

[18] Tallarek, U.; Leinweber, F. C.; Seidel-Morgenstern, A. *Chem. Eng. Technol.* **2002**, *25*, 1177–1181.

[19] Gritti, F.; Piatkowski, W.; Guiochon, G. *J. Chromatogr., A* **2003**, *983*, 51–71.

[20] Cabrera, K. *J. Sep. Sci.* **2004**, *27*, 843–852.

[21] Mazzeo, J. R.; Neue, U. D.; Kele, M.; Plumb, R. S. *Anal. Chem.* **2005**, *77*, 460A–467A.

[22] Kennedy, R. T.; Jorgenson, J. W. *Anal. Chem.* **1989**, *61*, 1128–1135.

[23] Guiochon, G.; Drumm, E.; Cherrak, D. *J. Chromatogr., A* **1999**, *835*, 41–58.

[24] Shalliker, R. A.; Broyles, B. S.; Guiochon, G. *J. Chromatogr., A* **2000**, *888*, 1–12.

[25] Shalliker, R. A.; Wong, V.; Broyles, B. S.; Guiochon, G. *J. Chromatogr., A* **2002**, *977*, 213–223.

[26] Maier, R. S.; Kroll, D. M.; Bernard, R. S.; Howington, S. E.; Peters, J. F.; Davis, H. T. *Phys. Fluids* **2003**, *15*, 3795–3815.

[27] Khirevich, S.; Höltzel, A.; Hlushkou, D.; Tallarek, U. *Anal. Chem.* **2007**, *79*, 9340–9349.

[28] Khirevich, S.; Höltzel, A.; Seidel-Morgenstern, A.; Tallarek, U. *Anal. Chem.* **2009**, *81*, 7057–7066.

[29] Abia, J. A.; Mriziq, K. S.; Guiochon, G. A. *J. Chromatogr., A* **2009**, *1216*, 3185–3191.

[30] Abia, J. A.; Mriziq, K. S.; Guiochon, G. A. *J. Sep. Sci.* **2009**, *32*, 923–930.

[31] Ishizuka, N.; Kobayashi, H.; Minakuchi, H.; Nakanishi, K.; Hirao, K.; Hosoya, K.; Ikegami, T.; Tanaka, N. *J. Chromatogr., A* **2002**, *960*, 85–96.

[32] Bruns, S.; Müllner, T.; Kollmann, M.; Schachtner, J.; Höltzel, A.; Tallarek, U. *Anal. Chem.* **2010**, *82*, 6569–6575.

[33] Bruns, S.; Tallarek, U. *J. Chromatogr., A* **2011**, *1218*, 1849–1860.

[34] Courtois, J.; Szumski, M.; Georgsson, F.; Irgum, K. *Anal. Chem.* **2007**, *79*, 335–344.

[35] Hlushkou, D.; Bruns, S.; Tallarek, U. *J. Chromatogr., A* **2010**, *1217*, 3674–3682.

[36] Hlushkou, D.; Bruns, S.; Höltzel ,A.; Tallarek, U. *Anal. Chem.* **2010**, *82*, 7150–7159.

[37] Roux, R.; Abi Jaoudé, M.; Demesmay, C. *J. Chromatogr., A* **2009**, *1216*, 3857–3863.

[38] Hara, T.; Makino, S.; Watanabe, Y.; Ikegami, T.; Cabrera, K.; Smarsly, B.; Tanaka, N. *J. Chromatogr., A* **2010**, *1217*, 89–98.

[39] Kanamori, K.; Yonezawa, H.; Nakanishi, K.; Hirao, K.; Jinnai, H. *J. Sep. Sci.* **2004**, *27*, 874–886.

[40] Motokawa, M.; Ohira, M.; Minakuchi, H.; Nakanishi, K.; Tanaka, N. *J. Sep. Sci.* **2006**, *29*, 2471–2477.

[41] Malitson, I. H. *J. Opt. Soc. Am.* **1965**, *55*, 1205–1208.

[42] Rasband, W. S. *ImageJ*; U.S. National Institutes of Health: Bethesda, MD, **1997-2006**; http://rsb.info.nih.gov//ij/.

[43] Bochkanov, S.; Bystritsky, V. *ALGLIB*; www.alglib.net.

[44] Aste, T.; Di Matteo, T. *Phys. Rev. E* **2008**, *77*, 021309.

[45] Giddings, J. C. *Dynamics of Chromatography, Part1: Principles and Theory*, Marcel Dekker, New York, **1965**.

[46] Gritti, F.; Guiochon, G. *J. Chromatogr., A* **2009**, *1216*, 4752–4767.

[47] Hlushkou, D.; Bruns, S.; Seidel-Morgenstern, A.; Tallarek, U.; *J. Sep. Sci.* **2011**, *34*, 2026–2037.

[48] Khirevich, S.; Daneyko, A.; Höltzel, A.; Seidel-Morgenstern, A.; Tallarek, U. *J. Chromatogr., A* **2010**, *1217*, 4713–4722.

[49] Schenker, I.; Filser, F. T.; Gauckler, L. J.; Aste, T.; Herrmann, H. J. *Phys. Rev. E* **2009**, *80*, 021302.

[50] Kobayashi, H.; Tokuda, D.; Ichimaru, J.; Ikegami, T.; Miyabe, K.; Tanaka, N. *J. Chromatogr., A* **2006**, *1109*, 2–9.

[51] Hara, T.; Kobayashi, H.; Ikegami, T.; Nakanishi, K.; Tanaka, N. *Anal. Chem.* **2006**, *78*, 7632–7642.

Chapter 4

Morphology and Separation Efficiency of Low-Aspect-Ratio Capillary Ultrahigh Pressure Liquid Chromatography Columns

Authors:

Stefan Bruns, James P. Grinias, Laura E. Blue, James W. Jorgenson, and Ulrich Tallarek

State of Publication:

Published April 22, 2012 in *Analytical Chemistry*, Vol. 84, No. 10, p. 4496–4503.

Abstract

We derive a quantitative relationship between the bed morphology and the chromatographic separation efficiency of capillary columns packed with sub-2 μm particles, covering capillary inner diameters from 10 to 75 μm. Our study focuses on wall effects and their impact on band broadening at increasing column-to-particle diameter (aspect) ratios. We approach these complex effects by a morphological analysis of reconstructed column segments composed of several thousand particles that were imaged by confocal laser scanning microscopy. Radial interparticle porosity profiles including wall effects are quantified through an integral porosity deviation, a scalar measure that proves to be a general descriptor of transcolumn porosity heterogeneity. It correlates with the associated transcolumn eddy dispersion, which dominates band broadening in the capillaries and is visualized in the plate height curves by a simple velocity-proportional term. Our comprehensive approach identifies the packing structure features that contribute to decreased efficiency as reflected, e.g., in subtle variations of the wall effect at different aspect ratios, or a particle size-segregation effect in larger-diameter columns as a result of an increased number of packing voids near the wall−bed interface.

4.1 Introduction

Innovative supports for high-performance liquid chromatography (HPLC) columns introduced to the wider community over the past decade include sub-3 μm solid core−porous shell particles [1,2] and fully porous sub-2 μm particles [3,4]. The idea behind sub-2 μm particles is to increase separation efficiency by reducing the particle size, albeit at the expense of increased pressure requirements, necessitating specialized equipment [5−7]. The original concept of the core−shell particles is to improve separation efficiency by restricting intraparticle diffusion to the thin porous shell [8−11], while maintaining hydraulic permeability associated with the overall particle diameter. Both particle types have aroused enthusiasm for enabling outstanding separation efficiencies [12−17] but also revealed the paramount importance of good and often subtle packing protocols behind homogeneously packed beds and the key role of intrinsic support properties like the particles' surface roughness [18−20].

In HPLC we pack columns by a rapid, high-pressure slurry packing process that experience has told us to be most appropriate in terms of separation efficiency [21] The packing process involves several parameters, among them physicochemical properties of the particles, interparticle forces, slurry preparation, and the applied pressure. Owing to the difficulty in probing packing microstructure systematically as a function of all process parameters, column packing and bed consolidation are largely treated phenomenologically and considered an art rather than a science [22]. Whereas a real column packing is the result of its formation process and has definite properties that cannot be altered at will by the researcher, computer-generated packings allow the variation of packing properties (e.g., particle size distribution, bed density) and the packing protocol *independent* of other parameters. This approach provides extremely important insight and is a prerequisite for the systematic derivation of correlations between packing microstructure and transport coefficients, including hydraulic permeability, effective diffusion, and eddy dispersion [23−25].

Because the slurry packing process cannot currently be approached comprehensively by simulations, refined morphology−transport relationships of packed beds require insight based on experimental data from high-resolution techniques that enable the physical reconstruction of the packing microstructure. We recently showed that confocal laser scanning microscopy (CLSM) can be used to visualize and reconstruct the interparticle void space of a chromatographic bed prepared with 2.6 μm core−shell particles [26]. The CLSM approach is generally applicable to silica-based materials; it has been applied to monoliths in

capillary [27] and analytical [28] column formats and defines a unique platform for fundamental comparisons between particulate and monolithic supports using the statistical measures derived from their reconstructions. Here, we apply the CLSM approach to the reconstruction and morphological analysis of the bed microstructure in ultrahigh pressure liquid chromatography (UHPLC) capillary columns packed with sub-2 μm particles. We focus on a single parameter in the slurry packing and bed consolidation process, the column inner diameter (varied from d_c = 10 to 75 μm) and its impact on the resulting bed morphology.

Capillary packings at low column-to-particle diameter (aspect) ratio have been frequently studied for use with liquid chromatography [29−32], supercritical fluid chromatography [33], and electrochromatography [34,35], and they also played a key role in early UHPLC research [36−39]. These studies cover a wide range of packing protocols, particle properties, and applications. It is not surprising that the relation between a packing protocol, the resulting bed morphology and macroscopic separation efficiency, as well as the general impact of the aspect ratio are still insufficiently understood; the individual packing process plays a more important role than a purely geometrical parameter represented by the aspect ratio. But how can we approach and understand the optimal packing conditions in a particular case? Recent simulations show that eddy dispersion in low-aspect-ratio *random* sphere packings obtained with different packing protocols even approaches fluid dispersion in confined *regular* pillar arrays [40]. We therefore need further systematic research on the preparation of more homogeneous beds.

In this work, we quantify key morphological differences of the capillary UHPLC column packings. Together with their complementary chromatographic analysis, the CLSM approach allows the interpretation of packing microstructure in terms of separation efficiency. Additionally, morphological descriptors can be established that characterize bed heterogeneity with respect to the applied slurry packing protocol and varied aspect ratio.

4.2 Experimental Section

4.2.1 Preparation and Analysis of Capillary UHPLC Columns. The procedures for preparation and chromatographic characterization [3,21,36,37,39] as well as CLSM-based reconstruction [26] of the capillary packings use established protocols. They are described in detail in the Supporting Information, and relevant aspects are repeated here only for the ease of reading. The column preparation procedure for the six columns was identical. Briefly, outlet-fritted fused-silica capillaries with inner diameters (d_c) ranging from 10 to 75 μm were packed with an upward slurry packing method up to 2000 bar using 1.7 μm Acquity BEH particles in a 3 mg/mL acetone slurry. Columns were then flushed with water/acetonitrile mobile phase at 2800 bar, and a frit was placed at the inlet. To test column efficiency, a carbon fiber microelectrode was placed at the column outlet for amperometric detection of ascorbic acid and a series of catechols. The data was collected using a custom-written LabView 6.0 data recorder program, and an iterative statistical moments algorithm was used to calculate retention time and the number of theoretical plates.

Fluorescence activity of the C18-functionalized, end-capped packing material was realized by the adsorption of the lipophilic dye Bodipy 493/503. For optical imaging with a confocal microscopy system the capillaries were saturated by and immersed in a fused-silica refractive index matching liquid [26]. The optical setup allowed a physical resolution of ~169 nm laterally and ~470 nm along the optical axis. Recorded stacks of 100−600 equispaced optical slices at 126 nm distance were restored, registered, and reconstructed to give a three-dimensional digitized representation of a column segment by an automated identification of each observed particle and the application of a best spherical fit (Figure 4.1; see also the Supporting Information). The spatial information in these reconstructions enabled the computation of morphological parameters, like the interparticle porosity (ε) and mean particle diameter (d_p), as a function of the radial position in the column.

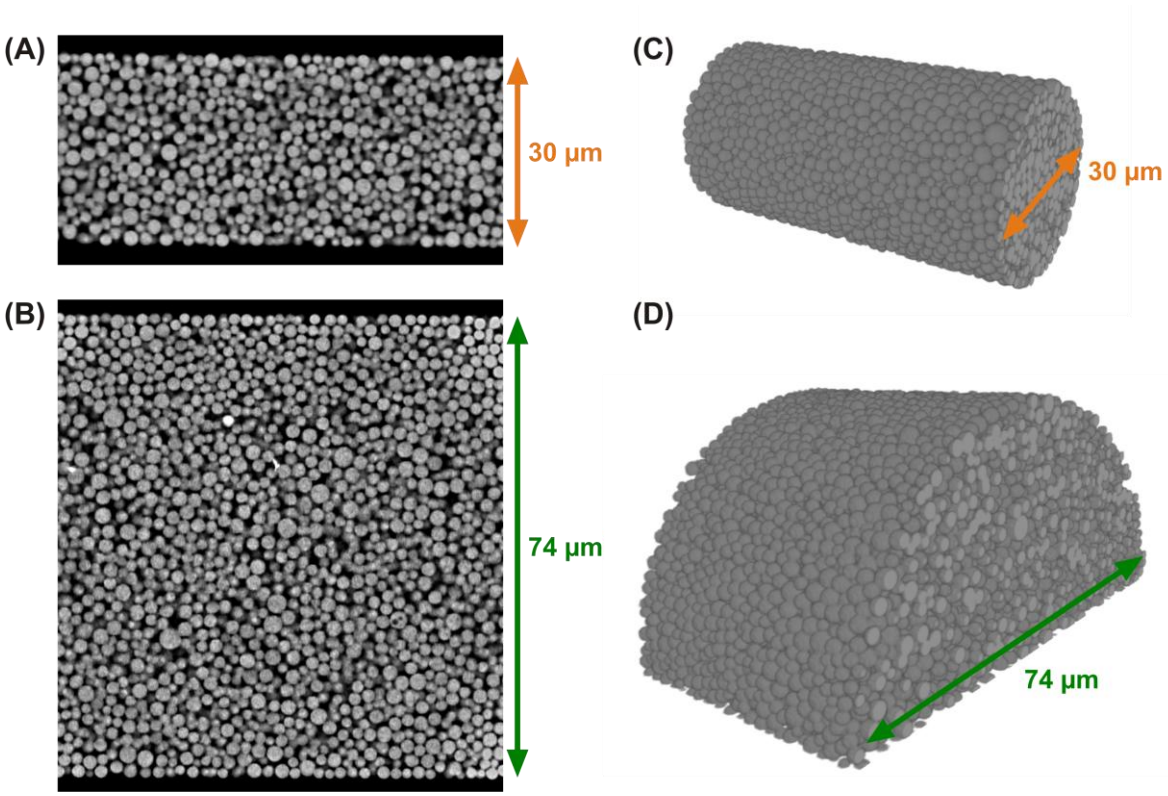

Figure 4.1: Physical reconstruction of the low-aspect-ratio capillary UHPLC columns. (**A** and **B**) Exemplary optical sections recorded for a 30 µm i.d. and a 75 µm i.d. column packing. (**C** and **D**) Volume renderings of the respective reconstructed column volumes. For details of the reconstruction process, see the Supporting Information.

4.3 Results and Discussion

4.3.1 Separation Efficiency of Capillary UHPLC Columns. Capillary packings in this work have bed lengths (L_{bed} ~20 cm) such that $L_{bed}/d_c > 5000$ at any aspect ratio. Thus, in contrast to the dimensions of modern analytical columns (e.g., 2.1 mm i.d. × 50 mm length, $L_{bed}/d_c \sim 25$) this allows the full lateral equilibration of analyte molecules between any velocity extremes that may exist over the column cross section, e.g., due to wall effects (which cause a transcolumn velocity bias and consequently require transcolumn equilibration). In general, several parameters together determine whether a time-independent behavior of the transient longitudinal dispersion coefficient $D_L(t)$ is observed during chromatographic analysis between sample injection (which corresponds to $t = 0$) and sample elution from the column. The column dimension constraint L_{bed}/d_c can be evaluated by the following criterion [41]

$$\frac{L_{bed}}{d_c} > 0.06 \frac{u_{av} d_p}{\langle D_T \rangle} \left(\frac{d_c}{d_p} \right) \qquad \text{(Eq. 4.1)}$$

where $u_{av}d_p/\langle D_T \rangle$ is a dimensionless number that characterizes the ratio of longitudinal advective to transverse dispersive transport (u_{av} is the average mobile phase flow velocity and $\langle D_T \rangle$ is the average rate of spreading in transverse direction). Contrary to modern analytical columns, this criterion is satisfied with all capillary packings and operating conditions in this work so that the longitudinal dispersion coefficient $D_L(t)$ reaches its long-time limit and becomes constant. The resulting asymptotic D_L is a global signature of packing heterogeneity and is related to the chromatographic plate height H by [42]

$$D_L = \frac{H u_{av}}{2} = \frac{h v D_m}{2} \qquad \text{(Eq. 4.2)}$$

where D_m is the diffusion coefficient of the analyte molecules in the bulk mobile phase, $h = H/d_p$ is the reduced plate height, and $v = u_{av}d_p/D_m$ is the reduced velocity, which characterizes the ratio of advective to diffusive transport in a packing.

Thus, the plate height data (h−v) recorded for the packed capillaries account for laterally fully equilibrated wall effects, which are identified and analyzed below. To compare the plate height curves at increasing aspect ratio, d_c/d_p, and predict the impact of the increasing column diameter we rely on a plate height equation $h = f(v)$ that properly describes the nature of the individual eddy dispersion contributions, particularly transcolumn dispersion. By applying the random-walk relation- ship to a model of eddy dispersion incorporating the coupling between transverse diffusion and spatial velocity fluctuations (i.e., diffusion and flow mechanisms) Giddings [42] developed a plate height equation by analogy to conductors in parallel. Through a detailed analysis of plate height curves recorded over a wide range of reduced velocities ($0.1 \leq v \leq 500$) for bulk, i.e., unconfined, and complementary cylindrical confined packings with aspect ratios of d_c/d_p = 10 and 20 (which are in the range of aspect ratios investigated in the current work, d_c/d_p = 5−38), we have shown that the comprehensive Giddings equation for $h = f(v)$ can be expressed in the following form [40,43]

$$h = h_{\text{diff}} + \sum_{i=1}^{3} h_{\text{eddy},i} + h_{\text{kin}}$$
$$= \frac{b}{v} + \sum_{i=1}^{3} \frac{2\lambda_i}{1 + (2\lambda_i/\omega_i)v^{-1}} + cv \qquad \text{(Eq. 4.3)}$$

where the first term ($h_{\text{diff}} = b/v$) and the last one ($h_{\text{kin}} = cv$) account, respectively, for longitudinal diffusion driven by the concentration gradient along the zone profile and the mass transfer kinetics from the bulk solution into and across the stationary phase. Remaining terms in eq. 4.3 characterize eddy dispersion ($h_{\text{eddy},i}$) and represent the transchannel contribution (i = 1), which refers to the velocity bias across individual channels between adjacent particles, the short-range inter- channel contribution (i = 2), which refers to the velocity bias on a lateral length scale of 1−2 d_p, and the transcolumn contribution (i = 3), which refers to the confinement-based transcolumn velocity bias (“wall effects”). ω_i and λ_i are structural parameters characteristic of each eddy dispersion contribution given by [42]

$$\omega_i = \omega_{\alpha,i}{}^2 \omega_{\beta,i}{}^2 / 2 \qquad \text{(Eq. 4.4a)}$$

$$\lambda_i = \omega_{\lambda,i} \omega_{\beta,i}{}^2 / 2 \qquad \text{(Eq. 4.4b)}$$

For each type of velocity disparity *i* the parameters $\omega_{\lambda,i}$ and $\omega_{\alpha,i}$ represent the distances in a packing that need to be traveled by a pure flow mechanism (longitudinal advection) and by a pure diffusion mechanism (lateral diffusion), respectively, to exchange molecules between the involved velocity extremes. The parameter $\omega_{\beta,i}$ characterizes the actual velocity maldistribution of a given type of velocity disparity *i* (which originates in a fundamental point-to-point velocity difference for fluid flow through a packing) and relates the extreme values of the velocity to the mean velocity. The ratio $v_{1/2,i} = 2\lambda_i/\omega_i$ is the reduced transition velocity at which the corresponding plate height term ($h_{\text{eddy,i}}$ in eq 4.3) reaches half of its limiting value and thereafter starts to flatten noticeably [42]. At high velocities $h_{\text{eddy,i}}$ approaches the constant value $2\lambda_i$, whereas at low velocities $h_{\text{eddy},i}$ approaches $\omega_i v$ and is thus proportional to velocity.

From our previous analysis we obtained the following estimates for the transition velocities characterizing the three eddy dispersion contributions in eq 4.3: $v_{1/2,1} \approx 200$ (transchannel), $v_{1/2,2} \approx 4$ (short-range interchannel), and $v_{1/2,3} > 200$ (transcolumn) [40,43]. Because the reduced transition velocity is a rough dividing point between the dominance of diffusion and flow mechanisms of lateral exchange in a packing at lower and higher velocities, respectively, the high transition velocities of the transchannel and transcolumn contributions indicate that over a wide range of reduced velocities, certainly in chromatographic practice with $v < 30$, these effects lose their coupling characteristics between diffusion and flow mechanisms of eddy dispersion and reduce to simple mass transfer velocity- proportional terms, i.e., with $(2\lambda_i/\omega_i) \gg v$, the transchannel and transcolumn contributions can be expressed just as $\omega_i v$. Of the three eddy dispersion contributions only the short-range interchannel dispersion retains its coupling characteristic and eq 4.3 can be simplified

$$h = \frac{b}{v} + \omega_1 v + \frac{2\lambda_2}{1 + (2\lambda_2/\omega_2)v^{-1}} + \omega_3 v + cv \qquad \text{(Eq. 4.5)}$$

This explains why the van Deemter equation remains an accurate representation of the band broadening processes in that case ($\nu < 30$) [44].

Our attention focuses on transcolumn eddy dispersion in eq 4.5 ($\omega_3 \nu$) and the dependence on wall effects. In a study that only varies the aspect ratio through an increase of the column diameter this contribution should dominate the observed differences in separation efficiency. According to eq 4.4a the value of ω_i is calculated from $\omega_{\alpha,i}$, the ratio of the characteristic lateral diffusion length (e.g., $d_c/2$, the column radius, for a transcolumn velocity bias) to the particle diameter (d_p), and $\omega_{\beta,i}$, the relative difference between velocity extremes and mean velocity that characterize a particular velocity bias. Thus, ω_3 is given by [42]

$$\omega_3 = \frac{{\omega_{\alpha,3}}^2 {\omega_{\beta,3}}^2}{2} = \frac{1}{2}\left(\frac{d_c}{2d_p}\right)^2 \left(\frac{\Delta\nu}{\nu}\right)^2 \qquad \text{(Eq. 4.6)}$$

This equation illustrates that $\omega_{\alpha,3}$ is a purely geometrical parameter, which represents the impact of the aspect ratio d_c/d_p (i.e., the reduced plate height in eq 4.5 is expected to increase with the square of the column diameter), whereas $\omega_{\beta,3}$ is the parameter of interest in our study, because it bears the intrinsic morphological differences of the capillary packings at different aspect ratio, which result in individual transcolumn velocity profiles and $\Delta\nu/\nu$ contributions. How a particular slurry packing protocol manifests itself in this parameter ($\omega_{\beta,3}$) is an unresolved question.

The complex interplay between general geometrical (d_c/d_p) and individual morphological ($\Delta\nu/\nu$) factors of the investigated column packings is studied in Figure 4.2. Whereas Figure 4.2A shows a representative chromatogram for well-performing columns, Figure 4.2B compares the plate height curves from all capillary packings of this work for the least retained analyte, with d_c/d_p ranging from ~5 (d_c = 10 µm) up to ~38 (d_c = 75 µm). Additionally, Figure 4.S1A in the Supporting Information shows a representative chromatogram for a poor performing column indicating no peak asymmetry, and Supporting Information Figure 4.S1B compares the plate height curves for the most retained analyte. Solid lines in Figure 4.2B (and Supporting Information Figure 4.S1B) are best fits of the data to eq 4.5 and only included as a guide to the eye; these data are too limited ($\nu < 25$) to

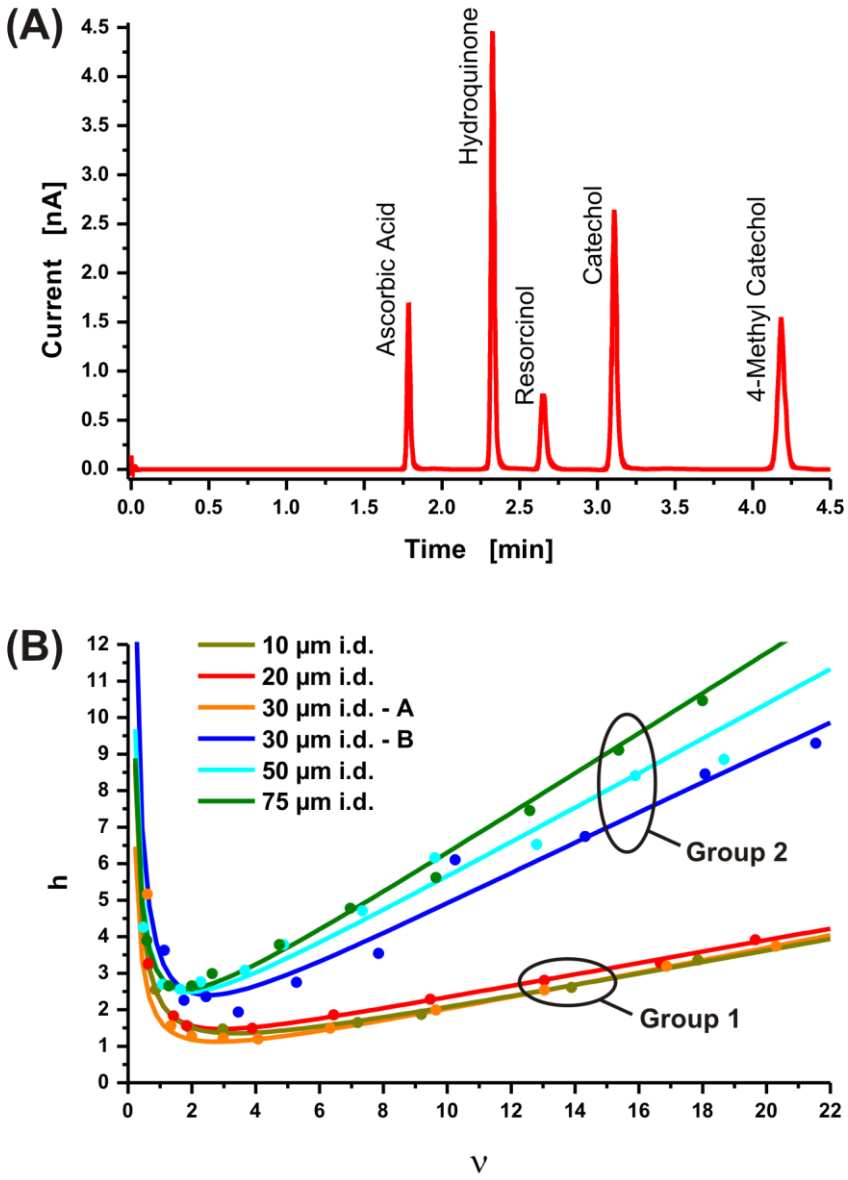

Figure 4.2: Chromatographic analysis of the low-aspect-ratio capillary UHPLC columns. (**A**) Exemplary chromatogram recorded with a 30 µm i.d. column (u_{av} = 1.9 mm/s). Mobile phase: 50/50 (v/v) water/acetonitrile with 0.1% trifluoroacetic acid. (**B**) Plot of the reduced plate height $h = H/d_p$ (hydroquinone) vs the reduced velocity $\nu = u_{av}d_p/D_m$ for all column diameters (d_p = 2.0 µm, the number-mean obtained from electron microscopy, cf. Supporting Information. Solid lines are best fits of the data to eq 4.5.

provide a meaningful analysis of the individual eddy dispersion contributions ($h_{eddy,i}$) with eq 4.5. This is not the only reason we use the CLSM-based approach to unravel differences in packing microstructure. In addition, we notice that the reduced plate height at, e.g., $\nu = 5$, increases abruptly from $h \approx 1.5$ for the best columns with an aspect ratio of $d_c/d_p = 5$, 10, and 15 to $h \approx 3.7$ for columns with $d_c/d_p = 25$ and 38. Rather than showing a smooth trend at increasing aspect ratio the plate height curves fall into two groups, which is indicated in Figure 4.2B (and also seen in Supporting Information Figure 4.S1B).

A straightforward prediction with eq 4.6 is not possible. Whereas the geometrical consequences of the increasing aspect ratio d_c/d_p ($\omega_{\alpha,3}$) are easily calculated, the individual transcolumn velocity profiles and $\Delta v/v$ contributions ($\omega_{\beta,3}$) are unknown. Apparently, the packing microstructures are not self-similar, and a marked change in bed morphology between group 1 and group 2 packings (Figure 4.2B) should be observed in their physical reconstructions. This is emphasized by the two 30 μm i.d. columns which belong to different groups; they have the same d_c/d_p, but obviously quite different $\Delta v/v$ characteristics. Our findings also highlight the fact why a general consensus from previous studies, covering a wide range of packing protocols, particle properties, and applications, about the impact of the aspect ratio dc/dpon the separation efficiency of packed capillaries cannot be reached. The individual packing structure, which reflects different packing protocols, particle properties, and applications, is of paramount importance, and its physical reconstruction is required for further progress.

4.3.2 Transcolumn Porosity Profiles. We previously demonstrated that CLSM is a suitable tool to reconstruct complete transcolumn segments of capillary-type stationary phases, which allowed the correlation of the results of a morphological analysis (including the recorded transcolumn porosity profiles) with the chromatographic separation efficiency [26,27]. Figure 4.3 highlights the distribution of interparticle porosity near the wall of the packed capillaries. These profiles were obtained from reconstructions of the packing microstructure in an observation window located at half-length ($L_{bed}/2$) of the chromatographically characterized capillary columns (see the image analysis in the Supporting Information for the computation and analysis of interparticle porosity).

The importance of this wall region (covering a distance of ~5 d_p from the wall) stems from its impact on the local porosity and velocity distribution [43,45]. The geometrical wall effect associated with this region reflects the inability of spherical particles to form a close

packing against the locally flat and hard surface of the column wall [46]. The first particle layer of the bed in contact with the wall is highly ordered and differs from subsequent layers, because the interstitial space between the wall and the first layer cannot be partially occupied by other particles. In subsequent particle layers the degree of microstructural order relaxes toward the packing bulk. The geometrical wall effect can be seen in Figure 4.3 in the porosity oscillations whose amplitudes decrease over a distance of a few particle diameters toward bulk porosity (ε_{bulk}). The oscillations cause a radial variation in the flow velocity and are responsible for the transcolumn contribution to eddy dispersion ($\omega_3 v$ in eq 4.5) [40,43].

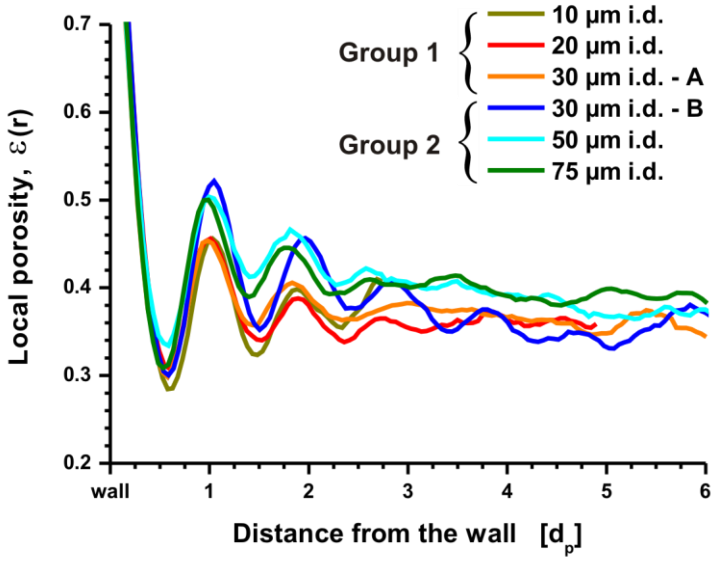

Figure 4.3: Radially resolved profiles of the interparticle void volume fraction or porosity $\varepsilon(r)$ for the wall region of the reconstructed column packings.

Figure 4.3 provides the likely cause for the grouping of the plate height curves observed in Figure 4.2B: there is a strong correlation for groups 1 and 2 in the macroscopic plate height data and local porosity oscillations that are caused by the ordering of particles at the column wall. Whereas columns with a minimum plate height of $h_{min} \leq 1.5$ (group 1) never exceed a porosity of 0.46 beyond the first particle layer, columns with $h_{min} \geq 2.3$ (group 2) show a porosity of about 0.50 between the first and the second particle layer. The

porosity of group 2 columns remains at a higher level, until the porosity oscillations reduce after 3−4 d_p and bulk behavior is approached.

A closer inspection of packing voids, which are primarily located near the column wall−packed bed interface (Table 4.1), reveals that larger column diameters yield a higher number of voids and therefore a looser packing at the wall. Thus, in the vicinity of the column wall (over a distance of 2−3 d_p) average porosity is shifted to higher values for group 2 packings (Figure 4.3), which aggravates the transcolumn velocity bias ($\Delta v/v$), in addition to the already enhanced lateral equilibration length resulting from a larger column diameter (d_c/d_p). This also explains the different separation efficiencies at identical aspect ratio for the 30 µm i.d. packings. The increased transcolumn eddy dispersion manifests itself in a larger slope of the plate height curves in Figure 4.2B, agreeing with the predictions of eqs 4.5 and 4.6.

Eventually, in chromatography we are more interested in the engendered zone spreading due to a certain transcolumn porosity profile than in the profile itself. To derive a measure for the transcolumn contribution to eddy dispersion that may result from the porosity profiles in Figure 4.3, we compute the integral local deviations from the bulk

Table 4.1: Analysis of packing voids [a], interparticle porosity [b], and integral porosity deviation (IPD) [c].

Column diameter	Largest void [µm]	No. of voids	Voids per mm² of curved surface area	ε	ε_{bulk}	IPD
10 µm i.d.	2.1	4	$7 \cdot 10^2$	0.452	0.377	0.10
20 µm i.d.	1.8	2	$5 \cdot 10^2$	0.416	0.361	0.13
30 µm i.d.–A	2.4	3	$5 \cdot 10^2$	0.402	0.360	0.13
30 µm i.d.–B	2.6	16	$29 \cdot 10^2$	0.418	0.355	0.39
50 µm i.d.	2.5	9	$23 \cdot 10^2$	0.406	0.364	0.43
75 µm i.d.	2.2	24	$47 \cdot 10^2$	0.403	0.376	0.49

[a] A packing void is defined as interstitial space in the reconstructions that can be occupied by at least 25% of the particles from the particle size distribution (see also the image analysis in the Supporting Information).

[b] ε is the average interparticle porosity (interparticle void volume fraction) of the whole reconstructed packing, and ε_{bulk} is the average interparticle porosity of the bulk packing region (without wall region).

[c] The IPD is calculated from the transcolumn porosity profiles using eq 4.7.

porosity and consider all porosity inequalities $\varepsilon(r) - \varepsilon_{bulk}$ (where r denotes the radial position in the bed) that an analyte experiences when diffusing from the wall ($r = 0$) to the center of the bed ($r = r_c$, the column radius). We propose an integral porosity deviation (IPD) as a scalar measure of transcolumn eddy dispersion as

$$\mathrm{IPD} = \int_0^{r_c} (\varepsilon(r) - \varepsilon_{bulk})\, \mathrm{d}r \qquad \text{(Eq. 4.7)}$$

This calculation, which is performed over the whole column cross section, is illustrated in Figure 4.4 with a zoom into the wall region, because this region is the major contributor to the IPDs of the investigated packings. The 20 µm i.d. packing (representing group 1 packings, Figure 4.4A) demonstrates a "more balanced" porosity oscillation with respect to ε_{bulk} than the 75 µm i.d. packing (representative of group 2 packings, Figure 4.4B), which is more loosely packed in the wall region and therefore contributes mostly positive deviations in $\varepsilon(r) - \varepsilon_{bulk}$ to its IPD. This gives a significantly higher IPD for the 75 µm i.d. packing than for the 20 µm i.d. packing, where the denser packing in the wall region (closer to ε_{bulk}) results in a stronger balance (compensation) of positive and negative porosity deviations and the lower IPD. The IPDs of all packings are shown in Table 4.1. They not only provide a clear distinction between the group 1 and group 2 packings and therefore quantify the data in Figure 4.3 from the physical reconstruction but also resolve more subtle details within these groups. For example, the 10 µm i.d. packing demonstrates the smallest slope of all plate height curves (Figure 4.2B, $\nu > 5$), in agreement with its lowest IPD, whereas the 75 µm i.d. packing has the largest slope and the highest IPD. Table 4.1 also summarizes the average interparticle porosities of the bulk packing regions (ε_{bulk}) and the average interparticle porosities of the whole reconstructed packings (ε). They illustrate the influence of wall regions that are more loosely packed than the bulk regions on ε in low-aspect-ratio packings. Whereas all capillaries have similar packing densities in their bulk (as reflected by ε_{bulk}), the resulting ε is generally higher and indicates an increase with decreasing aspect ratio (highlighted by the 10 µm i.d. column) where the critical wall region occupies a larger fraction of the whole bed volume [47]. Here, this trend is somewhat blurred because group 2 packings are more loosely packed in the wall region than group 1 packings.

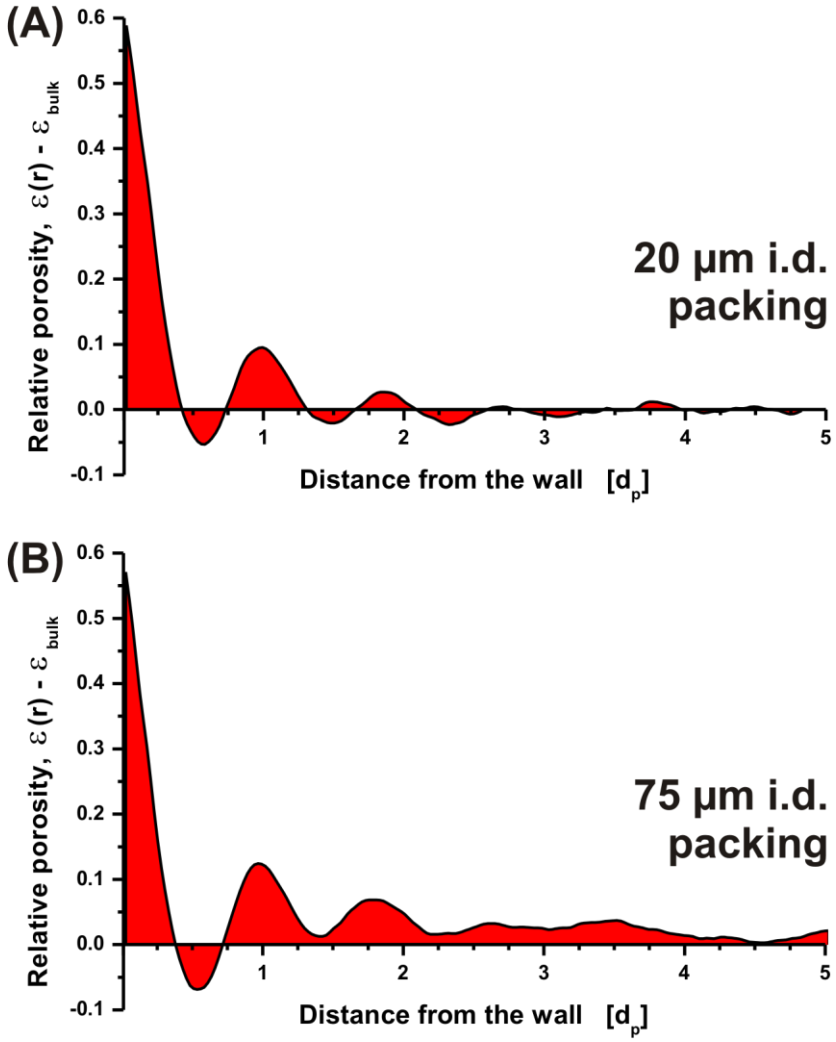

Figure 4.4: Calculation of the integral porosity deviation (IPD) using transcolumn porosity profiles of the reconstructed packings and eq 4.7 (the values of ε_{bulk} are given in Table 4.1, dr =100 nm): (**A**) 20 µm i.d. column representing group 1 packings; (**B**) 75 µm i.d. column representing group 2 packings (cf. Figures 4.2B and 4.3). Shown is a zoom into the critical wall region, by covering a distance of 5 d_p from the wall (instead of the full column radius involved in the calculation of the IPDs).

The IPD proves to be an excellent measure of transcolumn porosity heterogeneity (itself a global result from the slurry packing process), which strongly correlates with the transcolumn eddy dispersion reflected by a simple velocity-proportional term in eq 4.5 ($\omega_3 v$) and the slope of the plate height curves in Figure 4.2B. This comprehensive approach

for confined packed beds provides systematic progress on the quantitative relationships between packing protocol, bed morphology, and separation efficiency. It complements previous studies on the quantification of bulk packing disorder and its correlation with transport properties like the diffusive tortuosity [25] and eddy dispersion [23].

4.3.3 Particle Size Segregation Effect. In 1962 Giddings mentioned [48] that for dry-packed columns the particle size distribution would not be constant over the column cross section. He found that the mean particle size increased from the column center to the column wall. His interpretation was that during the dry packing process a cone of particles would form in the column center. Subsequent particles hitting the cone would roll down to the wall if not caught in a void (which is more likely for smaller particles). Various studies have been conducted since on the subject of particle size segregation, yet only few can be transferred to a column that is slurry packed under high axial pressure.

During the evaluation of this study we observed that poorer performing columns (group 2; larger column diameters) showed the enrichment of smaller particles near the column wall and of larger ones in the column center. Thus, a size segregation of the particles occurred that contributes to an uneven transchannel dispersion ($\omega_1 v$ in eq 4.5) along the column radius, together with the actual porosity profile. This effect is illustrated in Figure 4.5. Compared to the size segregation reported by Giddings for dry-packed columns the effect in the slurry-packed capillaries is smaller. Yet, an increase of the mean particle size from ~1.9 μm at a distance of one dpfrom the wall to ~2.1 μm at 10 d_p from the wall (for the 75 μm i.d. column, Figure 4.5C) enhances local transchannel dispersion, because ω_1 depends on the lateral pore dimensions in the bed, which in turn reflect local packing density and particle size [23,42].

Although at this point the origin of the size segregation in slurry-packed capillaries (Figure 4.5) is speculative, it is likely the result of a statistical process during consolidation of the bed. If we start with a loose and metastable packing where the packing voids are primarily located near the wall−bed interface, which is still the case in the reconstructed final packings, bed consolidation aims at maximizing bed density by opening and filling the remaining voids. The filling of voids is more likely done by a smaller than by a larger particle, which in turn creates a new void that again is occupied more likely by a smaller particle. The avalanching of the smaller particles yields a consolidated bed where they have been depleted from the center, depending on the aspect ratio and number of voids

initially present in a packing (cf. Table 4.1). Thus, the size segregation increases with the column diameter (Figure 4.5) and will be affected by the particles' size distribution and surface roughness.

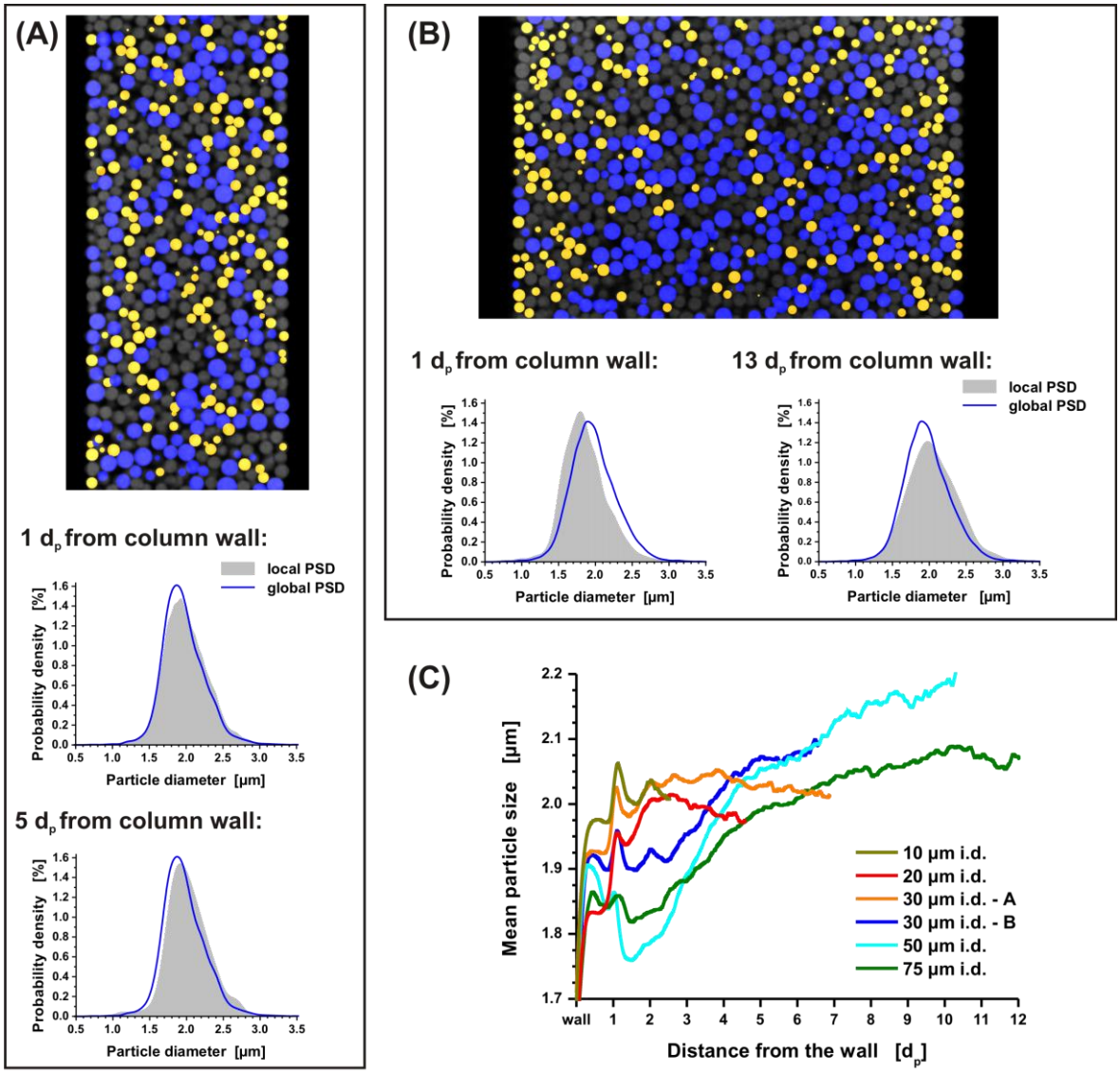

Figure 4.5: Particle size segregation in slurry-packed low-aspect-ratio capillary UHPLC columns: (**A**) 30 µm i.d. column (group 1 packings); (**B**) 75 µm i.d. column (group 2 packings). Particles that are smaller in the three-dimensional reconstruction than the first quartile of the particle size distribution appear in yellow; particles larger than the third quartile are blue. Local particle size distributions from the wall and bulk regions are shown as examples (for their calculation, see the image analysis in the Supporting Information). (**C**) Evaluation of the entire set of reconstructed column packings: plot of the mean particle size from the local particle size distributions vs radial position in the bed.

4.4 Conclusions

We have quantified the impact of wall effects in capillary UHPLC columns at varied column-to-particle diameter ratio on the separation efficiency. Subtle variations in wall effects (Figure 4.3) are visualized in the plate height curves (Figure 4.2B) through a simple velocity-proportional term ($\omega_3 v$, eq 4.5), which, however, is difficult to quantify given the limited range of plate height data ($v < 25$) and general lack of knowledge of packing microstructure. This may explain why previous studies on the aspect ratio d_c/d_p in packed capillaries covering different packing protocols, particle properties, and applications have come to diverse conclusions: the actual velocity bias $\Delta v/v$ in eq 4.6, which reflects packing process and particle properties in a global sense, is far more important and difficult to predict than plain geometrical changes (d_c/d_p in eq 4.6).

The applied CLSM approach allowed us to conduct a detailed morphological analysis of reconstructed column segments (cf. Figure 4.1) and record radial porosity profiles as a signature of the packing structure and wall effects. We have shown that the disproportionate increase in reduced plate height with increasing aspect ratio in Figure 4.2B results from a marked change in transcolumn porosity profiles, which reveal looser packed wall regions for group 2 packings (Figure 4.3). Whereas porosity oscillations near the flat wall cannot be avoided, the mean value characterizing these fluctuations should be as close to the bulk porosity ε_{bulk} as possible. This is better realized by group 1 than by the group 2 packings. With the IPD (eq 4.7) we proposed a measure that includes all porosity deviations with respect to εbulk that an analyte encounters as it diffuses from the wall to the center of the bed (Figure 4.4). The IPD is a scalar measure of transcolumn contributions, which dominate eddy dispersion in these packings, and can be used to quantify transcolumn porosity heterogeneity in any type of stationary phase. It explains separation efficiencies of all studied columns based on their packing microstructure and a rigorous morphological analysis. In particular, the slopes of the plate height curves represent the different contributions from wall effects, which are the result of variations in the packing quality achieved during the preparation of these columns. The IPDs (Table 4.1) adequately reflect the two groups of columns identified from the plate height curves and even distinguish between smaller variations within these groups. We establish a useful correlation between two dimensionless measures, one for the bed morphology (IPD, based on the radial porosity distributions) and one for the separation efficiency (slope of the plate height curves).

The larger-diameter packings (group 2) not only yielded looser packed wall regions but also showed a size segregation of particles along the column radius (Figure 5). The result is a gradual increase in mean particle size from the wall to the center of the bed that introduces an additional radial variation in transchannel dispersion ($\omega_1 v$ in eq 4.5). However, compared with the porosity profiles in Figure 4.3, its effect on the associated transcolumn contribution to eddy dispersion is negligible [40,43].

Simultaneously, it provides deep insight into the phenomena that occur during column packing and bed consolidation. Future work on the demystification of slurry packing will apply this new insight to improve the quality of packed capillaries and target other prominent parameters that influence bed morphology with respect to the observed wall and size-segregation effects. These include particle characteristics, like the particle size distribution and smoothness of the particles' external surface, as well as slurry properties.

4.5 Supporting Information

4.5.1 Chemicals and Materials. Fully porous Acquity 1.7 µm BEH particles were provided by Waters Corporation (Milford, MA). Fused silica capillary tubing of 10, 20, 30, 50, and 75 µm inner diameter was purchased from Polymicro Technologies, Inc. (Phoenix, AZ). HPLC grade acetonitrile and acetone and reagent grade trifluoroacetic acid (TFA) were purchased from Fisher Scientific (St. Louis, MO). Deionized water was obtained from a Millipore NANOpure water system (Billerica, MA). Test analytes ascorbic acid, hydroquinone, resorcinol, catechol, and 4-methyl catechol were purchased from Fisher Scientific (St. Louis, MO). Potassium silicate (Kasil) was used as received from PQ Corporation (Valley Forge, IA).

4.5.2 Preparation of the Capillary UHPLC Columns. The process to preparing the capillary UHPLC columns has been reported previously [21,36,37,39,40]. Outlet frits were placed in capillary column blanks by pushing a 1–2 mm plug of 2.5 µm bare nonporous silica particles (Bangs Laboratories, Fishers, IN) 0.5 mm into the capillary using a tungsten wire to allow for the insertion of a carbon microfiber electrode. Acquity particles were suspended in acetone at a concentration of 3 mg/mL and the slurry was then sonicated for

10 minutes using a Cole Parmer Ultrasonic Cleaner 8891 (Vernon Hills, IL). The slurry was placed in a packing reservoir and a fritted capillary column blank was then secured into the reservoir using a UHPLC fitting. With acetone used as a pushing solvent, 200 bar was applied to the fritted capillary column from a DSHF-300 Haskel pump (Burbank, CA) to initiate packing and then the pressure was increased 200 bar for every 1 cm of column bed packed until a maximum of 2000 bar was reached. Once the desired bed length was reached, column pressure was slowly leaked until atmospheric pressure was obtained.

The column was then placed into a UHPLC injection apparatus connected to a DSXHF-903 Haskel pump (Burbank, CA) and flushed with at least 15 column volumes at 2800 bar with the mobile phase to be used for column characterization. The pressure was then slowly released and re-initiated at 700 bar where a temporary inlet frit was formed by using a heated wire stripper (Teledyne Interconnect Devices, San Diego, CA). The column was clipped to the appropriate length and a new inlet frit was formed using the Kasil method [49]. The column inlet was gently pushed on a glass microfiber filter (Reeve Angel, Clifton, NJ) that was previously wetted with 1:1 (v:v) ratio of Kasil and formamide. The column was then placed in an oven at 85°C overnight to solidify the inlet frit.

4.5.3 Chromatographic Analysis. A UHPLC injection apparatus was used to inject 200 µM of an isocratic test mixture of L-ascorbic acid (dead time marker), hydroquinone, resorcinol, catechol, and 4-methyl catechol. The mobile phase for chromatographic evaluation was 50/50 (v/v) water/acetonitrile with 0.1% TFA (column 30 µm i.d.-B was evaluated using 70/30 (v/v) water/acetonitrile with 0.1% TFA to improve the resolution for peak analysis). Amperometric detection was achieved by amplifying the current generated from an 8 µm diameter (200 µm in length) carbon fiber microelectrode placed in the end of a packed capillary and held at +1.1 V vs. Ag/AgCl reference electrode. Current-to-voltage conversion was achieved by using a model SR750 current amplifier (Stanford Research Systems, Sunnyvale, CA) with a 109 V/A gain and a 3 dB low pass bandwidth filter set at 3 Hz. A 16-bit A/D converter was set at 21 Hz data acquisition rate and connected to an Intel Core 2 Duo desktop computer. Data was collected using a custom-written recorder program written with LabView 6.0 (National Instruments, Austin, TX).

Reduced parameter plots (*h*–*v*) were generated by separating the test mixture at a variety of mobile phase velocities. Chromatograms were frequency filtered digitally to remove high frequency noise while low frequency baseline drift was removed by background sub-

traction. Using Igor 6.0 (Wavemetrics, Inc., Lake Oswego, OR), an iterative statistical moments algorithm with ± 3σ integration limits was applied to determine the theoretical plate count and retention time for each peak [32]. Extra-column band broadening effects from the injector and detector were found to be negligible (~1%, total), therefore plate heights were calculated with no attempt to correct for these effects. For the calculation of reduced parameters ($h = H/d_p$ and $\nu = u_{av}d_p/D_m$), the number-averaged particle size and pressure-dependent diffusion coefficient for each compound were used.

Figure 4.2A in the main article shows a representative chromatogram for well performing columns, whereas Figure 4.2B compares the plate height curves from all capillary packings for the least retained analyte (hydroquinone), with d_c/d_p ranging from ~5 (d_c = 10 µm) up to ~38 (d_c = 75 µm). Complementary, Figure 4.6A shows a representative chromatogram for a poor performing column indicating no peak asymmetry, and Figure 4.6B compares the plate height curves for the most retained analyte (4-methyl catechol). 4-methyl catechol forms the same groups as observed with hydroquinone, demonstrating that this difference in performance is not an artifact seen for a particular analyte.

4.5.4 Microscopic Imaging of Packing Microstructure. Images were acquired with a TCS SP5 confocal microscopy system equipped with a HCX PL APO 63x/1.3 GLYC CORR CS (21°) glycerol immersion objective lens (Leica Microsystems, Wetzlar, Germany) by focusing into a capillary segment where the polyimide coating has been removed with a drop of warm (170 °C) sulfuric acid. Fluorescent staining of the fully porous sub-2 µm particles was achieved by adsorbing the lipophilic dye Bodipy 493/503 (D-3922, Invitrogen, Karlsruhe, Germany) at the C18-modified particle surface. For this purpose, the day before imaging, the capillary was flushed with an acetone solution of this dye (0.5 mg/mL) until an intensely colored droplet formed at the column outlet. At the day of the measurement, the excess dye was removed by flushing the capillary with several column volumes of a fused silica refractive index matching liquid, 70/19/11 (v/v/v) glycerol/DMSO/water, calibrated to a refractive index of n_D = 1.4582 with an AR200 digital refractometer (Reichert Analytical Instruments, Depew, NY). Then, the capillary was fixed on a microscope slide and immediately transferred to the microscope stage. Aberrations in the optical setup were eliminated using a balancing technique that has been discussed in detail before [56]. Briefly, the capillary was embedded in a pool of the above mentioned refractive index matching liquid to eliminate the column wall to function as a lens. The matching liquid also served as an immersion medium for the microscope lens. With this

setup spherical aberrations become independent of sampling depth and can be minimized by a "type 0" coverslip (Gerhard Menzel GmbH, Braunschweig, Germany) and by fine-tuning the correction collar of the objective lens.

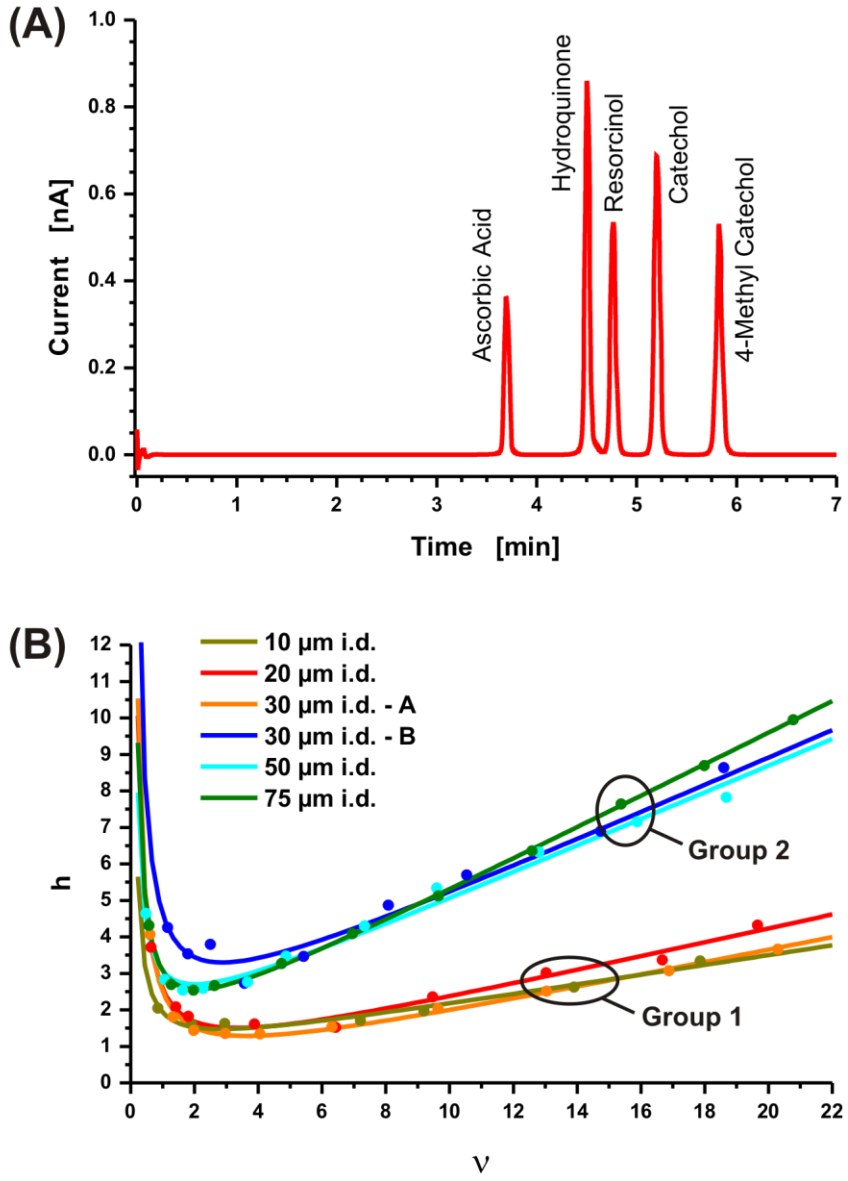

Figure 4.6: (**A**) Sample chromatogram for the poor performing 75 µm i.d. column (u_{av} = 0.9 mm/s). Mobile phase: 50/50 (v/v) water/acetonitrile with 0.1% TFA. (**B**) Plot of the reduced plate height $h = H/d_p$ (4-methyl catechol) vs. the reduced velocity $\nu = u_{av}d_p/D_m$ for all column diameters. Solid lines are best fits of the data to equation 4.5.

Excitation of the fluorophore Bodipy 493/503 was realized with a 488 nm Argon laser setting the pinhole of the microscope to 0.5 AU. Fluorescence emission was detected in the interval 491–515 nm. Under these conditions we can expect an approximate lateral resolution of 169 nm and an axial resolution of 470 nm [26,50].

Images were recorded as three-dimensional image stacks along the axis of the capillaries (xy-slices). They were received as 8-bit grayscale images at a sampling rate well below the Nyquist sampling rate with a step size of 30 nm laterally and 126 nm axially. The number of slices recorded for each stack depended on the amount of equispaced images that were needed to scan the capillary from top to bottom, e.g., 119 slices for a 10 µm i.d. capillary column and 457 slices for a 50 µm i.d. column. The image size was chosen to cover a plane of the entire column diameter and at least 70 µm along the column axis (Figure 4.7).

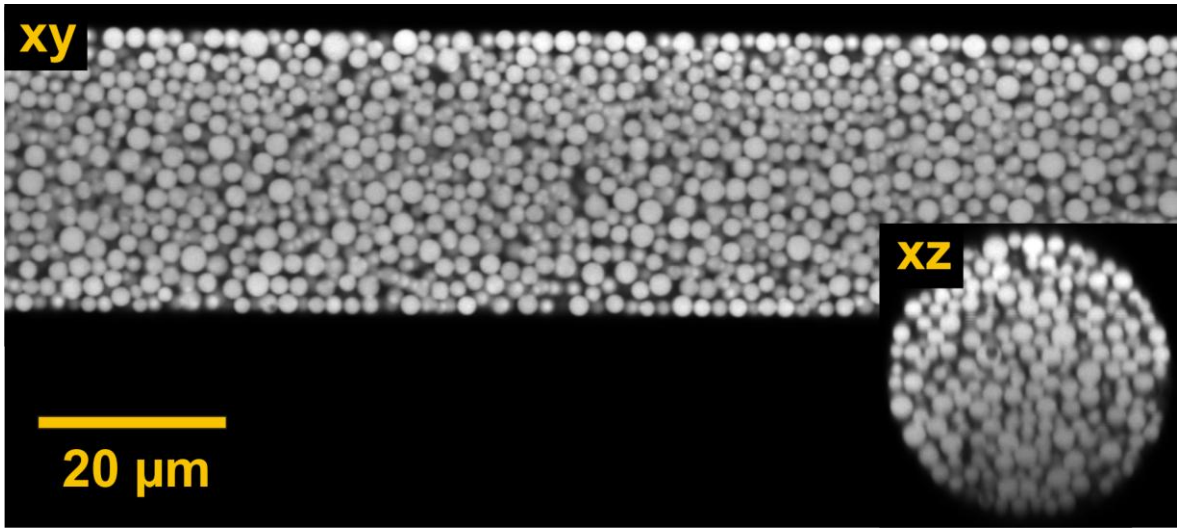

Figure 4.6: Exemplary optical slices through a 30 µm i.d. column (30 µm i.d.-A) packed with fully porous Acquity 1.7 µm BEH particles prior to image processing. The C18-functionalized, endcapped particles were stained by the adsorption of the lipophilic dye Bodipy 493/503.

4.5.5 Image Processing. Poisson-distributed photon noise in the images was reduced by use of the PureDenoise plug-in for ImageJ [51] provided by Luisier [52]. Bleaching of dye was corrected by fitting a second-order exponential decay to the acquired image stack's intensity distribution along the dimension of the optical axis (z-axis). For this purpose, a region of interest in the capillary was selected. Subsequently, Huygens maximum likeli-

hood iterative deconvolution (Scientific Volume Imaging, Hilversum, The Netherlands) was applied for image restoration using an automated background estimate from the deconvolution software ("in/near object"-estimate) and a signal-to-noise ratio of 15. Images were rotated three-dimensionally to have the column aligned with the borders of the image stack. A two-dimensional projection along the column axis then allowed the elimination of a possible drift of the column between slices. To calibrate the z-step of the image stack, a perfectly cylindrical confinement was assumed so that all objects were symmetrically distributed around the column axis (Figure 4.7).

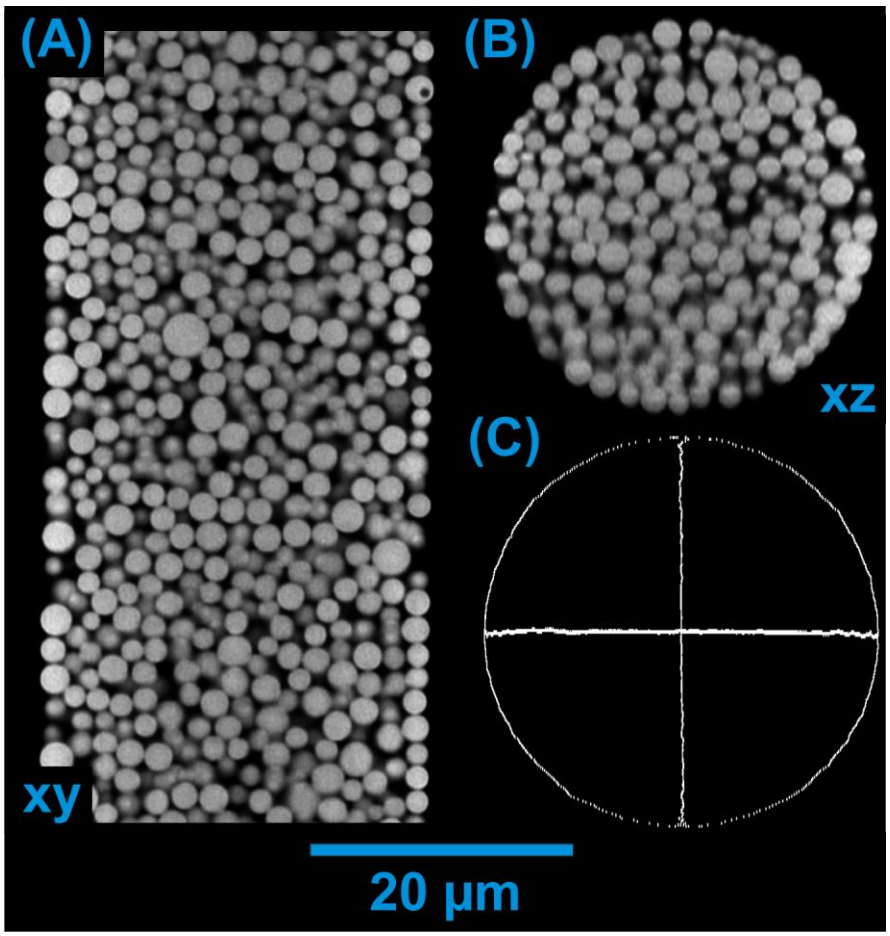

Figure 4.7: Optical slices of a 30 µm i.d. column (30 µm i.d.-B) after image restoration along the capillary axis (**A**) and along the optical axis (**B**). Panel (**C**) shows a two-dimensional projection of the detected column borders and center lines that were used to check the three-dimensional alignment of the recorded image stack.

Particles were detected by their property of defining high-intensity regions of low signal variance. For this purpose, the image stacks were duplicated. An unsharp mask followed by thresholding was applied to one of these stacks. Then, the other stack was variance-filtered, thresholded, and inverted. A logic AND operation provided clusters whose three-dimensional centroids defined the locations of particle centers (Figure 4.8) [51].

Segmentation of the recordings was achieved by subjecting the acquired list of particle centers and each deconvolved image stack to a custom algorithm written with Visual Studio C# 2008 (Microsoft Corporation, Redmond, WA). A best fit for each particle was determined by varying the input particle centers in all three dimensions and expanding a circular region of interest around these centers. The growing step terminated when either a variance threshold (specific of each recorded image stack) was exceeded for the pixels covered by the next larger circle (indicating imprecise sphere location), or the mean intensity of these pixels would drop below 55% of the highest mean intensity found for a circle at this location (indicating the half height of the intensity signal). The radius and the center of the largest circle that could be fitted defined the location and the radius of each particle (Figure 4.9).

A three-dimensional reconstruction with defined regions of the void space and particulate space was then drawn for each column segment assuming a perfect sphericity of the particles. These reconstructions were manually screened and corrected for any missing and falsely fitted particles by using an overlay of the deconvolved and reconstructed image stack. At least 3000 particles and 45 µm along the column axis were reconstructed for each column (cf. Table 4.2). For columns with an inner diameter of $\leq$ 30 µm an entire column segment was reconstructed (see Figure 4.1C), while we limited our reconstructions to the upper half of the larger-diameter columns (Figure 4.1D). This allowed all regions in the bed (wall and bulk regions) to be represented according to their effective distribution in the column.

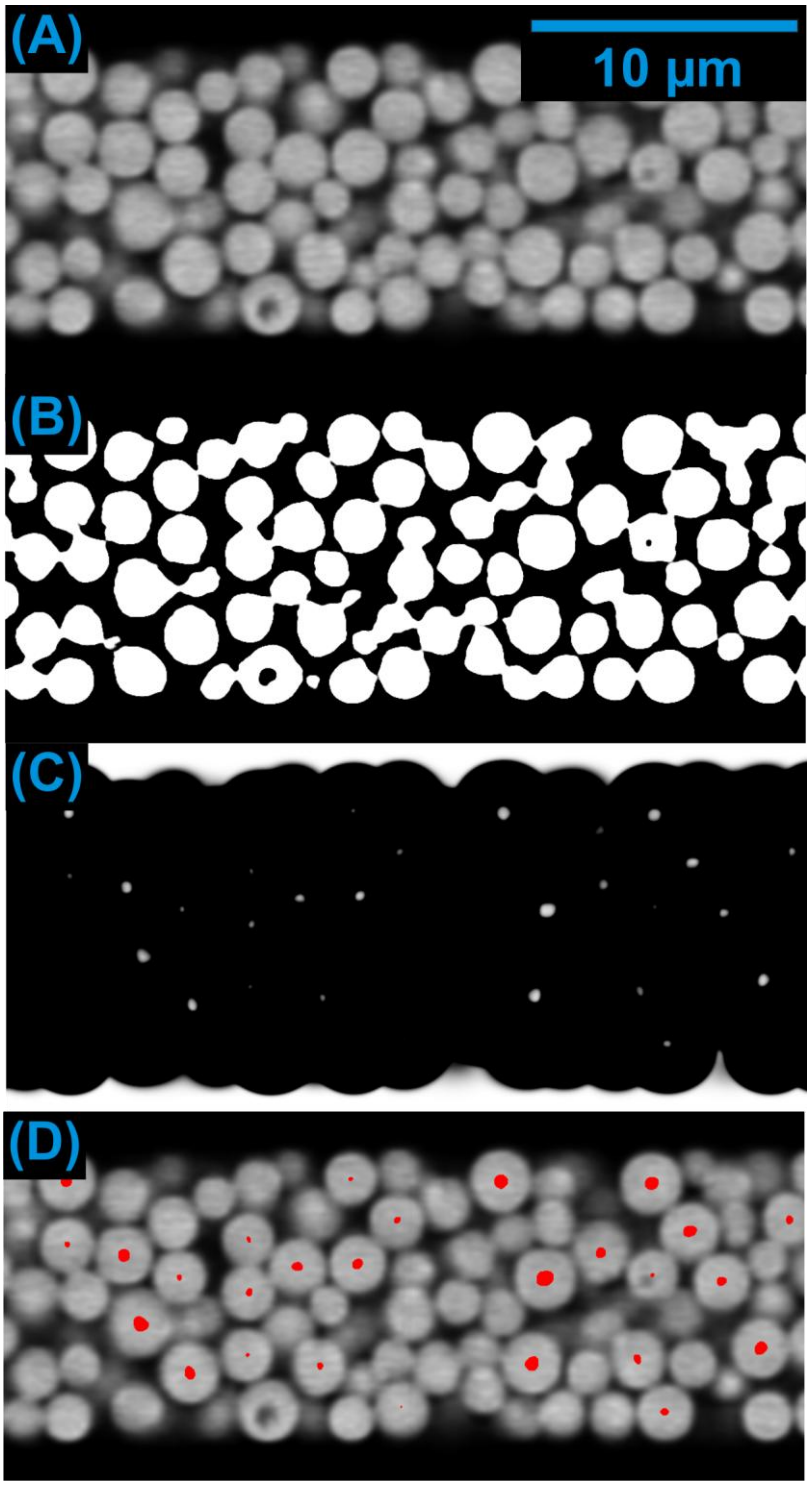

Figure 4.8: Section from a deconvolved particle image (**A**) which has been transformed by an unsharp mask of 25 pixels radius and a mask weight of 0.99 in (**B**). Panel (**C**) displays the inverse result of applying a variance filter with 30 pixel radius to (**A**). Red dots in panel (**D**) mark the result of a logical AND operation with (**B**) and (**C**). Subsequent three-dimensional centroiding allowed the location of possible centers of the marked particles. After fitting of these particles, smaller particles would be detectable by subtracting the detected particles from (**B**) and applying a smaller variance filter to (**A**). Particles that were not fully porous, like the one seen at the bottom of the bed, would often be missed (or fitted incorrectly) and were therefore segmented manually.

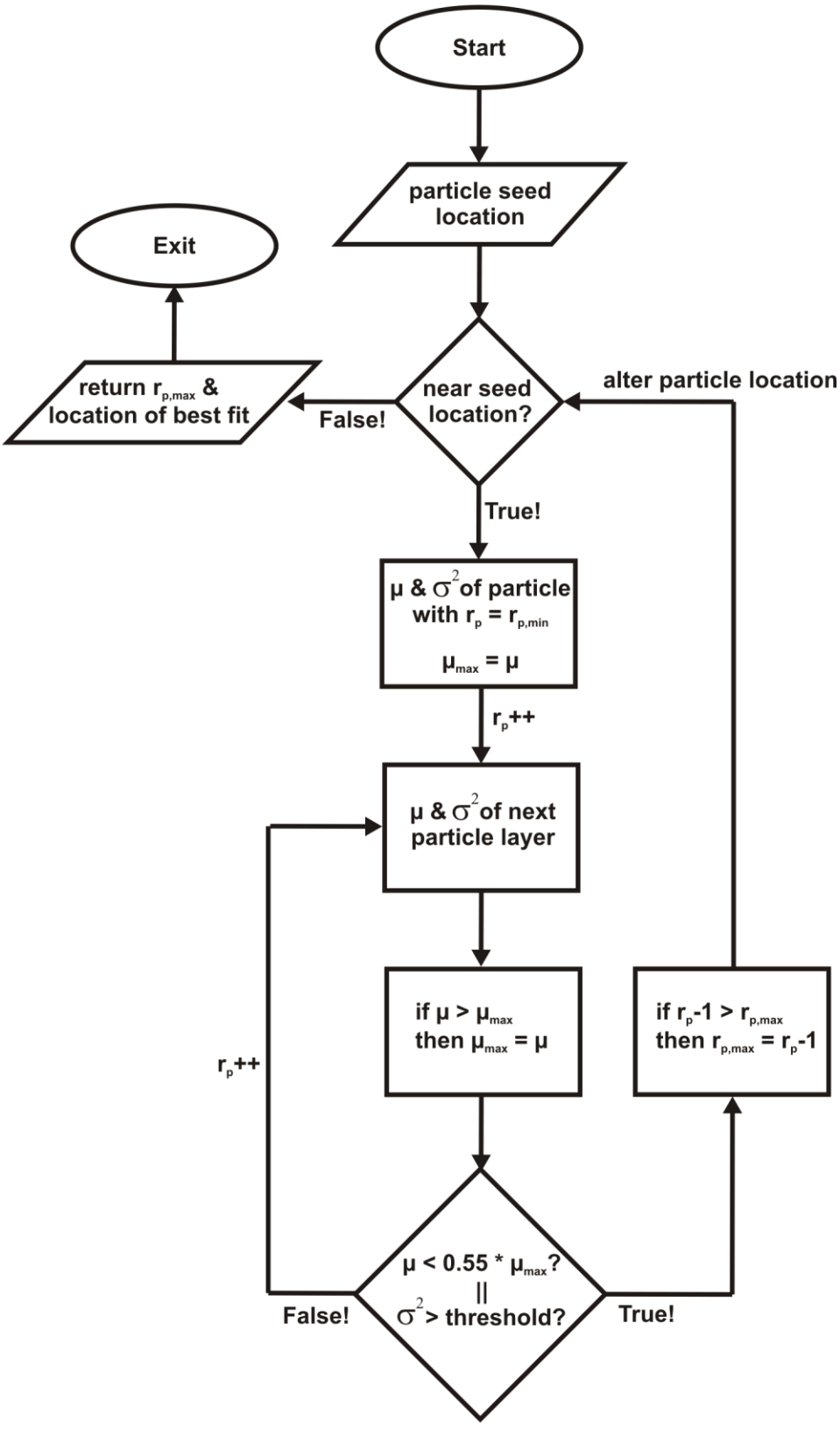

Figure 4.9: Programming flowchart outlining the subroutine used to determine a best-fitting sphere for each particle location (μ denotes the mean intensity, and σ² is the variance of the microscopic image's signal intensity; r_p is the currently computed particle radius). The output $r_{p,max}$ denotes the radius of the best fitting sphere, whereas $r_{p,min}$ represents the minimal sphere radius analyzed.

Table 4.2: Basic reconstruction parameters of the analyzed columns [a].

Column diameter	Fitted particles	Reconstructed length [µm]	Recontructed volume [pL]	d_p [µm]	d_S [µm]	ε	ε_{bulk}
10 µm i.d.	3041	180	17.8	1.99	2.27	0.452	0.377
20 µm i.d.	3655	65	22.6	1.93	2.19	0.416	0.361
30 µm i.d.–A	6967	65	46.2	2.00	2.23	0.402	0.360
30 µm i.d.–B	6050	58	41.2	1.96	2.24	0.418	0.355
50 µm i.d.	8543	55	47.4	1.96	2.28	0.406	0.364
75 µm i.d.	14955	45	92.5	1.97	2.22	0.403	0.376

[a] The reconstructed bed length refers to the dimension of the reconstruction along the column axis; d_p is the number-averaged particle diameter, and d_S is the Sauter mean diameter; ε is the external porosity (interparticle void volume fraction) of a packing, and ε_{bulk} is the bulk porosity (without wall region).

4.5.6 Image Analysis. Integrity of the reconstructions was checked by comparing the resulting particle size distributions (PSDs) with a PSD that was acquired from 100 particles in scanning electron microscopy (SEM) images of the packing material. SEM images were obtained on a Hitachi S-4700 cold cathode field emission SEM equipped with a Through the Lens (TTL) detector (Tokyo, Japan). Exemplary PSDs are provided in panel (**A**) of Figure 4.10. The mean values (d_p) for the PSDs varied between 1.96 and 2.00 µm. They are summarized in Table 4.2 together with the Sauter mean diameter and are in good agreement with values from the SEM-based PSD (d_p = 2.01 µm). The standard deviation of the CLSM-based PSDs varied between 0.30 and 0.35, while the SEM-based PSD had a standard deviation of 0.28.

Interparticle porosity was analyzed in the reconstructed column segments by calculating a two-dimensional projection of the ratio of void voxels to the total amount of voxels along the column axis; see panel (**B**) in Figure 4.10. Each porosity value of less than 0.99 was defined to be located in the column, whereas larger values were assigned to the capillary wall. Now, the pixels were sorted by their Euclidean distance from the column wall and binned with 100 nm step size. Resulting one-dimensional radial porosity profiles for the wall region are provided in Figure 4.3 of the main article.

The calculation of the radially resolved PSDs utilized in Figure 4.5 of the main article was performed by assigning a distance from the column wall to each particle center and analyzing the PSD in dependence from these distances with a moving window of one dp (at a sampling rate of 0.1 µm). Local PSDs with a count of less than 200 particles were discarded for being of minor significance and are not shown in the figure.

The analysis of packing voids was performed by calculating the Euclidean distance of each void pixel from the closest particle surface. A packing void was defined to be present when the distance from the next particle surface exceeded the radius associated with the first quartile of the macroscopic PSD. Since most packing voids were located at the wall–bed interface, the number of packing voids was counted and related to the approximate capillary surface area that was reconstructed, as shown in Table 4.1 of the main article.

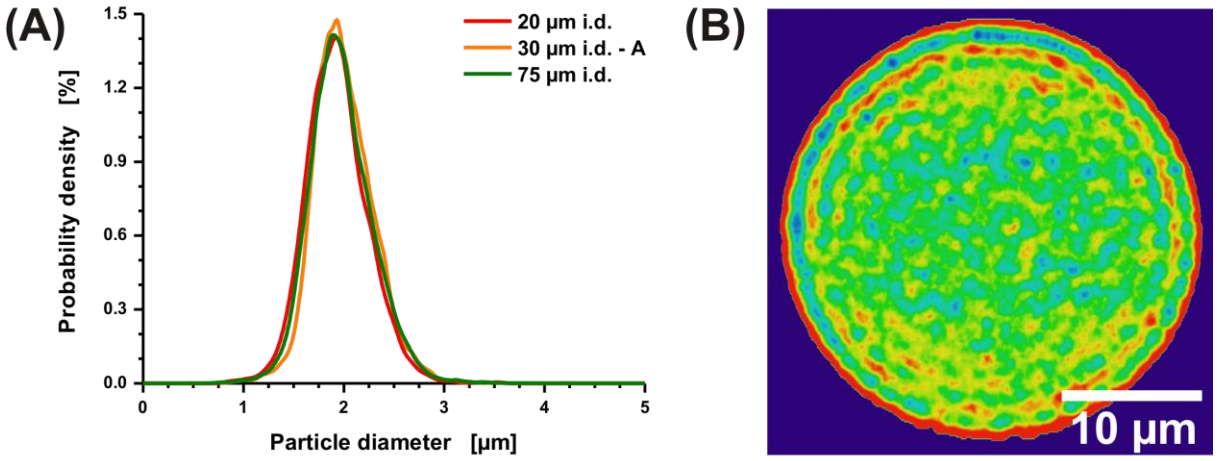

Figure 4.10: (**A**) Exemplary probability density fits of three particle size distributions computed from the reconstructions of the packings. (**B**) Color-coded two-dimensional porosity profile of a 30 µm i.d. capillary column.

Acknowledgements

CLSM work was supported by the Deutsche Forschungsgemeinschaft DFG (Bonn, Germany) under Grant TA 268/5. Column preparation work was supported by Waters Corporation (Milford, MA), and J.P.G. was supported by the National Science Foundation Graduate Research Fellowship (Arlington, VA) under Grant DGE-0646083.

References

[1] Kirkland, J. J.; Langlois, T. J.; DeStefano, J. J. *Am. Lab.* **2007**, *39*, 18−21.

[2] Guiochon, G.; Gritti, F. *J. Chromatogr., A* **2011**, *1218*, 1915−1938.

[3] Patel, K. D.; Jerkovich, A. D.; Link, J. C.; Jorgenson, J. W. *Anal. Chem.* **2004**, *76*, 5777−5786.

[4] Mazzeo, J. R.; Neue, U. D.; Kele, M.; Plumb, R. S. *Anal. Chem.* **2005**, *77*, 460A−467A.

[5] Wu, N.; Lippert, J. A.; Lee, M. L. *J. Chromatogr., A* **2001**, *911*, 1−12.

[6] , L. A. *Anal. Chem.* **2005**, *77*, 7489−7494.

[7] Jorgenson, J. W. Annu. Rev. *Anal. Chem.* **2010**, *3*, 129−150.

[8] Cavazzini, A.; Gritti, F.; Kaczmarski, K.; Marchetti, N.; Guiochon, G. *Anal. Chem.* **2007**, *79*, 5972−5979.

[9] Felinger, A. *J. Chromatogr., A* **2011**, *1218*, 1939−1941.

[10] Omamogho, J. O.; Hanrahan, J. P.; Tobin, J.; Glennon, J. D. *J. Chromatogr., A* **2011**, *1218*, 1942−1953.

[11] Gritti, F.; Omamogho, J.; Guiochon, G. *J. Chromatogr., A* **2011**, *1218*, 7078−7093.

[12] , L. A. *J. Sep. Sci.* **2010**, *33*, 2547−2557.

[13] Gritti, F.; Guiochon, G. *J. Chromatogr., A* **2010**, *1217*, 5069−5083.

[14] Guillarme, D.; Ruta, J.; Rudaz, S.; Veuthey, J.-L. Anal. *Bioanal. Chem.* **2010**, *397*, 1069−1082.

[15] Omamogho, J. O.; Glennon, J. D. *Anal. Chem.* **2011**, *83*, 1547−1556.

[16] Gritti, F.; Guiochon, G. *J. Chromatogr., A* **2011**, *1218*, 1592−1602.

[17] Carr, P. W.; Stoll, D. R.; Wang, X. *Anal. Chem.* **2011**, *83*, 1890−1900.

[18] Yew, B. G.; Ureta, J.; Shalliker, R. A.; Drumm, E. C.; Guiochon, G. *AIChE J.* **2003**, *49*, 642−664.

[19] Gritti, F.; Guiochon, G. *Chem. Eng. Sci.* **2010**, *65*, 6327−6340.

[20] Gritti, F.; Leonardis, I.; Abia, J.; Guiochon, G. *J. Chromatogr., A* **2010**, *1217*, 3819−3843.

[21] Neue, U. D. *HPLC Columns: Theory, Technology, and Practice*; Wiley-VCH: New York, **1997**.

[22] Kirkland, J. J.; DeStefano, J. J. *J. Chromatogr., A* **2006**, *1126*, 50−57.

[23] Khirevich, S.; Daneyko, A.; Höltzel, A.; Seidel-Morgenstern, A.; Tallarek, U. *J. Chromatogr., A* **2010**, *1217*, 4713−4722.

[24] Daneyko, A.; Höltzel, A.; Khirevich, S.; Tallarek, U. *Anal. Chem.* **2011**, *83*, 3903−3910.

[25] Khirevich, S.; Höltzel, A.; Daneyko, A.; Seidel-Morgenstern, A.; Tallarek, U. *J. Chromatogr., A* **2011**, *1218*, 6489−6497.

[26] Bruns, S.; Tallarek, U. *J. Chromatogr., A* **2011**, *1218*, 1849−1860.

[27] Bruns, S.; Hara, T.; Smarsly, B. M.; Tallarek, U. *J. Chromatogr., A* **2011**, *1218*, 5187−5194.

[28] Hormann, K.; Müllner, T.; Bruns, S.; Höltzel, A.; Tallarek, U. *J. Chromatogr., A* **2012**, *1222*, 46−58.

[29] Karlsson, K.-E.; Novotny, M. *Anal. Chem.* **1988**, *60*, 1662−1665.

[30] Kennedy, R. T.; Jorgenson, J. W. *Anal. Chem.* **1989**, *61*, 1128−1135.

[31] Cole, L. J.; Schultz, N. M.; Kennedy, R. T. *J. Microcolumn Sep.* **1993**, *5*, 433−439.

[32] Hsieh, S.; Jorgenson, J. W. *Anal. Chem.* **1996**, *68*, 1212−1217.

[33] Li, W.; Pyo, D.; Wan, Y.; Ibañez, E.; Malik, A.; Lee, M. L. *J. Microcolumn Sep.* **1996**, *8*, 259−268.

[34] Witowski, S. R.; Kennedy, R. T. *J. Microcolumn Sep.* **1999**, *11*, 723−728.

[35] Eeltink, S.; Rozing, G. P.; Schoenmakers, P. J.; Kok, W. Th. *J. Chromatogr., A* **2004**, *1044*, 311−316.

[36] MacNair, J. E.; Lewis, K. C.; Jorgenson, J. W. *Anal. Chem.* **1997**, *69*, 983−989.

[37] MacNair, J. E.; Patel, K. D.; Jorgenson, J. W. *Anal. Chem.* **1999**, *71*, 700−708.

[38] Wu, N.; Collins, D. C.; Lippert, J. A.; Xiang, Y.; Lee, M. L. *J. Microcolumn Sep.* **2000**, *12*, 462−469.

[39] Mellors, J. S.; Jorgenson, J. W. *Anal. Chem.* **2004**, *76*, 5441−5450.

[40] Daneyko, A.; Khirevich, S.; Höltzel, A.; Seidel-Morgenstern, A.; Tallarek, U. *J. Chromatogr., A* **2011**, *1218*, 8231−8248.

[41] Hamdan, E.; Milthorpe, J. F.; Lai, J. C. S. *Chem. Eng. J.* **2008**, *137*, 614−635.

[42] Giddings, J. C. *Dynamics of Chromatography, Part 1: Principles and Theory*; Marcel Dekker, New York, **1965**.

[43] Khirevich, S.; Höltzel, A.; Seidel-Morgenstern, A.; Tallarek, U. *Anal. Chem.* **2009**, *81*, 7057−7066.

[44] Usher, K. M.; Simmons, C. R.; Dorsey, J. G. *J. Chromatogr., A* **2008**, *1200*, 122−128.

[45] Maier, R. S.; Kroll, D. M.; Bernard, R. S.; Howington, S. E.; Peters, J. F.; Davis, H. T. *Phys. Fluids* **2003**, *15*, 3795−3815.

[46] de Klerk, A. *AIChE J.* **2003**, *49*, 2022−2029.

[47] Ehlert, S.; Rösler, T.; Tallarek, U. *J. Sep. Sci.* **2008**, *31*, 1719−1728.

[48] Giddings, J. C.; Fuller, E. N. *J. Chromatogr.* **1962**, *7*, 255−258.

[49] Maiolica, A.; Borsotti, D.; Rappsilber, J. *Proteomics* **2005**, *5*, 3847–3850.

[50] Wilhelm, S.; Gröbler, B.; Gluch, M.; Heinz, H. *Confocal Laser Scanning Microscopy — Optical Image Formation and Electronic Signal Processing*; Monography, Carl Zeiss: Jena, Germany, **2008**.

[51] Rasband, W. S. *ImageJ*; U.S. National Institutes of Health: Bethesda, MD, **1997-2006**; http://rsb.info.nih.gov//ij/.

[52] Luisier, F. *PureDenoise*; Biomedical Imaging Group, École Polytechnique Fédéral de Lausanne, **2010**; http://bigwww.epfl.ch/algorithms/denoise.

Chapter 5

Influence of Particle Properties on the Wall Region in Packed Capillaries

Authors:

Stefan Bruns, Daniela Stoeckel, Bernd M. Smarsly, and Ulrich Tallarek

State of Publication:

Published December 14, 2012 in *Journal of Chromatography A*, Vol. 84, p. 53–63.

Abstract

Analytical columns (4.6 mm i.d.) packed with core–shell particles have shown a significantly reduced eddy dispersion contribution to band broadening compared to conventional fully porous particles. It has been speculated if this is caused by the narrow particle size distribution (PSD) of the core–shell particles, as an intrinsic advantage, or by an improved packing structure that specifically reduces the transcolumn velocity biases caused by wall effects. A recent simulation study has pointed against the former proposition [A. Daneyko et al., Anal. Chem. 83 (2011) 3903]. It is more likely that the slurry packing process for core–shell particles results in bed morphologies with reduced wall effects compared to the fully porous particles with a wide PSD. To access the latter proposition experimentally we slurry packed capillary columns (100 μm i.d.) with different fully porous (wide PSDs) and core–shell (narrow PSDs) particles and imaged their bed structures three-dimensionally using confocal laser scanning microscopy. This allowed us to resolve and analyze the bed morphology in these columns locally on all length scales contributing to eddy dispersion. On the transcolumn scale we observed a systematic difference between core–shell and fully porous particles: In the vicinity of the column wall the core–shell particles packed denser (closer to the bulk packing densities) and with a higher regularity than the fully porous particles. The bulk regions of all packings were effectively indistinguishable. This provides experimental evidence that the reduced eddy dispersion contribution with core–shell

packings should be attributed to a higher transcolumn homogeneity rather than to an improved bed morphology on smaller length scales, e.g., to a reduced short-range disorder.

5.1 Introduction

When the core–shell particle concept was first introduced to chromatography during the late 1960s for the separation of macromolecules by Horváth et al. [1,2] and Kirkland [3,4] it did not succeed in finding widespread application due to the development of ever finer, spherical, fully porous particles. Only in 2006 Advanced Materials Technologies (Wilmington, DE) manufactured the first Halo particles with a nominal diameter (d_p) of 2.7 µm and returned core–shell particles to the attention of chromatographers [5,6]. Since then core–shell particles provide an inviting alternative to the conventional fully porous sub-2 µm particles even for the separation of small analytes. Under these conditions the shorter diffusion length through the porous shell compared to fully porous particles becomes irrelevant in its contribution to band broadening. Still, columns packed with core–shell particles almost show the same loading capacity as fully porous particles while operated at lower backpressures than columns packed with sub-2 µm particles. When applied with modern HPLC equipment columns packed with sub-3 µm core–shell particles exhibit minimum reduced plate heights (h_{min}) below 1.6 in the popular 4.6 mm i.d. column format [6–9], whereas conventional fully porous particles typically yield $h_{min} \sim 2.0$ under similar conditions. Consequently, core–shell particles have been complimented not only for reducing transparticle diffusion lengths, but also for improving the kinetic performance of the columns packed with these particles. This has been marketed to originate from a narrower particle size distribution (PSD), which is at about 3–6% relative standard deviation (RSD) for core–shell particles compared to 10–20% RSD for the available fully porous particles. It is assumed that eddy dispersion is reduced by an improved bed morphology [7,10], but exactly how a narrow PSD works to achieve a more homogeneous packing and thus higher column efficiency remains unclear [11].

In a systematic approach to study band broadening in columns packed with $d_p = 2.7$ µm Halo and $d_p = 2.6$ µm Kinetex core–shell particles Gritti and Guiochon [8] used peak parking experiments with a diffusion model based on the effective medium theory. This allowed the quantification of individual band broadening contributions from longitudinal diffusion, eddy dispersion, and mass transfer resistance. They demonstrated that the high

efficiencies for columns packed with core–shell particles result from the combination of a 10% smaller longitudinal diffusion term and a 30% lower eddy dispersion term compared to columns packed with conventional fully porous particles. Whether the exceptional low eddy dispersion term with core–shell packings (for small and medium sized analytes) is an intrinsic feature of a narrow PSD in the bulk packing region of a column, or a result of reduced wall effects and smaller transcolumn velocity biases, still remained an open question [9]. Notably, the latter proposition is expected to originate from a changed shear stress distribution across the column during the slurry packing process with core–shell particles that are rougher than most fully porous particles [9,12].

Detailed eddy dispersion simulations from our group recently demonstrated that the width of a PSD is negligible in chromatographic praxis when considering the bulk region of the beds [13]. In that work, the investigated PSDs were modeled according to experimentally acquired PSDs of sub-2 µm fully porous and sub-3 µm core–shell particles. Computer-generated bulk, i.e., unconfined packings without walls (infinitely wide) allowed to study the influence of the PSD on hydraulic permeability and eddy dispersion independent from all other parameters, e.g., the packing process or individual particle properties, while keeping realistic unimodal and continuously distributed PSDs [13]. By contrast, the experimental approach of blending particles often yields bimodal distributions [12]. The simulations demonstrated that hydraulic permeability of a bulk packing (an "infinite diameter column") does not depend on the underlying PSD, whereas eddy dispersion was affected only to an extent that is not noticeable in chromatographic praxis. This is consistent with earlier experimental studies using larger particles [12,14,15]. Here, the width of the PSD remained insignificant regarding separation efficiency as long as the $d_{p,90}/\ d_{p,10}$ ratio did not exceed ~2 [14].

In these simulations with bulk packings [13] the overall interstitial porosity dominated the magnitude of eddy dispersion. Experimentally, the core–shell particles often even pack looser than the conventional fully porous particles [16,17]. These findings suggest that the reduced eddy dispersion for core–shell particles should not be associated with transchannel and short-range interchannel disorder (on a length scale of up to 1–2 d_p) characterizing bulk packings, but with a changed bed morphology in the vicinity of the column wall, leading specifically to a smaller transcolumn contribution to eddy dispersion.

The importance of transcolumn contributions to separation efficiency has been highlighted in theoretical and experimental studies (see, e.g., [18–24]). Numerical simulations

nowadays allow to quantify the contributions to eddy dispersion on all relevant time and length scales in packed beds [13,22,24–26]. The ability to highlight single process parameters is an invaluable tool to understand the relationship between the microscopic structure of a packed bed and its transport properties. Yet, the very complex physical interactions taking place during the slurry packing process have seldom been studied systematically and are not fully understood; an algorithmic approach that comprises the slurry packing process with all its process parameters comprehensively is still missing. To study process parameters applied during column packing that are relevant to the resulting bed morphology complementing the simulations with a three-dimensional visualization of these morphologies therefore becomes invaluable. The strongest benefit of three-dimensional imaging is the capability to resolve and analyze bed structures locally, whereas traditional chromatographic characterization only yields averaged parameters for an entire column.

We applied confocal laser scanning microscopy (CLSM) to approach the morphology of different chromatographic bed types, i.e., silica based monoliths and particulate beds [27–31]. Most recently, we started to investigate the effect of single isolated parameters altered during the slurry packing process on the final bed morphology in capillary columns [31]. These were packed with 1.7 µm Acquity BEH particles and their i.d. was varied from 10 to 75 µm. When the column-to-particle diameter ratio (d_c/d_p) was increased above 20 the efficiency of these columns dropped from $h_{min} \approx 1.4$ to $h_{min} \approx 2.5$. This observation correlated directly with a morphological change near the capillary wall. Larger i.d.'s and poorer performing capillaries were packed looser in the immediate wall region, resulting in an increased transcolumn eddy dispersion contribution. Opposed to capillary columns that allow to measure band broadening for laterally fully equilibrated wall effects [22,24,31], the separation efficiencies traditionally acquired for analytical and narrow-bore columns are always recorded in the pre-asymptotic regime, i.e., with non-equilibrated wall effects. Here, 2.1 mm i.d. columns often perform worse than 4.6 mm i.d. columns, which was explained by Gritti and Guiochon [32] as a consequence of the larger volumetric fraction occupied by the crucial and often heterogeneous wall region in the 2.1 mm i.d. columns. Still, the physical laws relevant to bed formation remain the same for capillary fused silica and analytical steel columns.

The goal of this work is to visualize and elucidate the influence of the PSD on the transcolumn bed morphology of packed columns. For that purpose we slurry packed 100 µm i.d. capillary columns with several commercially available packing materials:

wide-PSD fully porous and narrow-PSD core–shell particles. A fixed packing protocol was employed for all particles and the packed beds were imaged and reconstructed by CLSM. When applied to capillary type packings this optical microscopy method can be used to image the entire cross-section of the column under noninvasive conditions, which is impossible for narrow-bore and analytical column packings. It is an experimental setup that allows us to study the interplay of the packing material with the confining capillary wall and to visualize the transition of the bed morphology to its behavior in the bulk region of a packing. Here, we adapt this approach to analyze systematic differences in the bed morphology for wide-PSD fully porous and narrow-PSD core–shell packing materials.

5.2 Eddy Dispersion in Packed Capillaries

A discussion of morphology–transport relationships with respect to the separation efficiency requires a deep understanding of the interconnections between experimentally acquired plate heights and the length scales of eddy dispersion contributions that originate in the morphology of packed beds. These connections have been made by Giddings' theory of eddy dispersion [33]. He developed a plate height equation which is by now the only eddy dispersion model with a sound physical background. In analogy to conductors in parallel Giddings applied the random-walk relationship to a model of eddy dispersion. Based on the additivity of variances he assumed that a chromatographic bed could be described with at least three distinct length scales that involve coupling between transverse diffusion and spatial velocity fluctuations. The equation for reduced plate height $h = f(v)$ in his model is given by

$$h = \frac{b}{v} + \sum_{i=1}^{3} \frac{2\lambda_i}{1 + (2\lambda_i/\omega_i)v^{-1}} + cv \qquad \text{(Eq. 5.1)}$$

where $h = H/d$ is the reduced plate height and v is the reduced velocity defined as $v = u_{av}d/D_m$ (u_{av} is the average mobile phase velocity, d represents a mean particle diameter, and D_m is the diffusion coefficient of the analyte or tracer molecules in the bulk mobile phase).

The first term of the plate height equation (b/v) accounts for longitudinal molecular diffusion driven by the concentration gradient along the zone profile, while the last term (cv) accounts for the mass transfer kinetics into and across the stationary phase [33]. Remaining terms in Eq. 5.1 characterize eddy dispersion by the universal structural parameters λ_i and ω_i: The transchannel contribution (i = 1) refers to velocity biases across individual channels between adjacent particles; the short-range interchannel contribution (i = 2) refers to velocity biases on a length scale of 1–2 d_p caused by the random positions of the particles in the bed; and transcolumn dispersion (i = 3) refers to a confinement-based velocity bias (wall effects) caused, e.g., by the inability of rigid particles to pack closely against the column wall (so-called geometrical wall effect). Apart from the average external bed porosity transcolumn contributions are one of the main contributors to eddy dispersion [22,24,31] that determine the difference between a well packed and a mediocre packed capillary [31].

Of the various statistical parameters that can be calculated for PSDs, we use the surface-mean or Sauter mean particle diameter $d_S = \sum n_i d_i^3 / \sum n_i d_i^2$ for the normalization of plate height data ($h = H/d_S$) and fluid velocity ($v = u_{av} d_S / D_m$), because it ensures a comparison of packed beds under the condition of equal total external surface area. Whereas the use of d_S in connection with the permeability is unquestioned, because in laminar flow the viscous drag on a particle is proportional to the surface area orthogonal to the flow direction, normalization of plate height data by d_S requires explanation [13]. The flow nonuniformity in the interparticle void space of a packing is caused by the no-slip velocity boundary condition at the particles' surfaces. Thus, the surface area has an impact on eddy dispersion that originates from the nonuniformity of the flow field. In turn, the normalization by d_S ensures that the packings are compared under the condition of equal total external surface area, which is important when different PSDs are involved.

Importantly, Eq. 5.1 is only valid when the lateral equilibration of dispersion contributions is complete. While this cannot be realized with narrow-bore and analytical columns, capillary columns typically have bed lengths of more than a thousand column diameters; it allows full lateral equilibration of the analyte between velocity extremes that may exist over the whole column cross section. Comprehensive simulation studies of eddy dispersion in packed beds have shown that in a range of reduced velocities common in chromatographic praxis (v < 30) the comprehensive Giddings equation for a capillary type stationary phase can be expressed in the following form [22,24]

$$h = \frac{b}{\nu} + \omega_1 \nu + \frac{2\lambda_2}{1 + (2\lambda_2/\omega_2)\nu^{-1}} + \omega_3 \nu + c\nu \qquad \text{(Eq. 5.2)}$$

i.e., transchannel and transcolumn dispersion contributions lose their coupling characteristic and reduce to simple velocity-proportional terms ($\omega_1 \nu$ and $\omega_3 \nu$, respectively). This behavior is resolved when plate height data are acquired and subsequently analyzed with Eq. 5.1 over a sufficiently wide velocity range for laterally fully equilibrated wall effects and the corresponding asymptotic dispersion coefficients, as performed in [22,24]. Experimental confirmation of Eq. 5.2 can be found in [31]. In that work the packing material and therefore the mass transfer resistance remained unchanged, whereas the linear slope of the plate height curves varied, which depended primarily on the transcolumn heterogeneities in the beds and the associated $\omega_3 \nu$ in Eq. 5.2. The structural parameter ω_3 of transcolumn eddy dispersion is approached by [33]

$$\omega_3 = \frac{{\omega_{\alpha,3}}^2 {\omega_{\beta,3}}^2}{2} = 0.5 \left(\frac{d_c}{2d_p}\right)^2 \left(\frac{\Delta\nu}{\nu}\right)^2 \qquad \text{(Eq. 5.3)}$$

where $\omega_{\alpha,3}$ represents the characteristic lateral diffusion length for transcolumn equilibration (column radius, $d_c/2$) and $\omega_{\beta,3}$ describes the relative difference between the involved velocity extremes (near-wall and bulk velocities). Whereas $\omega_{\alpha,3}$ is a purely geometrical parameter that contains the aspect ratio (d_c/d_p), $\omega_{\beta,3}$ characterizes the individual transcolumn velocity profiles that develop with a particular bed morphology. How a specific parameter in a slurry packing protocol manifests itself in this parameter ($\omega_{\beta,3}$) is an unresolved question. It is the ability of the CLSM approach to resolve all morphological features locally on the length scales that are relevant to eddy dispersion, from the transchannel contribution manifested in the local interstitial pore volumes up to the transcolumn contribution visible in the porosity distribution along the capillary diameter. In our previous studies we derived chord length distributions and radial porosity profiles as morphological measures to describe heterogeneity on these length scales [27–31]. In the present work these measures are applied to compare bed morphologies of wide-PSD fully porous and narrow-PSD core–shell packing materials.

5.3 Experimental Section

5.3.1 Chemicals and Materials. Six 100 µm i.d. cylindrical fused silica capillaries each packed with a different type of stationary phase material were employed in this study. 365 µm o.d., polyimide coated, fused silica capillary tubing was purchased from Polymicro Technologies (Phoenix, AZ). These capillaries were packed with the following C18 modified stationary phases: d_p = 3 µm Atlantis particles (Waters Corporation, Milford, MA), 3 µm Luna and 2.6 µm Kinetex particles (Phenomenex, Aschaffenburg, Germany), 3.5 µm Zorbax and 2.5 µm Poroshell particles (Agilent Technologies, Waldbronn, Germany), and 2.7 µm Halo particles (Advanced Materials Technologies, Wilmington, DE). All solvents (glycerol, HPLC grade acetonitrile (ACN), dimethylsulfoxide (DMSO), methanol, tetrahydrofurane (THF), acetone) and thiourea were supplied by Sigma–Aldrich Chemie (Taufkirchen, Germany). A Milli-Q gradient water purification system (Merck Millipore, Darmstadt, Germany) was used to provide HPLC grade water. The dye Bodipy 493/503 (Life Technologies, Darmstadt, Germany) was utilized as a lipophilic fluorophore for microscopic imaging.

5.3.2 Slurry Packing of Capillaries. A fixed packing protocol that is known to provide reproducible results (e.g., average packing densities) [34] was used for all particles, instead of optimizing the packing procedure for each material individually. This allowed us to unravel how particles with different properties (e.g., PSD and surface roughness) respond to a given set of boundary conditions during the packing process. We were particularly interested in providing an answer to the key question whether distinct morphological properties (in the packing bulk and the wall region) can be associated with the group of wide-PSD fully porous particles and the group of narrow-PSD core–shell particles.

The fused silica capillaries were slurry packed using a Well-Chrom K-1900 pneumatic pump (Knauer, Berlin, Germany). A 500 µm i.d. glass-lined metal tubing was used as the slurry reservoir. SSI two-way and three-way valves (ERC, Riemerling, Germany) were placed between the pneumatic pump and slurry reservoir for pressure release and slurry injection, respectively. A stainless steel union with a 1 µm mesh stainless steel frit (Upchurch Scientific, Oak Harbor, WA) was placed at the capillary outlet before the packing process started. For slurry preparation 50 mg of the dry particles was suspended in 1 mL THF while applying ultrasound (15 min). Degassed methanol was used as the pack-

ing solvent for the consolidation of the beds. Starting with 100 bar the packing pressure was increased to 500 bar and held at this value until a sufficient filling of the capillaries (about 250 mm) was achieved. Next, the pressure was raised up to 600 bar and the bed was further consolidated in an ultrasonic bath (Bandelin Electronic, Berlin, Germany) at 35 kHz for 45 min. As shown by Ehlert et al. [34] the use of ultrasound is critical for obtaining densely packed capillaries. When the packing did not settle further, the system was depressurized slowly (2–3 h) and the capillary was removed from the packing device. The packing solvent was exchanged for degassed water containing 1 g/L sodium chloride. Replacing the packing solvent for an electrolyte solution has shown to be necessary for obtaining mechanically stable frits [34]. Afterwards, the packed capillary was again connected to the packing pump and flushed with the aqueous solution for at least 30 min at 500–600 bar to ensure complete exchange of the packing solvent. Then, the packing was fixed by an inlet and an outlet frit, which were sintered using an FSM-05SV arc fusion splicer (Fujikura, Tokyo, Japan). In all cases, the final bed length (Lbed) of the capillaries was ~200 mm. Finally, the packed capillaries were cut directly at the inlet frit and the outlet frit and were examined with a MH 300 light microscope (VWR International, Darmstadt, Germany) for faulty frits and packing defects.

5.3.3 Chromatographic Characterization. Plate height curves (plate height H vs. average mobile phase velocity u_{av}) were acquired using an 1100 series HPLC system from Agilent Technologies (Waldbronn, Germany) consisting of a degasser, a nanopump, and a diode-array UV detector. The system was controlled by Agilent ChemStation software. Manual sample injection was performed via a two-position injection valve with a 4 nL internal loop (Model CN4 from Vici AG Valco Europe, Schenkon, Switzerland). The loop was flushed using a syringe (Hamilton, Reno, NV). An interfacing capillary (15 µm i.d., 90 cm length) connected the nanopump outlet with the injection valve. For detection, a fused-silica capillary (50 µm i.d.) was utilized as UV capillary cell. The total length of this capillary (from the column outlet to the detection window) was fixed at 10 cm. A flow metering device (Model SLG-1430-025, Sensirion, Staefa, Switzerland) was installed behind the analytical system to measure precisely the actual volumetric flow rates. All experiments were carried out at 298 ± 1 K under isocratic elution conditions.

The mobile phase consisted of water/ACN 20/80 (v/v). Thiourea served as dead-time marker and as unretained tracer (1 mg/mL) detected at 210 nm. Plate heights were calcu-

lated by the method of moments. The first and second moments (M_1 and M_2) of the peaks were estimated by fitting each individual peak with an exponentially modified Gauss function. Due to the relatively small volume of the packed capillaries, the effect of the extracolumn volume becomes significant for the performance of the columns. Therefore, extracolumn band profiles were recorded by connecting the detection capillary directly with the injector. The first and second moments ($M_{1,\mathrm{extra}}$ and $M_{2,\mathrm{extra}}$) of thiourea with this configuration were estimated and the column HETP was then calculated according to [17]

$$H = L_{\mathrm{bed}} \frac{M_2 - M_{2,\mathrm{extra}}}{\left(M_1 - M_{1,\mathrm{extra}}\right)^2} \qquad \text{(Eq. 5.4)}$$

While extracolumn contributions to band broadening could be accounted for by following this procedure, we note that possible effects of the sintered frits are still included in the final plate height data. Three successive injections were made for a given column and flow rate and the plate heights averaged to account for the error from manual injection.

5.3.4 Microscopic Imaging. Images were acquired with a TCS SP5 confocal microscopy system equipped with a HCX PL APO 63×/1.3 GLYC CORR CS (21°) glycerol immersion lens (Leica Microsystems, Wetzlar, Germany) by focusing into a capillary segment where the polyimide coating was removed with a drop of warm sulfuric acid. For a fluorescent signal the C18 modified particles were stained with Bodipy 493/503 prior to imaging by pumping an acetone solution of this dye (0.5 mg/mL) through the capillaries until an intensely colored droplet formed at the column outlet, indicating that the column was flushed with excess dye [31]. Subsequently, the dye solution was flushed out of the column using a fused silica refractive index matching liquid composed of glycerol/DMSO/water 70/19/11 (v/v/v), leaving the dye adsorbed onto the particles' surfaces. The liquid was calibrated to a refractive index of n_{D} = 1.4582 with an AR200 digital refractometer (Reichert Analytical Instruments, Depew, NY), matching the refractive index of the silica based particles and the fused silica capillary wall. The capillaries were fixed on microscope slides and immersed into the fused silica refractive index matching liquid to avoid aberration of the fluorescence signal by focusing through the curved surface of the capillary walls. An optical setup that allows to record optical slices at the diffraction limit independent from

sampling depth was then realized by applying a “type 0” coverslip (Gerhard Menzel, Braunschweig, Germany) and exchanging the immersion medium of the microscope lens with the fused silica refractive index matching liquid as well. A detailed discussion of this setup and the optimization procedure can be found in a previous paper [28].

To achieve a high level of depth discrimination during optical sectioning the pinhole of the microscope was set to 0.5 AU. Excitation of the fluorophore Bodipy 493/503 was performed with a 488 nm Argon laser. Fluorescence emission was detected in the interval 491–515 nm which yields an approximate lateral resolution of 169 nm and an axial resolution of 470 nm [31,35]. Stacks of 150–200 images were recorded perpendicular to the capillary axis close to the center of the capillary, covering its entire diameter and at least 70 µm in the direction of the capillary axis. Sampling of the images was performed well below the Nyquist sampling rate at a scanning step size of 30 nm laterally and 126 nm along the optical axis, covering a volume of approximately 100 µm × 70 µm × 20 µm.

5.3.5 Image Processing and Capillary Reconstruction. All images were corrected for Poisson-distributed photon noise of the detection system by applying the PureDenoise plug-in for ImageJ [36] provided by Luisier [37]. The decay of the signal intensity along the optical axis was corrected by fitting a secondorder exponential decay to a region of interest in the center of the capillary. Subsequently, Huygens maximum likelihood iterative deconvolution (Scientific Volume Imaging, Hilversum, The Netherlands) was applied for image restoration yielding images of improved contrast and resolution. An exemplary optical slice before and after these processing steps, illustrating the improvements in signal-to-noise ratio and contrast [28,31], is shown in Fig. 5.1.

Further processing steps were conducted using custom software written in Microsoft Visual Studio 2008 C# (Microsoft Corporation, Redmond, WA). Images were rotated to

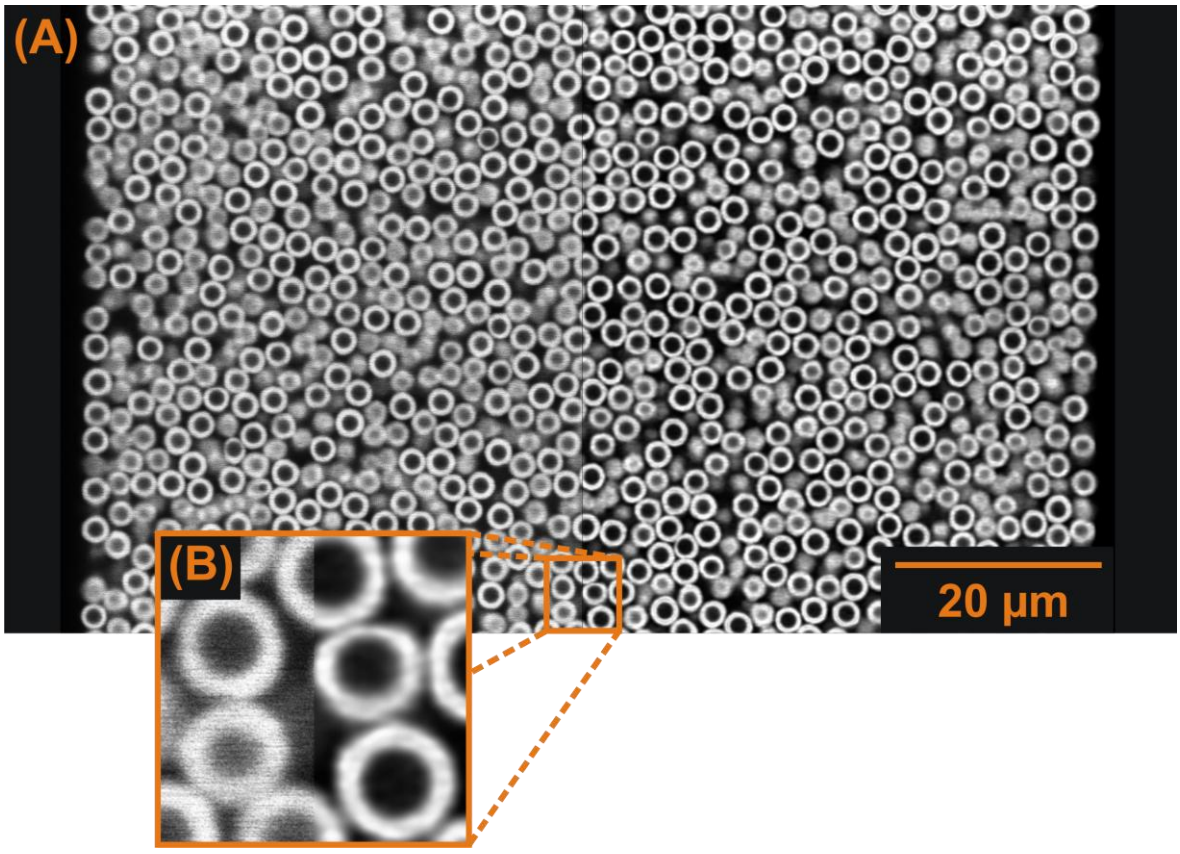

Figure 5.1: Optical slice through the center of a 100 µm i.d. cylindrical fused silica capillary packed with 2.6 µm Halo particles (**A**). The left side of the images shows the slice before image processing and the right side afterwards. For a better illustration of the improvements in signal-to-noise ratio and contrast a zoom into a 7 µm × 7 µm region is also shown (**B**).

align the column with the borders of the image stack. A potential drift of the column was corrected for by assuming a perfect cylindrical layout of the capillary. This also allowed a fine-tuning of the z-step (effective slice-to-slice distance of the two-dimensional images).

The centers of fully porous particles were detected by their property of defining high-intensity regions of low signal variance. For this purpose the image stacks were duplicated. An unsharp mask followed by thresholding was applied to one of these stacks. Then the other stack was variance-filtered, thresholded, and inverted. A logic AND operation provided clusters whose three-dimensional centroids defined the locations of particle centers [31]. The centers of core–shell particles were identified by a bandpass filtering technique presented in [28], providing a list of all particle centers in the captured capillary volume. Since the cores of the core–shell particles are nonporous no dye was adsorbed leaving dark

spots in the recorded images. Therefore, recorded image stacks of the core–shell particles were subjected to a three-dimensional watershed transformation prior to the next processing step. Seed locations for the watershed transformation were the detected particle centers, marking the core region of the particles in the images as foreground.

The size of a particle was determined by a variation of the particle center while looking for the 'best fitting' particle size, as described in [31]. A three-dimensional reconstruction was achieved by assuming perfect sphericity of the particles and coloring the images in a binary representation, with the foreground of the images defining solid phase and the background of the images defining void phase (Fig. 5.2). In a segmented image the external porosity is defined as the ratio of background voxels divided by the total amount of voxels in the considered volume segment. The capillary walls confining the reconstructions were defined to be the rows of voxels parallel to the capillary axis with a porosity larger than 0.99. Additionally, all reconstructions were cropped at their unconfined image borders to avoid unregistered particles to be part of the analyzed capillary volume.

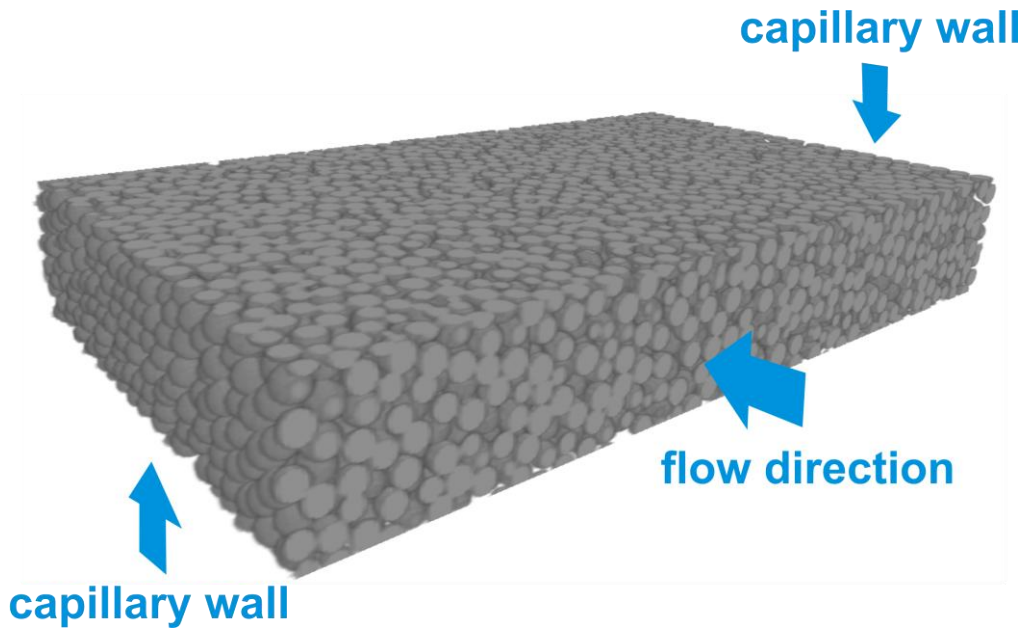

Figure 5.2: Volume rendering of a reconstructed packing of 2.6 µm Halo particles in a 100 µm i.d. cylindrical fused silica capillary as applied in the morphological analysis. The reconstruction covers a capillary segment of 100 µm × 58 µm × 15 µm.

5.3.6 Morphological Analysis. To characterize the size of the interparticle flow-through pores and their heterogeneity chord length distributions (CLDs) of 10^6 chords were calculated from random seed locations in the void region of each reconstructed capillary segment, as described by Courtois et al. [38]. From each location 32 angularly equispaced vectors were projected until they either hit a particle's surface or projected out of the image boundaries; the latter case was followed by discarding the chord, while in the former case a pair of opposing vectors was collected and recorded, effectively describing a linear particle-to-particle distance in the reconstructed bed. The resulting chords were binned at a bin size of 0.1 µm and a k–Γ function was fitted to the histogram using the Levenberg–Marquardt algorithm [39]. An exemplary distribution is shown in Fig. 5.3 [28–30].

The interparticle void volume fraction or external bed porosity ε of the reconstruction was computed by dividing the amount of background voxels by the total amount of voxels in the examined volume segment. In the following, ε_{ext} refers to the average external porosity of the whole reconstruction, $\varepsilon(r)$ denotes the local porosity at radial position r in a column, and ε_{bulk} is the bulk value calculated as the mean in the region from $r = 10\ d_p$ (i.e., sufficiently far away from the wall) to $r \approx 50$ µm, which is the capillary center. For transcolumn porosity profiles a two-dimensional projection of the porosity was calculated along the column axis, which was then processed into a one-dimensional profile using a radial transformation based on the Euclidean distances of the projection from the allocated capillary wall. Finally, all data points were smoothed with a moving window of 0.1 µm to provide a continuous radial porosity profile (cf. Fig. 5.3).

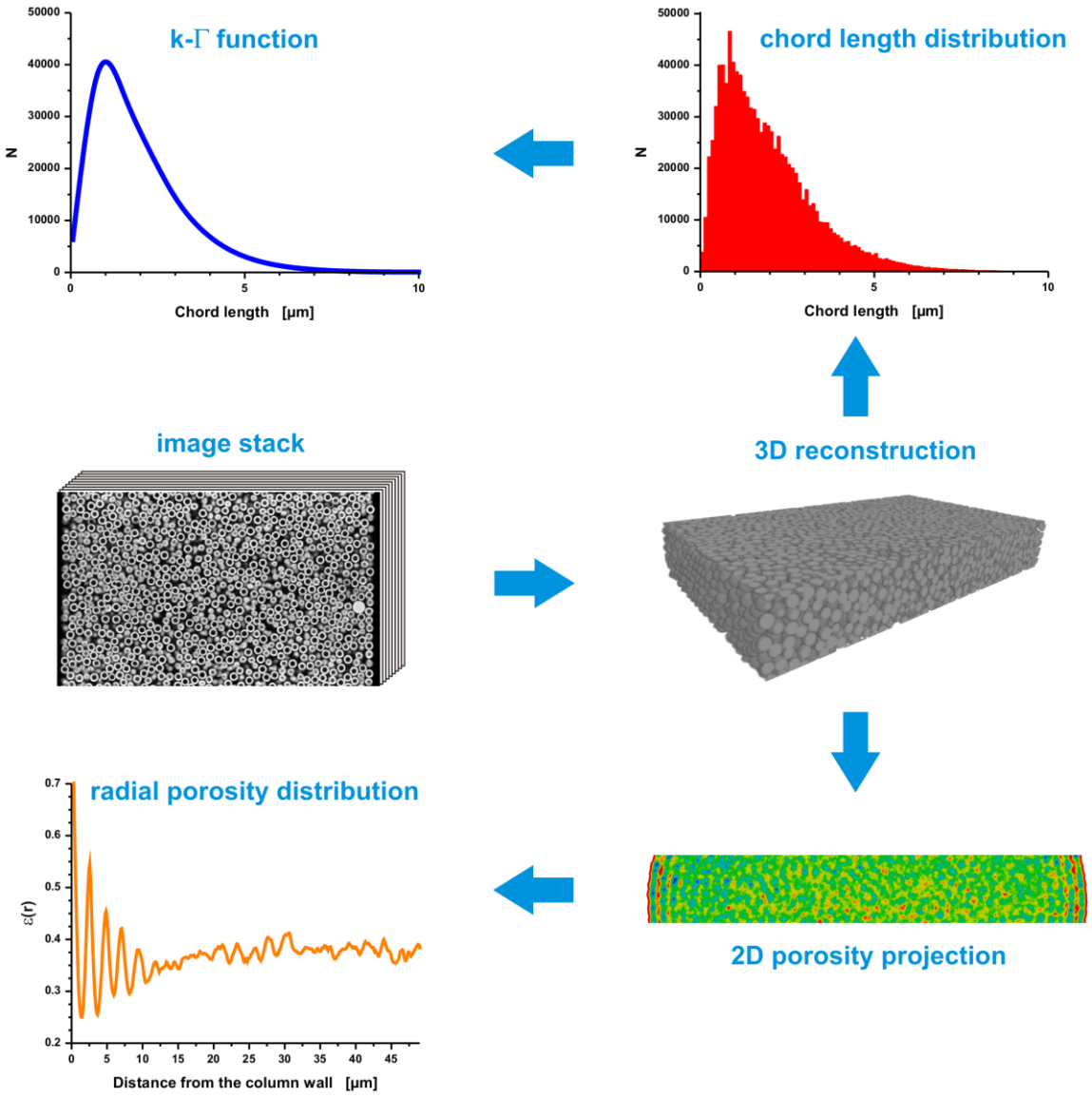

Figure 5.3: Workflow of the reconstruction analysis. An image stack of 100–200 images is recorded and reconstructed to give a central capillary segment covering the entire diameter of the capillary (cf. Fig. 5.2). A chord length distribution from 10^6 chords is fitted with a *k*–*Γ* function, providing information about the mean pore size and the statistical dispersion of the pore size distribution. A two-dimensional projection of the bed porosity (i.e., averaged along the column axis) allows to create a radial porosity distribution $\varepsilon(r)$, providing information about flow inequalities present on the transcolumn length scale.

5.4 Results and Discussion

5.4.1 Particle Properties. The particles studied in this work are fully porous Atlantis, Luna, and Zorbax particles as well as core–shell Halo, Kinetex, and Poroshell particles. Besides the obvious difference in their intraparticle morphology the width of the PSD is the most apparent variation between these particle types. Due to their manufacturing process the fully porous particles have relatively wide PSDs with a RSD of 9.4–18%. The core–shell particles, in contrast, are produced by coating monosized nonporous beads with a porous shell and the RSD of their PSDs is much smaller (2.8–6.0%). Individual PSDs attained from CLSM and scanning electron microscopy (SEM) images are presented in Fig. 5.4. Their statistical parameters are summarized in Table 5.1. Recent simulation studies from our group have shown that reducing the PSD's RSD for a particulate stationary phase from 25.3% to 3.4% in bulk (unconfined) packings decreases eddy dispersion only by an amount that is negligible in chromatographic praxis [13], i.e., $\Delta h < 0.1$ (at identical external bed porosity); this was already discussed in the Introduction. Therefore, the heterogeneity in the bulk properties of the investigated packings should be almost indiscernible. If there is an intrinsic advantage of a narrow PSD it rather has to result from the interplay of the particles with the confining column wall and the ordering of the particles in its vicinity. Consequently, morphological differences that affect the separation efficiency should become evident on the transcolumn length scale. The packing density is the parameter with the highest impact on the column permeability and flow velocity inequalities [13,20,22,24–26]. Therefore, transcolumn heterogeneities have to be visible in sufficiently resolved radial porosity profiles, which we acquired from the recorded CLSM images.

Since light microscopy is diffraction-limited CLSM cannot resolve the surface roughness of the particles. Alongside the PSD the surface roughness of the particles is another parameter that could have a noticeable effect on the bed morphology. Surface roughness contributes to shear stress of the particles with the column influencing the bed morphology near the wall, whereas particle–particle shearing affects the bulk morphology of the bed [9,12]. The insets in Fig. 5.5 show SEM images of an exemplary particle for each particle type. The manufacturing process of the core–shell particles typically yields surfaces that are at least slightly rough, as for Kinetex and Poroshell particles, whereas the fully porous particles are often very smooth (Atlantis and Luna). Zorbax and Halo are the two roughest materials used in this study, but these are mere qualitative observations and studies that quantify the roughness of the particles (e.g., by means of atomic force microscopy) are required.

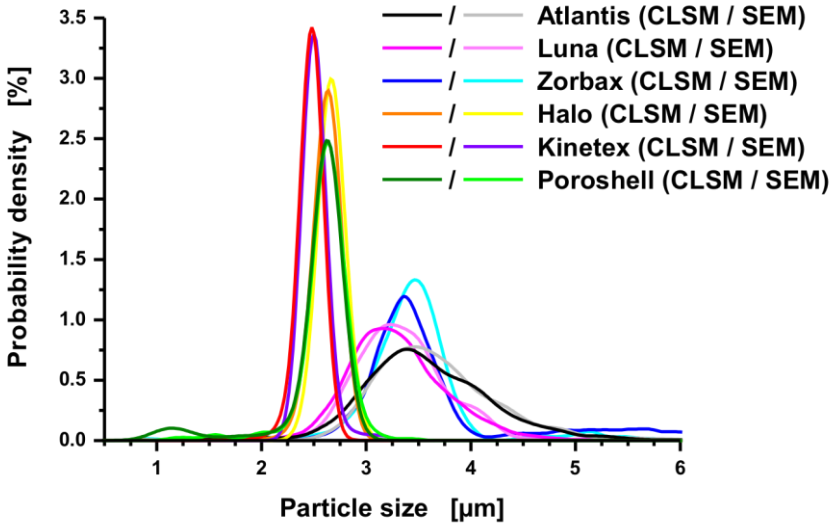

Figure 5.4: Particle size distributions (PSDs) of the employed packing materials. SEM based PSDs were obtained from a probability density estimate using the diameters of 200 particles determined manually. For the CLSM based PSDs a probability density estimate of the distribution was made on the reconstructed particles: 3.5–6.0 × 10^3 particles were used for the larger fully porous particles and 8.4–12.7 × 10^3 particles for the smaller core–shell particles.

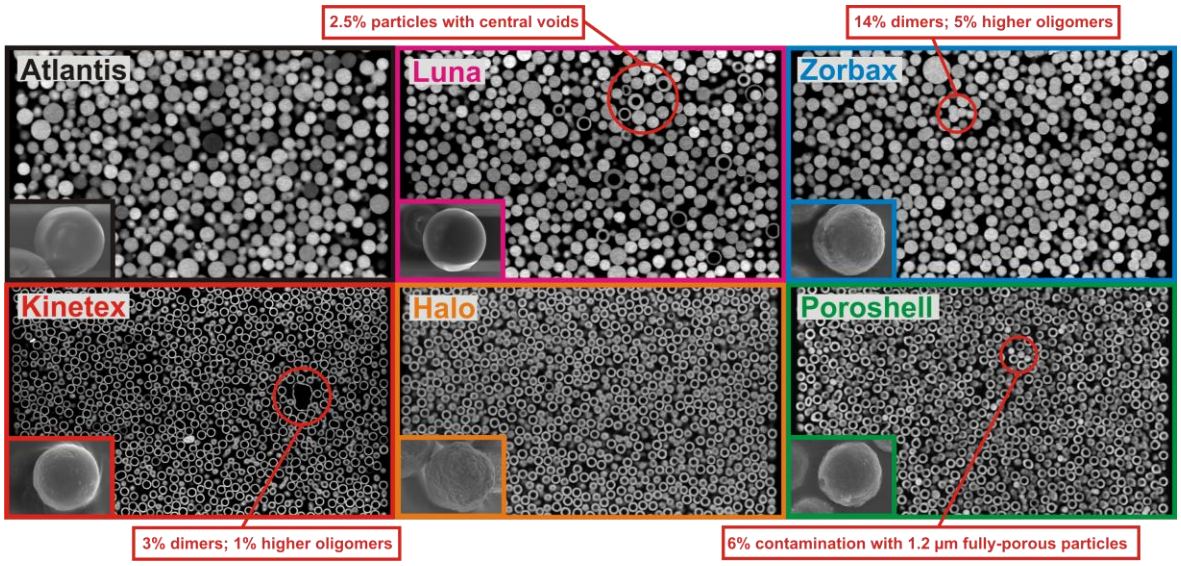

Figure 5.5: Illustration of particle characteristics in the reconstructed packings. Shown are optical slices through the center of the 100 µm i.d. cylindrical fused silica capillary columns (top row: fully porous particles, bottom row: core–shell particles). Apart from their different intraparticle porosity the core–shell particles differ from the fully porous particles primarily in the width of their PSD (cf. Fig. 5.4 and Table 5.1). The core–shell particles have PSDs with ca. 3–6% RSD, while the RSD of the PSDs for the fully porous particles is much higher (about 10–20%). The comparison of the particles in chromatographic practice is complicated by the differing surface roughness (see SEM insets in the images), the presence of agglomerated particles, and various kinds of imperfections, as noted in the figure.

Table 5.1: Morphological parameters determined from the reconstructed capillary segments. Unless stated otherwise, they were calculated for an entire reconstruction (including wall and bulk regions of the bed).

	Halo	Kinetex	Poroshell	Atlantis	Luna	Zorbax
PSD[a]						
No. of particles	8346	10100	7979	3483	3905	3846
Mean [µm]	2.62	2.48	2.53	3.58	3.31	3.33
Mode [µm]	2.64	2.48	2.63	3.38	3.16	3.36
Median [µm]	2.64	2.46	2.64	3.54	3.24	3.36
d_S [µm]	2.65	2.48	2.65	4.16	3.72	3.46
RSD [%]	4.6	2.8	6.0	18	15	9.4
CLD[b]						
μ [µm]	1.91	2.05	2.13	2.91	2.76	2.68
μ [d_p]	0.72	0.83	0.81	0.82	0.85	0.78
k	1.96	1.96	1.94	1.93	1.94	1.96
Mode [µm]	0.85	0.85	0.85	1.15	1.05	1.15
Mode [d_p]	0.32	0.35	0.32	0.32	0.32	0.34
Porosity[c]						
ε_{ext}	0.37	0.39	0.38	0.39	0.41	0.38
ε_{bulk}	0.36	0.40	0.38	0.38	0.41	0.37
IPD[d]						
Global value	–0.01	–0.14	–0.12	0.20	0.16	0.09
Wall region	0.05	–0.02	–0.07	0.22	0.17	0.12
Transition region	–0.07	–0.13	–0.06	–0.02	–0.01	–0.03

[a] All particle statistics were calculated from the distribution around the main maximum in the PSDs (cf. Fig. 5.4), ignoring contaminations and agglomerated particles (cf. Fig 5.5).

[b] A *k*–*Γ* function Eq. 5.5 was fitted to the CLDs (cf. Fig. 5.3) to analyze their mean chord length (μ) and statistical dispersion ($k = \mu^2/\sigma^2$, where σ is the statistical standard deviation of a CLD):

[c] Bulk porosity was calculated from all foreground and background voxels that were at least at 10 d_p distance from the capillary wall, i.e., ε_{bulk} refers to radial positions $r \geq 10\ d_p$ ($r = 0$ at the column wall), and ε_{ext} is the average external porosity of the whole reconstruction.

[d] To split the IPD (Eq. 5.6) into contributions from different regions in a packing the wall region was defined to extend by 5 d_p into the bed ($0 \leq r \leq d_p$); the transition region was defined to range from a distance of 5 d_p from the column wall up to 10 d_p into the bed ($5\ d_p \leq r \leq 10\ d_p$).

Some additional qualitative differences between the particles are already apparent from a visual inspection of the CLSM and SEM images recorded during this study. The features are superimposed on any PSD effect. These specific particle properties are illustrated with Fig. 5.5. Notably, Atlantis and Luna packings show an increased variability in the particle-to-particle fluorescence intensity when compared with the fully porous Zorbax particles (top row in Fig. 5.5) and the fully porous 1.7 µm Acquity BEH particles from our previous study [31]. While the Atlantis and Luna particles show a particle-to-particle signal intensity variation of 19–21% RSD, the signal intensity of the Zorbax and Acquity particles only varied by 11–13%. Since all capillaries were saturated with the fluorescent dye prior to imaging this indicates a lower regularity in the adsorption properties for the former particle types, which may result from a mixing of batches with slightly different C18 surface coverage and/or different properties of the intraparticle mesopore space.

Further, in the Luna column 2.5% of the particles appeared with a non-fluorescent core region. So, these particles are only partially mesoporous with a nonporous solid or void core region (which is indistinguishable by CLSM). Some of these particles were only composed of a hollow porous shell with another particle located inside, suggesting a void core region for these 2.5% of the particles. Such voids were also observed in a recent study by Kane et al. [40] for Fusokk and Kromasil silica particles using focused ion beam sectioning. Zorbax and Atlantis particles did not show any void cores, but Zorbax particles were frequently merged to form agglomerates of two or more particle bodies; a feature the Zorbax particles primarily share with Kinetex particles (Fig. 5.5). Yet, the amount of present dimers is considerably lower for Kinetex while the irregular shaped agglomerates would frequently be composed of more than a dozen particles, taking up a significant bed volume.

In the Poroshell packing we found 6% fully porous particles of ~1.2 µm diameter. We eliminated the possibility of a contaminated packing apparatus by repeating the packing and imaging steps. A plausible explanation could be that we are either dealing with spalled shells of particles that did not withstand the pressure during slurry packing, or that these particles formed as fully porous particles during the coating of the solid cores with the shell.

5.4.2 Pore Scale Properties. We start our analysis of heterogeneities in the reconstructed packings by looking at the transchannel and short-range interchannel length scales in these beds (individual pore scale and local packing disorder, respectively). The CLDs can characterize the pore space of the packings [28], and opposed to mercury intrusion porosity (MIP), which assumes a cylindrical pore in the calculation of pore sizes, the CLDs do not require any assumption on the pore shape. This property enabled us to apply CLDs to reconstructions of monolithic materials in recent publications and compare their pore sizes and heterogeneity [27,29,30]. A CLD is a statistical distribution of the linear surface-to-surface distances. In the current work, this applies to the interparticle void space of the packings. The random porous adsorbents used as chromatographic beds are materials with a correlative disorder, i.e., the CLD is an unimodal distribution [41,42]. Its mode describes the typical correlation length in the material, which compares well with pore size measures acquired by MIP [27]. Chords that stretch from pore to pore provide a tail to the distribution. Heterogeneities in the packing contribute to widen the CLD. We found that CLDs for packed beds and silica monoliths can be well described by a *k*–*Γ* function [28–30,43,44]

$$f(l_{\mathrm{chord}}) = \frac{k^k}{\Gamma(k)} \frac{l_{\mathrm{chord}}^{k-1}}{\mu^k} \exp\left(-\frac{k \cdot l_{\mathrm{chord}}}{\mu}\right) \qquad \text{(Eq. 5.4)}$$

where l_{chord} denotes chord length, μ is a first-moment parameter provided by the mean chord length, k relates to the statistical dispersion of the CLD (it is defined by μ and the statistical standard deviation σ of the distribution: $k = \mu^2/\sigma^2$), and $\Gamma(k)$ is the gamma function. Thus, Eq. 5.5 provides a descriptor for the size of the flow-through pores in a packing (μ), which reflects the transchannel scale of eddy dispersion, and a parameter for the packing homogeneity (k) on a length scale of 1–2 d_p, which reflects the short-range interchannel scale of eddy dispersion [28–30,43,44].

Table 5.1 summarizes parameters μ and k computed as global averages, i.e., for the entire reconstruction. Notably, the reconstructed beds yield almost identical values for μ and the mode if normalized by the length mean particle diameter. The Halo packing was the densest bed and formed the only exception (here, the value for μ was 0.7 d_p compared to 0.8 d_p for the other reconstructions). The values of k for all packings were found to range from 1.93 to 1.96. Their variations are negligible compared to those we found for different

monolithic materials [29]. In that study eleven hybrid silica capillary monoliths were analyzed by their CLDs. The size of the flow-through pores was the most important factor for the separation efficiency of the monoliths (μ ranged from 3.6 to 5.7 µm). The variation of k was ten times higher than in the present study (k ranged from 2.23 to 2.51). Still, a noticeable correlation with separation efficiency was not observed, but capillary monoliths that performed worse than expected from their mean pore size displayed heterogeneities on the transcolumn length scale. Therefore, the data obtained for the packings in the current work (μ and k in Table 5.1) and their implications agree with the simulation study of Daneyko et al. [13], i.e., there are no systematic differences in the short-range disorder and bulk bed morphology identifiable with the CLD method that would explain a superior kinetic performance of the core–shell packings, or even an intrinsic advantage of a narrow PSD in that respect.

5.4.3 Transcolumn Porosity Profiles. The Kozeny–Carman equation shows that porosity is the single most important contributor to the permeability of a packing [13]. Any porosity biases over the column cross-section directly translate into velocity biases causing eddy dispersion [18–25]. A well resolved porosity profile along the diameter of a column is an efficient tool to estimate eddy dispersion contributions on the transcolumn length scale [22,24,31,45]. We found that capillaries packed with 1.7 µm Acquity BEH particles showed a disproportionate increase in transcolumn eddy dispersion (cf. $\omega_3 v$ in Eq. 5.2) when the aspect ratio was increased above $d_c/d_p \approx 20$ [31]. The radial transcolumn porosity profiles of these packings were found to decline from the capillary wall-bed interface toward the bulk region of the columns. Better performance of a column implied a denser packed wall region with fewer defects in the bed. Larger voids in the packings were primarily located next to the capillary wall, providing preferential flow paths. Simulations by Schure and Maier [46] have illustrated that the presence of systematic defective positions in a packing has a stronger impact on eddy dispersion than randomly distributed defects. While the former ordering of defects, e.g., their systematic placement next to the column wall, describes an increase in transcolumn heterogeneity, the latter random distribution of defects introduces heterogeneity on smaller length scales in a packing.

Fig. 5.6 shows radial porosity distributions that were computed for the reconstructed columns applied in this study. To obtain a quantitative description of the heterogeneities in the observed profiles we adapted the integral porosity deviation (IPD) parameter we intro-

duced in [31]. This is done by summation of all porosity deviations from the bulk porosity value of a bed (ε_{bulk}) in its radial porosity profile:

$$\mathrm{IPD} = \int_0^{0.5d_c} (\varepsilon(r) - \varepsilon_{bulk})\, dr \qquad \text{(Eq. 5.4)}$$

where r is the radial position in a reconstruction with respect to the column wall; r was scaled by d_p in Fig. 5.6 to generate comparable results. $\varepsilon(r)$ is the local external porosity and ε_{bulk} is the bulk porosity calculated as the mean in the region from r = 10 d_p (sufficiently far away from the wall) to $r \approx 50$ µm, which is the capillary center. The IPD is a simple scalar measure that characterizes radial porosity distributions by their local deviations from ε_{bulk} and integrates over all porosity inequalities $\varepsilon(r)$–ε_{bulk} from the column wall (r = 0) to the center of the bed ($r = d_c/2$). It is a descriptor of transcolumn porosity heterogeneities: the larger the porosity difference between the wall and the bulk region of a packing, the larger the IPD.

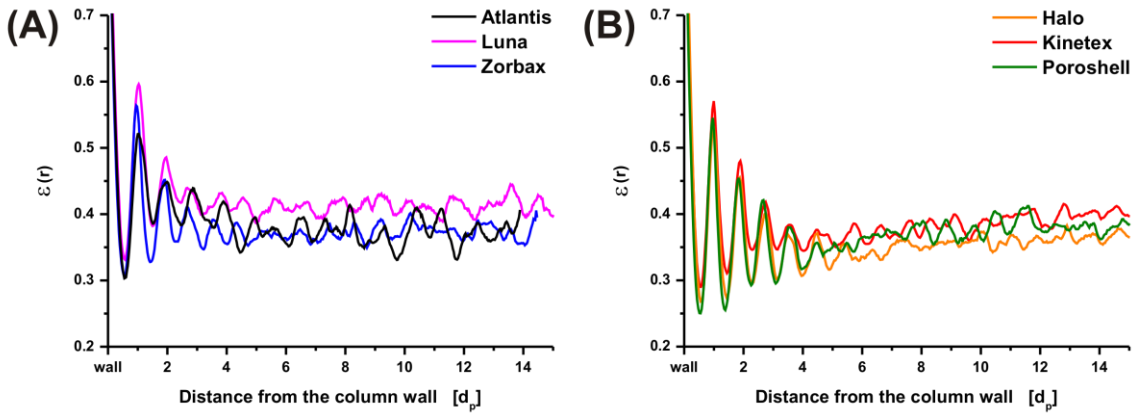

Figure 5.6: Radial porosity profiles $\varepsilon(r)$ of the reconstructed capillaries packed with wide-PSD fully porous particles (**A**) and narrow-PSD core–shell particles (**B**), covering a distance from the capillary wall (r = 0) into the bulk structure of the beds. The radial distance r is scaled by d_p to generate comparable results.

Table 5.1 provides ε_{bulk} and the IPD values that were computed for the different beds in this study. Higher bulk porosities of ε_{bulk} = 0.41 and 0.40 were recorded for the Luna and Kinetex columns, respectively. This did not affect the overall shape of their porosity profiles, but shifted them upwards (Fig. 5.6). The contribution of the bulk packing region to the IPD is zero by definition. In case of the fully porous materials (Atlantis, Luna, and Zorbax) the resulting global IPD value was always positive and dominated by the deviations from bulk porosity that take place in a region of ~5 d_p next to the capillary wall, which is the region governed by the geometrical wall effect. We could not identify larger voids next to the capillary wall in these sonicated beds. Nevertheless, the positive IPDs of 0.20, 0.16, and 0.09, respectively, illustrate that the wall region in these beds is looser packed than the bulk, which confirms our previous findings for the low-aspect ratio ultra-high pressure liquid chromatography capillary columns packed with wide-PSD 1.7 µm Acquity BEH particles [31].

In case of the reconstructions prepared from the narrow-PSD Halo, Kinetex, and Poroshell packings the amplitudes of the porosity oscillations in the ~5 dp wide immediate wall region are larger and distributed closer around the bulk porosity ε_{bulk} than for all studied fully porous packings, as summarized in Fig. 5.7. This demonstrates

(i) a more regular morphology next to the column wall for the core–shell materials, which is expected for a narrower PSD [47] and

(ii) that packing density in the wall region is higher (and therefore closer to the bulk density) for the core–shell than for the fully porous particles. It is also seen in the IPD contribution from the wall region that is closer to zero for the narrow-PSD than for the wide-PSD materials (Table 5.1).

In our experiments the absolute value of the wall IPD contribution decreased monotonically with the PSD's RSD irrespective of the particle type. For example, the fully porous particle type with the narrowest PSD (Zorbax) showed the most pronounced porosity oscillations in the group of the wide-PSD materials.

The global IPD of the core–shell packings was also always negative (Table 5.1), but differed substantially from their wall IPD contribution. It is therefore not possible to describe porosity profiles of the core–shell packings by just a random bulk region plus an ordered wall region. For all core–shell packings we additionally identified a transition region between wall region and the bulk packing region that introduces further heterogeneity

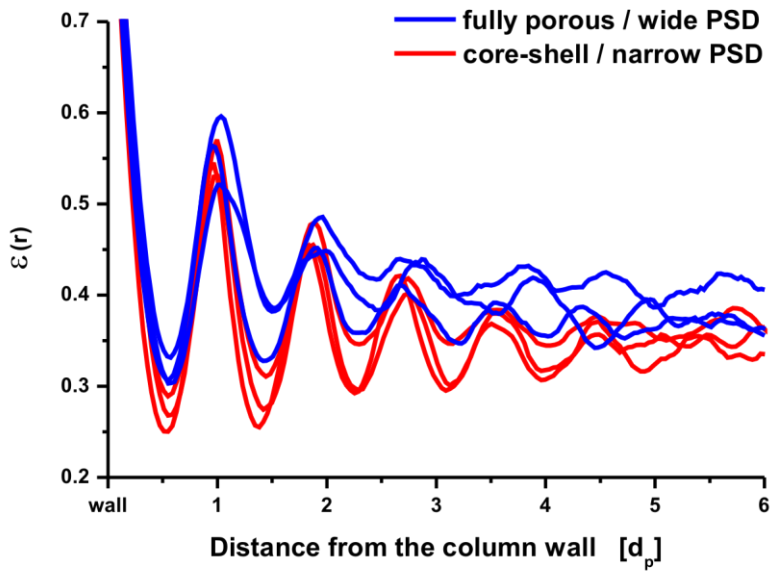

Figure 5.7: Radial porosity profiles $\varepsilon(r)$ in the critical wall region that is dominated by the geometrical wall effect ($0 \leq r \leq 5\ d_p$). The wide-PSD fully porous particles and narrow-PSD core–shell particles are grouped for a better visualization and comparison of the packing density near the column wall-bed interface. Porosity oscillations for the core–shell particles are larger and distributed closer around the bulk porosity ε_{bulk} (indicating a more ordered and denser packing) than with the fully porous particles. The radial distance r is scaled by d_p to generate comparable results.

in the radial porosity profile. This transition region ranges from a distance of ~5 d_p from the column wall up to 9–10 d_p into the beds and was always denser packed than the bulk region, as shown in Fig. 5.8 (see yellow region in Fig. 5.8B). It provides a "parabolic shape" to the porosity profile that we have already seen in a previous study with Kinetex particles [28]. In the present work the largest negative contribution from the transition region to the global IPD was found in the loosely packed Kinetex column. However, a transition region is virtually non-existent in the wide-PSD Luna column, which was also loosely packed (Fig. 5.6A). We currently do not understand the origins of this transition region with the narrow-PSD packings (Fig. 5.8B). Apparently, the presence of a pronounced transition region might result from increased repulsive forces and shear stress during slurry packing that prohibit the formation of a dense bulk packing [9,12], whereas the bed morphology in the ~5 d_p wall region of the column is dominated by the geometry of the applied particles. Therefore, one of our next studies will focus on the bed morphology for a smooth

narrow-PSD material, e.g., a column packed with the new Titan monodisperse porous silica particles from Supelco (Bellefonte, PA). If such materials do not show a pronounced transition region in their radial porosity profiles, this will indicate a shear stress effect in the core–shell packings and yield a further systematic improvement in bed morphology for more efficient separations.

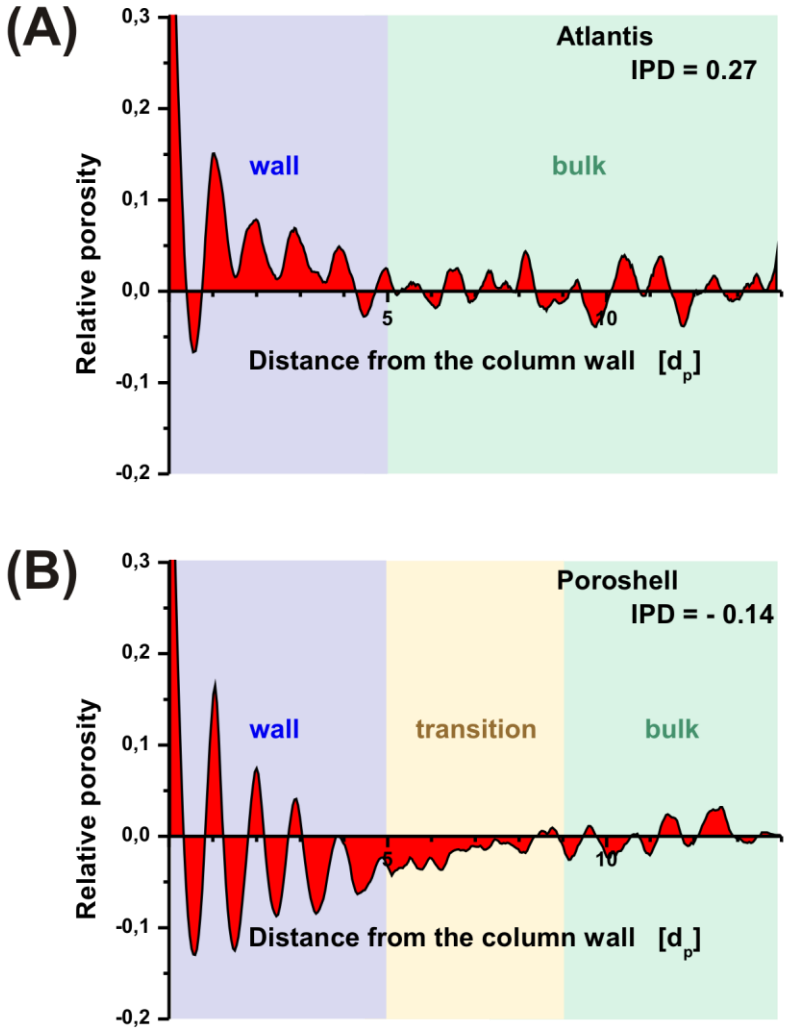

Figure 5.8: Representative radial porosity profiles, as displayed by the relative porosity $\varepsilon(r)–\varepsilon_{bulk}$, for a capillary column packed with wide-PSD fully porous particles (**A**) and a capillary column packed with narrow-PSD core–shell particles (**B**). The color-coded background illustrates the different bed morphologies: blue indicates the region affected by the geometrical wall effect, yellow signals a transition region, and green labels the bulk packing region.

To summarize, the core–shell particles pack with heterogeneities that are less pronounced than in packings obtained with the fully porous particles: For the narrow-PSD materials their absolute IPD values in the considered wall and transition regions (cf. Table 5.1) are smaller than the absolute IPD values in the wall region of the columns packed with the wide-PSD materials. This is certainly beneficial to the reduction of transcolumn eddy dispersion also in analytical columns since the maximum flow velocity disparity is reduced. On the other hand, transcolumn heterogeneities in the core–shell packings reach by ~10 d_p into the bed and cover a larger volume than in packings obtained with fully porous particles, where heterogeneities reach by ~5 d_p into the bed. This might be especially problematic with typical aspect ratios in capillary columns ($d_c/d_p < 50$). To illustrate the impact of an increased heterogeneous volume in a capillary (as observed here with the core–shell particles) we assume a 100 µm i.d. column packed with 2.6 µm core–shell particles: a 5 d_p wide wall region covers 45% of the total bed volume, whereas a 10 dp wide region already occupies 77%. In a 4.6 mm i.d. column packed with 2.6 µm particles these values reduce to just 1.1% and 2.2%, respectively. Thus, it seems unsurprising that we failed to pack a highly efficient capillary column with core–shell particles up to this point; also, we are unaware of any work that claims this achievement. Fig. 5.9 shows reduced plate height curves of thiourea under kinetic conditions for the capillaries used in the morphological analysis. In-line with the results of our morphological analysis we do not see a systematic advantage for capillaries packed with core–shell particles over those packed with fully porous particles. Aspect ratios range from d_c/d_p ~28 for the Atlantis column up to ~40 for Kinetex and Poroshell columns. At these aspect ratios, h_{min} values from 2.2 to 2.6 for Atlantis, Halo, and Poroshell columns are comparable to the h_{min} values achieved in [31] with an optimized experimental setup. The poorer performance of the Kinetex and Luna columns can be simply explained by their looser packed bulk region ($\varepsilon_{bulk} \geq 0.40$, cf. Table 5.1) [13]. In essence, the core–shell particles show a different bed morphology for the wall region in 100 µm i.d. capillary columns than the fully porous particles. However, at these low aspect ratios the observed morphological differences do not result in a clear improvement of separation efficiency for the core–shell particles, as reported with analytical columns.

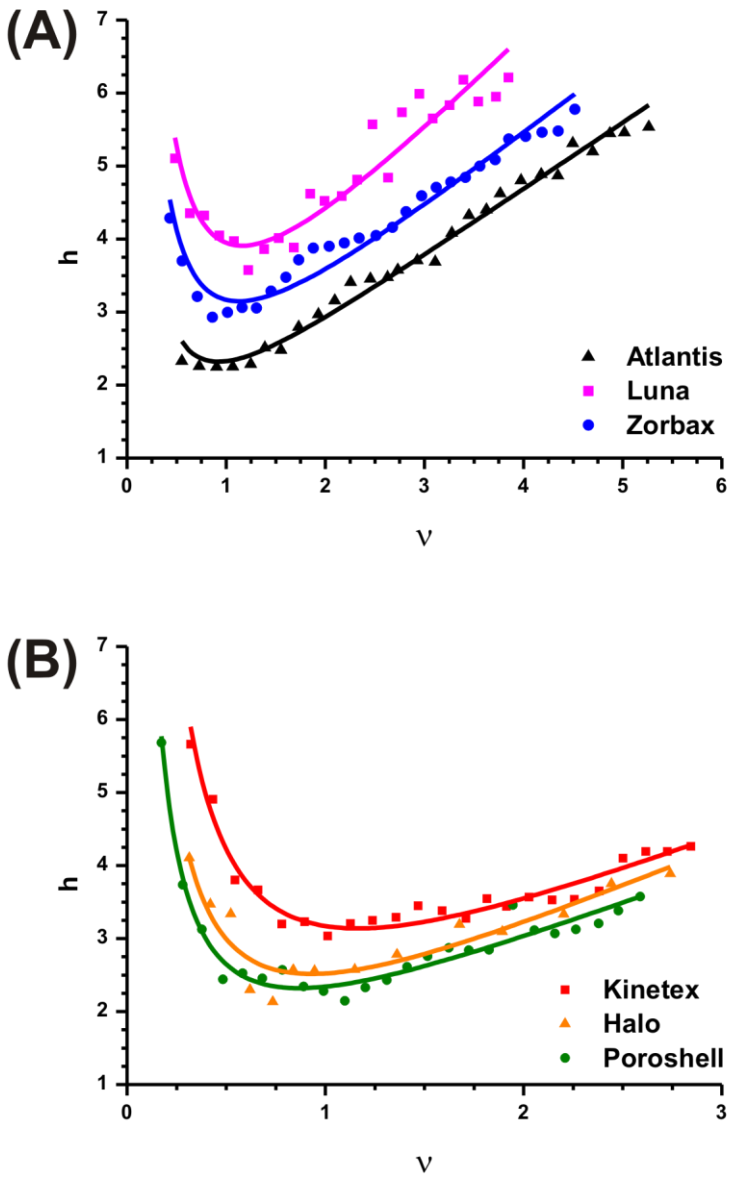

Figure 5.9: Reduced plate height curves (reduced plate height $h = H/d_S$ vs. reduced velocity $v = u_{av}d_S/D_m$) of thiourea (unretained; $D_m = 2.0 \times 10^{-9}$ m^2s^{-1}) for 100 µm i.d. fused-silica capillaries packed with wide-PSD fully porous particles (**A**) and with narrow-PSD core–shell particles (**B**). Solid lines represent best fits of Eq. 5.2 to the *h*–*v* data. Mobile phase: water/ACN 20/80 (v/v).

5.5 Conclusions

Our observations illustrate that the maximum velocity inequality caused by transcolumn heterogeneities is smaller in packed beds of narrow-PSD core–shell particles than in those prepared from wide-PSD fully porous particles. This originates in a different transcolumn bed morphology. The fully porous particles are always looser packed in the wall region than in the bulk, whereas the core–shell particles pack denser and with a higher regularity in the first few particle layers next to the column wall. The local porosity in the layers affected by the geometrical wall effect is closely distributed around the bulk porosity value due to the narrow PSD of the core–shell particles. However, the heterogeneous volume in these packings is increased due to the presence of a low-porosity transition region between wall and bulk regions. Overall, these findings provide an explanation why especially larger diameter analytical columns show a superior kinetic performance with these narrow-PSD core–shell particles and only a shallow increase of their plate height curves beyond the plate height minimum [8].

The CLD analysis of the reconstructed packings did not show any improved morphology for the core–shell particles characterizing their bulk properties, i.e., a denser and more regular interstitial pore network. This strengthens the findings of Daneyko et al. [13] who concluded that there is no intrinsic advantage of a narrow PSD for separation efficiency in the bulk of the packings; an idea that used to be widespread in the chromatographic community [48].

The locally higher packing densities in the region from ~5 d_p from the column wall up to 9–10 d_p into the beds, as observed for the core–shell packings (Figs. 5.6B and 5.8B), are expected to stem from a parabolic shear stress distribution across the column diameter during slurry packing [9,12]. Whether the low-porosity transition region is a result of higher shear stress caused by the particles' surface roughness or an additional PSD effect requires further experiments with smooth narrow-PSD materials. Such materials are now available as core–shell particles prepared by Omamogho et al. [49], or as the fully porous Titan particles from Supelco, and will be in the focus of our future studies.

Acknowledgments

This work was supported by the Deutsche Forschungsgemeinschaft DFG (Bonn, Germany) under grant TA 268/5-1.

References

[1] Horváth, C. G.; Preiss, B. A.; Lipsky, S. R. *Anal. Chem.* **1967**, *39*, 1422–1428.

[2] Horváth, C. G.; Lipsky, S. R. *J. Chromatogr. Sci.* **1969**, *7*, 109–116.

[3] Kirkland, J. J. *J. Chromatogr. Sci.* **1969**, *7*, 7–12.

[4] Kirkland, J. J. *Anal. Chem.* **1969**, *41*, 218–220.

[5] DeStefano, J. J.; Langlois, T. J.; Kirkland, J. J. *J. Chromatogr. Sci.* **2008**, *46*, 254–260.

[6] Kirkland, J. J.; Langlois, T. J.; DeStefano, J. J. *Am. Lab.* **2007**, *39*, 18–21.

[7] Gritti, F.; Leonardis, I.; Shock, D.; Stevenson, P.; Shalliker, A.; Guiochon, G. *J. Chromatogr., A* **2010**, *1217*, 1589–1603.

[8] Gritti, F.; Guiochon, G. *J. Chromatogr., A* **2010**, *1217*, 8167–8180.

[9] Guiochon, G.; Gritti, F. *J. Chromatogr., A* **2011**, *1218*, 1915–1938.

[10] Cabooter, D.; Fanigliulo, A.; Bellazzi, G.; Allieri, B.; Rottigni, A.; Desmet, G. *J. Chromatogr., A* **2010**, *1217*, 7074–7081.

[11] Gritti, F.; Guiochon, G. *J. Chromatogr., A* **2012**, *1221*, 2–40.

[12] Gritti, F.; Farkas, T.; Heng, J. Guiochon, G. *J. Chromatogr., A* **2011**, *1218*, 8209–8221.

[13] Daneyko, A.; Höltzel, A.; Khirevich, S.; Tallarek, U. *Anal. Chem.* **2011**, *83*, 3903–3910.

[14] Halász, I.; Naefe, M. *Anal. Chem.* **1972**, *44*, 76–84.

[15] Dewaele, C.; Verzele, M. *J. Chromatogr.* **1983**, *260*, 13–21.

[16] Gritti, F.; Cavazzini, A.; Marchetti, N.; Guiochon, G. *J. Chromatogr., A* **2007**, *1157*, 289–303.

[17] Gritti, F.; Guiochon, G. *J. Chromatogr., A* **2007**, *1166*, 30–46.

[18] Shalliker, R. A.; Broyles, B. S.; Guiochon, G. *J. Chromatogr., A* **2000**, *888*, 1–12.

[19] Maier, R. S.; Kroll, D. M.; Bernard, R. S.; Howington, S. E.; Peters, J. F.; Davis, H. T. *Philos. Trans. R. Soc. Lond., A* **2002**, *360*, 497–506.

[20] Khirevich, S.; Höltzel, A.; Hlushkou, D.; Tallarek, U. *Anal. Chem.* **2007**, *79*, 9340–9349.

[21] Abia, J. A.; Mriziq, K. S.; Guiochon, G. *J. Chromatogr., A* **2009**, *1216*, 3185–3191.

[22] Khirevich, S.; Höltzel, A.; Seidel-Morgenstern, A.; Tallarek, U. *Anal. Chem.* **2009**, *81*, 7057–7066.

[23] Guo, H.; Frey, D. D. *J. Chromatogr., A* **2010**, *1217*, 6214–6229.

[24] Daneyko, A.; Khirevich, S.; Höltzel, A.; Seidel-Morgenstern, A.; Tallarek, U. *J. Chromatogr., A* **2011**, *1218*, 8231–8248.

[25] Khirevich, S.; Höltzel, A.; Ehlert, S.; Seidel-Morgenstern, A.; Tallarek, U. *Anal. Chem.* **2009**, *81*, 4937–4945.

[26] Khirevich, S.; Daneyko, A.; Höltzel, A.; Seidel-Morgenstern, A.; Tallarek, U. *J. Chromatogr., A* **2010**, *1217*, 4713–4722.

[27] Bruns, S.; Müllner, T.; Kollmann, M.; Schachtner, J.; Höltzel, A.; Tallarek, U. *Anal. Chem.* **2010**, *8*, 6569–6575.

[28] Bruns, S.; Tallarek, U. *J. Chromatogr., A* **2011**, *1218*, 1849–1860.

[29] Bruns, S.; Hara, T.; Smarsly, B. M.; Tallarek, U. *J. Chromatogr., A* **2011**, *1218*, 5187–5194.

[30] Hormann, K.; Müllner, T.; Bruns, S.; Höltzel, A.; Tallarek, U. *J. Chromatogr., A* **2012**, *1222*, 46–58.

[31] Bruns, S.; Grinias, J. P.; Blue, L. E.; Jorgenson, J. W.; Tallarek, U. *Anal. Chem.* **2012**, *84*, 4496–4503.

[32] Gritti, F.; Guiochon, G. *J. Chromatogr., A* **2012**, *1262*, 107–121.

[33] Giddings, J. C. *Dynamics of Chromatography, Part1: Principles and Theory*, Marcel Dekker, New York, **1965**.

[34] Ehlert, S.; Rösler, T.; Tallarek, U. *J. Sep. Sci.* **2008**, *31*, 1719–1728.

[35] Wilhelm, S.; Gröbler, B.; Gluch, M.; Heinz, H. *Confocal Laser Scanning Microscopy – Optical Image Formation and Electronic Signal Processing*; Monography, Carl Zeiss: Jena, Germany, **2008**.

[36] Rasband, W. S. *ImageJ*; U.S. National Institutes of Health: Bethesda, MD, **1997-2006**; http://rsb.info.nih.gov//ij/.

[37] Luisier, F. *PureDenoise*; Biomedical Imaging Group, École Polytechnique Fédéral de Lausanne, **2010**; http://bigwww.epfl.ch/algorithms/denoise.

[38] Courtois, J.; Szumski, M.; Georgsson, F.; Irgum, K. *Anal. Chem.* **2007**, *79*, 335–344.

[39] Bochkanov, S.; Bystritsky, V. ALGLIB, www.alglib.net.

[40] Kane, D. M.; Chater, R. J.; McPhail, D. S. *J. Microsc.* **2012**, *247*, 186–195.

[41] Levitz, P.; Tchoubar, D. J. *J. Phys. I* **1992**, *2*, 771–790.

[42] Levitz, P. *Adv. Colloid Interface Sci.* **1998**, *76–77*, 71–106.

[43] Aste, T.; Di Matteo, T. *Phys. Rev. E* **2008**, *77*, 021309.

[44] Schenker, I.; Filser, F. T.; Gauckler, L. J.; Aste, T.; Herrmann, H. J. *Phys. Rev. E* **2009**, *80*, 021302.

[45] Khirevich, S.; Höltzel, A.; Seidel-Morgenstern, A.; Tallarek, U. *J. Chromatogr., A* **2012**, *1262*, 77–91.

[46] Schure, M. R.; Maier, R. S. *J. Chromatogr., A* **2006**, *1126*, 58–69.

[47] Hlushkou, D.; Seidel-Morgenstern, A.; Tallarek, U. *Langmuir* **2005**, *21*, 6097–6112.

[48] Gritti, F.; Guiochon, G. *LC–GC North Am.* **2012**, *30*, 586–595.

[49] Omamogho, J. O.; Hanrahan, J. P.; Tobin, J.; Glennon, J. D. *J. Chromatogr., A* **2011**, *1218*, 1942–1953.

Chapter 6

Morphological Comparison of Silica-Based Monolithic and Particulate Beds by Confocal Laser Scanning Microscopy

Authors:

Stefan Bruns, Alexandra Höltzel, and Ulrich Tallarek

State of Publication:

Published June 1, 2013 in *LC-GC North America*, Vol. 31, p. 486–493.

Abstract

Confocal laser scanning microscopy enables the nondestructive, three-dimensional (3D) imaging of silica-based columns. The key morphological features responsible for the kinetic column performance can then be identified directly from the physically reconstructed bed structure, independent of size and form of the underlying structural element. We demonstrate this by comparing the bed morphology of a silica monolith with that of a sub-2 µm packing in capillary column format (20 µm i.d.). Our analysis reveals the main structural problem of the silica monolith and shows the direction along which its optimization should progress to reach the kinetic efficiency of a sub-2 µm packing. The morphological monitoring enabled by this approach offers constructive guidance to any optimization efforts in the preparation of silica-based monolithic and particulate columns.

6.1 Introduction

Porous silica in the form of particulate or monolithic beds is the most popular stationary phase support for small molecule separations [1]. Monolithic columns have overcome the limitations of particulate beds with respect to permeability and mass transfer resistance, but often show disappointing separation efficiencies [2]; presently, even the improved second generation of silica monoliths [3,4] cannot compete with well-packed particulate beds [5–7].

A similar situation in which a theoretical concept has not yet brought the expected outcome in practice is the size reduction of the structural elements of a bed. Smaller particle and domain sizes do not automatically guarantee better columns, only higher back pressure [8]. Shrinking the structural elements yields more efficient columns only when the homogeneity of the bed can be conserved in the process [9–11]. The bed morphology, specifically the distribution of the interstitial void space where eddy dispersion takes place, largely determines the kinetic column performance [12–14]. The heterogeneity of a monolithic or particulate bed contributes to eddy dispersion on different length scales [15–17]: the size of the individual channels (flow-through pores) between two neighboring solid elements (transchannel contribution) [18,19], a size equivalent to 1–2 particle diameters or domains (short-range interchannel contribution) [18,19], and the column radius (transcolumn contribution) [4,7,20–23].

With particulate beds, the size of each eddy dispersion contribution can be determined from chromatographic data and linked to the respective morphological features [14,23,24]. The method cannot be readily transferred to monolithic beds because the theory of eddy dispersion was first developed for discrete spheres as the underlying structural elements [15]. This does not mean that the origins of eddy dispersion are fundamentally different in monolithic beds, only that the comparison of particulate and monolithic beds by their column efficiency and hydraulic permeability cannot get at the morphological roots of the observed chromatographic output [25–28]. The same applies to comparative studies of silica-based monolithic columns with different domain sizes, for example, in efforts to reduce the macropore size [29–31]. For particulate beds, the particle size is used as a normalization parameter when comparing the chromatographically determined efficiencies of individual columns. This normalization works because the size of the particles and that of the interstitial flow-through pores are in a fixed relationship, so that when the size of the particles is reduced, the size of the flow-through pores also decreases. But the corresponding elements of a monolithic bed, skeleton thickness and macropore size, can be altered independently [2]; therefore, the domain size, although often treated as the analog of the particle size, is not a suitable normalization parameter for monolithic beds.

Yet, the morphology of particulate and monolithic beds can be analyzed through three-dimensional (3D) imaging methods: With local resolution, image analysis delivers an accurate characterization of the interstitial void space from individual pores up to the column cross-section. In our group, we have used confocal laser scanning microscopy (CLSM) for

silica-based (hard) materials [4,7,32–35] and serial block-face scanning electron microscopy for polymer-based (soft) materials [36]. Using CLSM, we have found the morphological cause behind the varying quality in a series of silica monoliths [34], investigated the influence of the capillary internal diameter on the packing morphology [7], and compared core–shell and fully porous particles with respect to the wall effects in packed capillaries [35]. Excepting one study [4], our CLSM investigations so far have been conducted with capillary columns because this format enables direct access to the bed morphology; that is, it is not necessary to extrude the bed from its conduit and cut the extruded bed into smaller samples. Also, a smaller column internal diameter allows reconstruction of longer bed segments and the amount of CLSM data involved is still manageable.

In this article, we demonstrate how the morphologies of chromatographic beds can be directly and quantitatively compared by image analysis, independent of size and form of the underlying structural element of the bed. As examples we selected two capillary columns of identical internal diameter (20 µm): a silica monolith and a packing of sub-2 µm particles.

6.2 Experimental

The investigated fused-silica capillary columns (20 cm × 20 µm), a tetramethoxysilane (TMOS) monolith prepared as described in the literature [30], and a packing of C18-modified, 1.7 µm Acquity BEH particles (Waters Corporation) prepared as shown in the literature [7] were kindly provided by Takeshi Hara and Dr. Bernd M. Smarsly (monolith) of Justus-Liebig-Universität, Giessen, Germany, and James P. Grinias, Laura E. Blue, and Dr. James W. Jorgenson (packing) of the University of North Carolina at Chapel Hill. All elements of the experimental approach have been described in detail elsewhere [7,32–34], so only the salient points are repeated here. For image contrast, the particulate bed was stained with Bodipy 493/503 (Life Technologies), a dye that physisorbs to the C18 chains, whereas the bare-silica skeleton of the monolith was chemically linked to the dye V450 [32]. A 65-µm-long segment from the medium section of each column was reconstructed from a set of consecutive optical slices (image stack, resolution: 30 × 30 × 120 nm, Figure 6.1) recorded on a TCS SP5 confocal microscopy system equipped with a HCX PL APO 63×/1.3 GLYC CORR CS (21°) glycerol immersion lens (Leica Microsystems). The refractive index mismatch between lens and sample was minimized through flushing and

embedding the investigated column with (as well as immersing the lens in) a 70:19:11 (v/v/v) liquid mixture of glycerol–DMSO–water, whose refractive index mimics the optical dispersion of fused silica. The remaining small mismatch was eliminated by a judiciously chosen cover slip ("type 0," 110 nm thickness). Contrast, signal-to-noise ratio, and resolution in the acquired images were improved by image restoration. The gray-scale images were then converted to binary data (in which each pixel belongs to either solid or void space) through segmentation. Images of the monolithic column were binarized by high-pass filtering; images of the particulate column were binarized by detecting the center of a particle and fitting a sphere with the appropriate diameter around it.

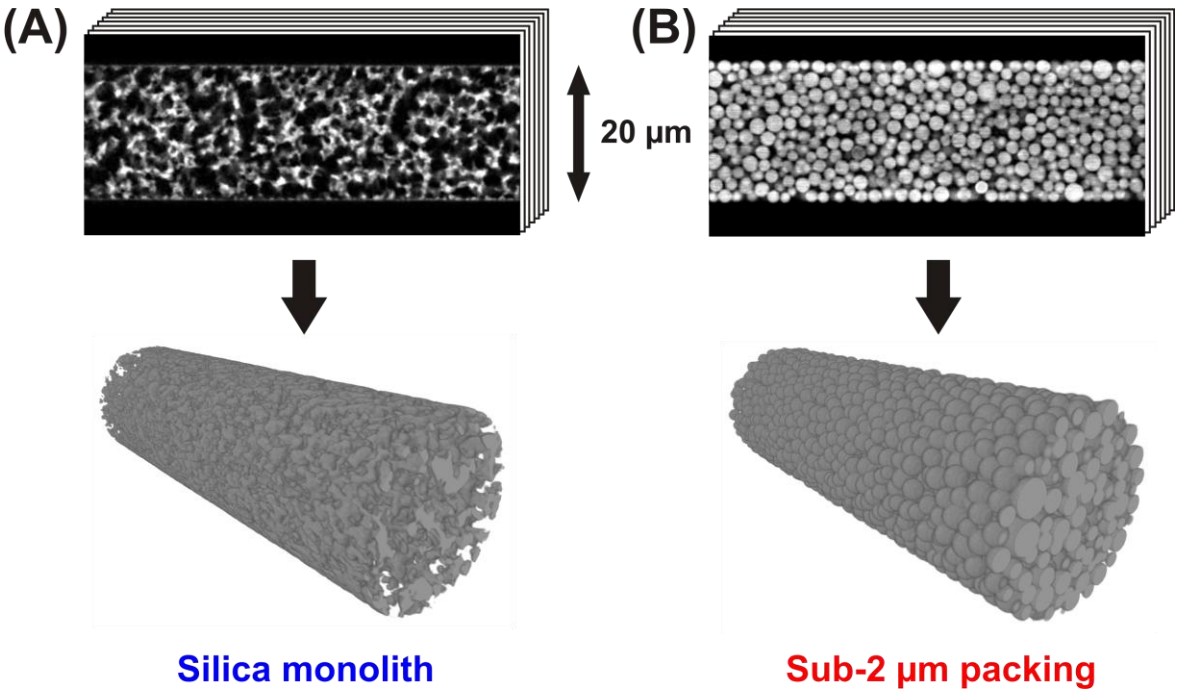

Figure 6.1: Physical reconstruction of the bed morphology of (**A**) a silica monolith and (**B**) a packing of sub-2 µm particles by confocal laser scanning microscopy. Segments (65 µm long) of each capillary column (20 µm i.d.) were reconstructed from image stacks of consecutive optical slices acquired parallel to the column axis.

6.3 Results and Discussion

Figure 6.1 schematically shows how the bed morphologies of the two capillary columns were physically reconstructed by CLSM. Images were acquired from parallel planes along the column axis. The resulting image stack represents a set of consecutive optical slices through a column, from wall to wall. The reconstructed segments cover 65 µm of each column. With the reconstructed morphologies available, our analysis of the two bed structures progressed from the pore scale to the column scale.

6.3.1 Pore Scale Properties. The interstitial void space in a particulate or monolithic bed is a network of flow-through pores whose size determines the amount of transchannel dispersion in the column. Unfortunately, the concept of linking an eddy dispersion term to the scale of individual flow-through pores is easier to understand than it is to obtain an accurate pore size distribution (PSD). The standard experimental method, mercury intrusion porosimetry (MIP), assumes a network of cylindrical pores; in reality, the flow-through pores in a column do not have a constant diameter, but often widen behind a constricted entrance (the pore neck). That MIP measures the diameter of the pore neck rather than the size of the actual pore is known as the ink-bottle effect [37]. Considering this drawback, an MIP-determined PSD should be interpreted with caution. With the reconstructed morphology of a packing (Figure 6.1), an accurate image of the interstitial void space is available, but that still poses the question: How do you define a pore within an open pore network or how do you arrive at the PSD from the reconstructed morphology? One possibility is the inscription of spheres into the void space [38,39]. Figure 6.2 shows the results of this approach applied to the reconstructed beds. Each void voxel was assigned the diameter of the largest sphere that could be inscribed at this location without intersecting with a solid voxel. Figures 6.2A and B show a monolithic and particulate bed, respectively, with the void space colored according to the diameters of the locally inscribed spheres. Figure 6.2C quantifies the results with the probability density distribution of the inscribed-sphere diameters for each voxel location in the void space. As expected, the inscribed-sphere diameters in the monolithic bed are, on average, more than twice the size of those in the particulate bed. The sub-2 µm packing shows a rather narrow and symmetrical distribution of inscribed-sphere diameters, whereas the monolith has a very broad, negatively skewed distribution. The latter reflects that fluctuations in skeleton thickness lead to

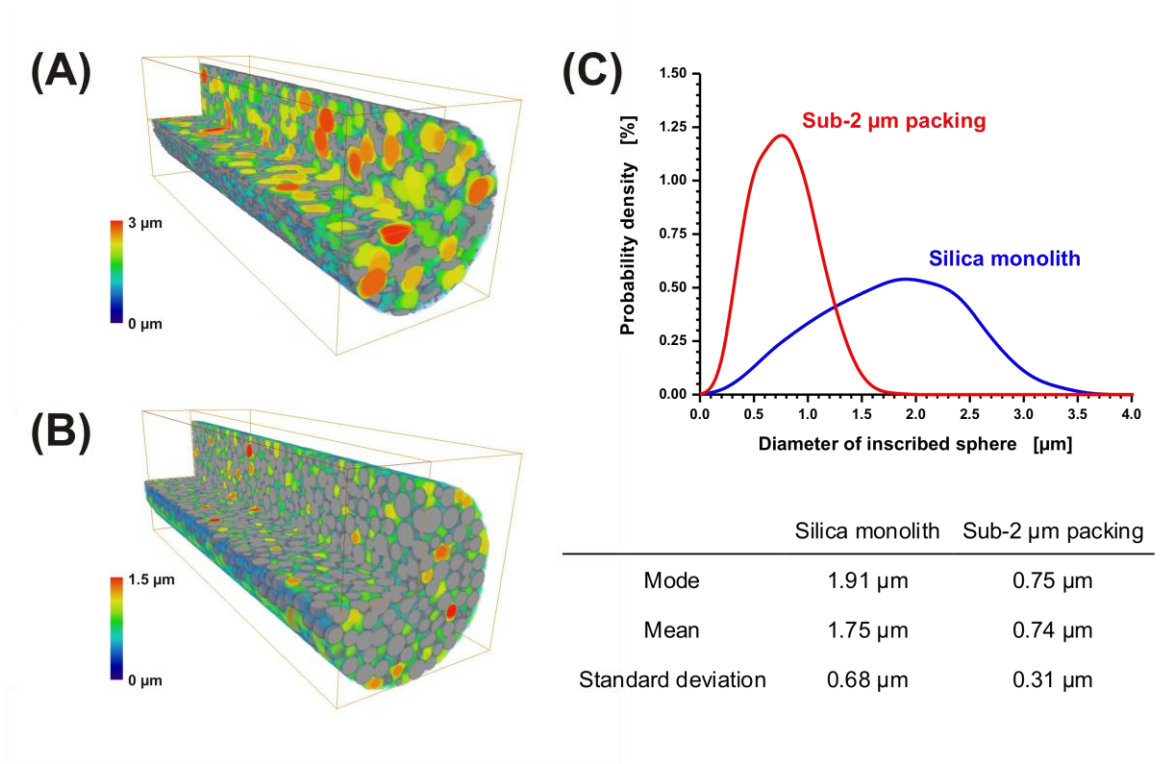

	Silica monolith	Sub-2 µm packing
Mode	1.91 µm	0.75 µm
Mean	1.75 µm	0.74 µm
Standard deviation	0.68 µm	0.31 µm

Figure 6.2: Void space characterization by inscribed spheres. Colors indicate the diameters of the largest spheres that can be fitted into the interstitial void space of (**A**) the reconstructed monolithic and (**B**) particulate bed without intersecting the solid phase (gray). (**C**) The probability density distribution of the inscribed-sphere diameters (shown with the corresponding statistical parameters) can be interpreted as a lower limit of the pore size distribution.

an irregular solid–void interface whose description requires a larger number of smaller spheres. Although the inscribed-spheres approach has visual appeal and targets pores as opposed to pore necks like MIP, the results are inaccurate. Inscribing spheres into the void space probes the adaptation of the pore space to a fixed, idealized geometry more than the dimensions of the flow-through pores themselves, which makes the resulting PSD only a lower limit of the range in which the true PSD lies. An accurate, though less immediately comprehensible, method to describe the interstitial void space distribution in a porous medium was introduced by Courtois and colleagues [40] for chromatographic beds. Here, the particle-to-particle (or skeleton-to-skeleton) distances in the bed are measured by chords that are extended in two opposite directions from random positions in the interstitial void space (Figure 6.3A). Chords are generated and their lengths collected until the resulting

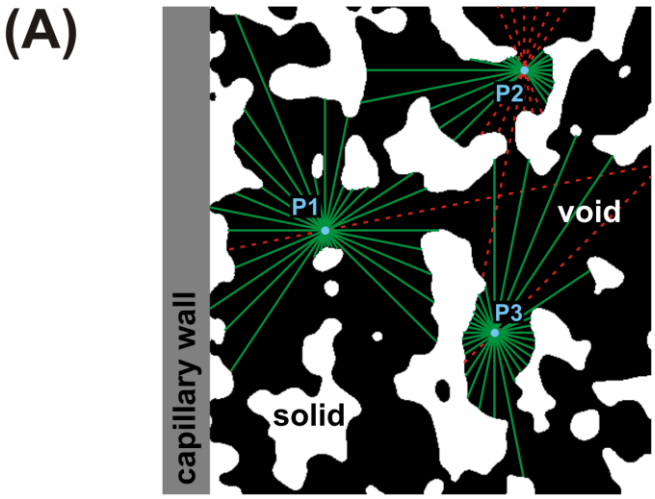

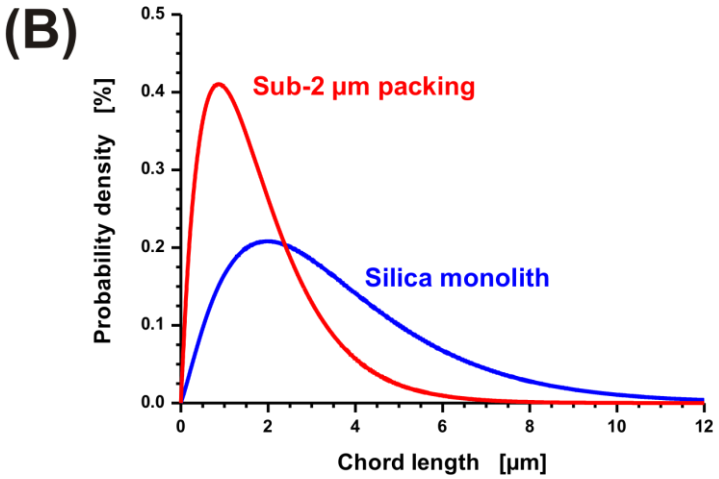

	Silica monolith	Sub-2 µm packing
Mode	1.97 µm	0.91 µm
μ	3.60 µm	1.78 µm
k	2.22	1.94

Figure 6.3: Quantitative void space characterization by chord length distributions. (**A**) From random points P1 to Pn in the interstitial void space of the reconstructed monolithic bed, the linear skeleton-to-skeleton distance (for the particulate bed, the particle-to-particle distance) is determined in 16 equiangular directions (green lines); chords that reach beyond the image boundary are rejected (red dashed lines). (**B**) *k*-gamma fit to a distribution of 10^6 chords and the corresponding statistical parameters that measure the pore-scale properties (average pore size, transchannel, and short-range interchannel heterogeneity) of the reconstructed monolithic and particulate bed.

histogram, known as a *chord length distribution* (CLD), remains constant. The CLDs of the reconstructed beds (Figure 6.3B) were established from 10^6 chords each and are statistically over-determined. The one-dimensional (1D) chords meticulously scan the complex geometry of the solid–void border in a porous medium, so that the CLD fully captures the morphology of the reconstructed interstitial void space. This accuracy is one essential advantage of the CLD method over the inscribed-spheres approach (and MIP). The other important advantage is that chords may occasionally reach into the next flow-through pore; such longer chords then contain information about the pore vicinity.

The interpretation of the received CLDs in terms of eddy dispersion contributions is helped by the circumstance that the CLDs follow a *k*-gamma function. The *k*-gamma function [41] was delineated as a descriptor of the void space distribution in computer-generated, coagulated colloids of monosized spheres [42]. With the first physical reconstructions completed, we discovered that the *k*-gamma function was also a good fit for the CLDs of the interstitial void space of experimental particulate and monolithic beds [4,33–35,43]. The *k*-gamma function is defined by the mean and the standard deviation of the CLD:

$$f(l_{\text{chord}}) = \frac{k^k}{\Gamma(k)} \frac{l_{\text{chord}}^{k-1}}{\mu^k} \exp\left(-\frac{k \cdot l_{\text{chord}}}{\mu}\right) \qquad \text{(Eq. 6.1)}$$

where l_{chord} is the chord length, Γ is the gamma-function, μ denotes the statistical mean of the distribution, and $k = (\mu/\sigma)^2$ relates the mean μ to the standard deviation σ of the distribution. Alternatively, μ or the mode of the CLD (which is reasonably close to the mode of the inscribed-spheres determined PSD, Figure 6.2C) can be used to characterize the size of the flow-through pores. In the monolithic bed, the flow-though pores (μ = 3.60 µm, mode = 1.97 µm) are about twice the size than those in the particulate bed (μ = 1.78 µm, mode = 0.91 µm). The size of the transchannel contribution to eddy dispersion scales with the µ-value of the CLD [34]. From the comparison of the received μ-values, we can predict that transchannel dispersion in the monolith is larger than in the sub-2 µm packing; in fact, it is comparable to the transchannel dispersion in a ~4 µm packing.

The value of *k* is dominated by the longer chords that make up the tail of the CLD and contain information on the local pore environment. Larger *k*-values represent a narrower

distribution relative to μ; that is, a higher bed homogeneity on the length scale of 1–2 particle diameters or domains [4,33–35,43]. The monolith (k = 2.22) is more homogeneous on the short-range interchannel scale than the sub-2 µm packing (k = 1.94), which would translate to a smaller contribution to eddy dispersion in the monolithic column. This finding agrees with our previous investigations: Among the capillary columns we have reconstructed by CLSM so far the particulate beds have fallen into the narrow range of k = 1.9–2.0 (33,35), whereas the silica monoliths have shown a wider range of k = 1.9–2.5 [34,43]. The maximum observed value (k = 2.9) was obtained for an analytical TMOS monolith column of the second generation [4]. Although our sample range is too small at present to predict the k-value range of monolithic beds, it is fairly reasonable to expect a narrow k-value range for well-packed particulate beds. These columns seem to possess a similar amount of order in the core region because the constraints of a dense packing near the random-close packing limit [44] leave little possibility for structural variation on the short-range interchannel length scale [18,35].

6.3.2 Column Scale Properties. Radial heterogeneities in the interstitial void space distribution on the scale of the column diameter are a serious threat to the separation efficiency of any column, but are particularly critical in capillary chromatography. Porosity biases in a column translate directly into permeability and velocity biases [21,22]. The extent to which such velocity extremes are experienced by an analyte and, thus, become apparent in the chromatographic output depends on the ratio of column internal diameter to column length [23]. Analytical columns are too short for their internal diameter to complete equilibration of the analyte over the column cross-section; thus, when the analyte arrives at the column outlet, it has not felt all transcolumn velocity biases existing in the bed. Consequently, the efficiency of analytical columns suffers less from existing radial heterogeneities than that of capillary columns, whose kinetic performance discloses every heterogeneity in the packing [7,16,19,22,45].

We first calculated the external porosity, ε_{ext}, of the reconstructed capillary segments from the amount of void voxels divided by the total amount of voxels. The results of ε_{ext} = 0.69 for the monolith and of ε_{ext} = 0.42 for the sub-2 µm packing are average values, such as could also be obtained by inverse size exclusion chromatography or Donnan exclusion [46], but say nothing about the void space heterogeneity. Figure 6.4A shows the radial porosity profiles $\varepsilon(r)$, the local porosity ε as a function of the distance r from the

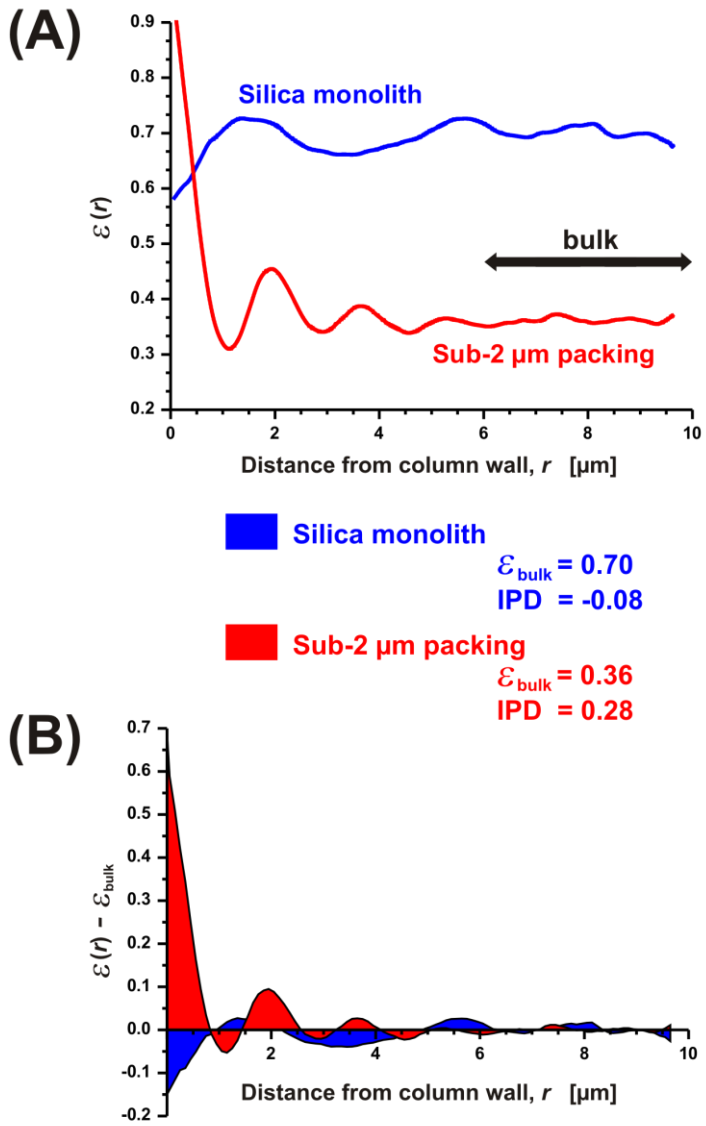

Figure 6.4: (**A**) Characterization of transcolumn heterogeneity by radial porosity profiles. The bulk porosity (ε_{bulk}) of the reconstructed capillary segments was estimated from the interstitial porosity in the core region (r = 6–10 µm), in which the stationary phase material is randomly distributed. (**B**) Subtraction of ε_{bulk} from the porosity profiles eliminated the large difference in average interstitial porosity between the monolithic and the particulate bed. The scalar resulting from integration over the area covered by these curves is the integral porosity deviation (IPD, equation 6.2). The IPD quantifies the local porosity variation over the column cross-section relative to the bulk porosity.

column wall (r = 0), obtained for both beds. The radial porosity profile of the monolith is relatively flat compared with that of the sub-2 µm packing, which shows the typical "damped oscillations" profile of particulate beds [7,22,35]. Because of the huge difference in external porosity, ε_{ext}, the porosity profiles of the two beds cannot be directly compared. Instead, the local porosity variation with respect to the average porosity in the bulk (core) region of each bed is compared. The bulk region of each bed (r = 6–10 µm) is indicated in Figure 6.4A. In the monolith, bulk (ε_{bulk}= 0.70) and external porosity (ε_{ext} = 0.69) are very close in value. In the sub-2 µm packing, the bulk porosity is ε_{bulk} = 0.36, while the local porosity at the column wall is ε = 1. To quantify the local porosity deviation with respect to the bulk porosity, we subtracted ε_{bulk} from the porosity profiles and integrated the remaining deviation over the column radius (Figure 6.4B). The resulting scalar is the integral porosity deviation (IPD) [7,35]:

$$\mathrm{IPD} = \int_0^{0.5d_c} (\varepsilon(r) - \varepsilon_{bulk})\, dr \qquad \text{(Eq. 6.2)}$$

where r is the distance from the column wall and d_c is the column internal diameter. The small IPD value of the monolithic bed (IPD = –0.08) reflects the flat porosity profile and the negative sign indicates a lower porosity at the column wall than in the bulk. The ~1 µm thick low-porosity region originates from the wetting layer of monolithic material at the capillary wall and is followed first by a region of higher porosity and then by another low-porosity region (r = 2.2–4.6 µm). This often observed morphological feature of capillary silica monoliths [34] is formed during the drying stage, when the bed shrinks and locally disconnects from the material layer at the wall. The high-porosity region reflects where the bed is stretched thin, and the low-porosity region reflects where the material has accumulated. Whereas the porosity profile of the monolith reflects its preparation history, the profile of the sub-2 µm packing and its IPD value (IPD = 0.28) reflect the fundamental limitations on the packing of hard spheres against a locally flat, hard column wall. For the first 3–5 µm from the capillary wall, the bed has a much higher porosity and also higher order than in the randomly packed bulk [7]. The absolute IPD value of the monolith is 3.5 times lower than that of the sub-2 µm packing. The high radial homogeneity of the monolithic bed promises low transcolumn dispersion and constitutes a substantial structural advantage of the monolithic over the particulate format. Unfortunately, columns pre-

pared in the past have often disappointed in this regard [2], which has led to reservations against silica monoliths in general.

6.4 Conclusions

We compared the bed morphologies of two 20 µm i.d. capillary columns with different silica-based support structures following their physical reconstruction by CLSM. According to our analysis, the monolith is more homogeneous than the sub-2 µm packing on the short-range interchannel and on the transcolumn scale, but loses significantly on the transchannel scale, with flow-through pores twice the size of those in the sub-2 µm packing. If the macropore size could be reduced while maintaining the present level of short-range interchannel and transcolumn homogeneity, the monolith would become superior to the sub-2 µm packing. The physical reconstruction of the bed morphology by CLSM allows users to monitor the morphological consequences of slurry packing and monolith preparation on scales of all lengths relevant to eddy dispersion: A CLD of the reconstructed interstitial void space delivers the parameters μ and k , which indicate the average pore size and the heterogeneity in the direct vicinity of a pore, respectively, while radial porosity profiles track changes in transcolumn heterogeneity. Decreasing μ while conserving k and the IPD value should be the goal of monolith preparation. Reduction of the transcolumn heterogeneity as indicated by a drop of the IPD value would have the strongest impact on the kinetic performance of slurry-packed particulate columns. Beyond all questions, image analysis provides pivotal insight into the morphological foundations of column performance. Besides guiding academic and industrial researchers in the preparation of better high performance liquid chromatography (HPLC) columns, the CLSM-based physical reconstruction of chromatographic beds delivers realistic models for flow and transport simulations to derive accurate mass transfer relationships for HPLC [19,47,48].

Acknowledgments

This work was supported by the Deutsche Forschungsgemeinschaft DFG (Bonn, Germany) under grants TA 268/5 and TA 268/6. The authors thank Takeshi Hara and Dr. Bernd M. Smarsly of Justus-Liebig-Universität, Giessen, Germany, and James P. Grinias, Laura E. Blue, and Dr. James W. Jorgenson of the University of North Carolina at Chapel Hill for generously providing the studied capillary columns.

References

[1] Unger, K. K.; Skudas, R.; Schulte, M. M. *J. Chromatogr., A* **2008**, *1184*, 393–415.

[2] Guiochon, G. *J. Chromatogr., A* **2007**, *1168*, 101–168.

[3] Cabrera, K. *LC-GC North Am.* **2012**, *S*, 56–60.

[4] Hormann, K.; Müllner, T.; Bruns, S.; Höltzel, A.; Tallarek, U. *J. Chromatogr., A* **2012**, *1222*, 46–58.

[5] Mazzeo, J. R.; Neue, U. D.; Kele, M.; Plumb, R. S. *Anal. Chem.* **2005**, *77*, 460A–467A.

[6] Gritti F.; Guiochon, G. *J. Chromatogr., A* **2010**, *1217*, 1485–1495.

[7] Bruns, S.; Grinias, J. P.; Blue, L. E.; Jorgenson, J. W.; Tallarek, U. *Anal. Chem.* **2012**, *84*, 4496–4503.

[8] Kirkland J. J.; DeStefano, J. J. *J. Chromatogr., A* **2006**, *1126*, 50–57.

[9] Jorgenson, J. W. *Annu. Rev. Anal. Chem.* **2010**, *3*, 129–150.

[10] Blue L. E.; Jorgenson, J. W. *J. Chromatogr., A* **2011**, *1218*, 7989–7995.

[11] Chamieh, J.; Zimmermann, Y.; Boos, A.; Hagège, A. *J. Colloid Interface Sci.* **2009**, *340*, 225–229.

[12] Gritti, F.; Guiochon, G. *J. Chromatogr., A* **2011**, *1218*, 3476–3488.

[13] Gritti, F.; Guiochon, G. *J. Chromatogr., A* **2012**, *1252*, 31–44.

[14] Gritti, F.; Guiochon, G. *LC-GC North Am.* **2012**, *30*, 586–595.

[15] Giddings, J. C. *Dynamics of Chromatography, Part1: Principles and Theory*, Marcel Dekker, New York, **1965**.

[16] Khirevich, S.; Höltzel, A.; Seidel-Morgenstern, A.; Tallarek, U. *Anal. Chem.* **2009**, *81*, 7057–7066.

[17] Gritti, F.; Guiochon, G. *J. Chromatogr., A* **2009**, *1216*, 4752–4767.

[18] Khirevich, S.; Daneyko, A.; Höltzel, A.; Seidel-Morgenstern, A.; Tallarek, U. *J. Chromatogr., A* **2010**, *1217*, 4713–4722.

[19] Hlushkou, D.; Bruns, S.; Höltzel, A.; Tallarek, U. *Anal. Chem.* **2010**, *82*, 7150–7159.

[20] Vandre, E.; Maier, R. S.; Kroll, D. M.; McCormick, A.; Davis, H. T. *AIChE J.* **2008**, *54*, 2024–2028.

[21] Abia, J. A.; Mriziq, K. S.; Guiochon, G. *J. Chromatogr., A* **2009**, *1216*, 3185–3191.

[22] Khirevich, S.; Höltzel, A.; Seidel-Morgenstern, A.; Tallarek, U. *J. Chromatogr., A* **2012**, *1262*, 77–91.

[23] Gritti, F.; Guiochon, G. *J. Chromatogr., A* **2012**, *1262*, 107–121.

[24] Gritti, F.; Guiochon, G. *J. Chromatogr., A* **2010**, *1217*, 5137–5151.

[25] Tanaka, N.; Kobayashi, H.; Ishizuka, N.; Minakuchi, H.; Nakanishi, K.; Hosoya, K.; Ikegami, T. *J. Chromatogr., A* **2002**, *965*, 35–49.

[26] Tallarek, U.; Leinweber, F. C.; Seidel-Morgenstern, A. *Chem. Eng. Technol.* **2002**, *25*, 1177–1181.

[27] Oláh, E.; Fekete, S.; Fekete, J.; Ganzler, K. *J. Chromatogr., A* **2010**, *1217*, 3642–3653.

[28] Gritti, F.; Tanaka, N.; Guiochon, G. *J. Chromatogr., A* **2012**, *1236*, 28–41.

[29] Motokawa, M.; Kobayashi, H.; Ishizuka, N.; Minakuchi, H.; Nakanishi, K.; Jinnai, H.; Hosoya, K.; Ikegami, T.; Tanaka, N. *J. Chromatogr., A* **2002**, *961*, 53–63.

[30] Hara, T.; Kobayashi, H.; Ikegami, T.; Nakanishi, K.; Tanaka, N. *Anal. Chem.* **2006**, *78*, 7632–7642.

[31] Skudas, R.; Grimes, B. A.; Thommes, M.; Unger, K. K. *J. Chromatogr., A* **2009**, *1216*, 2625–2636.

[32] Bruns, S.; Müllner, T.; Kollmann, M.; Schachtner, J.; Höltzel, A.; Tallarek, U. *Anal. Chem.* **2010**, *82*, 6569–6575.

[33] Bruns, S.; Tallarek, U. *J. Chromatogr., A* **2011**, *1218*, 1849–1860.

[34] Bruns, S.; Hara, T.; Smarsly, B. M.; Tallarek, U. *J. Chromatogr., A* **2011**, *1218*, 5187–5194.

[35] Bruns, S.; Stoeckel, D.; Smarsly, B. M.; Tallarek, U. *J. Chromatogr., A* **2012**, *1268*, 53–63.

[36] Müllner, T.; Zankel, A.; Mayrhofer, C.; Reingruber, H.; Höltzel, A.; Lv, Y.; Svec, F.; Tallarek, U. *Langmuir* **2012**, *49*, 16733–16737.

[37] Abell, A. B.; Willis, K. L.; Lange, D. A. *J. Colloid Interface Sci.* **1999**, *211*, 39–44.

[38] Hildebrand, T.; Rüegsegger, P. *J. Microsc.* **1997**, *185*, 67–75.

[39] Chiang, M. Y. M.; Landis, F. A.; Wang, X.; Smith, J. R.; Cicerone, M. T.; Dunkers, J.; Luo, Y. *Tissue Eng. Part C: Meth.* **2009**, *15*, 65–76.

[40] Courtois, J.; Szumski, M.; Georgsson, F.; Irgum, K. *Anal. Chem.* **2007**, *79*, 335–344.

[41] Aste, T.; Di Matteo, T. *Phys. Rev. E* **2008**, *77*, 021309.

[42] Schenker, I.; Filser, F. T.; Gauckler, L. J.; Aste, T.; Herrmann, H. J. *Phys. Rev. E* **2009**, *80*, 021302.

[43] Hlushkou, D.; Bruns, S.; Seidel-Morgenstern, A.; Tallarek, U. *J. Sep. Sci.* **2011**, *34*, 2026–2037.

[44] Baranau, V.; Hlushkou, D.; Khirevich, S.; Tallarek, U. *Soft Matter* **2013**, *9*, 3361–3372.

[45] Daneyko, A.; Khirevich, S.; Höltzel, A.; Seidel-Morgenstern, A.; Tallarek, U. *J. Chromatogr., A* **2011**, *1218*, 8231–8248.

[46] Jung, S.; Ehlert, S.; Pattky, M.; Tallarek, U. *J. Chromatogr., A* **2010**, *1217*, 696–704.

[47] Gritti, F.; Guiochon, G. *J. Chromatogr., A* **2012**, *1221*, 2–40.

[48] Daneyko, A.; Hlushkou, D.; Khirevich, S.; Tallarek, U. *J. Chromatogr., A* **2012**, *1257*, 98–115.

Chapter 7

Slurry Concentration Effects on Bed Morphology and Separation Efficiency of Capillaries packed with Sub-2 Micron Particles

Authors:

Stefan Bruns, Edward G. Franklin, James P. Grinias, Justin M. Godinho, James W. Jorgenson, and Ulrich Tallarek

State of Publication:

submitted August 11, 2013 to *Journal of Chromatography A.*

Abstract

Transcolumn dispersion limitations on the separation efficiency of chromatographic columns suggest the need for packing methods that increase bed homogeneity and minimize potential wall effects. Here we address the influence of the slurry concentration in the slurry packing process on the resulting morphology and separation efficiency of ultrahigh-pressure liquid chromatography capillary columns. 30–75 μm i.d. capillaries were packed with fully porous 0.9, 1.7, and 1.9 μm bridged-ethyl hybrid particles and 1.9 μm Kinetex core–shell particles. Capillaries prepared with higher slurry concentrations (20–100 mg/mL) showed higher separation efficiencies than those prepared using a low slurry concentration (2–3 mg/mL). The effect is explained by an analysis of transcolumn bed heterogeneities in three-dimensional reconstructions acquired from the packed capillaries using confocal laser scanning microscopy. The three-dimensional analysis of porosity distributions and local particle size illustrates that beds packed with higher slurry concentrations suppress particle size segregation, however, at the expense of a larger amount of packing voids. In core–shell packings, where only few packing voids were found, the higher slurry concentration allowed for an additional densification of the bed's wall region, as revealed by a radial analysis of the mean particle distances. Overall, wall effects are attenuated in packed columns prepared with both wide and narrow particle size distributions, which will allow for improved chromatographic performance.

7.1 Introduction

During recent years particles available for high-performance liquid chromatography (HPLC) have rapidly undergone a size reduction [1]. Currently, columns packed with the 1.3 µm Kinetex particles represent chromatographic beds composed of the smallest porous particles that have ever been commercially available for chromatography [2]. If this trend continues HPLC particles will soon enter the colloidal domain [3], where aspects related to the colloidal stability become important in the column packing, as recently shown with polymeric particles bearing ionizable functional groups [4]. Also other effects must be considered then by chromatographers, e.g., the contribution of slip-flow in the beds [5–7], frictional heating in small-bore columns [8–10], or long-range bed-morphological effects on eddy dispersion resulting from partially amorphous and crystalline regions in a packed column. However, considering modern ultrahigh-pressure liquid chromatography (UHPLC) instrumentation, the potential to operate columns with even smaller particles seems to be almost exhausted due to the pressure limitations of the current commercial equipment. Transchannel eddy dispersion, operating on the individual pore scale in a packing, is not the only dispersion contribution in a column that can be minimized. According to the recent perspective by Gritti and Guiochon [11], the transcolumn dispersion, which is caused by column cross-sectional heterogeneities in a packing, particularly wall effects, dominates the efficiency of particle-packed beds with up to 70% of the total dispersion in UHPLC columns at high velocities and hence provides a much greater (yet little explored) potential in plate height reduction than a further reduction of the particle size.

Commonly, a reduced plate height value in the minimum of the plate height curve of $h_{min} \approx 2$ is considered to represent a homogenous bed structure [12]. However, with increasing availability of core–shell particles, it is not uncommon to observe $h_{min} < 1.6$ (in the analytical column format) [13–16]. This has been marketed as an effect of a narrow particle size distribution (PSD). On the other hand, detailed eddy dispersion simulations in packed beds have demonstrated that there is no intrinsic advantage of a narrow PSD with a relative standard deviation (RSD) of ~3% over a wide PSD with a RSD of ~25% in an infinite-diameter column, i.e., in a bulk packing without wall effects [17]. It is the decidedly differing bed morphology in the wall region of the columns and transition to the randomly packed bulk region of the beds that enabled these improvements through a reduction in the transcolumn heterogeneity [18–21].

The radial homogeneity of a chromatographic bed strongly depends on the procedure that is applied to prepare the column packing. Silica particles are packed using a low-viscosity slurry method. How this can be performed efficiently has always been a secret among practitioners and companies since numerous parameters that influence the final bed morphology, like the packing pressure, slurry liquid and concentration, pushing solvent, or key steps like the bed densification via ultrasound, have to be screened (which is difficult since their coupling is highly complex) and tuned to any given particle (or even column) type. This implies that the adjustment of parameters in the slurry packing protocol to a new particle type, rather than the particle's production, is often the bottleneck in the time until its distribution on the market [22]. A better understanding of these parameters will help shorten this period.

The availability of instrumentation as well as computational resources to conduct large-scale three-dimensional reconstructions of chromatographic supports by, e.g., confocal laser scanning microscopy (CLSM) [20,23–27], serial block-face scanning electron microscopy [28,29], or focused ion-beam scanning electron microscopy [30] today make it possible to directly observe and also systematically screen the influence that a slurry packing parameter can exercise on the resulting packing microstructure of a chromatographic bed. In two recent publications we started to approach parameters in the slurry packing process and their influence on the bed morphology by studying capillary columns packed with different particle types [20] as well as by varying the capillary i.d. (for a given particle type), thus, the ratio of the column diameter (d_c) to the mean particle diameter (d_p) [31].

In this study, we investigate effects that the slurry concentration (c_s) used for column packing exerts on the final bed morphology. The literature presents a wide range of slurry concentrations in column packing. For example, Hsieh and Jorgenson used 3–17 mg/mL slurries to pack 5 µm particles in capillaries with column-to-particle diameter ratios (d_c/d_p) of ~2–7 [32]. Patel et al. used 10–30 mg/mL slurries to pack 1.0 µm nonporous particles for $d_c/d_p \approx 10–150$ [33], whereas Jung et al. and Ehlert et al. applied 50 mg/mL slurries for packing the noncylindrical channels of HPLC-microchips characterized by $d_c/d_p \approx 10–15$ [34–37]. Kirkland and DeStefano reported an optimal particle concentration between 70 and 150 mg/mL [22].

There is little doubt that the optimal slurry concentration strongly depends on the packing apparatus, slurry solvent, and the selected particle type. Still, when increasing the aspect ratio d_c/d_p and especially when moving from nano-HPLC to analytical HPLC the gen-

eral tendency is to use higher slurry concentrations for larger-diameter columns. But what are the reasons for this choice except empiricism? What are the drawbacks of high slurry concentrations at low aspect ratios and why are higher slurry concentrations becoming beneficial for larger aspect ratios? A complementary approach using HPLC analysis and CLSM on the same separation column has proven to be extremely useful in investigating such questions [25,31]. While HPLC provides information about the kinetic separation efficiency, and therefore about the quality of a column, CLSM allows to visualize and resolve systematic differences in bed microstructures that help to understand a loss or gain in separation efficiency caused by eddy dispersion. Here we report on observations made for several sets of capillary columns packed with 0.9, 1.7, and 1.9 µm C18 bridged-ethyl hybrid (BEH) particles [38] as well as with 1.9 µm C18 Kinetex particles. Packed capillaries were obtained with low slurry concentrations of c_s = 2–3 mg/mL and with at least ten-fold higher slurry concentrations (c_s = 20, 30, or 100 mg/mL).

7.2 Experimental

7.2.1 Chemicals and Materials. 30, 50, and 75 µm i.d. cylindrical fused silica capillary tubing was purchased from Polymicro Technologies (Phoenix, AZ). Capillary columns were packed with C18 modified fully porous 0.9, 1.7, and 1.9 µm BEH particles provided by Waters Corporation (Milford, MA) and with C18 modified 1.9 µm core–shell particles obtained by unpacking a 2.1 × 150 mm Kinetex column from Phenomenex (Torrance, CA). HPLC grade acetonitrile (ACN) and acetone, reagent grade trifluoroacetic acid (TFA), as well as the test analytes L-ascorbic acid, hydroquinone, resorcinol, catechol, and 4-methyl catechol were purchased from Fisher Scientific (St. Louis, MO). Kasil frits for packed capillaries were prepared with potassium silicate from PQ Corporation (Valley Forge, PA) and formamide from Sigma-Aldrich (St. Louis, MO). A Millipore NANOpure water system (Billerica, MA) was used to provide HPLC grade water. Additional solvents required for the optical setup of the imaging system such as dimethylsulfoxide (DMSO) and glycerol were purchased from Sigma-Aldrich Chemie (Taufkirchen, Germany). The dye Bodipy 493/503 (Life Technologies, Darmstadt, Germany) was utilized as a lipophilic fluorophore for the imaging of packing microstructure. The employed coverslips were “type 0” coverslips from Gerhard Menzel (Braunschweig, Germany).

7.2.2 Preparation of Capillary UHPLC Columns. The method used to prepare capillary UHPLC columns has previously been described [33,39–42]. For columns packed with 0.9 and 1.7 μm particles, outlet frits were formed by pushing a 1–2 mm plug of 2.5 μm bare nonporous silica particles (Bangs Laboratories, Fishers, IN) 0.5 mm into the capillary using a tungsten wire to allow for the insertion of a carbon microfiber detection electrode. Columns packed with 1.9 μm particles were fritted at the outlet using the Kasil method [43] by pushing the tubing onto a glass microfiber filter (Reeve Angel, Clifton, NJ) wetted with 1:1 (v:v) ratio of potassium silicate and formamide and then dried overnight at 85°C. Slurries were prepared by suspending the particles in acetone and then sonicating for 10 minutes with a Cole Parmer Ultrasonic Cleaner 8891 (Vernon Hills, IL).

To pack the columns, the slurry was placed in a packing reservoir and then securing the fritted column blank into the reservoir using an UHPLC fitting. Packing was initiated at 200 bar from a DSHF-300 Haskel pump (Burbank, CA) using acetone as a pushing solvent. As the column bed formed, the pressure was increased to 2000 bar and packing continued until the required bed length was reached. The column pressure was then released slowly until it reached atmospheric pressure. The packed column was then connected to a DSXHF-903 Haskel pump (Burbank, CA) using an UHPLC injection apparatus. After flushing the column with over 15 column volumes of 50/50 (v/v) water/ACN at 2800 bar, the pressure was slowly released. Flow was re-initiated at 700 bar to form a temporary inlet frit with a heated wire stripper (Teledyne Interconnect Devices, San Diego, CA). For all column inner diameters, the column was clipped to the desired length (~20 cm) and an inlet frit was formed with the Kasil method.

7.2.3 Chromatographic Analysis. To test the efficiency of the packed columns, 200 μM of an isocratic test mixture (L-ascorbic acid (dead-time marker), hydroquinone, resorcinol, catechol, and 4-methyl catechol) was injected using an UHPLC injection apparatus. The mobile phase used for evaluation was 50/50 (v/v) water/ACN with 0.1% TFA. Analytes were detected amperometrically by amplifying the current generated from an 8 μm × 300 μm carbon fiber microelectrode (held at +1.1 V vs. Ag/AgCl reference electrode) placed at the end of the packed bed [44]. Current-to-voltage conversion was conducted using an SR750 current amplifier (Stanford Research Systems, Sunnyvale, CA) with a 10^9 V/A gain and a 3 Hz, 3 dB low pass bandwidth filter. An Intel Core 2 Duo desk-

top computer with a 16-bit A/D converter was used to acquire data at 21 Hz. Data was collected with a custom written LabView 6.0 program (National Instruments, Austin, TX).

To generate reduced parameter plots (h–ν), the test mixture was separated over a range of mobile phase velocities. High frequency noise was removed from chromatograms using a digital frequency filter and low frequency baseline drift was eliminated by background subtraction. The retention times and theoretical plate counts were determined using an iterative statistical moments algorithm (±3σ integration limits) [32] written in Igor Pro 6.0 (Wavemetrics, Inc., Lake Oswego, OR). Extra-column band broadening effects were estimated to be negligible (1–2% of total peak variance), so observed plate heights were used with no correction.

7.2.4 Imaging of Packing Microstructure. After chromatographic characterization, all packed capillaries were stained with Bodipy 493/503 to provide a fluorescent signal. This was executed by flushing the capillaries with a 0.5 mg/mL acetone solution of the dye until an intensely colored droplet formed at the outlet of the capillary. Excess dye was removed by flushing the capillary with several column volumes of a fused silica refractive index matching liquid composed of 70/19/11 (v/v/v) glycerol/DMSO/water. The matching liquid was calibrated to a refractive index of $n_D = 1.4582$ with an AR200 digital refractometer (Reichert Analytical Instruments, Depew, NY). The capillaries were mounted on a microscope slide and immediately transferred to the microscope. The microscope system was a TCS SP5 equipped with a HCX PL APO 63×/1.3 GLYC CORR CS (21°) glycerol immersion objective lens (Leica Microsystems, Wetzlar, Germany). To compensate for a refractive index mismatch between fused silica and objective specifications the fused silica refractive index matching liquid was used both as immersion medium for the lens and as embedding medium for the capillary. A thinner than standard coverslip of ~110 µm thickness completed the optical setup that has already been discussed in detail previously [26].

Images were recorded in a detection window, where the polyimide coating was removed with a drop of warm sulfuric acid before staining, about 16 cm from the capillary outlet. Excitation of the dye was realized with a 488 nm Argon laser, setting the pinhole of the microscope to 0.5 AU. Fluorescence emission was detected in the interval 491–515 nm. A three-dimensional stack of images perpendicular to the capillary axis was recorded for each capillary by starting at the top of the capillary and moving progressively towards the capillary center with a step size of 126 nm. The step size between as well as the pixel size

within the images (30 nm) both comply with the Nyquist sampling criterion. All images had a size that covered a plane of the complete column diameter and at least 60 µm along the column axis. An orthoslice view of an exemplary recording is provided in Fig. 7.1A.

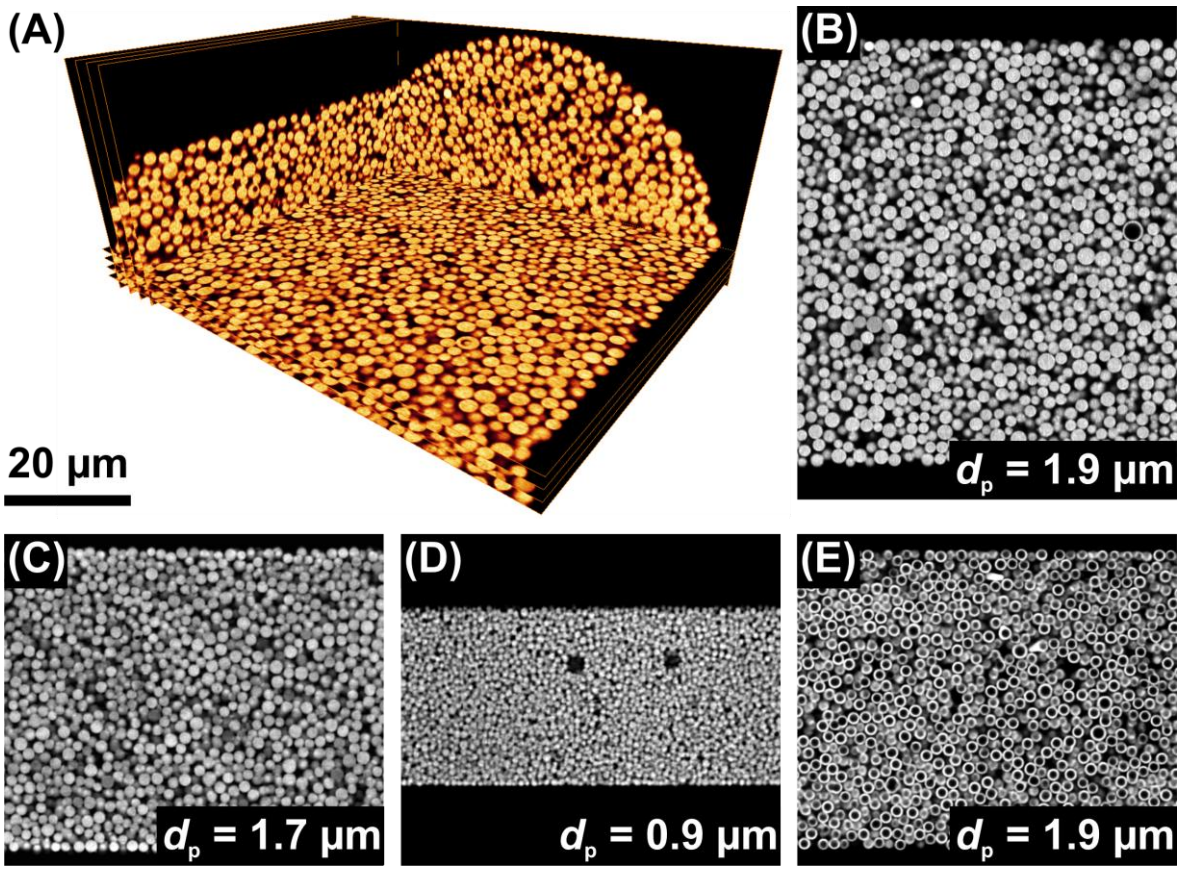

Figure 7.1: (**A**) Orthoslice view of restored CLSM images recorded for a 75 µm i.d. capillary column packed with 1.9 µm BEH particles. The shown volume coincides with the reconstructed volume. (**B–D**) Exemplary optical slices through capillaries packed with 1.9 µm (75 µm i.d.), 1.7 µm (50 µm i.d.), and 0.9 µm (30 µm i.d.) BEH particles. (**E**) Optical slice recorded for a 50 µm i.d. capillary packed with 1.9 µm Kinetex particles. The 20 µm scale bar refers to panels **B**–**E**.

7.2.5 Image Restoration and Capillary Reconstruction. To improve contrast and resolution of the raw microscopic images a multistep image restoration procedure was applied [20,31]. For this purpose we used custom software written in Microsoft Visual Studio 2008 C# (Microsoft Corporation, Redmond, WA), if not stated otherwise. Briefly:

(**a**) Photon noise in the images was reduced using the PureDenoise plug-in for ImageJ [45,46].

(**b**) Bleaching of the dye was corrected for by fitting a second-order exponential decay to a region of interest in the center of the capillary.

(**c**) Huygens maximum likelihood iterative deconvolution (Scientific Volume Imaging, Hilversum, The Netherlands) was applied for improved contrast and resolution.

(**d**) All images were rotated to have the capillary axis aligned with the *x*-axis of the images.

(**e**) Finally, a two-dimensional projection of the signal intensity along the column axis allowed to correct for a potential drift of the sample between slices and enabled a fine tuning of the effective slice-to-slice distance in the image stacks.

A quantitative analysis of packing microstructure requires to locate the particles in the imaged capillary volume and to estimate their size. This was only done for beds packed with the larger particles, since diffraction-limited resolution of the microscope would not allow for an accurate reconstruction of the submicron particles. Again, the required processing steps have already been discussed [20,26,31]. The salient points are:

(**a**) The particle centers of fully porous particles were located by their property of defining high-intensity regions of low signal variance, whereas the core–shell particles can be detected by bandpass filtering [26].

(**b**) With a preliminary list of particle centers from the previous step the location of each particle can be refined by estimating its size from a “best fit” depending on the local signal intensity and variance. An outline of the algorithm for this step can be found in the supporting information of [31].

(**c**) Particles that were missed by the algorithm were added manually; a voxelized three-dimensional reconstruction was realized by assuming a perfect sphericity of the particles coloring solid phase as foreground and void space as background.

To guarantee that the wall region is accurately characterized by the reconstruction at least 6000 particles were detected in the capillaries. The dimensions of the reconstructions and the statistical properties of the resulting PSDs are given in Table 7.1.

Table 7.1: Dimensions of the capillary segments reconstructed using CLSM and statistical properties of the obtained particle size distributions (PSDs).

Particles	1.7 µm BEH		1.9 µm BEH		1.9 µm Kinetex	
c_s [mg/mL]	3	30	3	100	3	30
Length [µm]	54	48	62.4	58.9	78	78
Depth [µm]	20.7	18.4	30.5	34.2	17.0	16.2
PSDs						
No. of particles	9249	6963	16769	17774	8175	7727
Mean, d_p [µm]	1.71	1.70	1.94	1.96	1.90	1.91
Mode [µm]	1.71	1.72	1.84	1.84	1.90	1.91
Median [µm]	1.68	1.68	1.92	1.92	1.92	1.92
RSD (%)	11.9	11.9	15.7	15.3	5.8	6.2

7.2.6 Reconstruction Analysis. In the reconstructed beds the packing density ρ is the ratio of the number of foreground voxels (voxels assigned to the particles) divided by the total number of voxels located in that column volume. (The external porosity ε, i.e., the interparticle void volume fraction, is $\varepsilon = 1 - \rho$.) For its calculation the capillary wall needs to be identified. This was realized by computing a porosity projection along the capillary axis and defining the capillary wall to be located above the first and below the last pixel column in each image that had a porosity ≤ 0.99. For transcolumn porosity profiles pixels in a two-dimensional porosity projection were binned according to their Euclidean distance from the allocated capillary wall. Radially resolved PSDs were calculated by assigning these distance values to the list of detected particles. A moving window of one d_p was used for this measure to generate continuous data. The particle list was also used for the computation of mean particle distances. Here the mean distance to all the neighboring particles

within a 1.5 d_p radius around each particle was calculated and binned according to the distance of the particles to the capillary wall with a moving window of one d_p. On average, 9–10 neighbors could be found in the considered volume for each particle located in the first particle layer next to the capillary wall and 13–15 neighbors for the deeper particle layers.

Packing voids were analyzed by calculating the Euclidean distance of each background voxel (void space) to the closest particle surface. The thresholding with the particle radius of the first quartile of the underlying PSD provided clusters of voxels that were counted and related to the reconstructed column volume, providing an estimate for the number of packing defects in the column.

7.3 Results and Discussion

Due to the differing preparation process the BEH particles show a much wider PSD, with a RSD of ~12–15%, than the Kinetex particles (RSD ≈ 6%, cf. Table 7.1). To take account for the varying particle properties our analysis is divided into a separate discussion of the fully porous particles and the core–shell particles.

7.3.1 Fully Porous Particles

7.3.1.1 Kinetic Separation Efficiency. The cylindrical fused-silica capillaries were packed with BEH particles. This was realized with 0.9 µm particles in 30 µm i.d. capillaries ($d_c/d_p \approx 33$) for c_s = 2 and 20 mg/mL; with 1.7 µm particles in 50 µm i.d. capillaries ($d_c/d_p \approx 29$) for c_s = 3 and 30 mg/mL; and with 1.9 µm particles in 75 µm i.d. capillaries ($d_c/d_p \approx 39$) for c_s = 3 and 100 mg/mL. The separation efficiency of all columns was characterized using hydroquinone as the analyte in a 50/50 (v/v) water/ACN mobile phase. Under these conditions hydroquinone is weakly retained (retention factor k' = 0.20) and reflects the kinetic separation efficiency. Importantly, its retention factor is nearly identical for all columns. This is a prerequisite in such a comparative study, because transcolumn equilibration of an analyte and the associated eddy dispersion, which are in the focus of our work, depend on the analyte's retention factor [11,47–49]. The efficiency data for hydroquinone are presented in the form of reduced plate height curves (Fig. 7.2), which plot reduced plate height $h = H/d_p$ against the reduced velocity $\nu = u_{av}d_p/D_m$, where d_p is the mean particle diameter (from Table 7.1), u_{av} is the average mobile phase flow velocity, and D_m represents the analyte's pressure-dependent diffusion coefficient in the bulk mobile phase [50].

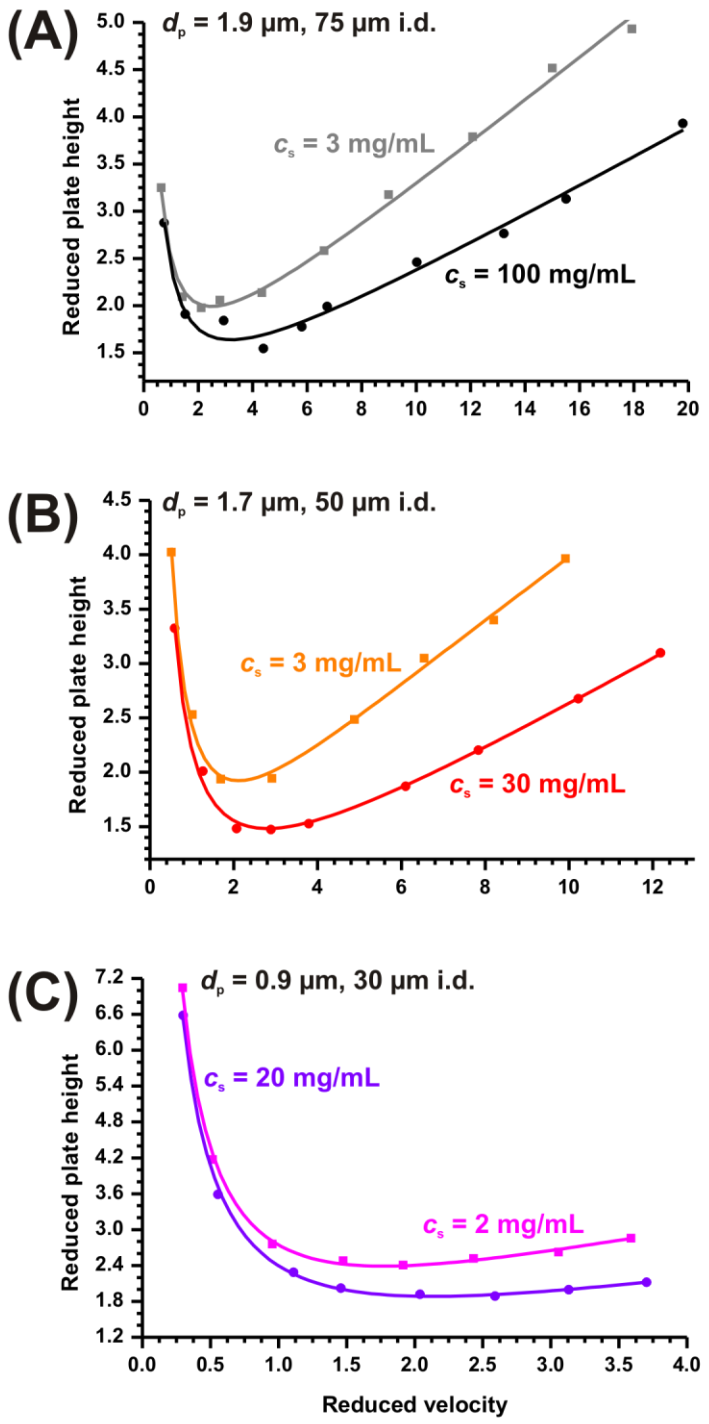

Figure 7.2: Reduced plate height curves (reduced plate height $h = H/d_p$ vs. the reduced velocity $\nu = u_{av}d_p/D_m$) for hydroquinone in a 50/50 (v/v) water/ACN mobile phase (k' = 0.20) recorded on the best performing fused-silica capillaries packed with 1.9, 1.7, and 0.9 µm BEH particles using different slurry concentrations (c_s). Solid lines are best fits of Eq. 7.1 to the h–ν data to guide the eye.

The data in Fig. 7.2 show a systematic improvement in column efficiency for the capillaries packed with higher slurry concentrations, i.e., h_{min} is reduced from 2.0 to 1.6 (d_p = 1.9 µm), from 1.9 to 1.5 (d_p = 1.7 µm), and from 2.4 to 1.9 (d_p = 0.9 µm). The slope of the h–ν curves is also smaller for the columns packed with higher slurry concentrations, which is most distinct for the smaller (1.7 and 0.9 µm) particles. In the classical van Deemter model [51] the slope of the plate height curve is related to mass transfer resistance. A reduction in the mass transfer resistance for columns packed with higher slurry concentrations, however, cannot be an appropriate explanation when identical particles are used in a comparative study. Furthermore, eddy dispersion cannot be regarded as a single and velocity-independent term [51], as the van Deemter model implies, and a better physical characterization of the h–ν dependence is achieved when transverse diffusion and spatial velocity fluctuations are coupled as suggested by Giddings [52].

In capillary HPLC typical bed lengths (L_{bed}) are ~20 cm so that the ratio L_{bed}/d_c is on the order of thousands, i.e., analyte molecules eluting from a column are completely equilibrated between velocity extremes that may exist over the column cross-section. The detailed simulations of flow and eddy dispersion in bulk and complementary confined sphere packings of Khirevich et al. [53] have taught us that for $\nu < 30$ (a velocity range that is barely exceeded in capillary HPLC) the transchannel and transcolumn eddy dispersion contributions lose their coupling characteristic and can be represented as simple velocity-proportional terms. The functional h–ν dependence is then adequately described by [53]

$$h = \frac{b}{\nu} + \omega_1 \nu + \frac{2\lambda_2}{1 + (2\lambda_2/\omega_2)\nu^{-1}} + \omega_3 \nu + c\nu \qquad \text{(Eq. 7.1)}$$

Here, (b/ν) is the contribution from longitudinal molecular diffusion driven by the concentration gradient along the zone profile, while the last term ($c\nu$) accounts for the mass transfer kinetics into and across the stationary phase. The eddy dispersion operating on different length scales is characterized by the remaining terms, with universal structural parameters λ_i and ω_i for each contribution. These parameters refer to: the velocity biases across individual flow-through channels, i.e., transchannel eddy dispersion (i = 1); short-range interchannel dispersion on the scale of 1–2 d_p (i = 2) caused by the random positions of

particles in the bed; and transcolumn dispersion (i = 3), which occurs on the scale of the column radius (or worse, on the scale of the column diameter), commonly caused by confinement-based effects, such as column inlet/outlet or column wall effects [11]. For example, at the column wall particles cannot realize a random-close packing (as in the bulk of the bed), which results in several particle layers next to the wall where the microstructural order and density of the bed differs locally from that in the bulk region. This effect is known as geometrical wall effect [31,53,54].

The average external porosity [17,20] and transcolumn effects [11,51] are main contributors to the overall band broadening and therefore differentiate between a well packed and a mediocre packed column. Thus, in view of Eq. 7.1, our analysis of the reduced plate height curves suggests either a denser (smaller ω_1) or a radially more homogeneous bed (smaller ω_3) for the capillaries packed with the higher slurry concentrations. Consequently, we focus on these two aspects in our subsequent analysis.

7.3.1.2 Packing Density and Radial Heterogeneity. A simple, straightforward guess for an improved bed microstructure is a higher average packing density [17,20]. Fig. 7.3A shows radial porosity profiles computed from reconstructed segments of capillaries packed with the 1.9 and 1.7 µm BEH particles. Regrettably, the 0.9 µm particles were too small to be analyzed quantitatively using CLSM, i.e., particles closer or farther away from the objective lens will cause the recorded optical slice to become blurred due to an insufficient axial resolution. From Fig. 7.3A it is evident that the smaller 1.7 µm particles are harder to pack densely than the larger 1.9 µm particles. The bulk porosity ε_{bulk}, starting at a distance of ~3 d_p from the capillary wall, is quite high for the 1.7 µm particles (ε_{bulk} = 0.44) and characterizes a rather loose packing [55], whereas ε_{bulk} = 0.39 indicates more densely packed beds for the 1.9 µm particles (although this value still deviates from the random-close packing limit even for monodisperse particles, with $\varepsilon_{bulk} \approx 0.36$ [56]). It therefore may appear intuitive to assume that the difference in the bulk packing densities explains the smaller slope of the h–ν curves in Fig. 2 for the 1.9 µm particles. However, the differences in the porosity profiles for the two slurry concentrations and a given particle diameter are much smaller than differences between the particles. It is therefore too ambitious to claim a systematic difference in the bed microstructure for a slurry concentration of 3 mg/mL compared to the 30 and 100 mg/mL, respectively, which is exclusively based on the analyzed porosity data.

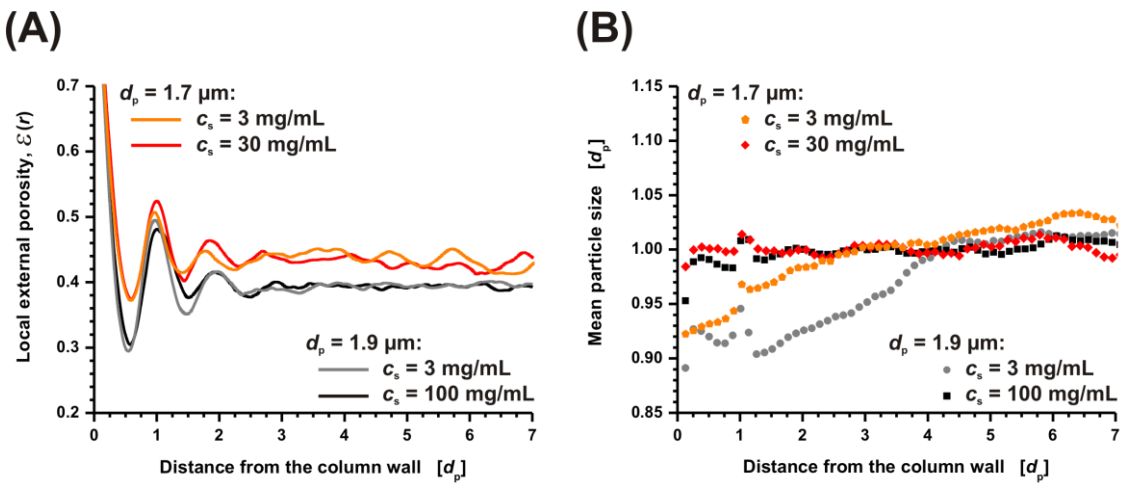

Figure 7.3: (**A**) Radial porosity profiles $\varepsilon(r)$ in the wall region of the reconstructed capillaries packed with the 1.7 and 1.9 µm BEH particles. (**B**) Locally resolved mean particle size. The distance from the capillary wall (r = 0) and the mean particle size are normalized by d_p (cf. Table 7.1).

In previous work we have already observed that with aspect ratios $d_c/d_p \geq 25$ the particles may tend to segregate according to their size [31]. In that observed case it means that smaller particles are more likely found in the vicinity of the column wall, while larger particles tend to be located in the column center at higher probability. Assuming all other effects as unchanged the particle segregation causes a nonuniform local transchannel eddy dispersion term over the whole capillary cross-section. Hence, it engenders a heterogeneity on the scale of the column radius or column diameter (depending on the actual radial symmetry of the effect), which increases the transcolumn eddy dispersion. Fig. 7.3B compares the mean particle size that we analyzed in our reconstructions, plotted against the radial position in a column. In this plot we see a clear trend that explains why higher slurry concentrations are needed for the larger i.d. columns. While with c_s = 3 mg/mL the mean particle size decreases to 90 and 92% of the global mean particle size in the first ~5 particle layers next to the capillary wall, the mean particle size for the higher slurry concentrations remains practically constant, independent of the radial position in a column. It can be interpreted as follows. At low slurry concentrations the particles are able to rearrange during bed consolidation that occurs while packing. Presumably, smaller particles fill voids in a packing more likely than larger particles. Importantly, these voids are often located in the

interface region between the column wall and particle bed, resulting in a depletion of the small particles from the column center.

These findings, in turn, suggest to analyze the number of packing voids in the reconstructed beds. We define a packing "defect" as a void volume that can be filled by at least 25% of the particles from the actual PSD. It is not surprising to find more defects in the capillaries packed with the 1.7 µm particles compared with those packed with the larger particles, since the beds are looser in their bulk region (Table 7.2). With the smaller particle sizes gaps become more frequent and also larger with respect to d_p. This is impressively seen for capillaries packed with the 0.9 µm particles (Fig. 7.1D). Although the total number of voids that we identified in each packing is on the order of just a few tens, a trend is visible: Capillaries packed with higher slurry concentrations commonly show more packing voids than the capillaries packed with low slurry concentration (3 mg/mL), which confirms that particles in a higher particle-density slurry become increasingly immobile during the bed consolidation and cannot fill the packing voids as effectively as from a dilute slurry.

Table 7.2: Analysis of packing defects in the CLSM-based reconstructions.[a]

	c_s [mg/mL]	No. of defects	Defects [nL^{-1}]
1.7 µm BEH	3	46	1.1×10^3
	30	70	2.2×10^3
1.9 µm BEH[b]	3	28	3.2×10^2
	100	37	3.9×10^2
1.9 µm Kinetex	3	2	4.3×10^1
	30	4	9.3×10^1

a) Void space that could be filled with particles from at least 25% of a PSD was defined as a defect and extrapolated to 1 nL of capillary volume for comparison.

b) Values for these capillaries are the averages from three reconstructions.

Thus, our analysis suggests that an increase of the slurry concentration to suppress particle size segregation has the tradeoff in generating a larger number of packing defects, which may substantially increase the eddy dispersion, depending on the actual number and distribution of the defects [57]. An intermediate slurry concentration provides the best results in terms of separation efficiency. Depending on the i.d. of a capillary the slurry concentration has to be high enough that particles cannot segregate, but still as low as possible to avoid unnecessary generation of packing voids. Since particle size segregation is not a critical issue in capillaries with $d_c/d_p < 25$, that is why these capillaries pack extremely well with a slurry concentration of only 3 mg/mL [31], and 20–100 mg/mL slurries are needed for the larger aspect ratios ($d_c/d_p \approx 29$–39) encountered in the present work.

7.3.2 Core–Shell Particles. With these results the next logical step was to investigate capillaries packed with the core–shell particles. The low RSD of these particles of only ~6% would not allow for effective particle size segregation, and if this was the exclusive reason for the separation efficiency to deteriorate at low slurry concentrations, no significant improvement should be observed as the slurry concentration is increased. Hence, we packed capillaries of 50 µm i.d. with 1.9 µm Kinetex core–shell particles ($d_c/d_p \approx 26$) using c_s = 3 mg/mL and 30 mg/mL and analyzed the column efficiency as for the fully porous particles. Compared to capillaries packed with the fully porous particles the gain in separation efficiency was less distinct but still present, i.e., h_{min} was reduced from 2.6 to 2.4 and also the slope of the reduced plate height curves flattened slightly (Fig. 7.4).

First of all, even the lower h_{min} value of 2.4 does not indicate a well-packed column. This is a problem we frequently observed when packing core–shell particles into capillary columns [20]. The reasons can be found in the transcolumn porosity profiles of the reconstructions that we built from these columns (Fig. 7.5A). The narrow PSD of the core–shell particles manifests itself in pronounced porosity oscillations in the wall region of the columns. This allows for a very regular (“crystal-like”) bed microstructure, and a minimum in the local porosity of 0.33 is reached after a distance of ~4 d_p from the column wall, whereas the fully porous particles show bulk behavior after ~3 d_p (cf. Fig. 7.3A). Beyond that minimum the porosity slowly increases towards the bulk value. This transition may take several d_p’s until the porosity profile is flat. Overall, it results in a wall effect that affects relatively large volumes of a capillary. Therefore, the performance of the capillary columns packed with core–shell particles is worse than demonstrated previously for the analytical column format, with $h_{min} < 1.6$ [16].

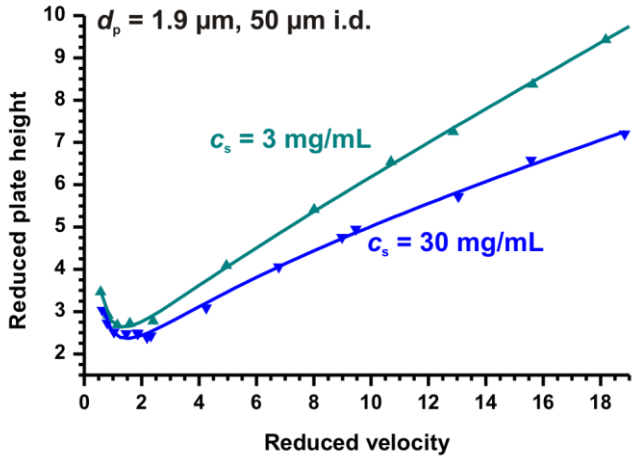

Figure 7.4: Reduced plate height curves (reduced plate height $h = H/d_p$ vs. the reduced velocity $\nu = u_{av}d_p/D_m$) for hydroquinone in a 50/50 (v/v) water/ACN mobile phase (k' = 0.20) recorded on the best performing fused-silica capillaries packed with 1.9 µm Kinetex particles using different slurry concentrations (c_s). Solid lines are best fits of Eq. 7.1 to the h–ν data to guide the eye.

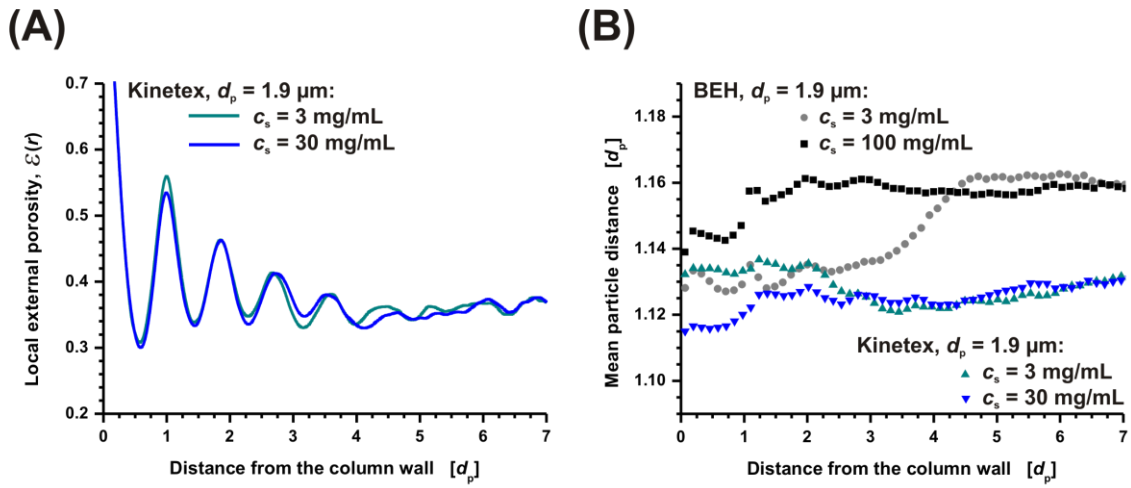

Figure 7.5: (**A**) Radial porosity profiles $\varepsilon(r)$ in the wall region of the reconstructed capillaries packed with the 1.9 µm Kinetex particles. (**B**) Locally resolved mean particle distance in a spherical volume of 1.5 d_p radius around each reconstructed particle (mean particle distance in capillaries packed with 1.9 µm BEH particles is provided as reference). The distance from the capillary wall (r = 0) and the mean particle distance are normalized by d_p (cf. Table 7.1).

On the other hand, the number of packing voids in these core–shell beds is extremely low (Table 7.2). In analytical columns, this is presumably a decided advantage of this particle type. Only two gaps have been identified in the capillary packed with c_s = 3 mg/mL, while four gaps were found for c_s = 30 mg/mL, resulting in 43 and 93 packing voids per nL of column volume, respectively. Still, this confirms the presence of more voids in beds packed with higher slurry concentrations.

As with Fig. 7.3A, the porosity profiles for the two slurry concentrations in Fig. 7.5A look very similar. Therefore, we decided to eliminate the uncertainty in the individual particle size from our characterization. The location (center) of a particle can be identified very precisely, and with all the particles having a similar size, the distance between particles provides a detailed look into the local porosity distribution. In Fig. 7.5B the mean distance between particles in the reconstructions is plotted against the radial position in the column. It is smaller for the Kinetex packings than for the 1.9 µm BEH packings (that are provided for comparison). The smaller mean particle distance indicates a denser packed wall region for the core–shell packings. Naturally, the mean particle distance drops in the immediate wall region ($\leq 1\ d_p$ from the wall), since only particles smaller than the mean particle diameter can approach the wall closer than by one d_p. For distances > 1 d_p from the wall the profile remains flat for the BEH packing with c_s = 100 mg/mL, illustrating a homogeneous bed microstructure, but remains at smaller particle distances (up to ~4.5 d_p from the wall) with c_s = 3 mg/mL, which is a result of the particle size segregation. For the core–shell columns the mean particle distance is constant in the region at 1–4.5 d_p from the wall for the higher slurry concentration (30 mg/mL) and starts to increase as we move on further towards the column center. This is a result of the transition to the bulk properties of the bed already observed in the porosity profiles (cf. Fig. 7.5A). The transition region is also present in the Kinetex packing obtained with c_s = 3 mg/mL. However, there is another region at 0–2.5 d_p from the wall showing increased mean particle distances that originate from a locally increased external porosity. Thus, our analysis of the Kinetex column packings suggests that the higher slurry concentration helped to compact the wall region. This is already implied by the small, but distinct differences in the porosity profiles of Fig. 7.5A and provides a reason for the slightly improved separation efficiency that is observed in Fig. 7.4.

7.4 Conclusions

In this study we illustrated how the slurry concentration used in the packing protocol affects the column efficiency and bed microstructure of capillaries packed with sub-2 µm fully porous and core–shell particles at column-to-particle diameter ratios $d_c/d_p > 25$. It was shown that higher slurry concentrations (20–100 mg/mL) provided columns with improved performance compared to capillaries packed at low slurry concentrations (2–3 mg/mL). Reasons for these improvements were found in the bed microstructures that we reconstructed from three-dimensional microscopic recordings acquired by CLSM. In the reconstructions we observed that higher slurry densities helped to attenuate transcolumn bed heterogeneities by suppressing particle size segregation at the expense of an increased number of packing voids. In the core–shell packings, where only a few packing voids could be identified, the higher slurry concentrations allowed for an additional densification of the critical wall region.

Our observations suggest that capillaries packed at $d_c/d_p < 25$ are preferably prepared at a very low slurry concentration to minimize the number of packing defects. This was revealed in our previous study when we packed 10, 20, and 30 µm i.d. capillaries with 1.9 µm BEH particles using a slurry concentration of 3 mg/mL. The resulting columns displayed extraordinary low h_{min} values, as low as 1.2 [31]. In the current work, capillary columns with larger aspect ratios (up to ~40) were packed efficiently using higher slurry concentrations of 20–100 mg/mL. The obtained h_{min} values of ≤ 1.6 even challenge the core–shell particles when realized in an analytical column format.

Although the literature does not present a study regarding the influence of an incremental increase in the slurry concentration on the separation efficiency of the prepared packings, the optimal slurry concentration for narrow-bore and analytical columns seems to be even higher [22]. By extrapolating our results to these larger column diameters, we consider the choice for a particular slurry concentration always as a compromise between wall effects (transcolumn bed heterogeneities) and overall packing defects.

Acknowledgement

This work was supported by the Deutsche Forschungsgemeinschaft DFG (Bonn, Germany) under grant TA 268/5-1. Column preparation work was supported by Waters Corporation (Milford, MA), and JPG was supported by the National Science Foundation Graduate Research Fellowship (Arlington, VA) under grant DGE-0646083. We thank J. Scott Mellors and J. Michael Ramsey (Department of Chemistry, University of North Carolina at Chapel Hill) for providing the Kinetex particles.

References

[1] Gritti, F.; Guiochon, G. *J. Chromatogr., A* **2012**, *1228*, 2–19.

[2] Farkas, T.; Chitty, M.; Layne, J.; Anspach, J.; Sanchez, C. *The New Cutting Edge in Reversed-Phase UHPLC Performance: 1.3 μm Core-Shell Particles*. Oral presentation at HPLC 2013, Amsterdam, The Netherlands, **2013**.

[3] Hiemenz, P. C.; Rajagopalan, R. *Principles of Colloid and Surface Chemistry. 3rd Ed.*, CRC Press, Taylor & Francis Group, Boca Raton, **1997**.

[4] Wahab, M. F.; Pohl, C. A.; Lucy, C. A. *J. Chromatogr., A* **2012**, *1270*, 139–146.

[5] Rogers, B. J.; Wirth, M. J. *ACS Nano* **2013**, *7*, 725–731.

[6] Wu, Z.; Rogers, B. J.; Wei, B.; Wirth, M. J. *J. Sep. Sci.* **2013**, *36*, 1871–1876.

[7] Wei, B.; Rogers, B. J.; Wirth, M. J. *J. Am. Chem. Soc.* **2012**, *134*, 10780–10782.

[8] Nováková, L.; Veuthey, J.-L.; Guillarme, D. *J. Chromatogr., A* **2011**, *1218*, 7971–7981.

[9] Gritti, F.; Martin, M.; Guiochon, G. *Anal. Chem.* **2009**, *81*, 3365–3384.

[10] de Villiers, A.; Lauer, H.; Szucs, R.; Goodall, S.; Sandra, P. *J. Chromatogr., A* **2006**, *1113*, 84–91.

[11] Gritti, F.; Guiochon, G. *Anal. Chem.* **2013**, *85*, 3017–3035.

[12] Guiochon, G. *J. Chromatogr., A* **2006**, *1126*, 6–49.

[13] Kirkland, J. J.; Langlois, T. J.; DeStefano, J. J. *Am. Lab.* **2007**, *39*, 18–21.

[14] Gritti, F.; Leonardis, I.; Shock, D.; Stevenson, P.; Shalliker, A.; Guiochon, G. *J. Chromatogr., A* **2010**, *1217*, 1589–1603.

[15] Gritti, F.; Guiochon, G. *J. Chromatogr., A* **2010**, *1217*, 8167–8180.

[16] Guiochon, G.; Gritti, F. *J. Chromatogr., A* **2011**, *1218*, 1915–1938.

[17] Daneyko, A.; Höltzel, A.; Khirevich, S.; Tallarek, U. *Anal. Chem.* **2011**, *83*, 3903–3910.

[18] Gritti, F.; Guiochon, G. *J. Chromatogr., A* **2013**, *1280*, 35–50.

[19] Gritti, F.; Guiochon, G. *LC–GC North Am.* **2012**, *30*, 586–595.

[20] Bruns, S.; Stoeckel, D.; Smarsly, B.; M. Tallarek, U. *J. Chromatogr., A* **2012**, *1268*, 53–63.

[21] Abia, J. A.; Mriziq, K. S.; Guiochon, G. *J. Chromatogr., A* **2009**, *1216*, 3185–3191.

[22] Kirkland, J. J.; DeStefano, J. J. *J. Chromatogr., A* **2006**, *1126*, 50–57.

[23] Bruns, S.; Höltzel, A.; Tallarek, U. *LC–GC North Am.* **2013**, *31*, 486–493.

[24] Hormann, K.; Müllner, T.; Bruns, S.; Höltzel, A.; Tallarek, U. *J. Chromatogr., A* **2012**, *1222*, 46–58.

[25] Bruns, S.; Hara, T.; Smarsly, B. M.; Tallarek, U. *J. Chromatogr., A* **2011**, *1218*, 5187–5194.

[26] Bruns, S.; Tallarek, U. *J. Chromatogr., A* **2011**, *1218*, 1849–1860.

[27] Bruns, S.; Müllner, T.; Kollmann, M.; Schachtner, J.; Höltzel, A.; Tallarek, U. *Anal. Chem.* **2010**, *82*, 6569–6575.

[28] Koku, H.; Maier, R. S.; Schure, M. R.; Lenhoff, A. M. *J. Chromatogr., A* **2012**, *1237*, 55–63.

[29] Müllner, T.; Zankel, A.; Mayrhofer, C.; Reingruber, H.; Höltzel, A.; Lv, Y.; Svec, F.; Tallarek, U. *Langmuir* **2012**, *49*, 16733–16737.

[30] Stoeckel, D.; Kübel, C.; Tallarek, U.; Smarsly, B. M. *3D Reconstruction of a Mesoporous Monolithic Silica Structure Using Scanning Transmission Electron Microscopy (STEM) Tomography*. Poster presentation at HPLC 2013, Amsterdam, The Netherlands, **2013**.

[31] Bruns, S.; Grinias, J. P.; Blue, L. E.; Jorgenson, J. W.; Tallarek, U. *Anal. Chem.* **2012**, *84*, 4496–4503.

[32] Hsieh, S. C.; Jorgenson, J. W. *Anal. Chem.* **1996**, *68*, 1212–1217.

[33] Patel, K. D.; Jerkovich, A. D.; Link, J. C.; Jorgenson, J. W. *Anal. Chem.* **2004**, *76*, 5777–5786.

[34] Jung, S.; Höltzel, A.; Ehlert, S.; Mora, J. A.; Kraiczek, K.; Dittmann, M.; Rozing, G. P.; Tallarek, U. *Anal. Chem.* **2009**, *81*, 10193–10200.

[35] Jung, S.; Ehlert, S.; Mora, J. A.; Kraiczek, K.; Dittmann, M.; Rozing, G. P.; Tallarek, U. *J. Chromatogr., A* **2009**, *1216*, 264–273.

[36] Ehlert, S.; Trojer, L.; Vollmer, M.; van de Goor, T.; Tallarek, U. *J. Mass Spectrom.* **2010**, *45*, 313–320.

[37] Ehlert, S.; Kraiczek, K.; Mora, J. A.; Dittmann, M.; Rozing, G. P.; Tallarek, U. *Anal. Chem.* **2008**, *80*, 5945–5950.

[38] Wyndham, K. D.; O'Gara, J. E.; Walter, T. H.; Glose, K. H.; Lawrence, N. L.; Alden, B. A.; Izzo, G. S.; Hudalla, C. J.; Iraneta, P. C. *Anal. Chem.* **2003**, *75*, 6781–6788.

[39] Neue, U. D. *HPLC Columns: Theory, Technology, and Practice*. Wiley-VCH, New York, **1997**.

[40] MacNair, J. E.; Lewis, K. C.; Jorgenson, J. W. *Anal. Chem.* **1997**, *69*, 983–989.

[41] MacNair, J. E.; Patel, K. D.; Jorgenson, J. W. *Anal. Chem.* **1999**, *71*, 700–708.

[42] Mellors, J. S.; Jorgenson, J. W. *Anal. Chem.* **2004**, *76*, 5441–5450.

[43] Maiolica, A.; Borsotti, D.; Rappsilber, J. *Proteomics* **2005**, *5*, 3847–3850.

[44] Knecht, L. A.; Guthrie, E. J.; Jorgenson, J. W. *Anal. Chem.* **1984**, *56*, 479–482.

[45] Luisier, F. *PureDenoise*; Biomedical Imaging Group, École Polytechnique Fédéral de Lausanne, **2010**; http://bigwww.epfl.ch/algorithms/denoise.

[46] Rasband, W. S. *ImageJ*; U.S. National Institutes of Health: Bethesda, MD, **1997-2006**; http://rsb.info.nih.gov//ij/.

[47] Gritti, F.; Guiochon, G. *AIChE J.* **2010**, *56*, 1495–1509.

[48] Gritti, F.; Guiochon, G. *J. Chromatogr., A* **2010**, *1217*, 6350–6365.

[49] Gritti, F.; Guiochon, G. *J. Chromatogr., A* **2013**, *1297*, 85–95.

[50] Kaiser, T. J.; Thompson, J. W.; Mellors, J. S.; Jorgenson, J. W. *Anal. Chem.* **2009**, *81*, 2860–2868.

[51] Gritti, F.; Guiochon, G. *J. Chromatogr., A* **2013**, *1302*, 1–13.

[52] Giddings, J. C. *Dynamics of Chromatography, Part 1: Principles and Theory*; Marcel Dekker, New York, **1965**.

[53] Khirevich, S.; Höltzel, A.; Seidel-Morgenstern, A.; Tallarek, U. *Anal. Chem.* **2009**, *81*, 7057–7066.

[54] Khirevich, S.; Höltzel, A.; Seidel-Morgenstern, A.; Tallarek, U. *J. Chromatogr., A* **2012**, *1262*, 77–91.

[55] Ehlert, S.; Rösler, T.; Tallarek, U. *J. Sep. Sci.* **2008**, *31*, 1719–1728.

[56] Baranau, V.; Hlushkou, D.; Khirevich, S.; Tallarek, U. *Soft Matter* **2013**, *9*, 3361–3372.

[57] Schure, M. R.; Maier, R. S. *J. Chromatogr., A* **2006**, *1126*, 58–69.

IV. Conclusions

This work established a new methodology to image, restore, reconstruct, and analyze silica-based stationary phase support in capillaries using confocal laser scanning microscopy (CLSM). This was done for capillaries of 10–100 µm i.d.. Staining methods were developed for common surface chemistries, i.e., bare-silica and C18 modified silica. The optical setup for imaging was optimized for resolution by balancing out all optical aberrations that occur due to the complex layout of the sample. The final restoration procedure comprises a correction for photon noise, axial signal intensity loss, and sample drift as well as deconvolution. To handle the large amount of data semi-automatic methods were developed in C# to detect particles and monolithic rods enabling a quantification of microstructural properties and heterogeneities in these columns. Structural descriptors that correlate with the individual length scales of eddy dispersion were established for this purpose. Chord length distributions were fitted by a *k*-gamma distribution to describe the transchannel and short-range interchannel scale of eddy dispersion while radial transcolumn plots were applied to characterize transcolumn contributions to eddy dispersion. The radial plots applied in the different studies were plots of porosity, pore size and particle size distributions as well as integral porosity deviation and mean particle distance.

Applications for the reconstruction method were found in cooperation with working groups that have their expertise in the preparation of capillary columns. The group of Prof. Smarsly (Justus-Liebig-Universität, Gießen, Germany) provided a series of monoliths that was evaluated to illustrate how monolith shrinkage deteriorates the separation efficiency of capillary monoliths (Chapter 3). Still, the studies also show that, if wall displacements can be avoided and microstructural features in these columns are further reduced, the monolithic format shows great potential for column technology because of it's higher structural homogeneity when compared with particulate columns (Chapter 6).

Capillaries packed by the same group with core–shell and fully porous particles helped to illustrate that these two types of material pack indistinguishable in the bulk region of a column but differently to a confining capillary wall (Chapter 5). While fully porous particles pack looser in the wall region of the bed than in the bulk, core–shell particles display a higher order and denser packing than fully porous particles in the first five particle layers next to the capillary wall. This was seen in pronounced oscillations within the transcolumn

porosity profiles that were computed from the reconstructions. These oscillations have a mean value below the bulk porosity value. A necessary consequence is that core–shell packed beds also show a transition region 5–10 d_p in the column where bulk porosity is approached. Hence, wall effects in core–shell packed beds are less pronounced but cover a larger capillary volume than wall effects in beds packed with fully porous particles.

Other studies that aimed at unraveling the influence of process parameters in the slurry packing process were performed in cooperation with the group of Prof. Jorgenson (University of North Carolina at Chapel Hill, Chapel Hill, North Carolina, United States). They packed capillaries of varying i.d. with sub-2 micron particles that were characterized for their chromatographic and microstructural properties (Chapter 4). The study showed that at column-to-particle diameter aspect ratios (d_c/d_p) above 25 separation efficiency drops due to increased transcolumn heterogeneities in the bed, i.e., the packing density in these columns is lower in the wall region than for columns packed at aspect ratios below 25. Additionally, it was possible to show that the mean particle size is not a constant along the column diameter. At $d_c/d_p > 25$ particles started to segregate with smaller particles being more likely located near the capillary wall than larger particles. These particles had a higher probability of being located in the capillary center when the capillaries were packed with slurry concentrations < 1%. The effect was further investigated in a study that questioned the effect of slurry concentration on bed morphology (Chapter 7). It was shown that higher slurry concentrations allow suppressing particle size segregation at the cost of an increased amount of packing voids in the bed improving h_{min} of capillaries packed with fully porous particles to ~1.5 at slurry concentrations of 2%–10%. With core–shell particles an improvement was also observed. Here, a slurry concentration of 3% enabled compacting the bed in the crucial wall region of the capillary which improved h_{min} from 2.6 to 2.4 when compared with a capillary packed at 0.3% slurry concentration.

The reconstruction method established in this work also supported other research projects. Hlushkou et al. [1–3] used CLSM-reconstructions of capillary monoliths to perform numerical simulations of flow and transport in these media illustrating the large impact of wall defects and highlighting the potential separation efficiency of silica monoliths in their absence. Hormann et al. [4] extended the reconstruction method to analytical scale silica monoliths. They characterized the morphological improvements of Chromolith High-Resolution columns over Chromolith Performance columns using the descriptors introduced in this work. Subsequent numerical simulations of the dispersive contributions in the

reconstructed column segments proved that the short-range interchannel contribution to eddy dispersion was in fact reduced as predicted by the chord length analysis [5]. The most important improvements in separation efficiency however were made by decreasing the radial heterogeneity of Chromolith High-Resolution columns compared to Chromolith Performance columns. Thus once again, these studies emphasize the importance of transcolumn contributions in modern HPLC columns and manufacturers will have to address them. CLSM-reconstructions have shown to be suitable tool to accompany that task. They provide a feasible approach to visualize and quantify microstructural features in an experimental column: an important step toward the understanding of morphology–transport relationships in HPLC.

References

[1] Hlushkou, D.; Bruns, S.; Tallarek, U. *J. Chromatogr., A* **2010**, *1217*, 3674–3682.

[2] Hlushkou, D.; Bruns, S.; Höltzel, A.; Tallarek, U. *Anal. Chem.* **2010**, *82*, 7150–7159.

[3] Hlushkou, D.; Bruns, S.; Seidel-Morgenstern, A.; Tallarek, U.; *J. Sep. Sci.* **2011**, *34*, 2026–2037.

[4] Hormann, K.; Müllner, T.; Bruns, S.; Höltzel, A.; Tallarek, U. *J. Chromatogr., A* **2012**, *1222*, 46−58.

[5] Hlushkou, D.; Hormann, K.; Höltzel, A.; Khirevich, S.; Seidel-Morgenstern, A.; Tallarek, U. *J. Chromatogr., A* **2013**, *1303*, 28–38.

Curriculum Vitae

--- Removed from digital version for privacy reasons! ---

List of Publications

Articles

Bruns, S.; Franklin, E. G.; Grinias, J. P.; Godinho, J. M.; Jorgenson, J. W.; Tallarek, U. *J. Chromatogr., A* **2013**, submitted. *"Slurry concentration effects on bed morphology and separation efficiency of capillaries packed with sub-2 micron particles"*.

Bruns, S.; Höltzel, A.; Tallarek, U. *LC-GC North Am.* **2013**, *31*, 486–493. *"Morphological Comparison of Silica Based Monolithic and Particulate Beds by Confocal Laser Scanning Microscopy"*.

Bruns, S.; Stoeckel, D.; Smarsly, B. M.; Tallarek, U. *J. Chromatogr., A* **2012**, *1268*, 53–63. *"Influence of Particle Properties on the Wall Region in Packed Capillaries"*.

Bruns, S.; Grinias J. P.; Blue, L. E.; Jorgenson, J. W.; Tallarek, U. *Anal. Chem.* **2012**, *84*, 4496–4503. *"Morphology and Separation Efficiency of Low-aspect-ratio Capillary Ultra-high Pressure Liquid Chromatography Columns"*.

Hormann, K.; Müllner, T.; **Bruns, S.**; Höltzel, A.; Tallarek, U. *J. Chromatogr., A* **2012**, *1222*, 46–58. *"Morphology and Separation Efficiency of a New Generation of Analytical Silica Monoliths"*.

Hlushkou, D.; **Bruns, S.**; Seidel-Morgenstern, A.; Tallarek, U. *J. Sep. Sci.* **2011**, *34*, 2026–2037. *"Morphology-transport Relationship for Silica Monoliths: From Physical Reconstruction to Pore-scale Simulations"*.

Bruns, S.; Hara, T.; Smarsly, B. M.; Tallarek, U. *J. Chromatogr., A* **2011**, *1218*, 5187–5194. *"Morphological Analysis of Physically Reconstructed Capillary Hybrid Silica Monoliths and Correlation with Separation Efficiency"*.

Bruns, S.; Tallarek, U. *J. Chromatogr., A* **2011**, *1218*, 1849–1860. *"Physical Reconstruction of Packed Beds and their Morphological Analysis: Core-shell Packings as an Example"*.

Hlushkou, D.; **Bruns, S.**; Höltzel, A.; Tallarek, U. *Anal. Chem.* **2010**, *82*, 7150–7159. *"From Pore Scale to Column Scale Dispersion in Capillary Silica Monoliths"*.

Bruns, S.; Müllner, T.; Kollmann, M.; Schachtner, J.; Tallarek, U. *Anal. Chem.* **2010**, *82*, 6569–6575. *"Confocal Laser Scanning Microscopy Method for Quantitative Characterization of Silica Monolith Morphology"*.

Hlushkou, D.; **Bruns, S.**; Tallarek, U. *J. Chromatogr., A* **2010**, *1217*, 3674–3682. *"High-performance Computing of Flow and Transport in Physically Reconstructed Silica Monoliths"*.

Oral Presentations

"From Pore Level Reconstruction to Morphological Analysis of Eddy Dispersion", plenary lecture, 06/16/2013, **HPLC 2013** – 39th International Symposium on High-Performance Liquid Phase Separations and Related Techniques, Amsterdam, The Netherlands.

"Slurry Packing Parameters and their Influence on Capillary Column Morphology", 06/20/2012, **HPLC 2012** – 38th International Symposium on High-Performance Liquid Phase Separations and Related Techniques, Anaheim, CA, USA.

"Morphology of Capillaries Packed with Sub-2 µm Particles at Low-Aspect-Ratio", 01/10/2012, **22. Doktorandenseminar** des AK Separation Science, Hohenroda, Germany.

"Physical Reconstruction of Packed Beds and their Morphological Analysis", 06/22/2011, **HPLC 2011** – 36th International Symposium on High-Performance Liquid Phase Separations and Related Techniques, Budapest, Hungary.

Poster Presentations

"Silica-based Monoliths and Particulate Beds: A Morphological Comparison", **HPLC 2013** – 39th International Symposium on High-Performance Liquid Phase Separations and Related Techniques, Amsterdam, The Netherlands.

"Morphological Characterization of Transcolumn Contributions in Capillary Chromatography", **ISC 2012** – 29th International Symposium on Chromatography, Toruń, Poland.

"Morphological Characterization of Transcolumn Contributions in Capillary Chromatography", **ISCC 2012** – 36th International Symposium on Capillary Chromatography, Riva del Garda, Italy.

"Insights into the Slurry Packing Process: Influence of Particle Size Distribution and Surface Roughness", **HPLC 2011** – 37th International Symposium on High-Performance Liquid Phase Separations and Related Techniques, Dalian, China.

"Morphological Analysis of Physically Reconstructed Capillary Hybrid Silica Monoliths and Correlation with Separation Efficiency", **HPLC 2011** – 36th International Symposium on High-Performance Liquid Phase Separations and Related Techniques, Budapest, Hungary.

"Non-destructive Morphological Characterization of the Morphology of Silica Monoliths by Confocal Laser Scanning Microscopy", **ISPPP 2010** – 30th European Symposium on the Separation of Proteins, Peptides and Polynucleotides, Bologna, Italy.

"Non-destructive Morphological Characterization of Silica-based Monolithic Capillary Columns by Confocal Laser Scanning Microscopy", **HPLC 2010** – 35th International Symposium on High-Performance Liquid Phase Separations and Related Techniques, Boston, MA, USA.

Awards

"Csaba Horváth Young Scientist Award", **HPLC 2012** – 38th International Symposium on High-Performance Liquid Phase Separations and Related Techniques, Anaheim, CA, USA.

"Shimadzu Best Poster Award", **ISCC 2012** – 36th International Symposium on Capillary Chromatography, Riva del Garda, Italy.

"Csaba Horváth Young Scientist Award Nominee", **HPLC 2011** – 36th International Symposium on High-Performance Liquid Phase Separations and Related Techniques, Budapest, Hungary.

"*Outstanding Poster Award*", **HPLC 2010** – 35th International Symposium on High-Performance Liquid Phase Separations and Related Techniques, Boston, MA, USA.

Erklärung der Eigenleistung

Die vorliegende Arbeit entstand durch Mithilfe verschiedener Koautoren, deren Beitrag im Folgenden ausgeführt wird:

Tibor Müllner half einen geeigneten Farbstoff für die Oberflächenmodifizierung des Monolithen zu finden und diesen herzustellen. Martin Kollmann und Prof. Dr. Joachim Schachtner stellten das Konfokalmikroskop zur Verfügung und halfen mir mich mit dem Gerät vertraut zu machen. Alle experimentellen Daten wurden von mir erfasst und ausgewertet. Das Manuskript wurde von mir ausgearbeitet und von Dr. Alexandra Höltzel und Prof. Dr. Ulrich Tallarek sprachlich überarbeitet, korrigiert und von Letzterem eingereicht.

Sämtliche experimentelle Daten in Kapitel 2 wurden von mir erfasst und ausgewertet. Dr. Steffen Ehlert half mir beim Packen der Kapillare. Prof. Dr. Tallarek half bei der Korrektur des Manuskripts und reichte dieses ein.

Die Kapillarmonolithen in Kapitel 3 wurden von Dr. Takeshi Hara unter der Aufsicht von Prof. Dr. Bernd Smarsly präpariert und chromatographisch ausgewertet. Bildgebung, Bildverarbeitung und Auswertung der Mikrostrukturen wurden von mir durchgeführt. Das Manuskript habe ich verfasst. Korrekturen wurden von Prof. Dr. Bernd Smarsly und Prof. Dr. Ulrich Tallarek vorgenommen. Letzterer reichte das Manuskript ein.

Die Kapillaren in Kapitel 4 wurden von James P. Grinias und Laura E. Blue gepackt und chromatographisch ausgewertet. Alle weiteren experimentellen Schritte sowie die Auswertung der Bilddaten wurden von mir durchgeführt. Prof. Dr. James W. Jorgenson und Prof. Dr. Ulrich Tallarek halfen bei der Korrektur des Manuskripts und reichten dieses ein.

Rasterelektronenmikroskpieaufnahmen in Kapitel 5 wurden von Daniela Stoeckel aufgenommen. Daniela Stoeckel packte die Kapillaren und bestimmte ihre Effizienz. Konfokale Bildgebung, Bildverarbeitung und Auswertung der Mikrostruktur der Partikelschüttungen wurden von mir durchgeführt. Das Manuskript wurde von mir erstellt und von

Prof. Dr. Bernd Smarsly und Prof. Dr. Ulrich Tallarek korrigiert. Prof Dr. Tallarek reichte das Manuskript ein.

Der Silicamonolith in Kapitel 6 wurde von Dr. Takeshi Hara präpariert. James P. Grinias und Prof. Dr. James W. Jorgenson stellten die gepackte Säule zur Verfügung. Die experimentellen Daten wurden von mir erfasst und die Ergebnisse in ein Manuskript überführt. Dr. Alexandra Höltzel half das Manuskript für den Leser ansprechend zu gestalten, während Prof. Dr. Ulrich Tallarek dieses korrigierte und einreichte.

Die in Kapitel 7 verwendeten Kapillaren wurden von Edward G. Franklin, James P. Grinias und Justin M. Godinho gepackt und chromatographisch ausgewertet. Weitere experimentelle Arbeiten, die Auswertung der Bilddaten, ihre Interpretation sowie die Erstellung des Manuskripts habe ich vorgenommen. Prof. Dr. James W. Jorgenson und Prof. Dr. Ulrich Tallarek halfen bei der Korrektur des Manuskripts. Letzterer reichte dieses ein.

Ort, Datum, Unterschrift Promovierender

Ort, Datum, Unterschrift Betreuer

Erklärung

Ich versichere, dass ich die vorliegende Dissertation mit dem Titel

Experimental Analysis and Reconstruction of the Morphology of Particulate and Monolithic Chromatographic Beds

selbständig, ohne unerlaubte Hilfe angefertigt und mich dabei keiner anderen als der von mir ausdrücklich bezeichneten Quellen und Hilfen bedient habe. Die Dissertation wurde in der jetzigen oder einer ähnlichen Form noch bei keiner anderen Hochschule oder Fachhochschule eingereicht und hat noch keinem sonstigen Prüfungszweck gedient.

_____

Ort, Datum, Unterschrift